INFORMATION TO USERS

This manuscript has been reproduced from the microfilm master. UMI films the text directly from the original or copy submitted. Thus, some thesis and dissertation copies are in typewriter face, while others may be from any type of computer printer.

The quality of this reproduction is dependent upon the quality of the copy submitted. Broken or indistinct print, colored or poor quality illustrations and photographs, print bleedthrough, substandard margins, and improper alignment can adversely affect reproduction.

In the unlikely event that the author did not send UMI a complete manuscript and there are missing pages, these will be noted. Also, if unauthorized copyright material had to be removed, a note will indicate the deletion.

Oversize materials (e.g., maps, drawings, charts) are reproduced by sectioning the original, beginning at the upper left-hand corner and continuing from left to right in equal sections with small overlaps. Each original is also photographed in one exposure and is included in reduced form at the back of the book.

Photographs included in the original manuscript have been reproduced xerographically in this copy. Higher quality 6" x 9" black and white photographic prints are available for any photographs or illustrations appearing in this copy for an additional charge. Contact UMI directly to order.

Seismic velocity structure and attenuation of the Arabian plate

Ghalib, Hafidh A. A., Ph.D.

Saint Louis University, 1992

U·M·I
300 N. Zeeb Rd.
Ann Arbor, MI 48106

SEISMIC VELOCITY STRUCTURE AND ATTENUATION

OF THE ARABIAN PLATE

Hafidh A. A. Ghalib, B.S., M.S., P-G.D.

A Dissertation Presented to the Faculty of the Graduate
School of Saint Louis University in Partial
Fulfillment of the Requirements for the
Degree of Doctor of Philosophy

1992

SEISMIC VELOCITY STRUCTURE AND ATTENUATION

OF THE ARABIAN PLATE

Hafidh A. A. Ghalib, B.S., M.S., P-G.D.

A Digest Presented to the Faculty of the Graduate
School of Saint Louis University in Partial
Fulfillment of the Requirements for the
Degree of Doctor of Philosophy

1992

DIGEST

This study consists of two distinct parts. Each describes an effort to advance our current understanding of the Arabian plate seismotectonic environment.

In the first part, the dispersive properties of long-period Rayleigh waves are used to investigate the plate's seismic velocity structure variation. The mixed-path fundamental- and higher-mode group velocity dispersion curves are calculated using a single-station method. To facilitate interpreting the variation, two approaches are followed in the analysis of data. First, the dispersion curves for each station are averaged according to their similarity and mixed-path orientation. Second, pure-path dispersion curves are estimated using the grid-dispersion inversion method. An iterative non-linear differential inversion technique and a single layer over half-space starting model are used to invert all the dispersion curves. The mixed-path models show significant variation in the plate's structure. Beneath a thick sedimentary layer, two discontinuities at 15-20 and 35-55 km depth are observed in the region. According to the three-dimensional model, the most dominant features are the Arabian shield and Mesopotamian foredeep. Within the crust the velocity is highest under the shield, but below 40 km depth it is lower than the rest of the plate.

In the second part, the attenuation of high-frequency seismic wave is investigated, and the developed "extended coda-Q" technique is applied to short period Lg coda waves. This technique is based on least squares principles, and provides a deterministic procedure for estimating the quality factor and its frequency dependence simultaneously. At 1 Hz an average

-1-

of $Q_0 = 214$, $\zeta = 0.6$, and $\gamma = 0.0045$ km^{-1} are found for the Arabian plate. The lowest Q_0 values are found along the Zagros. In comparison, the Arabian shield shows surprisingly low Q_0 values that may be attributed to its young age, intensive metamorphism and deformation.

COMMITTEE IN CHARGE OF CANDIDACY:

Professor Robert B. Herrmann,
        Chairperson and Advisor

Professor Brian J. Mitchell

Associate Professor Guy M. Smith

ACKNOWEDGEMENTS

TABLE OF CONTENTS

TABLE OF CONTENTS (CONT'D)

LIST OF TABLES

LIST OF TABLES (CONT'D)

LIST OF TABLES (CONT'D)

LIST OF TABLES (CONT'D)

LIST OF TABLES (CONT'D)

LIST OF ILLUSTRATIONS

LIST OF ILLUSTRATIONS (CONT'D)

LIST OF ILLUSTRATIONS (CONT'D)

LIST OF ILLUSTRATIONS (CONT'D)

LIST OF ILLUSTRATIONS (CONT'D)

LIST OF ILLUSTRATIONS (CONT'D)

LIST OF ILLUSTRATIONS (CONT'D)

LIST OF ILLUSTRATIONS (CONT'D)

LIST OF ILLUSTRATIONS (CONT'D)

LIST OF ILLUSTRATIONS (CONT'D)

CHAPTER 1

INTRODUCTION

The Arabian plate is composed of several diversified seismotectonic environments. It's boundaries are associated with seismically active zones consisting of continental collision, sea-floor spreading, transform faulting and subduction. The plate's major tectonic provinces, which are briefly reviewed in Chapter 2, include the Arabian shield and platform, the Mesopotamian foredeep and the Zagros folded belt. A large portion of the relatively young, intensely faulted and metamorphosed shield is exposed to the surface. The folded belt and most of the foredeep include very thick sedimentary layers from the time of the Tethys Ocean. Folding and faulting are extensive throughout the entire plate. In addition, evidence of recent volcanic activity can be found along the plate's western margin parallel to the Red and Dead Seas. Although the occurrence of plate margin earthquakes is more common than intraplate ones, through the centuries various regions of the plate have been devastated by moderate to large intraplate events. Historical manuscripts are rich with detailed descriptive accounts of many such catastrophic earthquakes. The most recent instrumentally recorded damaging event struck in North Yemen on December 13, 1982, with an estimated magnitude of $m_b = 6.0$ and a shallow depth of about 7.0 km.

Nevertheless, the Arabian plate is probably still one of the least studied seismotectonic regions of the Earth. In particular, very little is known about the variation of either its crustal and upper mantle velocity structures,

or attenuation of seismic waves within such a relatively large lithospheric block. In past decades, only a limited number of local and regional studies attempting to explain the physical or structural features of this plate have been published. In general, most of our present knowledge of the region has evolved from geological and shallow geophysical exploration surveys. It is unfortunate that academic research on the seismotectonics of the plate has not been fully supported, since it can also provide economic benefits. As an example, the information this research contributes is necessary for a variety of purposes, including the investigation of seismic waves propagation, locating earthquakes, developing local magnitude relations, assessment and mitigation of earthquake risk, and interpreting the composition and evolution of the plate.

This study consists of two distinct parts which represent a continuing effort to supplement our current understanding of the seismotectonic characteristics of the Arabian plate. The objective of the first part is to utilize the dispersive properties of long-period Rayleigh waves to investigate the vertical and lateral variations of the plate's seismic structure. The multiple filter single-station method is used to calculate the mixed-path fundamental- and higher-mode group velocity dispersion data presented in Chapter 3. To facilitate interpreting the crustal shear velocity structure variations, the dispersion data are treated in two different ways. By following the more traditional approach, the individual data sets for each station are averaged according to their general mixed-path orientation and dispersive similarities. The second approach utilizes the grid-dispersion inversion technique. This is a stochastic regionalization procedure used to extract pure-path group velocities from mixed-path dispersion data. In either case,

all the dispersion data regardless of their path type are inverted in the same manner using an iterative non-linear differential inversion technique and a horizontally layered half space starting model. The resulting shear velocity profiles and three-dimensional velocity and depth models, which illustrate the lateral variation of the crust in the region, are presented in Chapter 4.

In the second part of this study, the attenuation of high-frequency Lg coda waves propagating across the Arabian plate and the Zagros mountain belt is investigated. Toward this end, the "extended coda-Q" methodology is developed and presented in Chapter 5. This technique provides a deterministic procedure for the simultaneous estimation of the anelastic attenuation quality factor and its frequency dependence. Also, since it incorporates least-squares analysis, it allows calculation of statistical error parameters. In Chapter 6 the technique is applied to the coda of Lg waves to map the attenuation variation throughout the region, and the results of the extended coda-Q are compared with those obtained by other methods. Short-period vertical component seismograms are used in this analysis.

The majority of selected earthquakes occurred along the boundaries between the Arabian and the Iranian, Turkish or African plates. The locations, origin times, magnitudes and depths of the earthquakes were taken from the Preliminary Determination of Epicenters (PDE) reports and the Bulletin of the International Seismological Center (ISC). A list of the events used in the surface and coda waves parts of this analysis are given in appendices A and B, respectively.

All the seismograms, long- and short-period, were recorded by four stations equipped with the well known WWSSN (World Wide Standard Seismograph Network) type instruments. The names and locations of the

stations used are as follows,

Station List		
Name	Latitude (degrees)	Longitude (degrees)
SHI	29.6383 N	52.5199 E
TAB	38.0617 N	46.3258 E
EIL	29.5500 N	34.9500 E
JER	31.7719 N	35.1972 E

An essential requirement for investigating the lateral heterogeneities of a region is sufficient wave path coverage. Geographically, the forenamed stations are distributed around the northern half of the Arabian plate. Stations TAB and SHI are located along the Zagros mountain belt which constitutes the eastern and northeastern boundaries of the plate, whereas stations EIL and JER are located west of the Dead Sea transform fault system, the plate's northwestern boundary. Hence, for the purpose of this study the distribution of these stations has provided a convenient rather than a desirable arrangement of sources and receivers. This is due to the lack of seismic stations in the southern portions of the plate. However, it should be noted that plans to establish new seismological stations over the entire plate are currently underway.

CHAPTER 2

SEISMOTECTONIC ENVIRONMENT

2.1 Tectonic Setting

The Arabian plate is a relatively large lithospheric block surrounded by the African, Turkish and Iranian plates. Figure 2.1 shows the geographical relationship between these plates, and the location of the four WWSSN stations used in this study. Geologically, the Arabian plate is characterized by a diversified physiographic and tectonic environments. Adams and Barazangi (1984) and Jackson and McKenzie (1984) are among many investigators who provide detailed reviews and discussions of the seismotectonic framework of the Arabian plate. Hence, only a brief description of the tectonic setting that is relevant to this study, is presented here for completeness.

The Taurus and Zagros continental collision zones form the northern, northeastern and eastern boundaries of the Arabian plate (Figure 2.2). They are the result of continued convergence between the Arabian, Turkish and Iranian plates. The Taurus zone is diffused, but the Zagros is well defined and extends for about 1500 km in a NW-SE direction. The structural deformation of these zones probably dates back to the Mesozoic and Miocene times (Stocklin, 1974; Sengor and Kidd, 1979). The main thrust zone of these orogenic zones are flanked to the south and southwest by a simple folded belt, that extends well into the Mesopotamian foredeep. This belt is presumably created because of the thick (more than 1 km) plastic

-5-
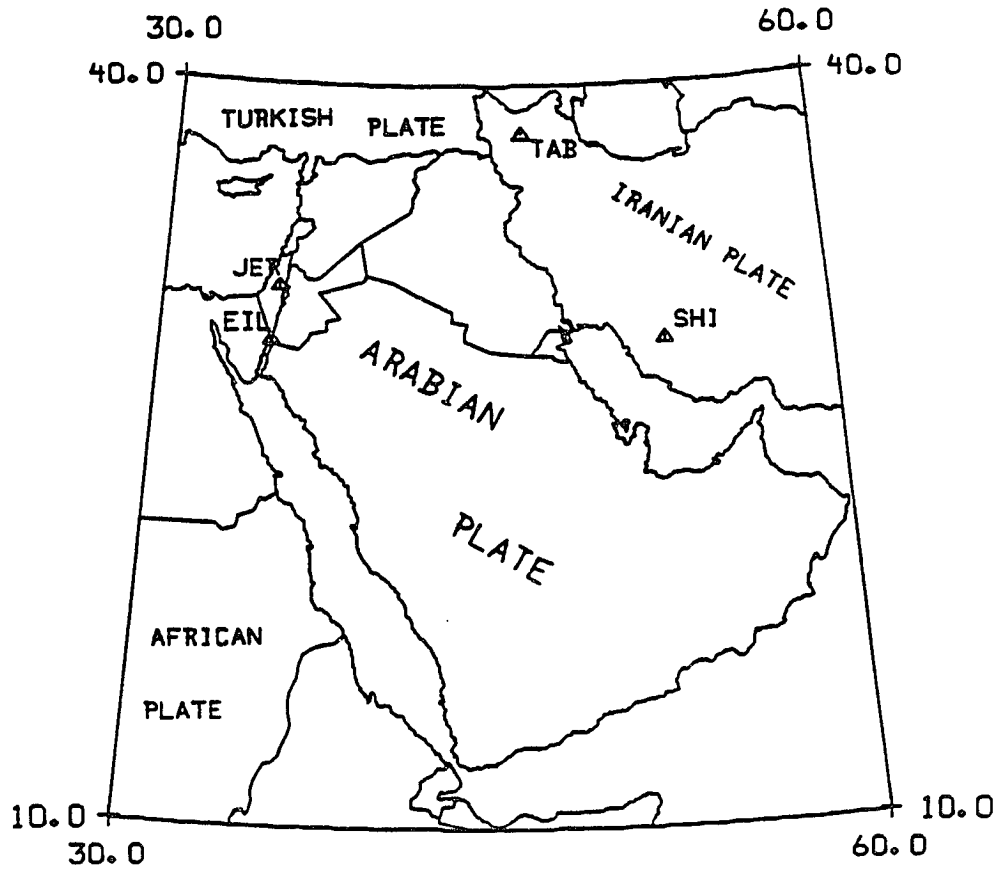
Figure 2.1. A map showing the location of the Arabian plate relative to the African, Turkish and Iranian plates, and the location of seismological stations used in this study.
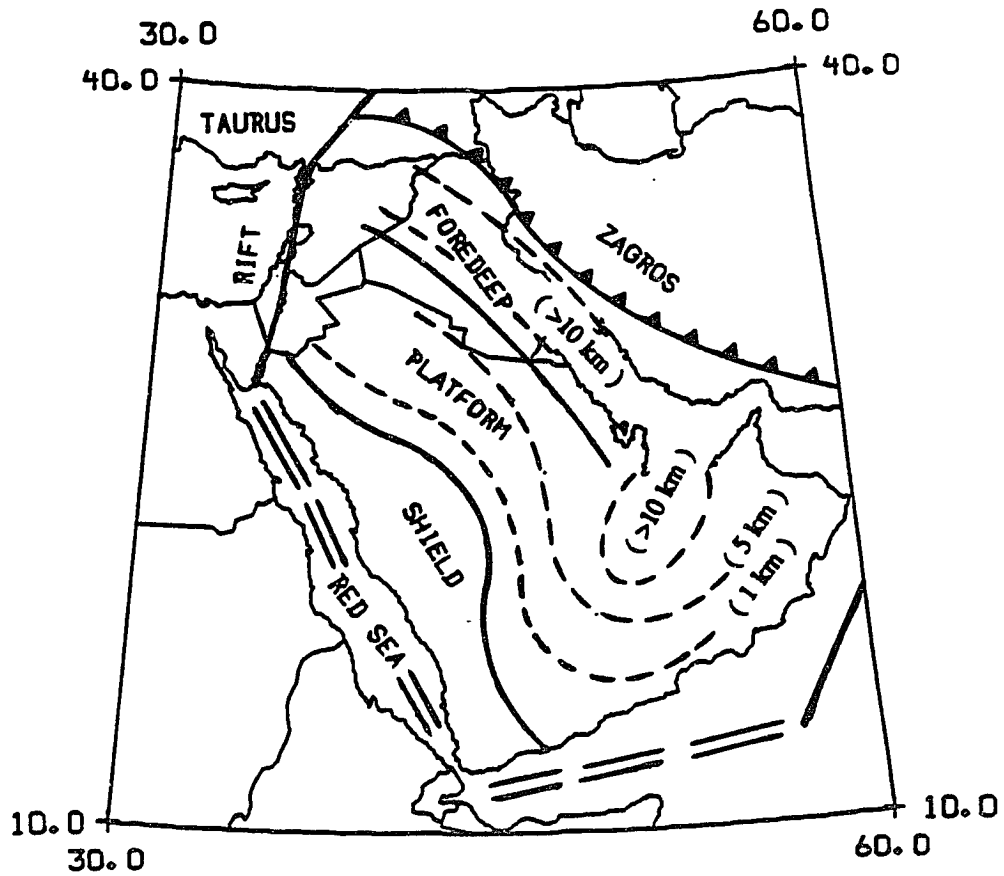
Figure 2.2. A schematic map showing the major tectonic units and boundaries of the Arabian plate. The dashed lines represent the thickness of sediments overlying the basement in the region (After Brown, 1972).

salt beds that decouple the sedimentary column from the basement of the plate (Falcon, 1967; Ala, 1974). On the contrary, faults are relatively scarce within the thick (5-10 km) sediments of this belt, and are mainly restricted to the Precambrian basement (e.g., Stocklin, 1968; Jackson, 1980; Jackson and Fitch, 1981; Berberian, 1981; Jackson and McKenzie, 1984).

The southern and southwestern boundaries of the Arabian plate are mainly delineated by active sea floor spreading in the Gulf of Aden and the Red Sea, respectively (e.g, McKenzie *et al.*, 1970; Whiteman, 1970; Ross and Schlee, 1973; Girdler and Style, 1974; Le Pichon and Francheteau, 1978; Cochran, 1981). The structure of the Gulf of Aden is characterized by an E-W trending main axial trough of regional expansion, whereas a main and axial troughs, which were developed during the Oligocene through Pliocene, characterize the structural features of the Red Sea. In addition, many NE-SW trending transform faults are known to intersect the oceanic trough of these major rift systems.

The northwestern margin of the Arabian plate is defined by the Dead Sea transform fault system (e.g., Freund, 1965; Freund *et al.*, 1970; Ben-Menahem *et al.*, 1976; Nur and Ben-Avraham, 1978; Ben-Avraham *et al.*, 1979; Garfunkel *et al.*, 1981; Zak and Freund, 1981). This N-S trending plate boundary, which was developed in multiple stages during the Middle Cenozoic, extends from the Red Sea to the Taurus convergence zone. Although, the predominant motion along the Dead Sea is left-lateral strike-slip, it is also considered a leaky transform system due to the existence of lateral extension and compression stress components and upwarping along the fault caused by the divergence between the Arabian and African plates.

The major tectonic regions of the Arabian plate consist of the shield, platform and the foredeep. Figure 2.2 shows the configuration of these tectonic units, and their relationship to the boundaries of the plate. Following the majority of geological and geophysical publications on the region, these units will be referred to throughout this study as the Arabian shield, Arabian platform and Mesopotamian foredeep.

The Arabian shield occupies approximately one third of the total area of the Arabian plate, and runs parallel to the eastern coast of the Red Sea. Its exposed Precambrian rocks consist of complex metamorphic, plutonic, magmatic and ophiolitic assemblages. The spread of thin basaltic lava flows over vast areas of the shield since the Miocene time, reflect the intensity of historic volcanism in the region (Neumann, 1963). Further evidence of the tectonic activity level is reflected by the abundance of major NW trending normal and strike-slip type faults (Brown, 1972). According to proposed models for the evolution of the shield, during the Upper Precambrian multiple collisions and accretions of either intra-oceanic island arcs or intra-cratonic systems are responsible for the development and origin of this tectonic unit (e.g., Al-Shanti, 1984).

The Arabian platform and Mesopotamian foredeep occupy the other two thirds of the plate. The Phanirozoic platform region is relatively stable, and consists of Palaeozoic and Mesozoic sedimentary layers. The thickness of sediments increase toward the east and northeast, following the gradual dip of the basement in those direction. Neither near surface faults nor folds are common within the vast platform region. In contrast, the Mesopotamian foredeep, which marks the location of the Tethys geosyncline, is characterized by significantly increased thickness of sediments and structural

deformation. The column of sediments in various parts of this region exceed 10 km, and are presumably separated from the basement by thick salt deposits (Falcon, 1967). The intensity of folding in the foredeep increases toward the northern, northeastern and eastern boundaries of the Arabian plate. In most cases the folds, which date back to the Upper Miocene-Lower Pliocene (Stocklin, 1968), run parallel to the extension of the Taurus and Zagros mountains. Furthermore, strike-slip, reverse and normal faults are also more common in the foredeep than the platform region.

2.2 Seismic History

Figure 2.3 shows a seismicity map of the Arabian plate for the period 1970-1979. An outstanding feature of the this plate is the high level of plate margin seismicity, which until recently has been exclusively monitored by stations located outside the region. The apparent low level of intraplate seismic activity is attributed by several investigators to the scarcity of local as well as regional seismological networks rather than the tectonic stability of the rigid interior of the plate (e.g., Alsinawi and Ghalib, 1973; Ghalib and Alsinawi, 1974; Alsinawi and Ghalib, 1975a; Barazangi, 1981; Ghalib et al., 1985; Adams and Barazangi, 1984). Evidence to that is the latest devastating earthquake in Yemen (December 13, 1982), instrumentally recorded microearthquake surveys in various countries of the region (e.g., Alsinawi and Beno, 1976; Merghelani and Gallanthine, 1980; El-Isa and Al-Shanti, 1989), and historical accounts of major earthquakes that occurred throughout the plate prior to this century (e.g., Willis, 1928; Ambraseys, 1961, 1971; Alsinawi and Ghalib, 1975b; Poirier et al., 1980a,b; Ben-Menahem and Aboodi, 1981).
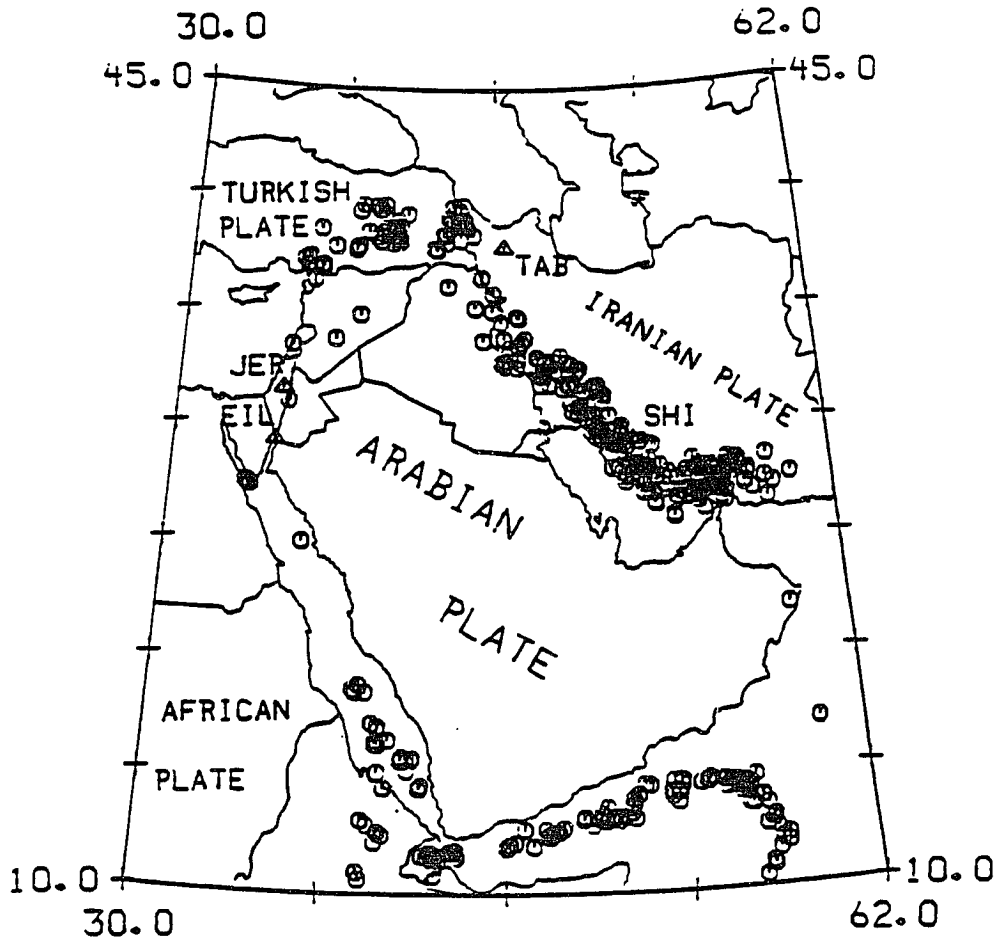
Figure 2.3. A seismicity map of the Arabian plate for the period 1970-1979.

The areas of dominant seismic activity, as shown in Figure 2.3, are limited to well defined narrow belts that coincide with the plate margins. This considerable concentration of earthquakes indicates strong correlation between the present seismicity, kinematics of the plate, and deformation patterns along its boundaries. In other words, the pattern of seismicity of the region is a manifestation of the translational motion toward the northeast and counterclock rotation of the Arabian plate. Evidence from plate tectonics, fault plane solutions in the Red Sea, Gulf of Aden and the Zagros regions, and other geophysical methods describe this pattern of continental deformation by the absolute or relative motion of the plates in the region in terms of their poles of rotation (e.g., Sborshchikov *et al.*, 1981; Jackson and McKenzie, 1984; Chase, 1978; Minster and Jordan, 1978; DeMets *et al.*, 1990). Consequently, convergence between the Arabian and Eurasian plates is occurring at about 4.8 cm/year in Iran and 4.3 cm/year in Turkey (Le Pichon, 1968).

The Zagros mountain range is probably one of the most seismically active continental regions on earth. The spatial distribution of earthquakes along this plate boundary defines an approximately 200 km wide and 1500 km long seismic belt, that is typical of a continental deformation zone. This dispersed seismic activity extends throughout the main thrust zone and folded belt of the Zagros, and appears to occur along a combination of reverse, thrust and strike-slip faults in the basement of the plate. Niazi *et al.* (1978), Berberian (1979), Jackson and Fitch (1979), Jackson (1980), Jackson and Fitch (1981), Kadinsky-Cade and Barazangi (1982), and Asudeh (1983) have all demonstrated that most of the events occur in the upper crust, and there are no evidences for the occurrence of mantle

earthquakes beneath the Zagros, as indicated by Nowroozi (1971, 1972). Their findings suggest that the exaggerated location of earthquakes published in seismological bulletins is due to the lack of reliable seismic velocity models for the region. In addition, the mislocation of events is caused by poor coverage, unoptimal distribution and scarcity of existing seismic stations.

In western Iran and northeastern Iraq the Zagros bends westward to join with the Taurus mountain range in southern Turkey. The seismic activity due to the convergence between the Arabian and Turkish plates is scattered over a wide region, where no distinct plate boundary is apparent from the spatial distribution of predominantly crustal earthquakes. Nowroozi (1971) and Jackson and McKenzie (1984) suggested that the earthquakes are associated with numerous faults, and that the fault plane solutions show significant degree of thrusting as well as right lateral strike-slip motion. The western end of this seismic zone presumably connects with the Dead Sea fault system through the east Anatolian fault zone in south western Turkey (Ambraseys and Barazangi, 1989).

Although, small to moderate earthquakes are frequent along the Dead Sea transform fault system, Ambraseys and Barazangi (1989) characterize the observed activity level during this century as a period of conspicuous seismic quiescence. Earthquake swarms, such as the one in the Gulf of Aqaba in 1983 (El-Isa et al., 1984), are also known to occur. Ben-Menahem et al. (1977), Ben-Menahem (1979), and Ben-Menahem and Aboodi (1981) have documented the occurrence of recent earthquakes along the Dead Sea, whereas, Ambraseys (1971, 1978) and Poirier et al. (1980a) have interpreted the relationship between the historical seismicity

and present configuration of the fault system. Ben-Menahem *et al.* (1976) and Garfunkel *et al.* (1981) indicate that most of the current seismicity along the Dead Sea rift is associated with either strike-slip or normal faults.

Figure 2.3 shows that many earthquakes have occurred along the axial trough and transform faults of the Red Sea and Gulf of Aden sea-floor spreading zones. The seismicity of these regions has been studied by Sykes and Landisman (1964), Fairhead and Girdler (1970), McKenzie (1970), McKenzie *et al.* (1970), Nowroozi (1971). Their results suggest that earthquakes associated with the axial trough and transform faults are of shallow depth, and that from fault plane solutions the tensional stress field is directed toward the NE-SW for the Red Sea and Gulf of Aden. Furthermore, in contrast with the Gulf of Aden, where the seismicity is equally distributed thought the region, most of the earthquake activity is confined to the central and southern portions of the Red Sea.

2.3 Review of Related Literature

Prior to the present study, information on the deep crust and upper mantle seismic structure of the Arabian plate has been generally limited to simplified average models of isolated areas. Keller and Russell (1980) summarized the results obtained from previous studies of the African plate and to a much lesser extent the Arabian plate. In this section, a brief review of the earlier studies relevant to this research is presented, and comparisons with some of these studies are discussed in Chapters 4 and 6.

Niazi (1968) was the first to deduce an average crustal model from the phase and group velocity measurements of fundamental-mode Rayleigh wave across the Arabian plate. The profile extends for 2689 km along a

great-circle path between station AAE in Ethiopia and SHI in Iran. Under the assumption that there are no drastic changes in the crustal structure along the wave path, his proposed flat layered model consists of a three-layered crust overlaying a two-layer upper mantle. It includes a typical continental crust, 35.0 km thick, covered with 0.5 km layer of unconsolidated sediments. The underlying mantle consists of a layer, 60.0 km thick, over a half-space. The corresponding shear velocities of these layers are 1.25, 3.4, 4.6 and 4.9 km/sec, respectively.

Similarly, Arkhangel'skaya *et al.* (1974) proposed a three-layered crustal model, 30 km thick, that fits their regionalized fundamental-mode Love and Rayleigh waves group velocity data. The structure along the northwestern section of the Arabian plate consists of a 0.5 km thick sedimentary layer overlaying two crustal layers that are 12.84 and 16.66 km thick. The corresponding shear velocities with increasing depth are 1.25, 3.38, 3.62 and 4.6 km/sec.

Knopoff and Fouda (1975) utilized the Hedgehog inversion procedure to obtain a relatively more detailed velocity structure of the Arabian plate. Using only Rayleigh wave fundamental-mode phase velocity dispersion data along three great circle paths between station pairs SHI-JER, SHI-HLW and SHI-AAE of the World Wide Standard Seismographic Network (WWSSN), they proposed two shear velocity models with crustal thicknesses of 35 ± 8 km. The models differ significantly in the number, thicknesses and shear velocities of their crustal layers. The first, so called high-velocity crust H, includes four layers with shear velocities of 2.83, 3.45, 3.67 and 3.86 km/sec. The second, low-velocity crust L (favored by the authors), consists of three layers with 2.82, 3.45 and 3.86 km/sec shear

velocities. As for the mantle structure, their model shows a pronounced low velocity channel with shear velocity of 4.25-4.45 km/sec which presumably occurs throughout the region. The top of this channel is 100-140 km deep. In addition, they concluded that the measured phase velocities and consequently the shear velocity structure for the Arabian stable shelf are lower than those for the Canadian shield and higher than those for the Gulf coastal plain of the United States.

Kadinsky-Cade *et al.* (1981) calculated Pn and Sn waves velocities using a linear regression approach to obtain slopes and intercept times. Owing to a relatively large scatter in their reduced travel-time versus distance data, only the apparent velocities of these phases were estimated, and no attempt was made to utilize the intercept times for calculating the thickness of the crust. The obtained Pn velocities beneath the Arabian plate were 8.1 ± 0.3 km/sec and 8.4 ± 0.3 km/sec for SHI and EIL stations data, respectively. The corresponding Sn velocity for SHI data was 4.6 ± 0.4 km/sec and 4.2 ± 0.8 km/sec for EIL data.

A more detailed compressional velocity model for the Zagros region was obtained by Asudeh (1983). His model consisted of a 15 km thick layer with a Pn velocity of 5.6 km/sec, an 18.0 km thick layer with a velocity of 6.5 km/sec, and 8.25 km/sec below 33.0 km depth. The latter velocity is significantly higher than the 7.85 km/sec of the ISC event location model for the Zagros region and the 8.08 km/sec of Asudeh (1983) Zagros model. Also, this higher mantle velocity structure is consistent with Asudeh (1982) model for the Zagros, which was derived from phase velocity dispersion of the fundamental Rayleigh wave between SHI and TAB stations. The Zagros surface wave model, however, exhibits distinct velocity

gradient to a depth of 46.0 km, and a slight increase in velocity to a depth of 100.0 km. The compressional velocity gradually increase to 4.43 km/sec, and reaches 7.77 km/sec at the bottom of the crust. Velocities in the upper mantle increase to 8.30 km/sec and 8.85 km/sec at 100.0 km depth. Below that, the velocity decreases to 8.44 km/sec at 200.0 km depth. The corresponding shear velocities in those layers are 2.66, 4.44, 4.70, 4.70, 4.98 and 4.74 km/sec.

Unlike the above studies, Mooney *et al.* (1985) interpreted a detailed seismic deep-refraction profile (1000 km long) recorded across the southern Arabian shield to delineate the major first- and second-order features of the crustal and upper mantle compressional wave velocity structure. Using two-dimensional ray-tracing techniques, they inferred that the Arabian shield is composed of two major layers, each about 20.0 km thick. The upper crustal layer has an average velocity of about 6.3 km/sec, overlain by a near-surface thin low velocity layer. The lower crustal layer consists of an upper section 10.0 km thick, which has an average velocity of 6.7 km/sec, and a lower section, in which the velocity increases from 6.8 to 7.3-7.8 km/sec. The Moho discontinuity beneath the shield varies from a depth of 43.0 km and mantle velocity of 8.2 km/sec in the northeast to a depth of 38.0 km and a mantle velocity of 8.0 km/sec depth in the southwest. Furthermore, below the Moho they inferred two velocity discontinuities, one at 59.0 km and another at 70.0 km depth. The compressional velocity within this section of the upper mantle increases with depth from 8.3 to 8.5 km/sec. In contrast with previous studies, Mooney *et al.* (1985) distinguished a complex and heterogeneous crust, which is probably derived from the suturing of island arcs in the Precambrian for the Arabian

shield.

Elsewhere along the northeastern boundary of the plate, the deep crustal structure of the Zagros collisional mountain belt region has been inferred from gravity observation. According to Snyder and Barazangi (1986), the crust beneath the Mesopotamian foredeep folded belt is characterized by a Moho discontinuity that dips about 1° to the northeast and increases in dip to about 5° under the main Zagros thrust zone. The crustal thickness within these regions increase towards the northeast from 40.0 km to 65.0 km beneath the Zagros zone.

Also prior to the present study, Kadinsky-Cade *et al.* (1981) investigated the crustal and uppermost mantle physical properties that characterize some of the continental plateaus of the Middle East. However, neither the Arabian shield nor platform were analyzed in detail. Using short-period seismograms recorded at several WWSSN stations, including SHI, TAB and EIL, they qualitatively examined and mapped the azimuthal variations of frequencies and amplitudes of Sn and Lg relative to Pn and Pg seismic waves at regional distances. In general, the pattern of Sn and Lg variation indicates that these high-frequency phases propagate efficiently across the northern Arabian plate. The variation of Sn is attributed to either high attenuation along their propagation paths, or the masking effect as a result of very efficient Pg wave propagation. The absence of Lg, on the other hand, is explained by (1) the presence of more than 150 km of oceanic crust along the propagation path (Oliver *et al.*, 1955), (2) a hypocenter located beneath the crust which does not excite Lg efficiently (Barazangi *et al.*, 1977), (3) considerable scattering due to the presence of lateral heterogeneities and variation in crustal structure along the propagation path of Lg

wave (e.g., Ruzaikin *et al.*, 1977; Kennett *et al.*, 1985), or (4) the existence of high crustal attenuation zones along the path (e.g., present study).

Finally, in a more recent study Şeber and Mitchell (1991) investigated the attenuation of surface waves across the Arabian peninsula. They used the amplitude spectra of fundamental-mode Rayleigh and Love waves to determine shear velocity (Q_β) models, and compare the results with theoretical spectra computed for earthquakes with reliable depth estimates and known fault-plane solutions. Their Q_β values over a period range of 5-30 sec vary from 60 along the Red Sea margin to 100-150 in the Arabian platform, and 65-80 in the eastern folded belt of the Mesopotamian foredeep. These attenuation results are low for the upper crust of a stable region like the Arabian plate. Şeber and Mitchell (1991) found that, at periods between about 1 and 30 sec Q_β appears to be independent of frequency in the region, and their surface wave Q_β models closely predict the coda Q at 1 Hz values reported in this study and by Ghalib *et al.* (1984).

CHAPTER 3

SURFACE WAVE DATA ANALYSIS

The relative effectiveness of various combinations of surface wave modes for inversion has been discussed by several investigators. For example, Der, Massé and Landisman (1970) concluded that although the best resolution can be obtained by combining all observations (i.e., group and phase velocity of Love and Rayleigh fundamental and first higher modes), the results are not greatly superior to those found from the fundamental and first higher Rayleigh modes alone. Mitchell and Herrmann (1979) also showed that simultaneous inversion of group and phase dispersion of Love and Rayleigh fundamental modes are not sufficient to resolve differences among models in Eastern United States, and thus recommended the use of higher-mode information. Furthermore, Bloch, Hales and Landisman (1969) proposed that more detailed earth models can be produced by inverting group rather than phase velocity dispersion data.

In the present study, Rayleigh wave fundamental and first higher-mode observations are exclusively used to investigate the Arabian plate seismic structure. The group velocities are determined using the single-station and modal isolation method originally proposed by Dziewonski, Bloch and Landisman (1969). No attempt is made here to calculate phase velocities, due to the scarcity of reliable fault-plane solutions required for estimating the initial phase of the earthquake sources. Utilizing only those earthquakes whose focal mechanisms are known would have significantly narrowed the scope of this work.

3.1 Rayleigh Wave Data

The long-period vertical component (LPZ) seismograms recorded at TAB, SHI, EIL and JER stations are used for the analysis of Rayleigh wave group velocities. The location coordinates of these stations are given in Chapter 1. Most of the selected earthquakes, which occurred between 1970 and 1979, come from one of five areas: the Zagros Mountains, the Arabian Sea, the Gulf of Aden, the Red Sea, the Dead Sea, or the Taurus Mountains. A list of the events and their parameters are given in Appendix-A. The reported (m_b) magnitudes for these earthquakes range from 4.5 to 5.6, whereas the reported depths, though questionable as indicated in Chapter 2, vary between 5 and 68 km. Figures 3.1 through 3.4 show the geographic distribution of the sources and receivers, as well as the wave propagation paths for each station-event combination. The lengths of these great circle paths range from 680 to 2823 km. In spite of the limited number of paths and less than desirable distribution of stations, the wave paths provide a reasonably good coverage over the entire plate.

Because the Arabian plate is surrounded by seismically active zones, a large number of recorded earthquakes are available for surface wave studies of the region. The recorded multi-mode Rayleigh waves traversing the plate exhibit normal dispersion generated by typically shallow crustal earthquakes. Seismograms with minimum apparent interference and contamination are selected for the analysis. Although more than 150 seismograms are digitized, only 104 are used in this study. Those rejected are on the basis of either their wave train dispersion qualities in terms of velocity scatter and limited period range, or origin time error resulting in systematically biased group velocities. Also, in order to ensure a group velocity range
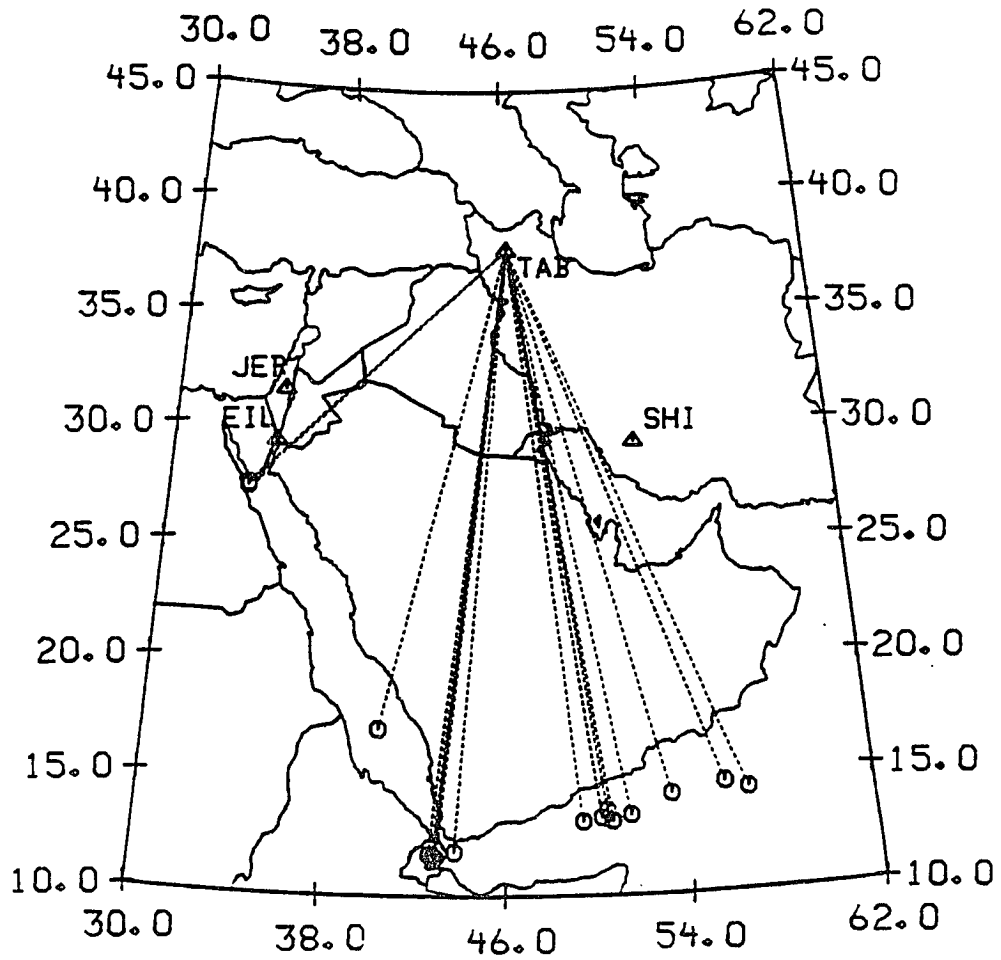
Figure 3.1. A map showing the individual Rayleigh wave propagation paths for TAB station.

- 22 -
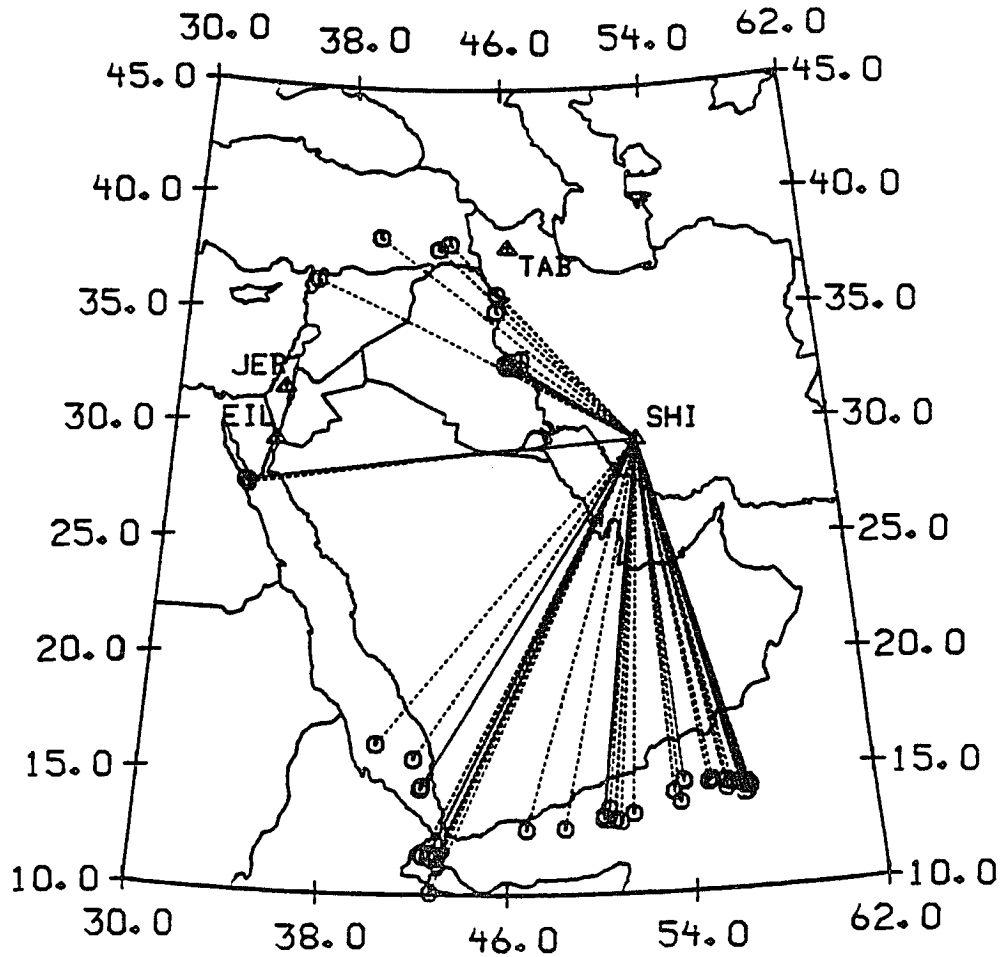
Figure 3.2. A map showing the individual Rayleigh wave propagation paths for SHI station.
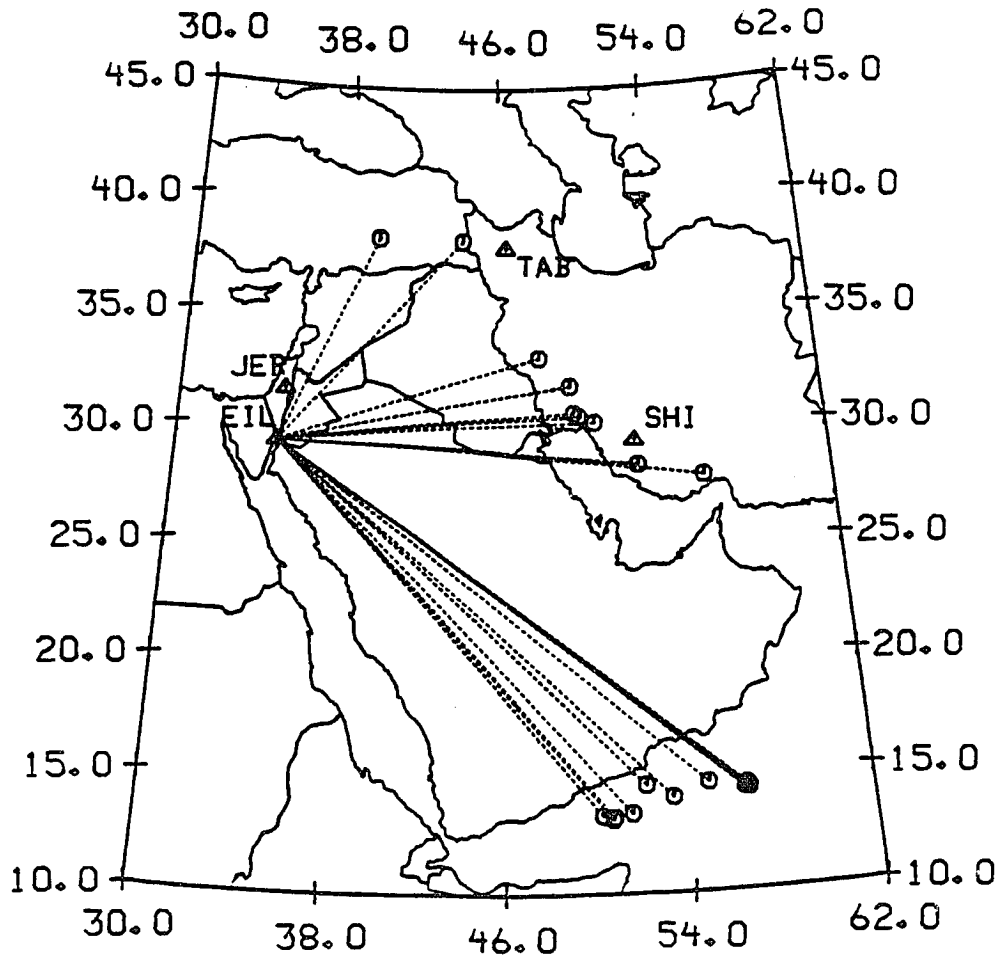
Figure 3.3. A map showing the individual Rayleigh wave propagation paths for EIL station.
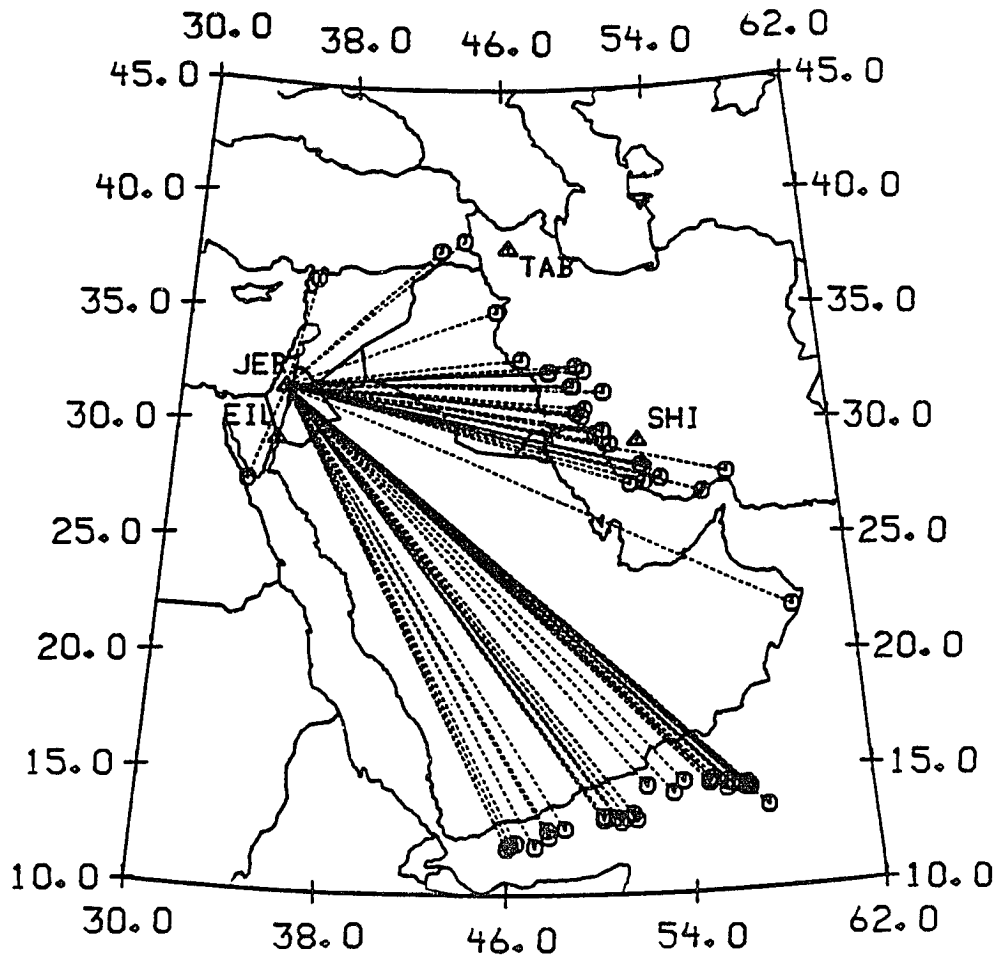
Figure 3.4. A map showing the individual Rayleigh wave propagation paths for JER station.

from about 2 to 5 km/sec, the length of digitized traces are varied from 5 to 10 minutes, depending on the epicentral distances. This in effect is a boxcar window, and it is done to provide consistency in digitizing all seismograms.

The seismograms are hand-digitized directly from their microfilms at irregular time intervals. The sampled pairs of x_i and y_i points, where $i = 1, ..., n$ and n the total number of samples, are then converted to evenly spaced data with a time interval of 0.5 second. Wiggins (1976) weighted average slope interpolation is performed on the digitized traces. The technique is based upon fitting piecewise continuous cubic polynomials to the data. This involves finding the weighted average slope s_i at each knot (x_i) as a function of the linear slopes $m_i = (y_i - y_{i-1}) / (x_i - x_{i-1})$ connecting between the sample points. In practice, it requires two (x_i, y_i) points on each side of the desired x position where the value of y is determined by a cubic polynomial. The slope s_i at each knot is given by a weighted average of the adjacent linear slopes m_i and m_{i+1}

$$s_i = \frac{w_i m_i + w_{i+1} m_{i+1}}{w_i + w_{i+1}}$$

and the weight,

$$w_i = \frac{1}{\max(|m_i|, \varepsilon)}$$

where ε is a small number (e.g., $\varepsilon = 0.001$) relative to the average value of m_i. The advantages of this technique over either linear or other spline interpolation procedures are that: (1) it prevents overshoots at inflection points and plateaus, (2) it forces the curves to have extrema at the sample

points, and (3) while consistently maintaining good match with the original analog seismograms, it requires the minimum number of samples needed to define a curve (i.e., peaks, troughs and inflection points). For this reason, when spectral analysis of time series is performed on the data, the technique significantly reduces the level of high frequency noise introduced by linear interpolation.

Furthermore, in order to minimize digitization error due to trace alignment, a base line perpendicular to the galvanometer swing is utilized to compensate for possible deviation between the light beam plane of motion and the drum axis (Mitchell and Landisman, 1969; James and Linde, 1971; Panza, 1976). The base line connects the ending and starting points of any two consecutive traces of a seismogram. Finally, the linear trend and DC offset are removed from the seismograms.

3.2 Group Velocity Determination

The multiple filter analysis technique, developed by Dziewonski, Bloch and Landisman (1969), was used to determine Rayleigh wave fundamental and higher-mode group velocity dispersion data. Following Herrmann's (1973) extension of this single-station and modal isolation technique, the recorded displacement seismogram f(t,r) of a propagating dispersed surface wave at time t and distance r can be represented by

$$f(t,r) = \frac{1}{2\pi} \int_{-\infty}^{\infty} F(\omega,r) \, e^{i\omega t} \, d\omega$$

$$= \frac{1}{2\pi} \int_{-\infty}^{\infty} \sum_{j=0}^{M} A_j(\omega,r) \, e^{i(\omega t - k_j r)} \, d\omega$$

where ω is the angular frequency, $F(\omega,r)$ is the Fourier transform of the

seismic signal, $A_j(\omega,r)$ is the complex amplitude of the *jth* mode, k_j is the wave number of the *jth* mode, and M+1 is the number of modes present in the signal.

Since more than one mode is present in the amplitude spectrum of the seismogram, narrow band-pass filtering is utilized to separate the desired spectrum from other modes. The employed symmetric Gaussian filter $H(\omega)$, centered at $\omega = \omega_0$, is defined as

$$H(\omega) = \begin{cases} \exp[-\alpha\,(\omega - \omega_0)^2 / \omega_0^2] & |\omega - \omega_0| \leq \omega_c \\ 0 & |\omega - \omega_0| \geq \omega_c \end{cases}$$

where ω_0 and ω_c are the filter center and cutoff angular frequencies, respectively. The parameter α controls the filter bandwidth, and hence, the filter resolution in the vicinity of each ω_0 and velocity value.

Filtering of the multi-mode signal at $\omega = \omega_0$ is accomplished by multiplying $H(\omega)$ by the real frequencies of $F(\omega,r)$, and a complex time function is generated by taking the inverse Fourier transform of the spectral amplitudes of various modes. The resultant filtered time signal, valid under the conditions $\omega_c \dfrac{\sqrt{\alpha}}{\omega_0} > 2$ and $\dfrac{\alpha}{\omega_0^2} >> \left| \dfrac{r}{2} \dfrac{d^2k}{d\omega_0^2} \right|$, is given by

$$g(t,r) = \frac{\omega_0}{2\pi} \frac{\sqrt{\pi}}{\alpha} \sum_{j=0}^{M} A_j(\omega_0,r)\, e^{i\left[\omega_0 t - k_{0j}r\right]}\, e^{-\frac{\omega_0^2}{4\alpha}\left[t - \frac{r}{U_{0j}}\right]^2}$$

where U_{0j} refers to the group velocity of the *jth* mode. The modulus of g(t,r) gives a series of approximately Gaussian envelopes which have a maximum amplitude at time $t = r / U_{0j}$. For a single mode the envelope duration, defined as the time from the peak until the amplitude decreases to

$e^{-\pi}$ of the maximum value, is given by the relation

$$t_d = T_0 \frac{\sqrt{\alpha}}{\pi}$$

where T_0 is the period corresponding to ω_0. Hence, no modal interference exists if the separation between the maxima of envelopes with the same order of magnitude is greater than $2t_d$.

In applying the multiple filter analysis technique, the Gaussian filter $H(\omega)$ is used with $\alpha = 16\pi$ and $\omega_c = 0.25\omega_0$. Figures 3.5 through 3.12 show examples from stations TAB, SHI, EIL and JER. Along with the original seismograms, displacement spectra, recovered ground motion records, and contoured dispersion diagrams, all the necessary earthquake parameters (e.g., date, origin time, magnitude and depth) are also included in these plots. In effect, each of these figures represents a summary of the practical steps which are followed in determining the group velocity dispersion curves. First, all the seismograms are expanded to 2048 samples by adding an appropriate number of zeros, and a fast Fourier transform is used to take these seismograms from the time domain to the frequency domain. At this stage, the computed spectra are corrected for amplitude and phase distortion caused by the instrument response, and equalized for geometrical spreading on a sphere to a reference distance of 9 degrees (1000 km). Second, as a result of filtering (i.e., multiplying in the frequency domain) the amplitude spectrum by $H(\omega - \omega_0)$ and taking the inverse Fourier transform, the moduli corresponding to the envelope of the complex seismogram are calculated at each group arrival time. By repeating this step for all center frequencies, a two dimensional array of instantaneous spectral amplitudes as a function of period and group velocity is
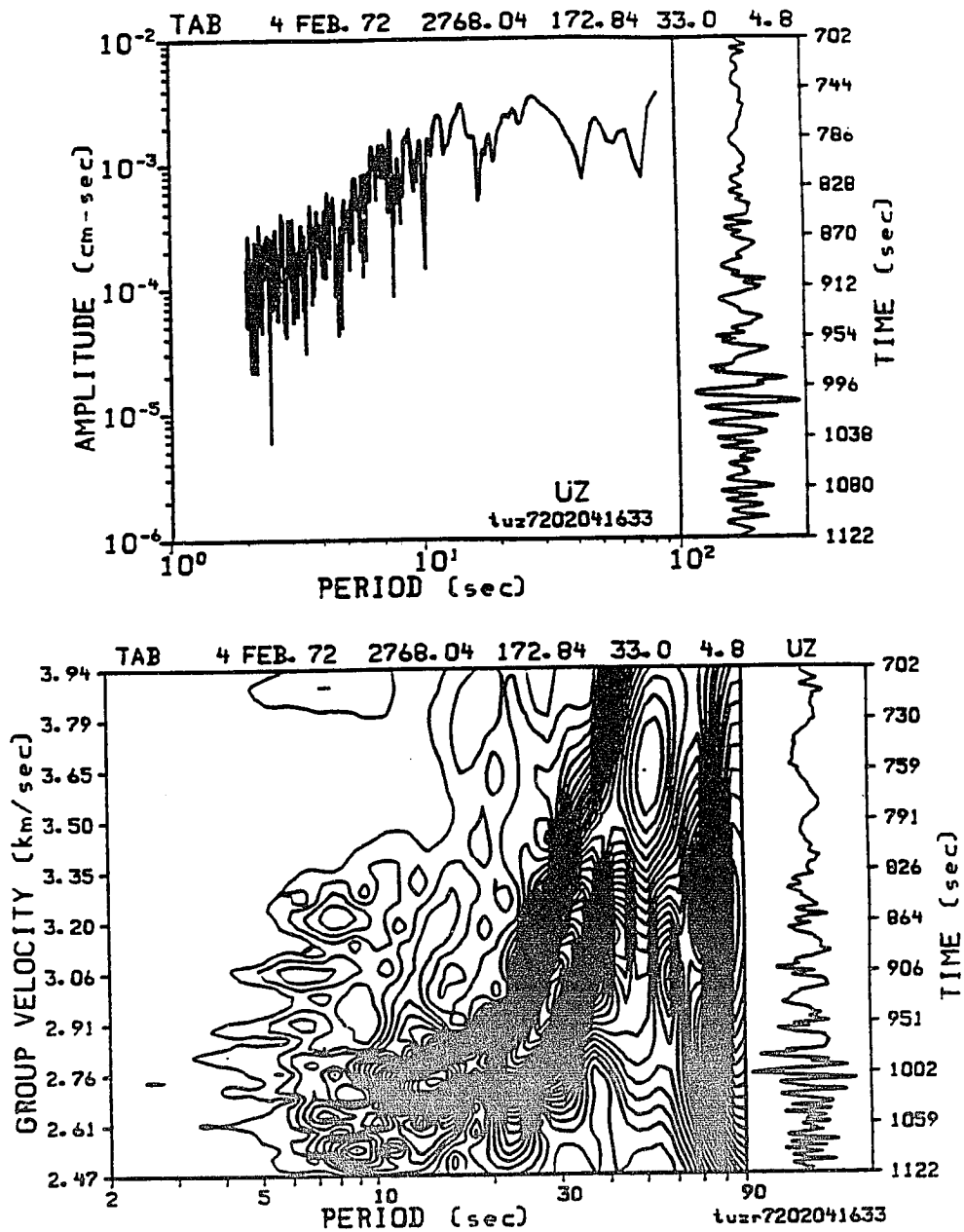
Figure 3.5. Example of an amplitude spectrum and dispersion curve of Rayleigh wave recorded at TAB station. The digitized seismogram is displayed in linear time scale adjacent to the spectrum, and the corrected ground displacement is plotted in linear group velocity scale adjacent to the dispersion contour diagram.

- 30 -
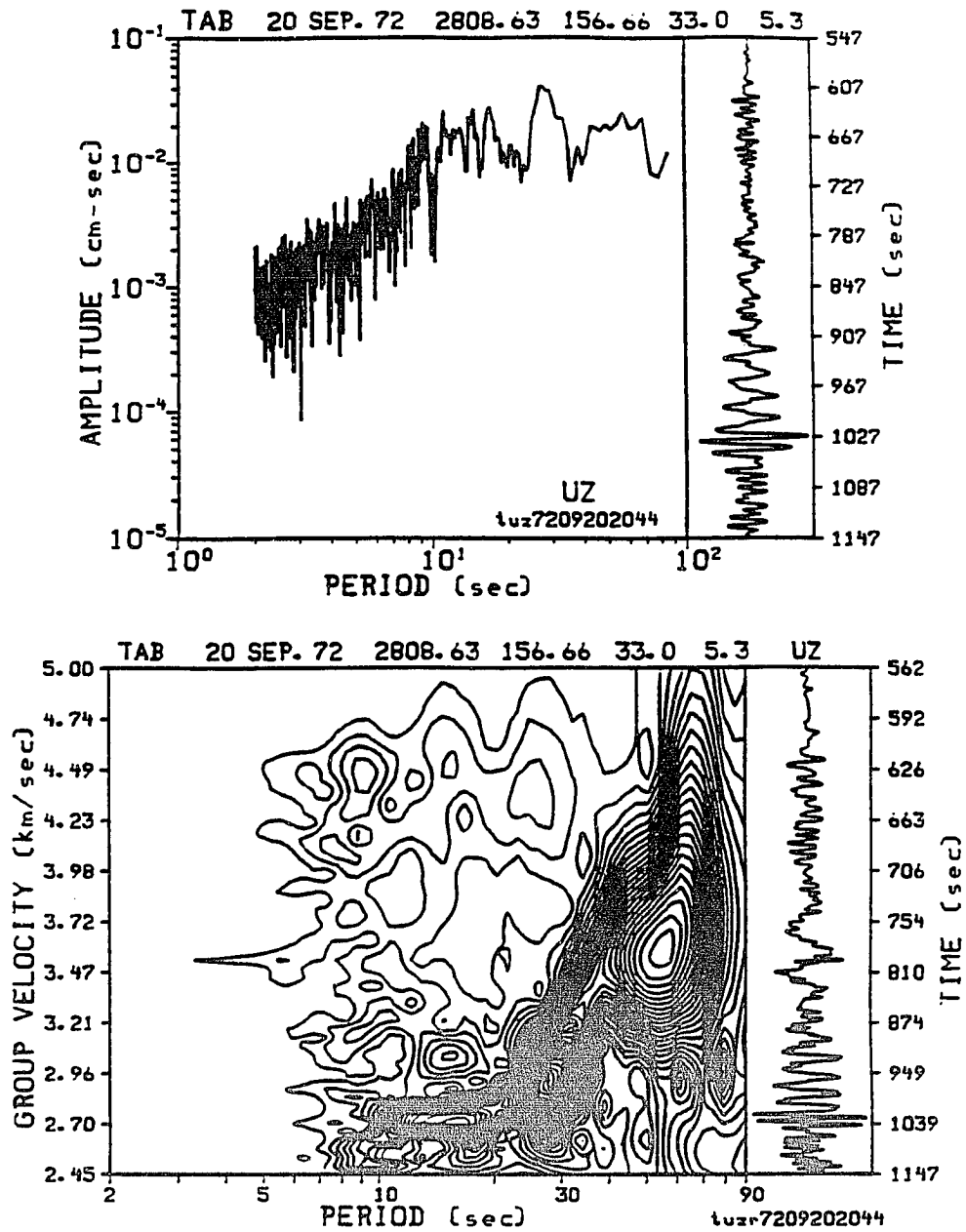
Figure 3.6. Example of an amplitude spectrum and dispersion curve of Rayleigh wave recorded at TAB station. The digitized seismogram is displayed in linear time scale adjacent to the spectrum, and the corrected ground displacement is plotted in linear group velocity scale adjacent to the dispersion contour diagram.

- 31 -
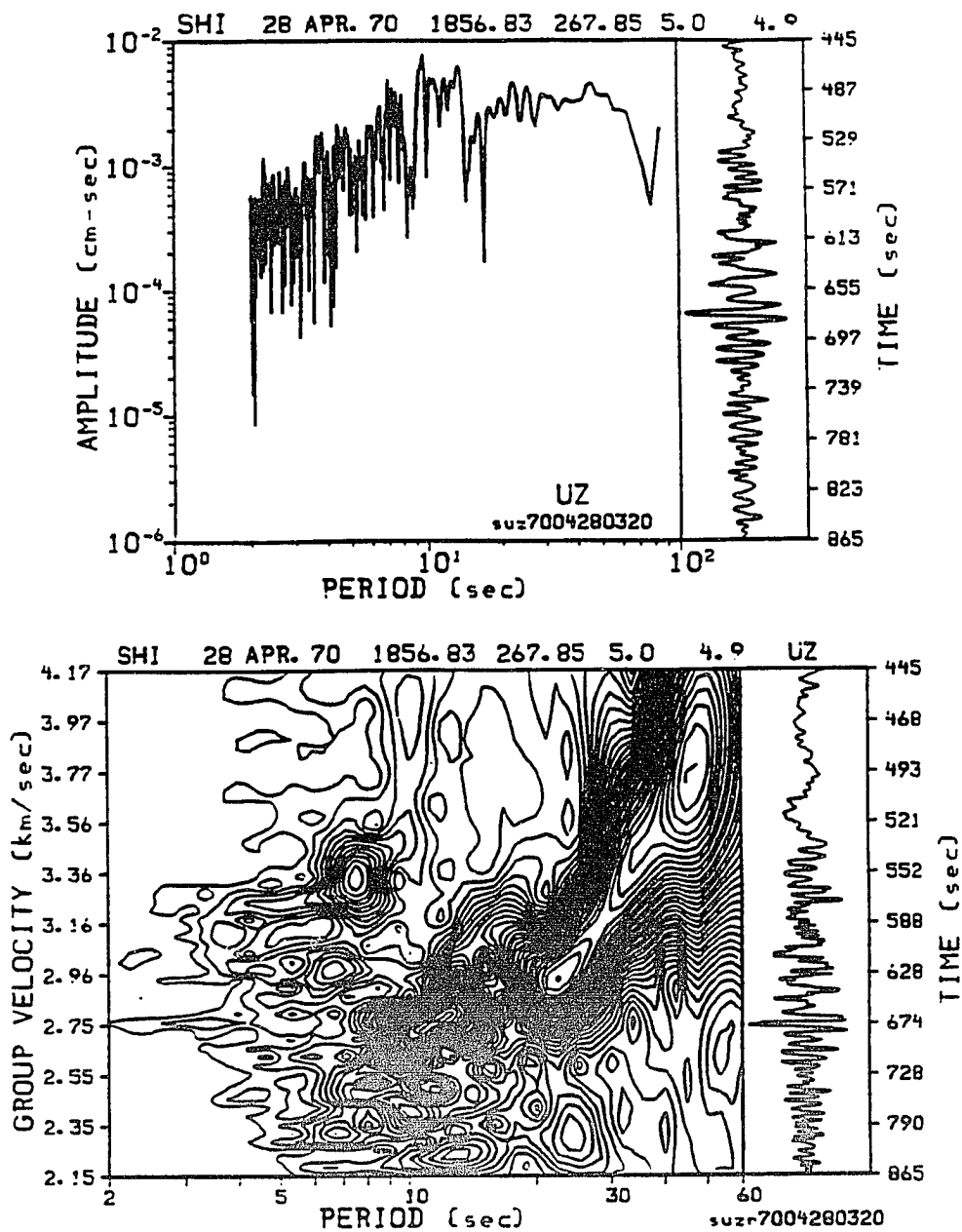
Figure 3.7. Example of an amplitude spectrum and dispersion curve of Rayleigh wave recorded at SHI station. The digitized seismogram is displayed in linear time scale adjacent to the spectrum, and the corrected ground displacement is plotted in linear group velocity scale adjacent to the dispersion contour diagram.

- 32 -
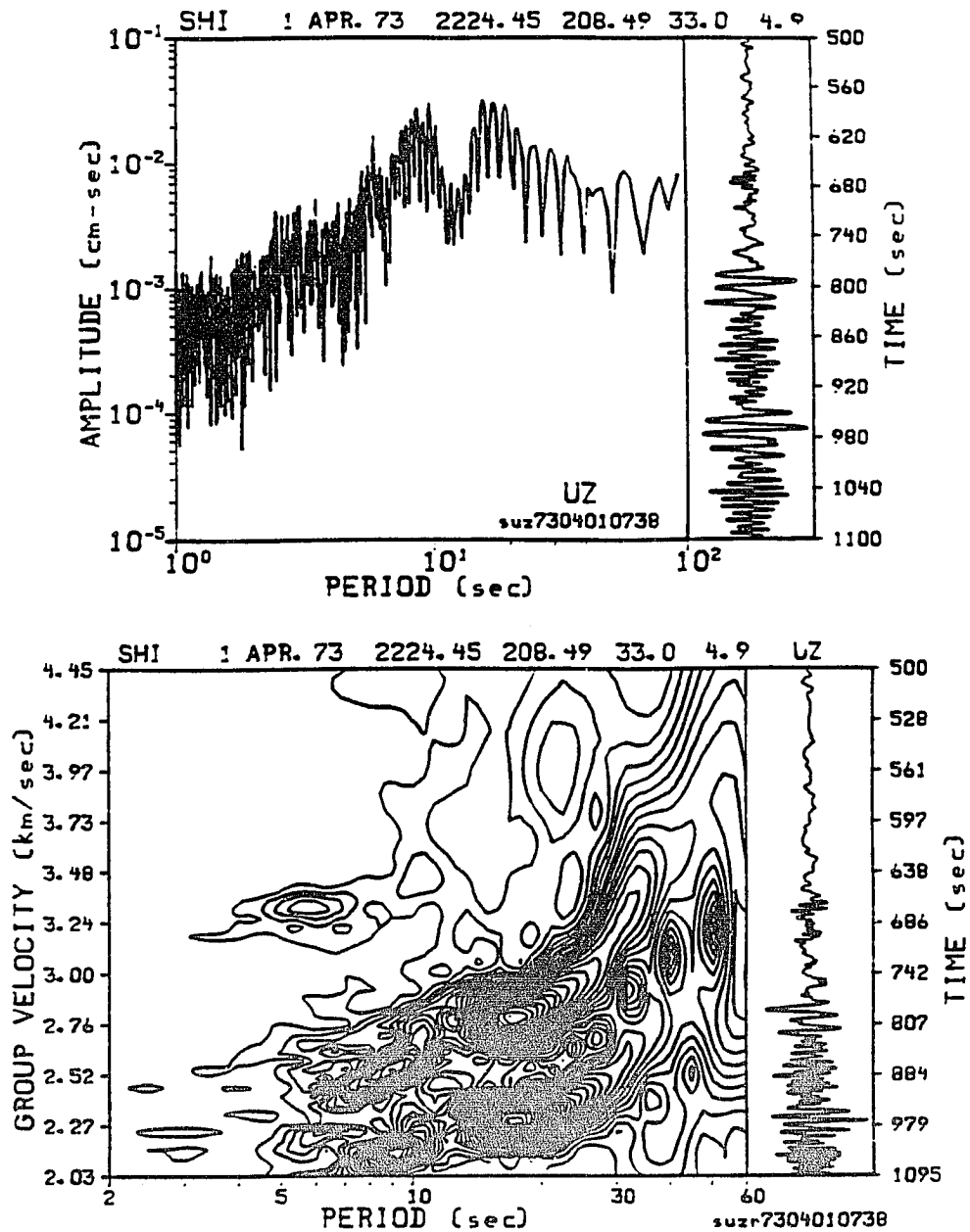
Figure 3.8. Example of an amplitude spectrum and dispersion curve of Rayleigh wave recorded at SHI station. The digitized seismogram is displayed in linear time scale adjacent to the spectrum, and the corrected ground displacement is plotted in linear group velocity scale adjacent to the dispersion contour diagram.

- 33 -
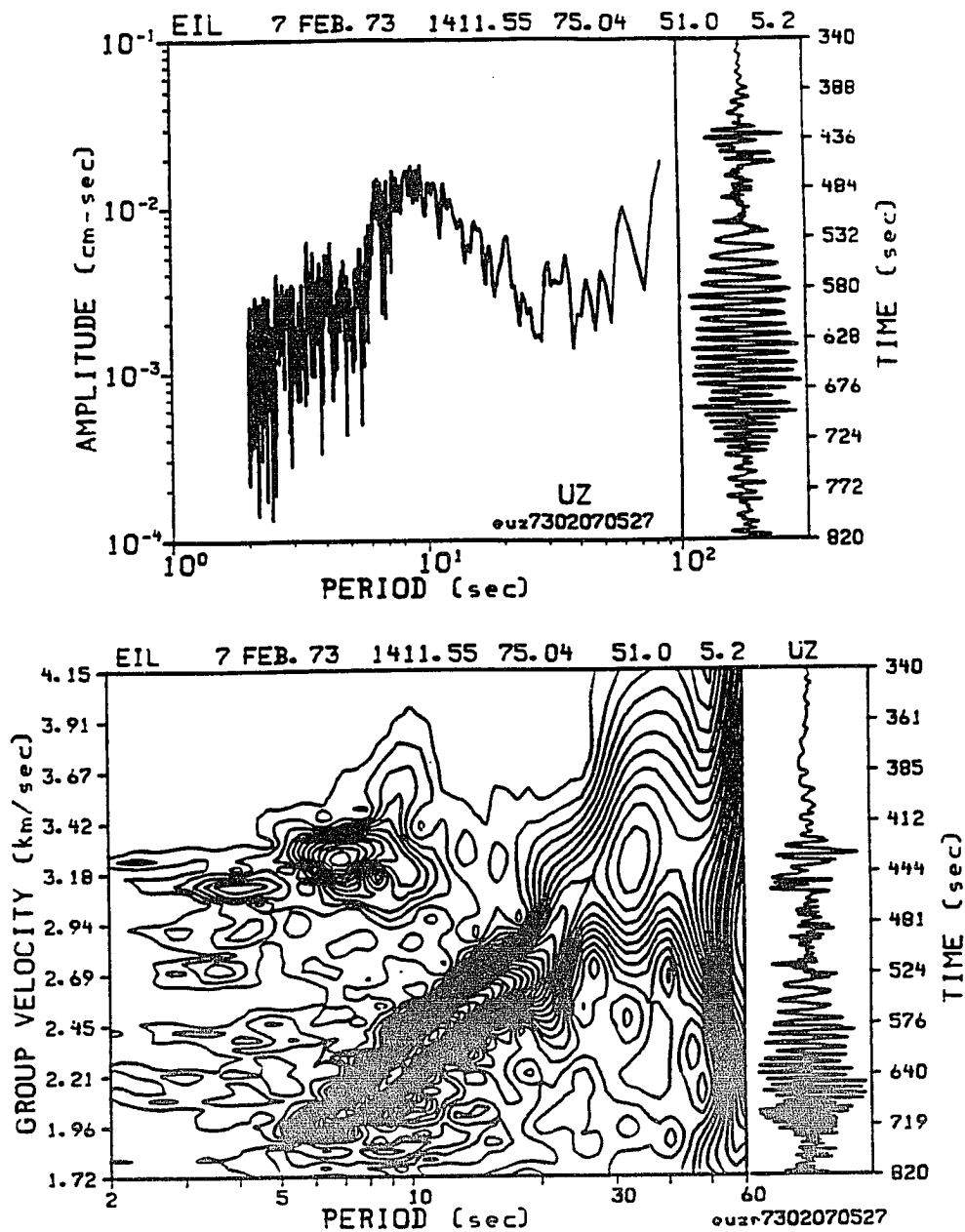
Figure 3.9. Example of an amplitude spectrum and dispersion curve of Rayleigh wave recorded at EIL station. The digitized seismogram is displayed in linear time scale adjacent to the spectrum, and the corrected ground displacement is plotted in linear group velocity scale adjacent to the dispersion contour diagram.

- 34 -
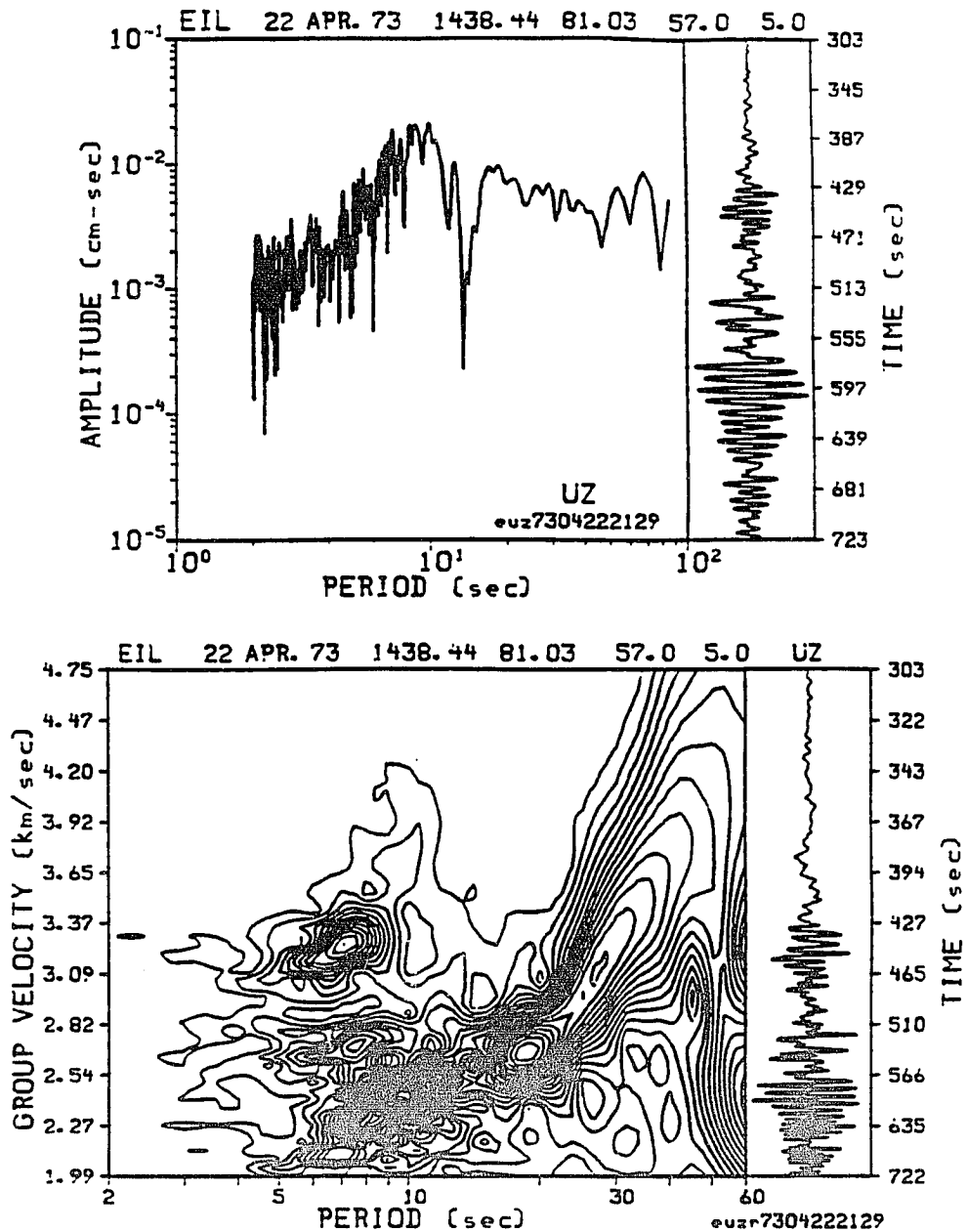
Figure 3.10. Example of an amplitude spectrum and dispersion curve of
Rayleigh wave recorded at EIL station. The digitized
seismogram is displayed in linear time scale adjacent to the
spectrum, and the corrected ground displacement is plotted
in linear group velocity scale adjacent to the dispersion con-
tour diagram.
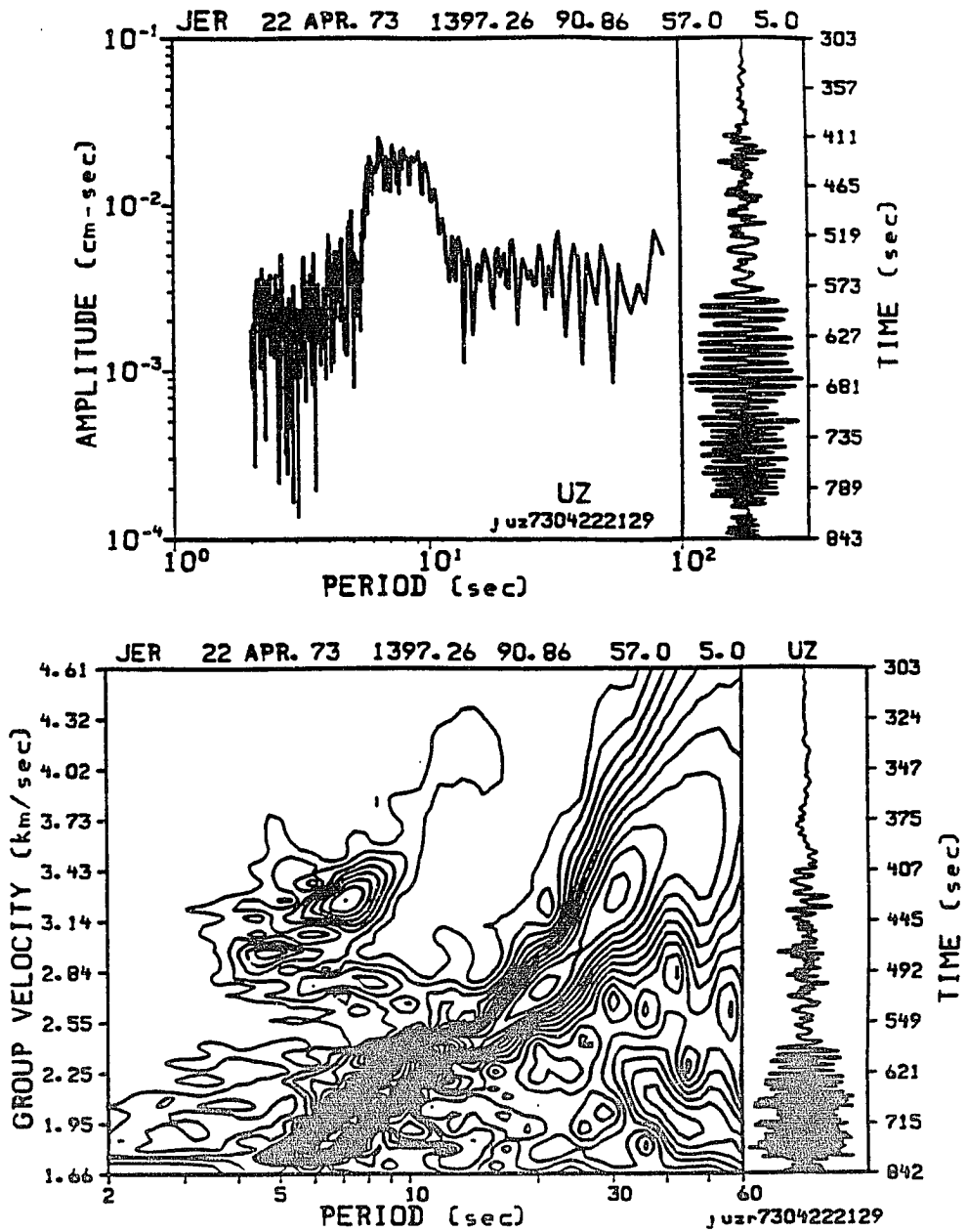
Figure 3.11. Example of an amplitude spectrum and dispersion curve of Rayleigh wave recorded at JER station. The digitized seismogram is displayed in linear time scale adjacent to the spectrum, and the corrected ground displacement is plotted in linear group velocity scale adjacent to the dispersion contour diagram.
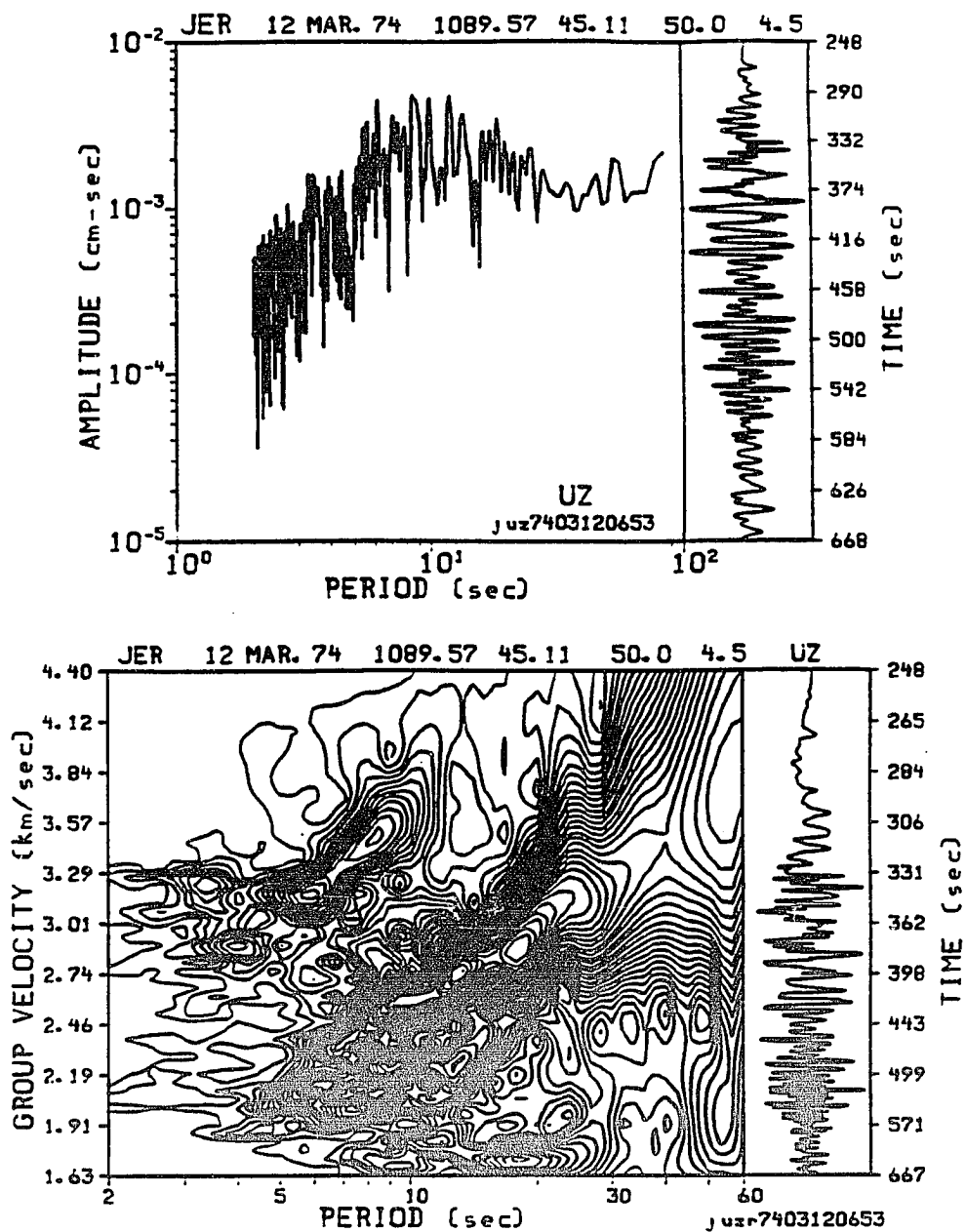
Figure 3.12. Example of an amplitude spectrum and dispersion curve of Rayleigh wave recorded at JER station. The digitized seismogram is displayed in linear time scale adjacent to the spectrum, and the corrected ground displacement is plotted in linear group velocity scale adjacent to the dispersion contour diagram.

constructed. Consecutive rows correspond to equal increments in group velocity, while consecutive columns correspond to equal increments in log period. Finally, the amplitudes are arbitrarily normalized to a maximum value of 99, and contoured so that the multi-mode dispersion curves can be inferred from the ridge crest of the contours.

It is important to note that, in Figures 3.5-3.12 the seismograms adjacent to the contour diagrams represent the recovered ground displacement signal, whereas those to the right of the amplitude spectra are the actual digitized records displayed with a linear time scale. Also, since the prominent features of seismograms can be directly related to the configuration of group velocity dispersion curves, the recovered time series are presented with a linear velocity scale. Consequently, at given periods, direct correlation between the group-delay times of the seismogram with the ridge crest of the instantaneous amplitudes can facilitate interpreting the observed arrival patterns. A fast Fourier transform is used to take the corrected spectra from the frequency to the time domain. The spectral edge cut-off effect on recovered seismograms is minimized by applying a Parzen window in the frequency domain (Jenkins and Watts, 1968; Harris, 1978).

Among the interesting features observed in Figures 3.5-3.12 is that the resultant dispersion curves exhibit typical continental fundamental and higher modes. With the exception of TAB (Figures 3.5 and 3.6), it is apparent from both the contour diagrams and accompanying seismograms that the higher-mode waves are well recorded at SHI, EIL and JER stations (Figures 3.7-3.12). It is also apparent that the fundamental and higher-mode dispersion curves are well determined and separated in time. In some cases, however, the continuity of the curves and contours is distorted by the

presence of amplitude minima or spectral holes. The effect of this phenomenon can be seen, for instance, in Figure 3.7 around the 17 sec period and 2.86 km/sec group velocity, as well as in Figure 3.10 around approximately 15 sec and 2.59 km/sec. For that reason, a close comparison of the amplitude spectra to the contour diagrams can significantly assist in interpreting the dispersion curves. On the other hand, the most striking observation pertinent to the effectiveness of the technique in resolving complex transient signals is demonstrated in Figure 3.8. In this example the event under consideration is immediately followed and partially overlapped by another event. Despite this complication, it is clear that not only the fundamental and higher modes of the first event are isolated, but also the fundamental-mode of the second event is separated as well. The obtained group velocities for the first event are also in good agreement with those from other events along the same path. It should be obvious, however, that group velocities of the second event are incorrect, since only the origin time and epicentral distance of the first event are included in the analysis.

Rayleigh wave dispersion curves at periods between 3 and 68 sec for the fundamental-mode and between 3 and 21 sec for the first higher-mode are determined using the single-station method described earlier. The associated group velocities range from 1.92 to 3.87 km/sec for the fundamental-mode and 2.74 to 4.36 km/sec for the first higher-mode. In practice, there are several possible sources of error that may contribute to the uncertainty of measured group velocities. Knopoff and Schwab (1968) showed that the initial phase of a point source depends on the angle of inclination of the source to the vertical. The effect is frequency dependent, and becomes more pronounced at long periods and short epicentral

distances. They also showed that correction for this effect is relatively more important to phase than group velocities determined by the single-station method. Despite the lack of source mechanism solutions, it is estimated that for the periods and path lengths considered in this study, the required source corrections are small enough to be neglected. In addition, Forsyth (1975) showed that finiteness of the source, uncertainty in the origin time and mislocation of the epicenter will lead to a systematic shift in the measured velocities and increased scatter in the data. However, since all the events have magnitudes of 5.5 or less, corrections for a finite source dimension and for motion along the fault surface are not necessary. On the other hand, although corrections due to uncertainty in the origin time are usually small, the mislocation of epicenters is expected to be the greatest source of error affecting the data in this study. For example, reported mislocations of earthquakes along the Zagros are often in the order of tens of kilometers (Ambraseys, 1978b; Berberian, 1979; Asudeh, 1983). Taking an error of 10-20 km in latitude and longitude, the velocity error varies between 0.02 and 0.05 km/sec, depending on the path length. This error can be estimated as approximately 0.03 km/sec for the various paths as a whole, but it is well within the data standard deviation.

3.3 Averaged Dispersion Data

Since many of the Rayleigh wave paths traverse the same geologic structures, their dispersion curves exhibit similar characteristics. Based upon this criterion, the individual group velocity curves for each station-path combination are grouped, and their average dispersion curves are determined along 19 representative paths. Maps showing the location of the

mean paths for stations TAB, SHI, EIL and JER are shown in Figures 3.13 through 3.16. The great circle paths in these figures offer a more extensive coverage of the various major tectonic units of the Arabian plate than any previously published study. Note that, the nomenclature adopted here to label the mean paths, as well as their averaged dispersion curves and shear velocity models discussed in Chapter 4, simply correspond to the station code (e.g., T for TAB, S for SHI, E for EIL and J for JER) followed by the mean back-azimuth in degrees. The asterisks in these figures outline the location of the Saudi Arabian deep seismic refraction profile across the Arabian shield, which will also be referred to in Chapter 4.

Traditionally, the reliability of averaged dispersion velocities at given periods is reported in terms of their deviation from the mean. Such information greatly influence the inversion process and the validity of resulting velocity models. From a statistics viewpoint, the variance of a simple random sample of a population is the average square deviation of each variate from the arithmetic mean (Zuwaylif, 1970). Symbolically,

$$s^2 = \sum_{i=1}^{n} \frac{(y_i - \bar{y})^2}{n - 1}$$

where y_i indicates the *ith* member of the sample (e.g., dispersion velocity at a given period), n is the sample size, $\bar{y} = \sum_{i=1}^{n} \frac{y_i}{n}$ is the arithmetic mean, and n−1 is the number of degrees of freedom. The standard deviation, on the other hand, is the square root of the variance. By definition, a range of one standard deviation on either side of the mean includes about 68% of the sample. A typical example to illustrate using the above approach is presented in Figure 3.17 and labelled "normal standard deviation". In this
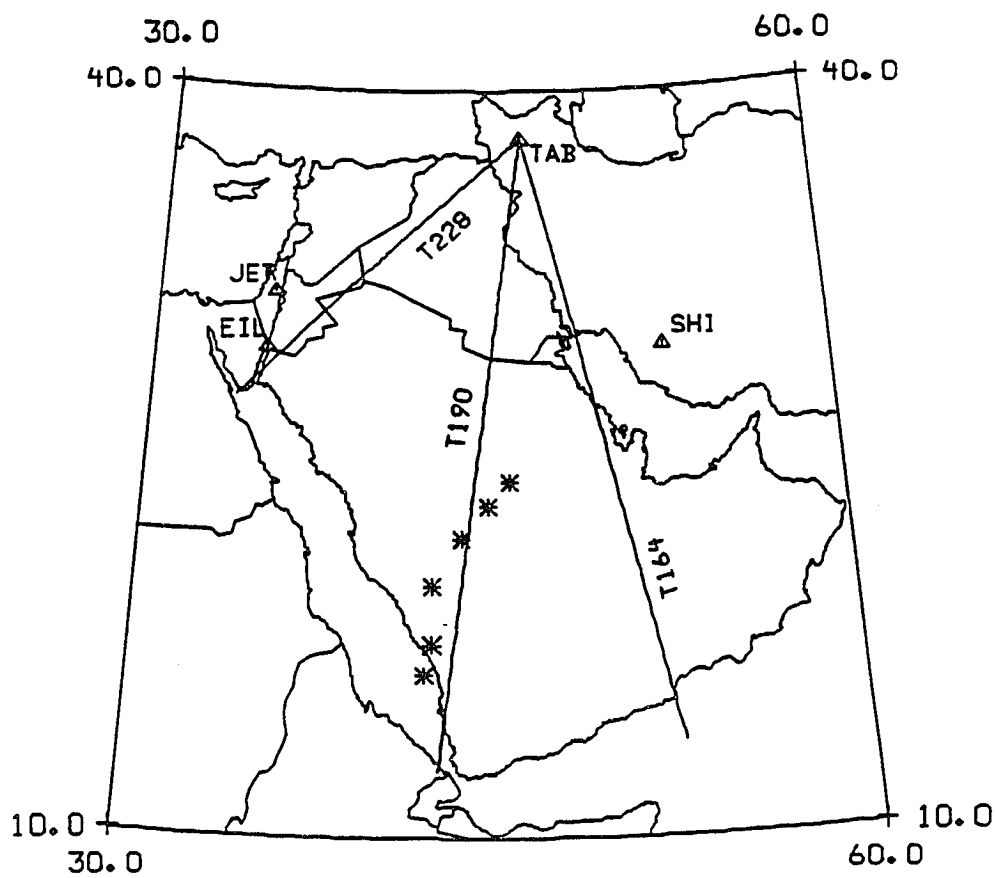
Figure 3.13. Averaged dispersion curve paths for TAB station. The aster-
isks represent the location of the shot points of the Saudi
Arabian deep seismic refraction profile across the Arabian
shield.
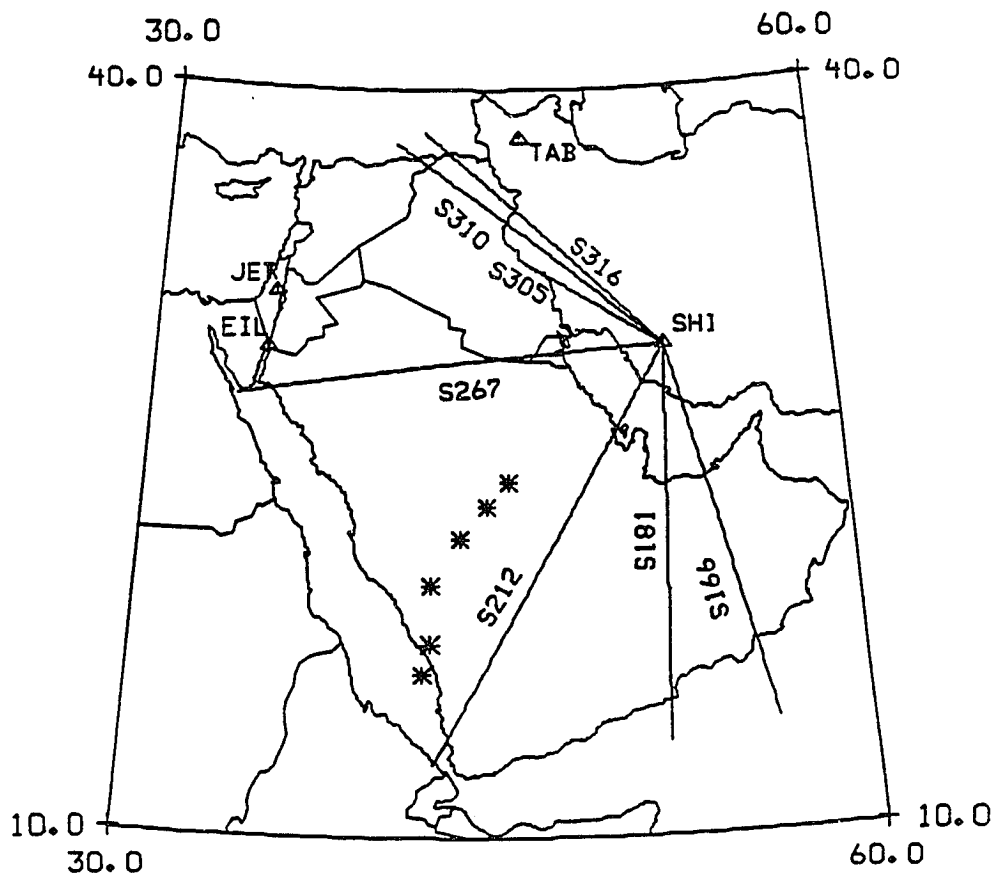
Figure 3.14. Averaged dispersion curve paths for SHI station. The aster-
isks represent the location of the shot points of the Saudi
Arabian deep seismic refraction profile across the Arabian
shield.
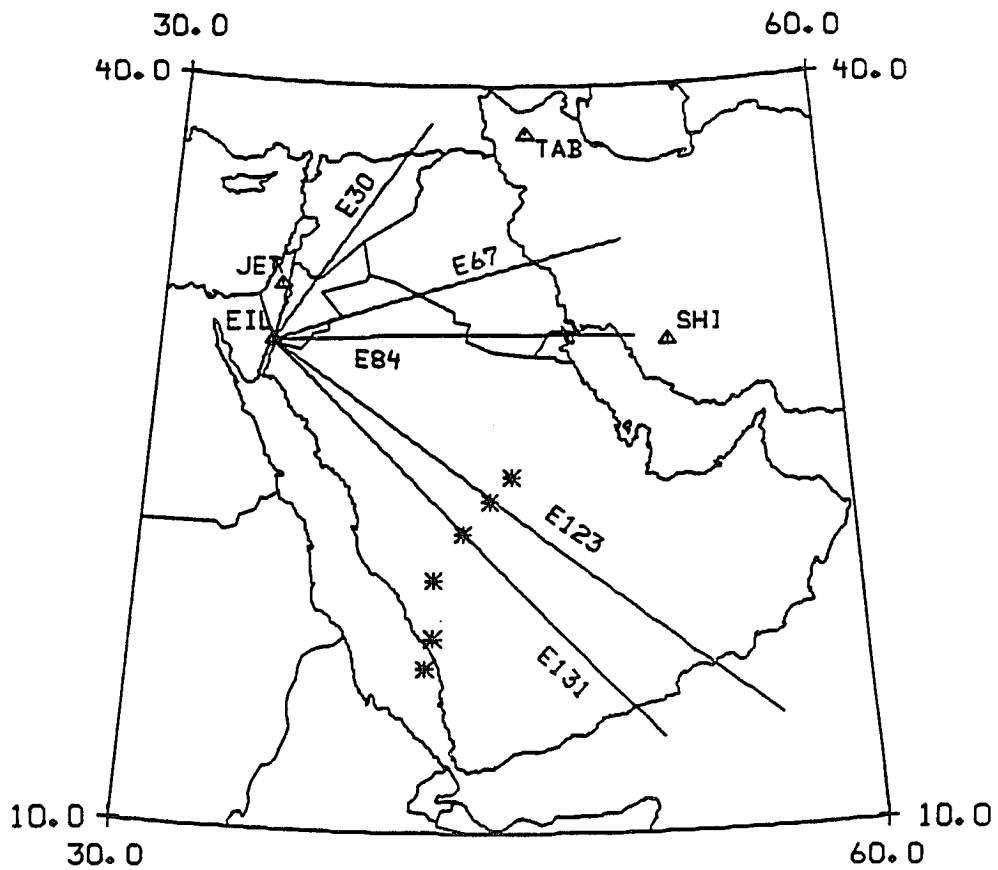
Figure 3.15. Averaged dispersion curve paths for EIL station. The aster-
isks represent the location of the shot points of the Saudi
Arabian deep seismic refraction profile across the Arabian
shield.

- 44 -
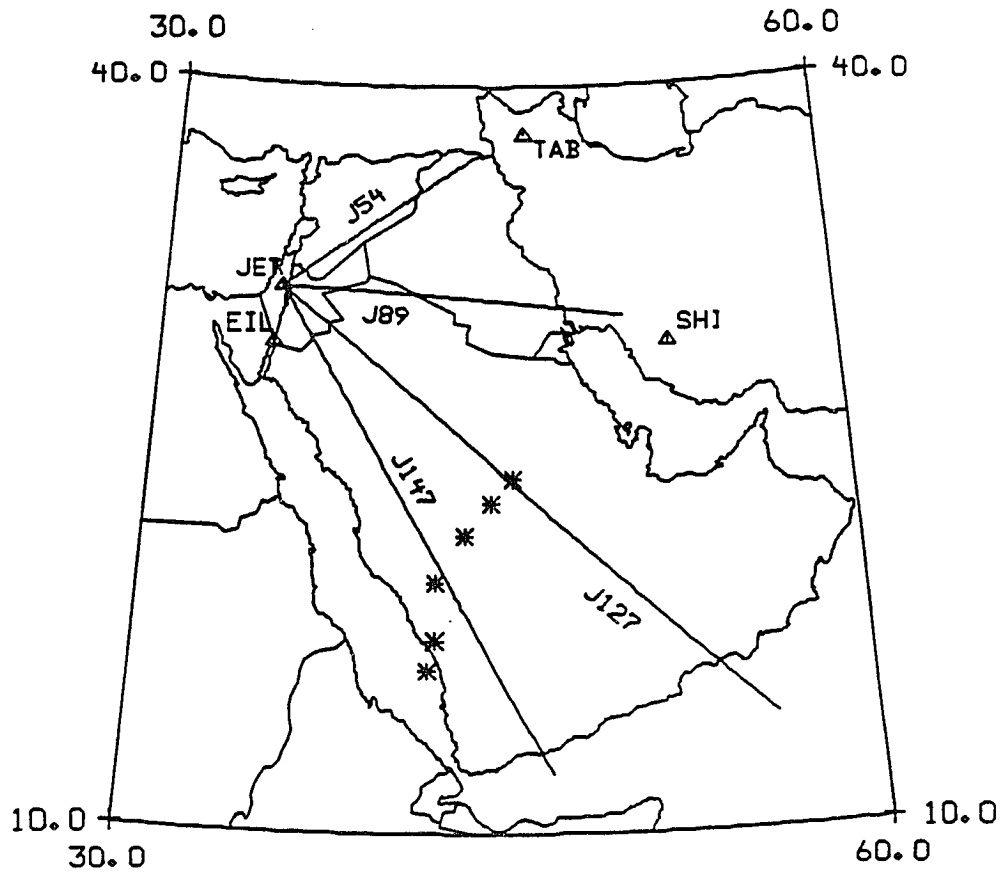
Figure 3.16. Averaged dispersion curve paths for JER station. The aster-
isks represent the location of the shot points of the Saudi
Arabian deep seismic refraction profile across the Arabian
shield.
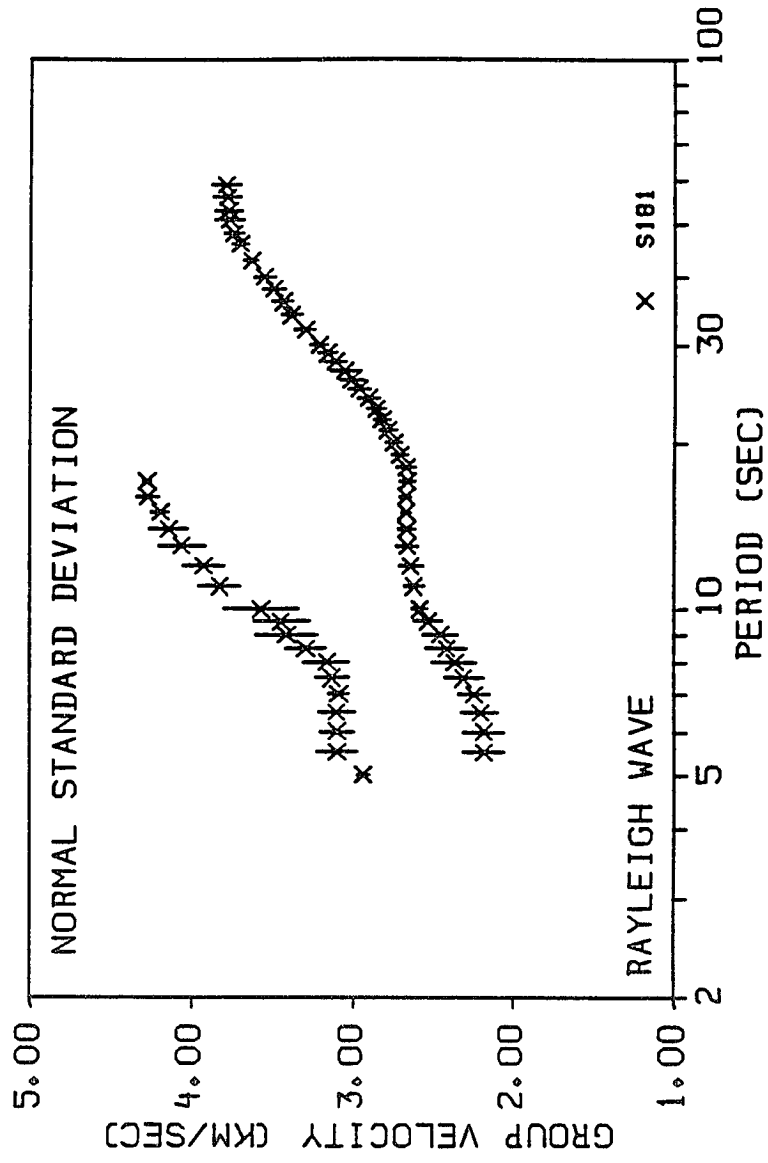
Figure 3.17. Example of an averaged dispersion curve with its group velocity standard deviations estimated using the traditional approach.

- 46 -

example, smaller error bars are associated with the fundamental-mode velocity measurements at periods between about 10-50 sec and larger ones outside this range. Also, larger error bars are generally associated with the higher-mode data. Although the lengths of these bars apparently reflect the reliability of data, there are some important disadvantages to applying the above approach in a problem of this sort. First, despite the fact that the dispersion velocity of surface waves is a function of period, the standard deviation of each sample is determined separately. In other words, the calculated arithmetic mean of each velocity sample at a given period is assumed to be independent. Second, although in practice the number of velocity measurements at given periods may not necessarily be equal, it is assumed that the arithmetic mean of a simple random sample provides a reliable estimate of the population mean. Consequently, the calculated standard deviations may overestimate the reliability of measured velocities for some periods and underestimate it for others.

To overcome drawbacks of the traditional standard deviation, an alternative formulation is proposed for surface wave analysis. The weighted standard deviation of a sample, denoted by σ_w, can be written as

$$\sigma_w = \frac{t(n)_{0.95}}{1.960} \left[\frac{n_{max}}{n} \right]^{1/2} \sigma \qquad (3.1)$$

where $t(n)_{0.95}$ is the student t-distribution 95% confidence limit for a given sample of size n, $t(\infty)_{0.95} = 1.960$, n_{max} is the size of the largest sample, and σ is the standard deviation. Figure 3.18 shows an example illustrating the "weighted standard deviation". To demonstrate the differences between the two approaches, the same dispersion data shown in Figure 3.17 is also used
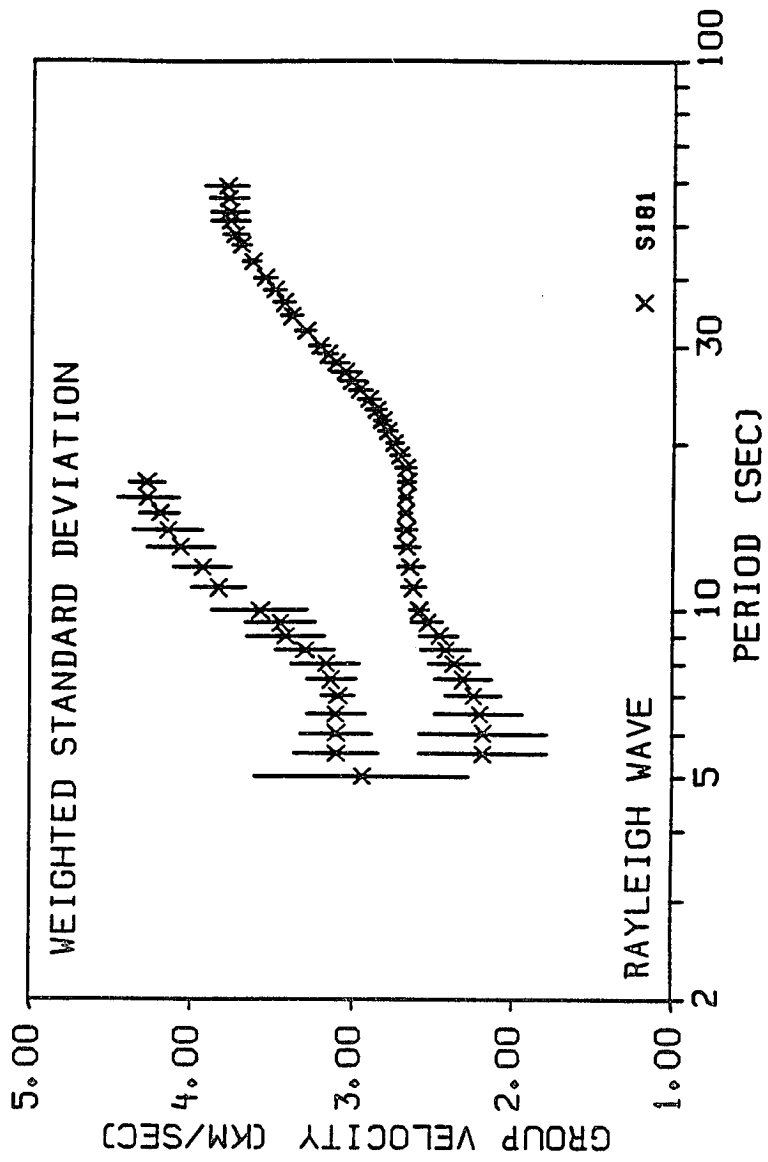
Figure 3.18. Example of an averaged dispersion curve with its group velocity standard deviations estimated using the proposed weighted approach.

- 48 -

in this example. In comparing the results, it is important to bear in mind that the effect of $t(n)_{0.95}/1.960$ and n_{max}/n in (3.1) decreases as n increases. Hence, for $n = n_{max}> >1$ the value of calculated σ_w approaches that of σ. Accordingly, in Figure 3.18 the fundamental mode samples between 10-40 sec exhibit no significant change in their standard deviation estimates. The most noticeable difference is the larger error bars exhibited by the higher-mode data, in general, and the fundamental-mode samples with periods less than 10 sec and greater than 40 sec. In this case n is less than n_{max}. A close examination of both examples shows that at some periods the traditional approach overestimates the reliability of averaged velocities. For instance, in Figure 3.17 the standard deviation of the fundamental-mode samples at periods less than 10 sec seems to be almost the same, whereas in Figure 3.18 the error bars increase at lower periods. Similar differences can also be observed with the higher-mode data. In conclusion, it is evident that (3.1) offers a more practical and realistic representation of the reliability of averaged dispersion velocities. The advantage it provides toward estimating a geologically acceptable velocity model, should especially be appreciated when inverting dispersion data iteratively.

Before contemplating the prominent characteristics of the averaged dispersion curves, it should be noted that in the following figures and tables not only the observed, but also the theoretical data are presented. The latter are derived from the shear velocity models discussed in Chapter 4. Furthermore, in Figures 3.19 through 3.37, the fundamental modes are labelled with the letter " F " and the first higher modes with " H1 ". The observed data are represented by the symbol " x ", and the theoretical dispersion curves by solid lines.

3.3.1 TAB Station Data

The calculated group velocity curves are divided into three groups, namely T164, T190 and T228. The averaged dispersion curves are presented in Figures 3.19 through 3.21. As indicated by their mean paths in Figure 3.13, they sample the eastern, central (in a NE-SW direction) and northern portions of the Arabian plate. One distinguishing feature common to all of these averaged curves is the absence of higher-mode data. They are omitted, because of their inconsistent group velocities, limited period range, and poor quality. Since the paths length vary from about 1650 to 2768 km, it is not unreasonable to assume that anelastic attenuation and low instrument magnification are responsible for the poor quality of recorded higher-mode waves at station TAB. For that reason, only the fundamental modes are considered in this case. The averaged Rayleigh wave group velocities and their weighted standard deviations are listed in Tables 3.1-3.3. Results of profiles T164, T190 and T228 are obtained from averaging over ten, six and two paths, respectively (see Figure 3.1). As expected, the estimated standard deviations clearly reflect the fact that profile T228 data exhibit more scatter than those of T164 and T190. Also, since paths T190 and T228 traverse all the tectonic units of the Arabian plate, it is not surprising that there is little or no difference between their velocities. However, it is interesting to observe that at periods less than about 12 sec, T228 data show lower values than T164. A more significant difference, is observed between 15-51 sec, where T164 dispersion curve exhibit lower velocities than either T190 or T228. This decrease in velocity can be attributed to the passage of Rayleigh waves through the thick sedimentary column of the Mesopotamian foredeep and the Zagros folded belt

Figure 3.19. Averaged fundamental-mode Rayleigh wave dispersion curve with weighted standard deviations for path T164.

- 51 -

Table 3.1. Average Rayleigh wave group velocity dispersion data for path T164.

Period	Fundamental-Mode		
	Observed	Theoretical	Standard
	Velocity	Velocity	Deviation
(sec)	(km/sec)	(km/sec)	(km/sec)
5.0	2.66	2.71	0.333
5.5	2.65	2.70	0.312
6.0	2.70	2.69	0.280
6.5	2.69	2.68	0.219
7.0	2.69	2.67	0.222
7.5	2.69	2.66	0.223
8.0	2.69	2.66	0.211
8.5	2.67	2.65	0.175
9.0	2.67	2.65	0.172
9.5	2.65	2.65	0.139
10.0	2.66	2.66	0.124
11.0	2.65	2.67	0.060
12.0	2.67	2.68	0.048
13.0	2.69	2.69	0.039
14.0	2.71	2.71	0.027
15.0	2.72	2.72	0.020
16.0	2.73	2.73	0.026
17.0	2.74	2.74	0.036
18.0	2.74	2.75	0.043
19.0	2.75	2.75	0.039
20.0	2.76	2.76	0.031
21.0	2.77	2.77	0.032
22.0	2.79	2.79	0.036
23.0	2.81	2.81	0.033
24.0	2.83	2.83	0.030
25.0	2.86	2.85	0.027
26.0	2.89	2.88	0.026
27.0	2.92	2.92	0.032
28.0	2.96	2.95	0.035
29.0	2.99	3.00	0.043
30.0	3.03	3.04	0.050

Table 3.1. Continued.

Period	Observed Velocity	Theoretical Velocity	Standard Deviation
(sec)	(km/sec)	(km/sec)	(km/sec)
32.0	3.12	3.12	0.043
34.0	3.21	3.21	0.033
36.0	3.29	3.29	0.040
38.0	3.37	3.36	0.040
40.0	3.43	3.43	0.046
43.0	3.51	3.51	0.046
46.0	3.56	3.57	0.041
48.0	3.60	3.60	0.053
51.0	3.64	3.65	0.063
53.0	3.67	3.67	0.059
56.0	3.70	3.70	0.083
59.0	3.72	3.72	0.105
61.0	3.74	3.74	0.107
64.0	3.79	3.75	0.224
68.0	3.72	3.77	0.355

The table header spans: **Fundamental-Mode**

Figure 3.20. Averaged fundamental-mode Rayleigh wave dispersion curve with weighted standard deviations for path T190.

- 54 -

Table 3.2. Average Rayleigh wave group velocity dispersion data for path T190.

	Fundamental-Mode		
Period (sec)	Observed Velocity (km/sec)	Theoretical Velocity (km/sec)	Standard Deviation (km/sec)
8.5	2.60	2.59	0.052
9.0	2.63	2.62	0.077
9.5	2.63	2.64	0.076
10.0	2.64	2.67	0.062
11.0	2.68	2.72	0.068
12.0	2.73	2.76	0.124
13.0	2.81	2.80	0.053
14.0	2.82	2.82	0.058
15.0	2.86	2.85	0.031
16.0	2.87	2.87	0.021
17.0	2.88	2.88	0.022
18.0	2.90	2.90	0.014
19.0	2.91	2.92	0.021
20.0	2.93	2.94	0.028
21.0	2.95	2.97	0.028
22.0	2.99	3.00	0.022
23.0	3.04	3.03	0.016
24.0	3.08	3.06	0.030
25.0	3.11	3.10	0.038
26.0	3.14	3.14	0.046
27.0	3.17	3.18	0.044
28.0	3.21	3.22	0.039
29.0	3.24	3.25	0.035
30.0	3.27	3.29	0.032
32.0	3.35	3.36	0.037
34.0	3.41	3.42	0.062
36.0	3.47	3.47	0.061
38.0	3.52	3.52	0.029
40.0	3.57	3.56	0.013
43.0	3.61	3.62	0.013
46.0	3.66	3.66	0.017
48.0	3.68	3.68	0.026
51.0	3.72	3.71	0.047
53.0	3.74	3.73	0.051
56.0	3.76	3.75	0.066
59.0	3.77	3.77	0.102
61.0	3.78	3.78	0.096
64.0	3.79	3.80	0.132
68.0	3.79	3.81	0.088
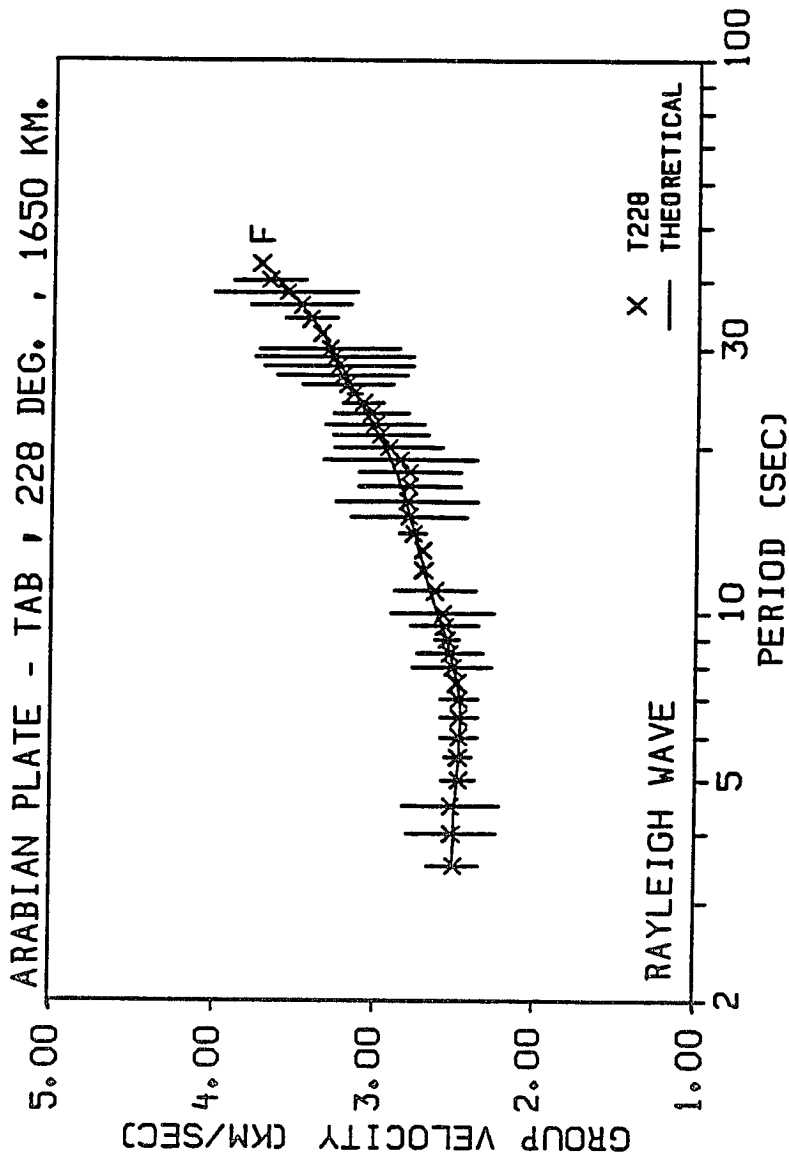
Figure 3.21. Averaged fundamental-mode Rayleigh wave dispersion curve with weighted standard deviations for path T228.

- 56 -

Table 3.3. Average Rayleigh wave group velocity dispersion data for path T228.

	Fundamental-Mode		
Period (sec)	Observed Velocity (km/sec)	Theoretical Velocity (km/sec)	Standard Deviation (km/sec)
3.5	2.50	2.51	0.160
4.0	2.52	2.50	0.278
4.5	2.52	2.50	0.303
5.0	2.47	2.48	0.101
5.5	2.48	2.47	0.081
6.0	2.47	2.47	0.115
6.5	2.47	2.47	0.115
7.0	2.47	2.47	0.115
7.5	2.49	2.48	0.011
8.0	2.51	2.50	0.252
8.5	2.53	2.53	0.209
9.0	2.55	2.55	0.077
9.5	2.56	2.58	0.213
10.0	2.58	2.61	0.322
11.0	2.63	2.66	0.251
12.0	2.70	2.70	0.011
13.0	2.70	2.73	0.000
14.0	2.77	2.76	0.083
15.0	2.80	2.79	0.361
16.0	2.81	2.82	0.444
17.0	2.79	2.85	0.316
18.0	2.79	2.88	0.318
19.0	2.86	2.92	0.480
20.0	2.93	2.95	0.338
21.0	2.98	2.99	0.300
22.0	3.01	3.03	0.310
23.0	3.04	3.07	0.236
24.0	3.09	3.10	0.128
25.0	3.14	3.14	0.045
26.0	3.19	3.17	0.285
27.0	3.22	3.20	0.408
28.0	3.24	3.23	0.461
29.0	3.27	3.26	0.495
30.0	3.30	3.29	0.435
32.0	3.35	3.35	0.018
34.0	3.42	3.41	0.161
36.0	3.48	3.48	0.316
38.0	3.57	3.55	0.442
40.0	3.67	3.62	0.223
43.0	3.73	3.73	0.018

(Figure 2.1) along the eastern portion of the plate.

3.3.2 SHI Station Data

In this case the dispersion curves are divided into seven groups. These are S166, S181, S212, S267, S305, S310 and S316. Their averaged Rayleigh wave group velocities and weighted standard deviations are displayed in Figures 3.22 through 3.28, and given in Tables 3.4-3.10. Two interesting points should be mentioned here regarding the observed characteristics of station SHI dispersion curves. First, in comparison with data from the other stations used in this study, there seem to be less pronounced, but consistent, variation in velocity throughout the period range among the paths. This is not surprising since except for S212 and S267, the rest of the paths lie entirely within the Mesopotamian foredeep and the Zagros folded belt. As shown in Figure 3.14, the paths for S305, S310 and S316 sample the northeastern portion of the Arabian plate, whereas S166 and S181 sample its southeastern region. The corresponding paths for S212 and S267, on the other hand, traverse the plate in NE-SW and roughly E-W directions, respectively. In other words, they both sample all the tectonic units in the area (Figure 2.1), including the Arabian platform and the northern and southern ends of the exposed shield region. For this reason there is little variation between their fundamental-mode group velocities (see Figures 3.24 and 3.25; Tables 3.6 and 3.7). This similarity between S212 and S267 dispersion curves is consistent with the conclusion of Knopoff and Fouda (1975) regarding the variation of Rayleigh waves phase velocity along approximately the same paths. The second point is that, the first higher Rayleigh-mode is exceptionally well recorded at SHI station. As shown in

Figure 3.22. Averaged fundamental and first higher-mode Rayleigh wave dispersion curves with weighted standard deviations for path S166.

- 59 -

Table 3.4. Average Rayleigh wave group velocity dispersion data for path S166.

	Fundamental-Mode			Higher-Mode		
Period (sec)	Observed Velocity (km/sec)	Theoretical Velocity (km/sec)	Standard Deviation (km/sec)	Observed Velocity (km/sec)	Theoretical Velocity (km/sec)	Standard Deviation (km/sec)
5.5	2.31	2.40	0.188	3.07	3.02	0.364
6.0	2.36	2.41	0.167	3.09	3.05	0.125
6.5	2.40	2.42	0.154	3.10	3.08	0.118
7.0	2.43	2.44	0.126	3.10	3.09	0.113
7.5	2.45	2.46	0.114	3.10	3.11	0.114
8.0	2.48	2.48	0.088	3.13	3.14	0.128
8.5	2.50	2.51	0.083	3.16	3.19	0.180
9.0	2.52	2.53	0.083	3.17	3.25	0.197
9.5	2.54	2.55	0.088	3.23	3.33	0.192
10.0	2.60	2.57	0.085	3.36	3.42	0.166
11.0	2.62	2.60	0.047	3.57	3.60	0.175
12.0	2.64	2.63	0.035	3.75	3.76	0.143
13.0	2.65	2.65	0.034	3.84	3.89	0.132
14.0	2.67	2.67	0.035	3.90	3.99	0.145
15.0	2.68	2.68	0.029	4.06	4.07	0.105
16.0	2.69	2.69	0.035	4.16	4.14	0.099
17.0	2.70	2.70	0.035	4.18	4.19	0.103
18.0	2.70	2.72	0.039	4.26	4.24	0.075
19.0	2.73	2.73	0.038	4.25	4.29	0.103
20.0	2.75	2.75	0.036	4.36	4.33	0.079
21.0	2.78	2.78	0.036	4.35	4.38	0.127
22.0	2.81	2.81	0.038			
23.0	2.85	2.84	0.038			
24.0	2.89	2.88	0.042			
25.0	2.93	2.93	0.034			
26.0	2.97	2.98	0.033			
27.0	3.02	3.03	0.041			
28.0	3.07	3.08	0.051			
29.0	3.12	3.13	0.053			
30.0	3.19	3.18	0.041			
32.0	3.28	3.28	0.039			
34.0	3.38	3.37	0.045			
36.0	3.44	3.45	0.048			
38.0	3.51	3.52	0.058			
40.0	3.58	3.58	0.045			
43.0	3.66	3.65	0.080			
46.0	3.72	3.71	0.095			
48.0	3.73	3.74	0.094			
51.0	3.76	3.78	0.096			
53.0	3.79	3.80	0.108			
56.0	3.84	3.83	0.244			
59.0	3.87	3.85	0.221			

Figure 3.23. Averaged fundamental and first higher-mode Rayleigh wave dispersion curves with weighted standard deviations for path S181.

- 61 -

Table 3.5. Average Rayleigh wave group velocity dispersion data for path
S181.

	Fundamental-Mode			Higher-Mode		
Period (sec)	Observed Velocity (km/sec)	Theoretical Velocity (km/sec)	Standard Deviation (km/sec)	Observed Velocity (km/sec)	Theoretical Velocity (km/sec)	Standard Deviation (km/sec)
5.0	2.12	2.13	0.087	2.94	2.98	0.663
5.5	2.19	2.15	0.400	3.10	3.00	0.263
6.0	2.19	2.19	0.400	3.10	3.02	0.221
6.5	2.21	2.24	0.277	3.10	3.05	0.181
7.0	2.25	2.29	0.175	3.09	3.10	0.098
7.5	2.31	2.35	0.181	3.13	3.15	0.149
8.0	2.37	2.40	0.163	3.17	3.22	0.209
8.5	2.42	2.45	0.154	3.30	3.31	0.179
9.0	2.46	2.49	0.123	3.42	3.42	0.238
9.5	2.54	2.53	0.097	3.45	3.54	0.215
10.0	2.59	2.56	0.056	3.57	3.65	0.294
11.0	2.63	2.61	0.072	3.83	3.85	0.171
12.0	2.64	2.64	0.082	3.93	3.99	0.174
13.0	2.66	2.66	0.078	4.06	4.07	0.209
14.0	2.67	2.67	0.062	4.14	4.13	0.215
15.0	2.68	2.68	0.038	4.20	4.17	0.122
16.0	2.68	2.69	0.040	4.27	4.22	0.191
17.0	2.67	2.69	0.054	4.28	4.30	0.114
18.0	2.68	2.71	0.065			
19.0	2.72	2.72	0.056			
20.0	2.75	2.74	0.054			
21.0	2.79	2.77	0.057			
22.0	2.83	2.81	0.055			
23.0	2.87	2.85	0.063			
24.0	2.91	2.90	0.072			
25.0	2.97	2.95	0.073			
26.0	3.02	3.01	0.081			
27.0	3.06	3.06	0.089			
28.0	3.11	3.12	0.076			
29.0	3.17	3.17	0.064			
30.0	3.22	3.22	0.061			

Table 3.5. Continued.

	Fundamental-Mode			Higher-Mode		
Period (sec)	Observed Velocity (km/sec)	Theoretical Velocity (km/sec)	Standard Deviation (km/sec)	Observed Velocity (km/sec)	Theoretical Velocity (km/sec)	Standard Deviation (km/sec)
32.0	3.31	3.31	0.067			
34.0	3.39	3.39	0.070			
36.0	3.44	3.45	0.069			
38.0	3.50	3.51	0.072			
40.0	3.56	3.56	0.069			
43.0	3.64	3.63	0.055			
46.0	3.70	3.68	0.062			
48.0	3.74	3.72	0.075			
51.0	3.77	3.76	0.115			
53.0	3.78	3.78	0.114			
56.0	3.78	3.82	0.115			
59.0	3.79	3.85	0.132			
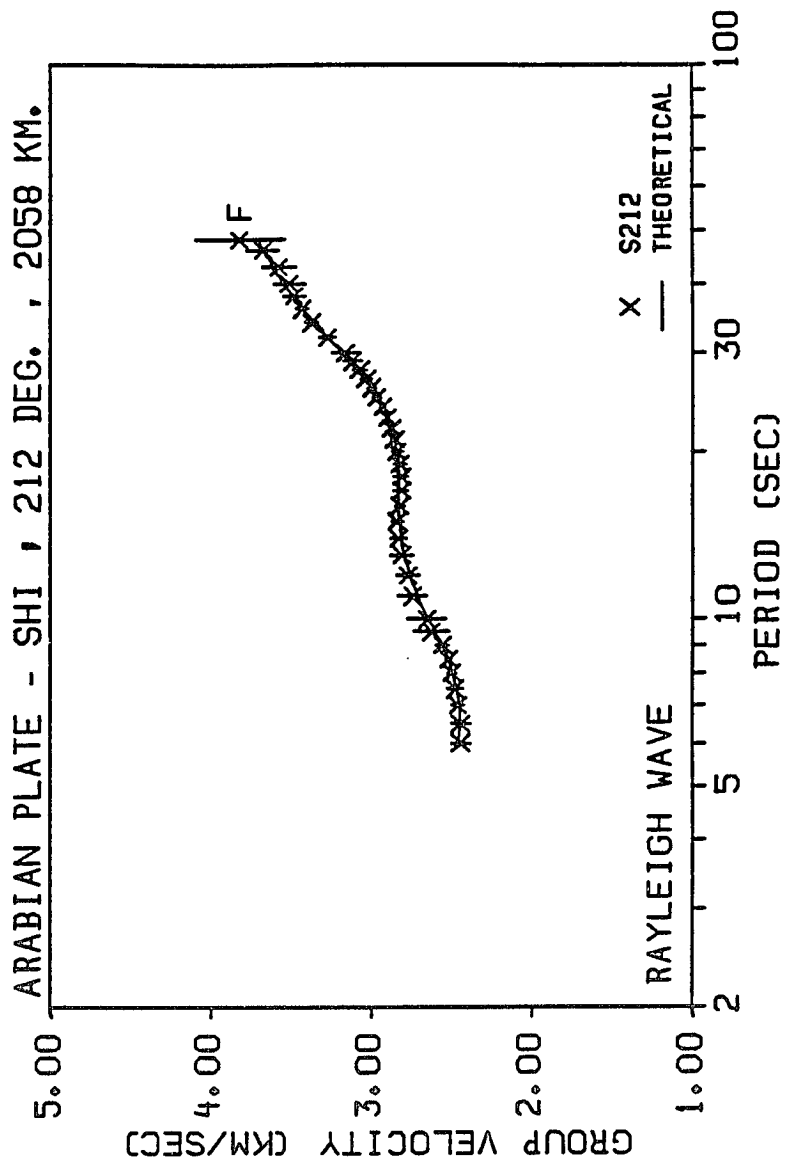
Figure 3.24. Averaged fundamental-mode Rayleigh wave dispersion curve with weighted standard deviations for path S212.

Table 3.6. Average Rayleigh wave group velocity dispersion data for path S212.

Period	Observed Velocity	Theoretical Velocity	Standard Deviation
(sec)	(km/sec)	(km/sec)	(km/sec)
	Fundamental-Mode		
6.0	2.45	2.46	0.059
6.5	2.45	2.45	0.059
7.0	2.46	2.45	0.038
7.5	2.48	2.47	0.047
8.0	2.50	2.49	0.028
8.5	2.52	2.53	0.016
9.0	2.56	2.57	0.038
9.5	2.63	2.61	0.108
10.0	2.66	2.65	0.117
11.0	2.74	2.71	0.089
12.0	2.78	2.76	0.070
13.0	2.81	2.80	0.065
14.0	2.83	2.82	0.052
15.0	2.84	2.83	0.038
16.0	2.83	2.83	0.031
17.0	2.82	2.83	0.042
18.0	2.82	2.83	0.041
19.0	2.83	2.84	0.038
20.0	2.84	2.84	0.032
21.0	2.86	2.86	0.026
22.0	2.88	2.87	0.015
23.0	2.90	2.90	0.014
24.0	2.93	2.93	0.018
25.0	2.97	2.96	0.028
26.0	3.00	3.00	0.030
27.0	3.03	3.05	0.033
28.0	3.07	3.09	0.042
29.0	3.12	3.14	0.061
30.0	3.16	3.18	0.082
32.0	3.27	3.27	0.046
34.0	3.37	3.35	0.037
36.0	3.43	3.42	0.038
38.0	3.48	3.49	0.069
40.0	3.51	3.54	0.098
43.0	3.57	3.62	0.104
46.0	3.67	3.67	0.094
48.0	3.82	3.70	0.281

Figure 3.25. Averaged fundamental and first higher-mode Rayleigh wave dispersion curves with weighted standard deviations for path S267.

Table 3.7. Average Rayleigh wave group velocity dispersion data for path S267.

Period (sec)	Fundamental-Mode			Higher-Mode		
	Observed Velocity (km/sec)	Theoretical Velocity (km/sec)	Standard Deviation (km/sec)	Observed Velocity (km/sec)	Theoretical Velocity (km/sec)	Standard Deviation (km/sec)
4.0				3.19	3.17	0.689
4.5				3.24	3.21	0.093
5.0				3.22	3.22	0.113
5.5				3.25	3.23	0.230
6.0				3.23	3.23	0.156
6.5	2.49	2.55	0.211	3.24	3.23	0.163
7.0	2.51	2.56	0.150	3.27	3.24	0.196
7.5	2.53	2.57	0.175	3.28	3.27	0.144
8.0	2.59	2.59	0.093	3.29	3.31	0.098
8.5	2.60	2.61	0.051	3.32	3.36	0.190
9.0	2.64	2.63	0.053	3.46	3.44	0.090
9.5	2.68	2.65	0.058	3.49	3.52	0.071
10.0	2.69	2.67	0.075	3.75	3.61	1.119
11.0	2.74	2.71	0.069			
12.0	2.75	2.74	0.066			
13.0	2.77	2.77	0.080			
14.0	2.77	2.79	0.035			
15.0	2.79	2.80	0.041			
16.0	2.81	2.81	0.041			
17.0	2.82	2.82	0.058			
18.0	2.84	2.84	0.020			
19.0	2.86	2.85	0.036			
20.0	2.87	2.87	0.057			
21.0	2.89	2.89	0.037			
22.0	2.91	2.92	0.039			
23.0	2.95	2.95	0.022			
24.0	2.99	2.98	0.055			
25.0	3.03	3.02	0.066			
26.0	3.07	3.06	0.083			
27.0	3.10	3.10	0.086			
28.0	3.14	3.14	0.037			
29.0	3.18	3.18	0.043			
30.0	3.20	3.22	0.060			
32.0	3.26	3.31	0.157			
34.0	3.38	3.38	0.455			
36.0	3.47	3.45	0.140			
38.0	3.55	3.52	0.236			
40.0	3.59	3.58	0.303			

Figure 3.26. Averaged fundamental and first Higher-mode Rayleigh wave dispersion curves with weighted standard deviations for path S305.

- 68 -

Table 3.8. Average Rayleigh wave group velocity dispersion data for path S305.

	Fundamental-Mode			Higher-Mode		
Period (sec)	Observed Velocity (km/sec)	Theoretical Velocity (km/sec)	Standard Deviation (km/sec)	Observed Velocity (km/sec)	Theoretical Velocity (km/sec)	Standard Deviation (km/sec)
3.0	2.03	2.04	0.030			
3.5	2.06	2.03	0.370			
4.0	2.09	2.06	0.152			
4.5	2.10	2.11	0.128			
5.0	2.16	2.18	0.175			
5.5	2.21	2.24	0.201	3.08	3.00	0.233
6.0	2.24	2.30	0.256	3.04	3.01	0.166
6.5	2.36	2.34	0.165	2.92	3.00	0.326
7.0	2.42	2.38	0.172	2.99	2.99	0.154
7.5	2.40	2.41	0.215	2.98	2.98	0.180
8.0	2.39	2.43	0.236	2.98	2.99	0.191
8.5	2.40	2.45	0.249	2.97	3.01	0.100
9.0	2.41	2.47	0.189	2.96	3.06	0.133
9.5	2.42	2.48	0.188	3.10	3.12	0.338
10.0	2.43	2.49	0.197	3.13	3.20	0.429
11.0	2.54	2.52	0.062	3.31	3.37	0.162
12.0	2.59	2.53	0.072	3.48	3.53	0.110
13.0	2.58	2.54	0.116	3.64	3.66	0.189
14.0	2.56	2.55	0.144	3.75	3.76	0.228
15.0	2.54	2.55	0.151	3.88	3.85	0.230
16.0	2.53	2.55	0.170	3.96	3.96	0.248
17.0	2.53	2.55	0.134			
18.0	2.54	2.55	0.110			
19.0	2.54	2.55	0.067			
20.0	2.54	2.55	0.031			
21.0	2.55	2.56	0.025			
22.0	2.56	2.56	0.011			
23.0	2.59	2.57	0.029			
24.0	2.62	2.59	0.057			
25.0	2.67	2.61	0.078			
26.0	2.73	2.64	0.140			
27.0	2.77	2.66	0.196			
28.0	2.81	2.70	0.240			
29.0	2.83	2.73	0.288			
30.0	2.85	2.77	0.335			
32.0	2.92	2.85	0.473			
34.0	3.24	2.93	1.131			

- 69 -
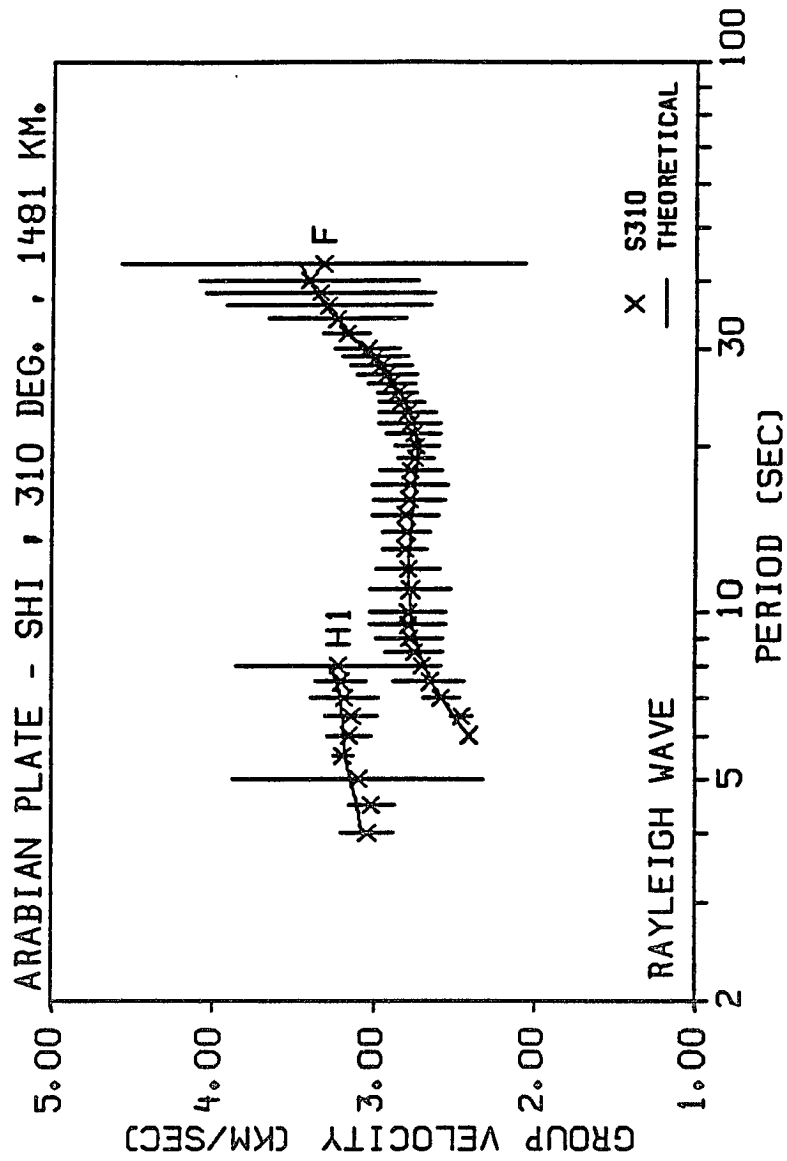
Figure 3.27. Averaged fundamental and first higher-mode Rayleigh wave dispersion curves with weighted standard deviations for path S310.

Table 3.9. Average Rayleigh wave group velocity dispersion data for path S310.

Period (sec)	Fundamental-Mode			Higher-Mode		
	Observed Velocity (km/sec)	Theoretical Velocity (km/sec)	Standard Deviation (km/sec)	Observed Velocity (km/sec)	Theoretical Velocity (km/sec)	Standard Deviation (km/sec)
4.0				3.04	3.08	0.163
4.5				3.02	3.11	0.141
5.0				3.10	3.15	0.775
5.5				3.19	3.18	0.062
6.0	2.41	2.42	0.010	3.16	3.19	0.133
6.5	2.46	2.51	0.070	3.14	3.20	0.163
7.0	2.59	2.59	0.114	3.18	3.21	0.210
7.5	2.66	2.65	0.221	3.21	3.24	0.159
8.0	2.71	2.69	0.106	3.22	3.28	0.632
8.5	2.76	2.72	0.178			
9.0	2.79	2.75	0.205			
9.5	2.79	2.76	0.237			
10.0	2.79	2.78	0.237			
11.0	2.78	2.79	0.253			
12.0	2.80	2.79	0.197			
13.0	2.81	2.79	0.142			
14.0	2.81	2.78	0.146			
15.0	2.81	2.77	0.206			
16.0	2.79	2.76	0.220			
17.0	2.78	2.75	0.234			
18.0	2.78	2.75	0.188			
19.0	2.75	2.75	0.111			
20.0	2.74	2.75	0.138			
21.0	2.77	2.76	0.167			
22.0	2.79	2.77	0.191			
23.0	2.80	2.80	0.178			
24.0	2.84	2.82	0.145			
25.0	2.87	2.86	0.125			
26.0	2.90	2.90	0.147			
27.0	2.93	2.94	0.187			
28.0	2.96	2.98	0.191			
29.0	3.00	3.03	0.197			
30.0	3.05	3.08	0.200			
32.0	3.18	3.16	0.139			
34.0	3.24	3.24	0.421			
36.0	3.29	3.31	0.632			
38.0	3.34	3.37	0.707			
40.0	3.41	3.41	0.677			
43.0	3.32	3.47	1.251			
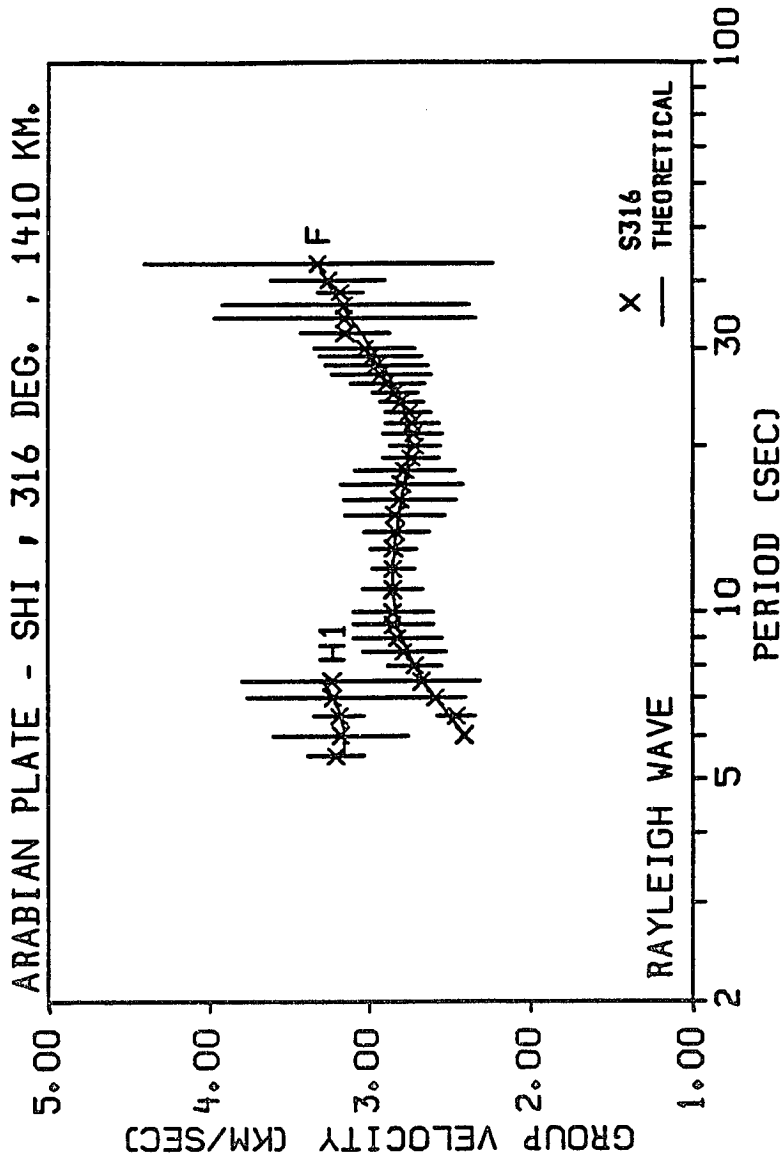
Figure 3.28. Averaged fundamental and first higher-mode Rayleigh wave dispersion curves with weighted standard deviations for path S316.

Table 3.10. Average Rayleigh wave group velocity dispersion data for path S316.

	Fundamental-Mode			Higher-Mode		
Period (sec)	Observed Velocity (km/sec)	Theoretical Velocity (km/sec)	Standard Deviation (km/sec)	Observed Velocity (km/sec)	Theoretical Velocity (km/sec)	Standard Deviation (km/sec)
5.5				3.21	3.15	0.174
6.0	2.42	2.41	0.014	3.18	3.15	0.422
6.5	2.46	2.51	0.115	3.18	3.18	0.154
7.0	2.59	2.59	0.186	3.23	3.22	0.536
7.5	2.67	2.66	0.360	3.23	3.29	0.564
8.0	2.72	2.71	0.169			
8.5	2.78	2.76	0.259			
9.0	2.82	2.79	0.277			
9.5	2.85	2.82	0.251			
10.0	2.85	2.83	0.251			
11.0	2.85	2.85	0.186			
12.0	2.85	2.85	0.131			
13.0	2.85	2.84	0.144			
14.0	2.83	2.83	0.201			
15.0	2.84	2.81	0.310			
16.0	2.81	2.80	0.349			
17.0	2.80	2.78	0.377			
18.0	2.78	2.77	0.312			
19.0	2.74	2.76	0.171			
20.0	2.71	2.76	0.156			
21.0	2.73	2.76	0.182			
22.0	2.74	2.77	0.169			
23.0	2.76	2.78	0.141			
24.0	2.80	2.80	0.133			
25.0	2.84	2.83	0.145			
26.0	2.89	2.85	0.229			
27.0	2.93	2.88	0.308			
28.0	2.96	2.92	0.314			
29.0	2.99	2.95	0.319			
30.0	3.03	2.98	0.314			
32.0	3.15	3.05	0.277			
34.0	3.15	3.11	0.811			
36.0	3.15	3.17	0.770			
38.0	3.18	3.22	0.142			
40.0	3.26	3.27	0.358			
43.0	3.32	3.32	1.084			

Figures 3.22 through 3.28, it is identified for all the paths but one. The corresponding higher-mode group velocities for path S212 are found to be inconsistent and had to be discarded. In addition, it can be observed that the higher-mode dispersion curves are measured over a relatively wide period range, i.e., from about 4 to 21 seconds. Within this range their velocity is found to vary between 2.92 and 4.36 km/sec. Finally, the higher modes seem to exhibit a variation similar to that of the fundamental-mode dispersion curves discussed earlier.

3.3.3 EIL Station Data

The calculated dispersion curves for this station seem to fall into five groups, namely E30, E67, E84, E123 and E131. Their averaged Rayleigh wave group velocities and weighted standard deviations are displayed in Figures 3.29-3.33, and listed in Tables 3.11-3.15. Unfortunately, the first higher-mode velocities along E123 and E131 are found to be inconsistent; hence, only those for E30, E67 and E84 are included. In general, the period range of the fundamental-mode extends from 4 to 59 sec, while the higher-mode extends from 3 to 12 sec. As expected, the highest group velocity values are observed along paths E123 and E131 which traverse the southwestern portion of the plate (Figure 3.15) and sample the Arabian shield in particular. Slightly lower velocities are observed along path E30 which traverses the northwestern portion of the plate. The lowest velocities are associated with paths E84 and E67 which, in common with path S267 of station SHI, sample all the plate's major tectonic units in roughly an E-W direction. Furthermore, careful inspection of the fundamental-mode data reveals significant variation in velocity at periods less than about 30 sec.
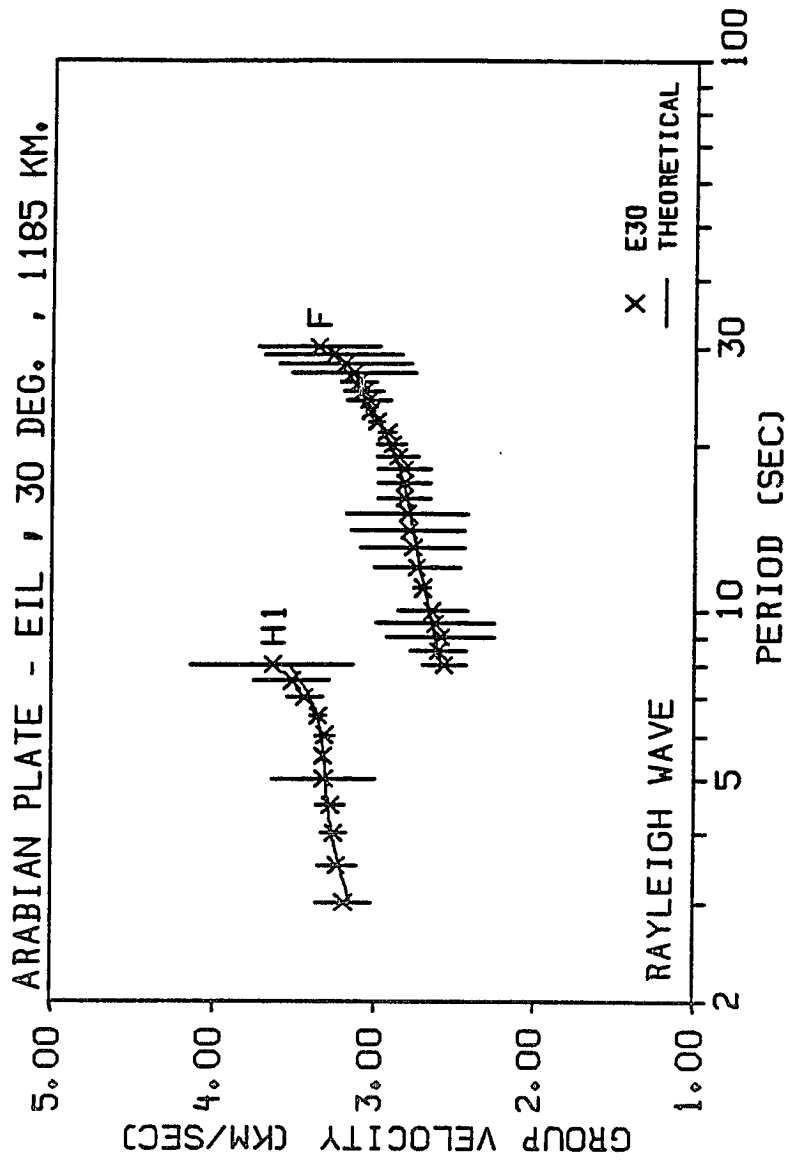
Figure 3.29. Averaged fundamental and first higher-mode Rayleigh wave dispersion curves with weighted standard deviations for path E30.

Table 3.11. Average Rayleigh wave group velocity dispersion data for path E30.

	Fundamental-Mode			Higher-Mode		
Period (sec)	Observed Velocity (km/sec)	Theoretical Velocity (km/sec)	Standard Deviation (km/sec)	Observed Velocity (km/sec)	Theoretical Velocity (km/sec)	Standard Deviation (km/sec)
3.0				3.19	3.15	0.173
3.5				3.23	3.22	0.124
4.0				3.25	3.27	0.078
4.5				3.27	3.29	0.090
5.0				3.32	3.31	0.321
5.5				3.32	3.32	0.009
6.0				3.31	3.33	0.057
6.5				3.35	3.36	0.049
7.0				3.44	3.40	0.111
7.5				3.52	3.46	0.234
8.0	2.57	2.59	0.135	3.64	3.54	0.502
8.5	2.61	2.61	0.174			
9.0	2.59	2.63	0.337			
9.5	2.63	2.65	0.371			
10.0	2.65	2.67	0.219			
11.0	2.71	2.70	0.053			
12.0	2.74	2.73	0.266			
13.0	2.77	2.75	0.326			
14.0	2.80	2.77	0.353			
15.0	2.80	2.79	0.381			
16.0	2.82	2.81	0.165			
17.0	2.82	2.84	0.165			
18.0	2.83	2.86	0.165			
19.0	2.87	2.89	0.135			
20.0	2.90	2.92	0.094			
21.0	2.94	2.95	0.054			
22.0	3.00	2.99	0.047			
23.0	3.04	3.03	0.027			
24.0	3.05	3.07	0.139			
25.0	3.08	3.11	0.118			
26.0	3.11	3.15	0.114			
27.0	3.14	3.19	0.387			
28.0	3.20	3.23	0.410			
29.0	3.27	3.26	0.425			
30.0	3.36	3.30	0.377			
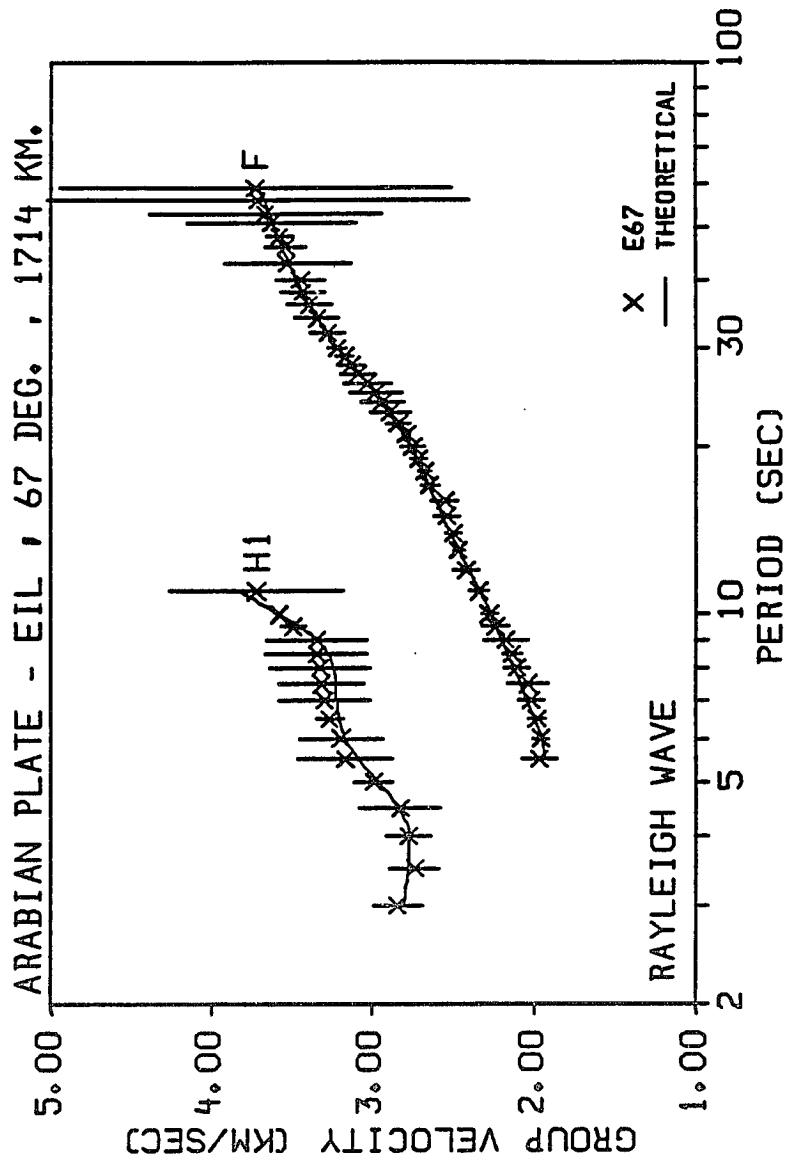
Figure 3.30. Averaged fundamental and first higher-mode Rayleigh wave dispersion curves with weighted standard deviations for path E67.

Table 3.12. Average Rayleigh wave group velocity dispersion data for path E67.

	Fundamental-Mode			Higher-Mode		
Period (sec)	Observed Velocity (km/sec)	Theoretical Velocity (km/sec)	Standard Deviation (km/sec)	Observed Velocity (km/sec)	Theoretical Velocity (km/sec)	Standard Deviation (km/sec)
3.0				2.84	2.80	0.152
3.5				2.74	2.78	0.150
4.0				2.77	2.77	0.137
4.5				2.83	2.84	0.249
5.0				2.99	2.96	0.113
5.5	1.97	1.93	0.110	3.17	3.08	0.295
6.0	1.96	1.96	0.046	3.19	3.16	0.262
6.5	1.99	2.00	0.056	3.26	3.20	0.083
7.0	2.02	2.05	0.079	3.30	3.22	0.285
7.5	2.04	2.09	0.124	3.31	3.22	0.265
8.0	2.11	2.13	0.082	3.32	3.24	0.311
8.5	2.14	2.17	0.060	3.34	3.27	0.318
9.0	2.18	2.21	0.135	3.35	3.34	0.314
9.5	2.24	2.24	0.083	3.49	3.45	0.079
10.0	2.28	2.27	0.049	3.58	3.58	0.009
11.0	2.34	2.34	0.061	3.72	3.82	0.538
12.0	2.42	2.41	0.077			
13.0	2.47	2.47	0.035			
14.0	2.50	2.52	0.052			
15.0	2.54	2.57	0.080			
16.0	2.55	2.61	0.083			
17.0	2.65	2.65	0.055			
18.0	2.67	2.68	0.039			
19.0	2.72	2.72	0.050			
20.0	2.75	2.76	0.078			
21.0	2.79	2.80	0.021			
22.0	2.84	2.84	0.073			
23.0	2.89	2.89	0.120			
24.0	2.94	2.94	0.135			
25.0	2.98	2.99	0.160			
26.0	3.03	3.04	0.147			
27.0	3.08	3.08	0.107			
28.0	3.13	3.13	0.073			
29.0	3.17	3.17	0.053			
30.0	3.21	3.21	0.056			

Table 3.12. Continued.

	Fundamental-Mode			Higher-Mode		
Period (sec)	Observed Velocity (km/sec)	Theoretical Velocity (km/sec)	Standard Deviation (km/sec)	Observed Velocity (km/sec)	Theoretical Velocity (km/sec)	Standard Deviation (km/sec)
32.0	3.27	3.28	0.108			
34.0	3.34	3.34	0.135			
36.0	3.39	3.39	0.144			
38.0	3.43	3.43	0.139			
40.0	3.44	3.47	0.156			
43.0	3.52	3.52	0.395			
46.0	3.54	3.56	0.127			
48.0	3.57	3.59	0.084			
51.0	3.62	3.62	0.529			
53.0	3.67	3.64	0.722			
56.0	3.71	3.67	1.313			
59.0	3.73	3.70	1.218			
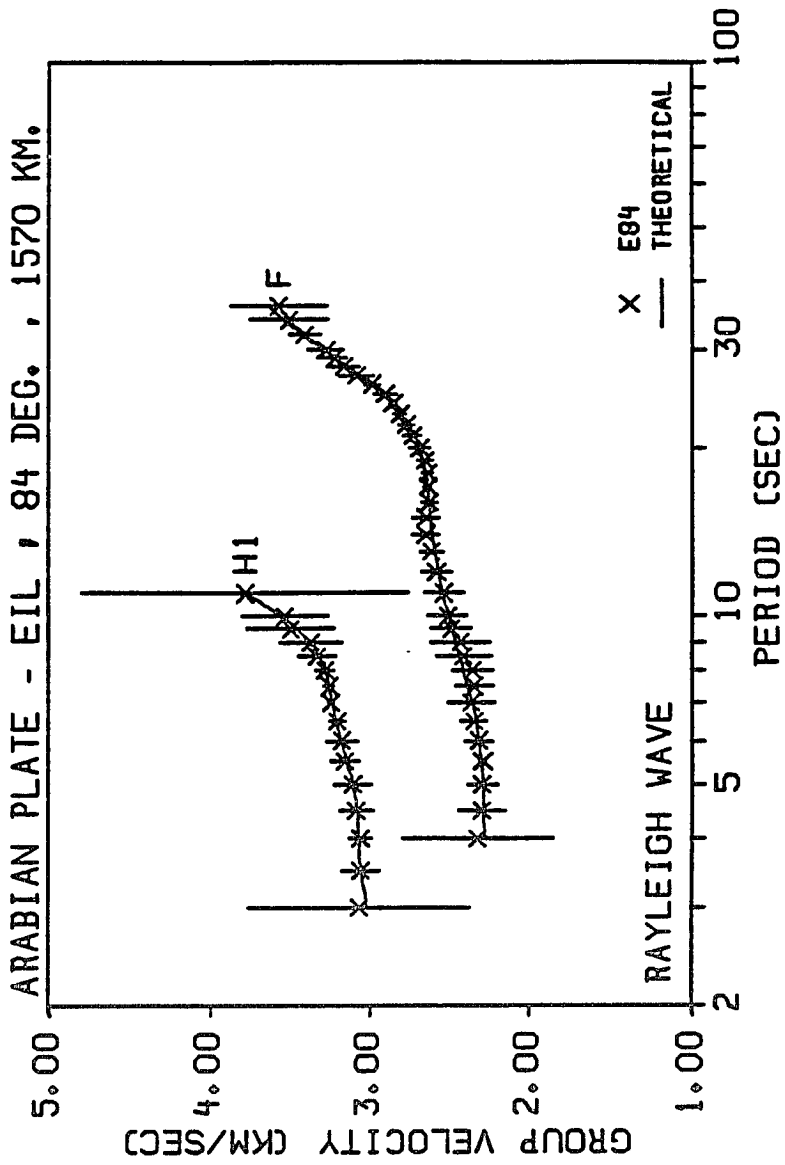
Figure 3.31. Averaged fundamental and first higher-mode Rayleigh wave dispersion curves with weighted standard deviations for path E84.

- 80 -

Table 3.13. Average Rayleigh wave group velocity dispersion data for path E84.

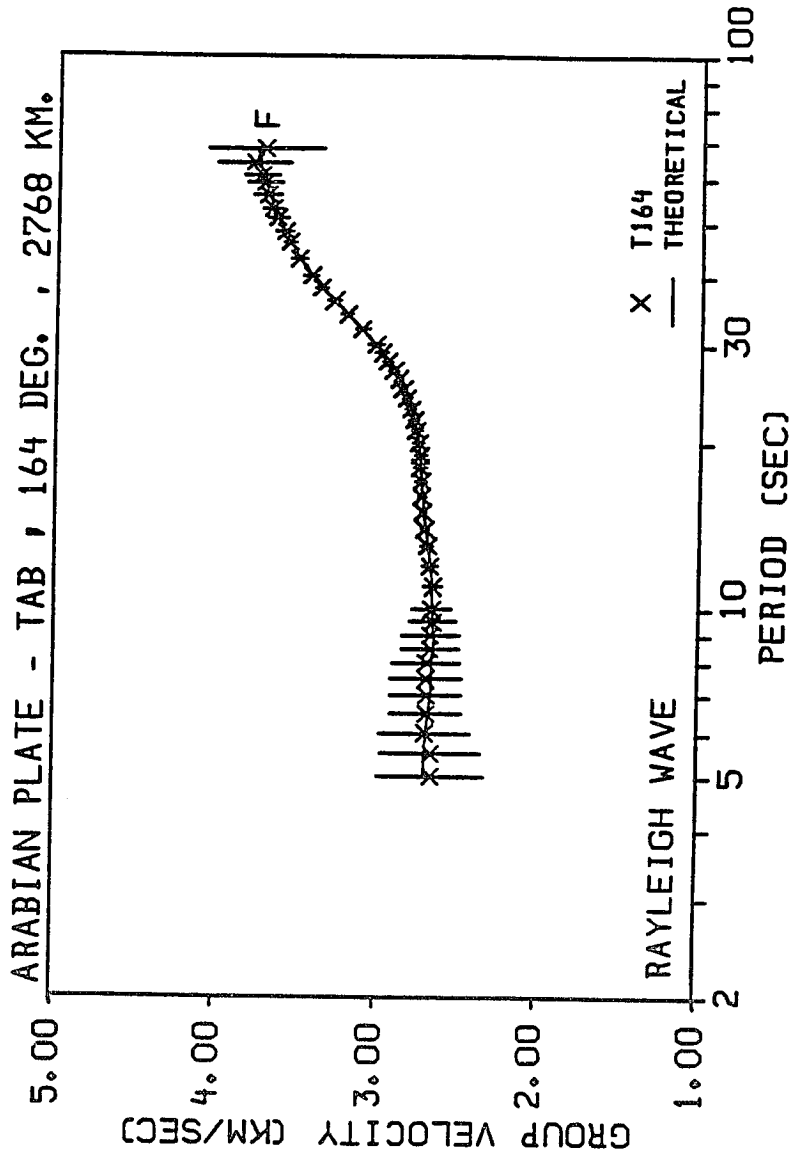|	Fundamental-Mode			Higher-Mode		
Period (sec)	Observed Velocity (km/sec)	Theoretical Velocity (km/sec)	Standard Deviation (km/sec)	Observed Velocity (km/sec)	Theoretical Velocity (km/sec)	Standard Deviation (km/sec)
3.0				3.07	3.02	0.696
3.5				3.06	3.06	0.116
4.0	2.32	2.28	0.471	3.06	3.07	0.071
4.5	2.30	2.28	0.148	3.08	3.08	0.105
5.0	2.29	2.29	0.093	3.10	3.11	0.118
5.5	2.29	2.30	0.019	3.16	3.15	0.086
6.0	2.32	2.31	0.086	3.18	3.18	0.100
6.5	2.35	2.34	0.082	3.20	3.21	0.046
7.0	2.36	2.36	0.147	3.24	3.24	0.020
7.5	2.34	2.39	0.114	3.26	3.26	0.032
8.0	2.35	2.42	0.127	3.28	3.28	0.058
8.5	2.41	2.44	0.170	3.33	3.32	0.118
9.0	2.43	2.47	0.188	3.37	3.38	0.194
9.5	2.49	2.49	0.130	3.50	3.46	0.272
10.0	2.51	2.51	0.121	3.54	3.55	0.267
11.0	2.54	2.54	0.122	3.78	3.77	1.022
12.0	2.58	2.57	0.092			
13.0	2.62	2.60	0.071			
14.0	2.65	2.61	0.084			
15.0	2.65	2.63	0.084			
16.0	2.63	2.64	0.050			
17.0	2.64	2.65	0.023			
18.0	2.64	2.66	0.035			
19.0	2.66	2.67	0.049			
20.0	2.69	2.69	0.061			
21.0	2.74	2.72	0.054			
22.0	2.77	2.76	0.052			
23.0	2.81	2.81	0.040			
24.0	2.86	2.86	0.023			
25.0	2.91	2.93	0.073			
26.0	2.99	2.99	0.045			
27.0	3.09	3.07	0.110			
28.0	3.16	3.14	0.094			
29.0	3.22	3.21	0.081			
30.0	3.28	3.29	0.112			
32.0	3.41	3.42	0.096			
34.0	3.51	3.54	0.243			
36.0	3.57	3.64	0.301			
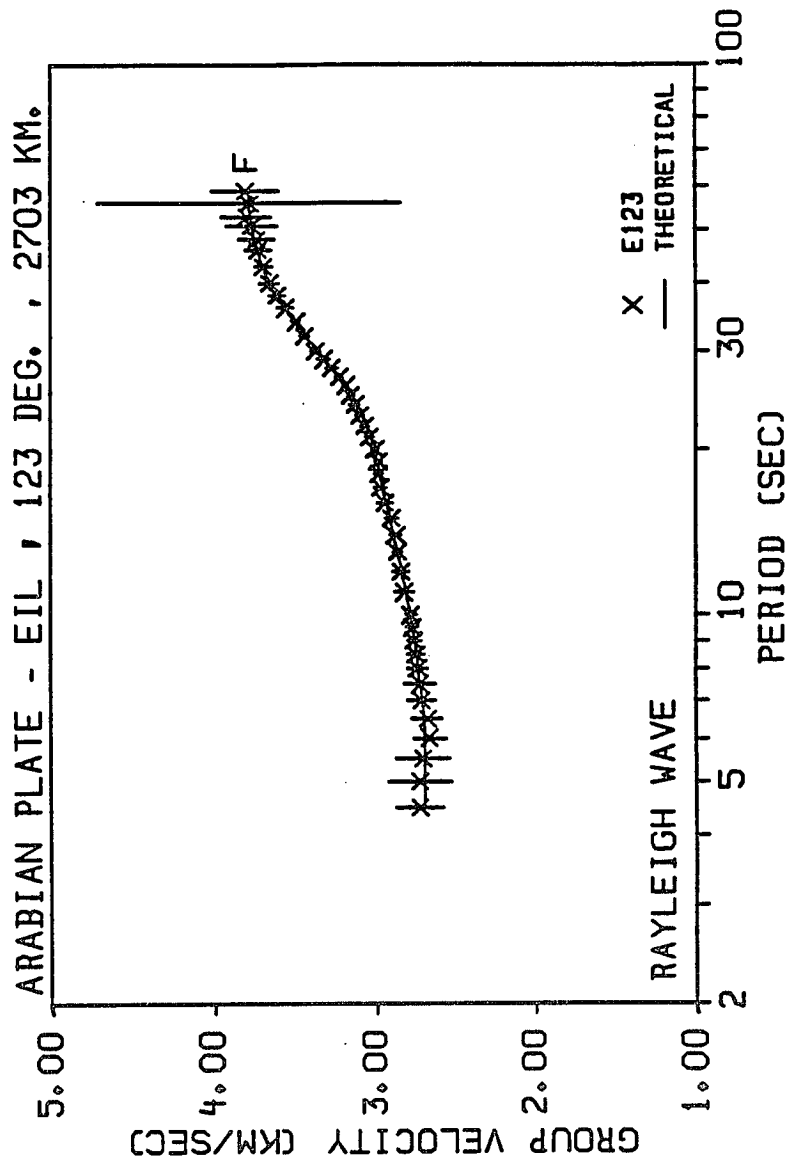
Figure 3.32. Averaged fundamental-mode Rayleigh wave dispersion curve with weighted standard deviations for path E123.

Table 3.14. Average Rayleigh wave group velocity dispersion data for path E123.

	Fundamental-Mode		
Period	Observed Velocity	Theoretical Velocity	Standard Deviation
(sec)	(km/sec)	(km/sec)	(km/sec)
4.5	2.73	2.70	0.145
5.0	2.73	2.69	0.199
5.5	2.71	2.69	0.166
6.0	2.66	2.70	0.102
6.5	2.68	2.70	0.093
7.0	2.72	2.71	0.090
7.5	2.73	2.73	0.095
8.0	2.74	2.74	0.065
8.5	2.75	2.75	0.055
9.0	2.76	2.76	0.044
9.5	2.78	2.77	0.040
10.0	2.78	2.79	0.032
11.0	2.82	2.81	0.060
12.0	2.84	2.84	0.045
13.0	2.86	2.87	0.032
14.0	2.88	2.89	0.037
15.0	2.90	2.91	0.040
16.0	2.94	2.93	0.047
17.0	2.97	2.95	0.035
18.0	2.98	2.97	0.027
19.0	2.98	2.99	0.023
20.0	3.01	3.01	0.024
21.0	3.04	3.04	0.028
22.0	3.07	3.06	0.027
23.0	3.10	3.09	0.028
24.0	3.13	3.12	0.033
25.0	3.15	3.16	0.026
26.0	3.19	3.19	0.017
27.0	3.23	3.23	0.023
28.0	3.28	3.27	0.040
29.0	3.32	3.31	0.041
30.0	3.37	3.35	0.033

Table 3.14. Continued.

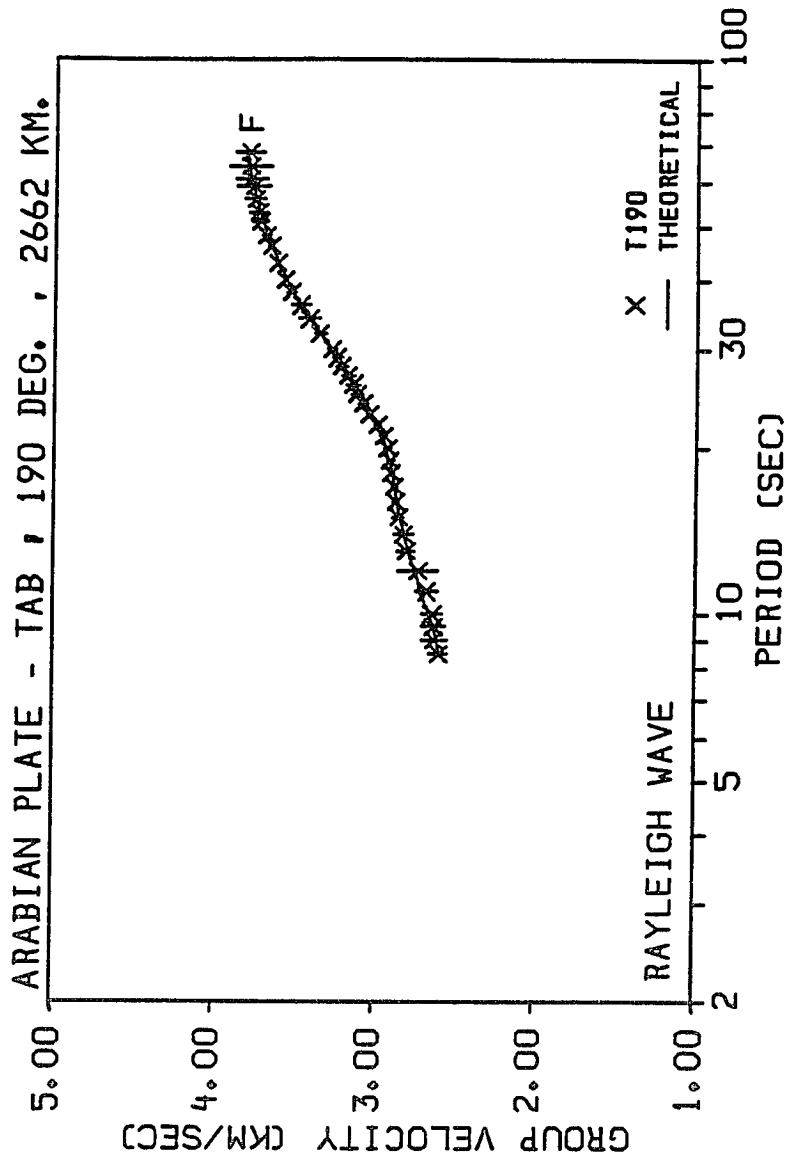| Period (sec)	Fundamental-Mode		
	Observed Velocity (km/sec)	Theoretical Velocity (km/sec)	Standard Deviation (km/sec)
32.0	3.44	3.43	0.030
34.0	3.49	3.50	0.027
36.0	3.56	3.56	0.046
38.0	3.61	3.61	0.050
40.0	3.65	3.65	0.058
43.0	3.69	3.70	0.054
46.0	3.73	3.73	0.079
48.0	3.73	3.75	0.112
51.0	3.76	3.76	0.161
53.0	3.79	3.77	0.151
56.0	3.78	3.78	0.937
59.0	3.80	3.79	0.206
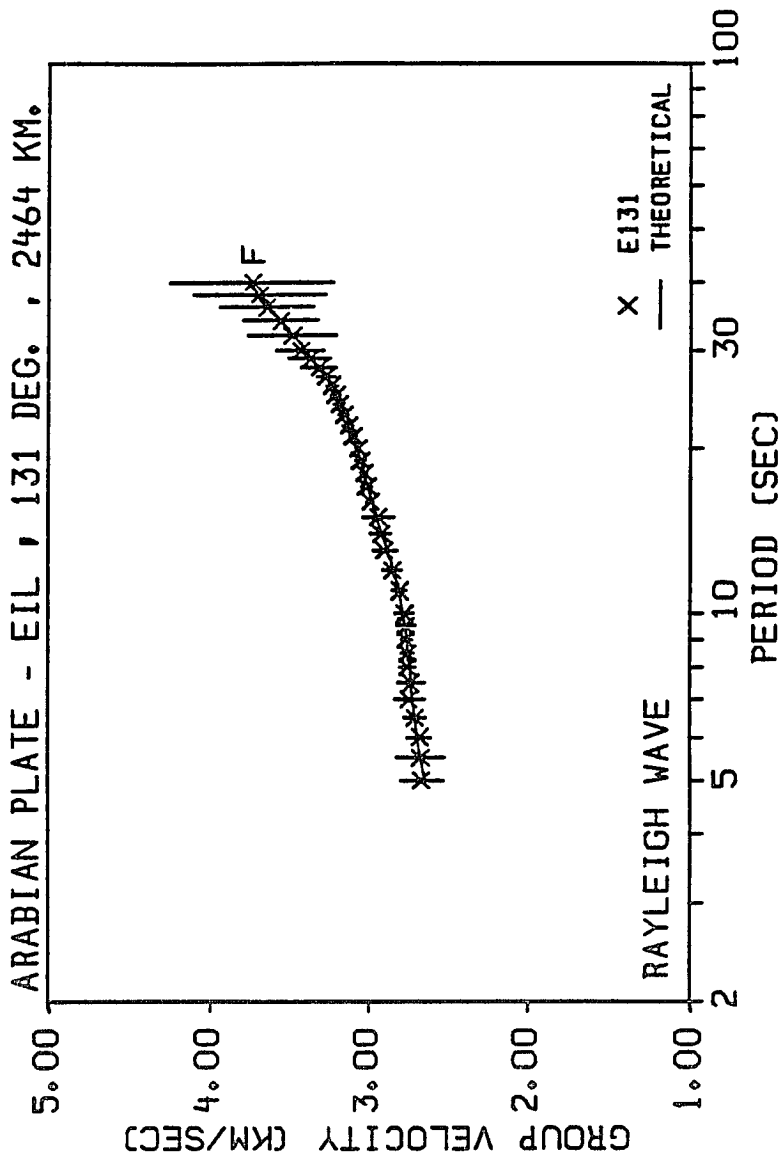
Figure 3.33. Averaged fundamental-mode Rayleigh wave dispersion curve with weighted standard deviations for path E131.

- 85 -

Table 3.15. Average Rayleigh wave group velocity dispersion data for path E131.

	Fundamental-Mode		
Period (sec)	Observed Velocity (km/sec)	Theoretical Velocity (km/sec)	Standard Deviation (km/sec)
5.0	2.66	2.65	0.134
5.5	2.67	2.68	0.147
6.0	2.68	2.70	0.075
6.5	2.71	2.71	0.071
7.0	2.74	2.72	0.093
7.5	2.74	2.73	0.083
8.0	2.76	2.74	0.050
8.5	2.75	2.75	0.037
9.0	2.76	2.76	0.030
9.5	2.77	2.77	0.057
10.0	2.77	2.78	0.056
11.0	2.81	2.82	0.044
12.0	2.86	2.85	0.060
13.0	2.90	2.89	0.070
14.0	2.92	2.92	0.064
15.0	2.94	2.96	0.098
16.0	2.99	2.99	0.024
17.0	3.01	3.01	0.038
18.0	3.03	3.03	0.024
19.0	3.05	3.06	0.035
20.0	3.07	3.08	0.016
21.0	3.10	3.10	0.026
22.0	3.13	3.12	0.032
23.0	3.16	3.15	0.032
24.0	3.19	3.18	0.034
25.0	3.21	3.21	0.034
26.0	3.24	3.25	0.038
27.0	3.27	3.28	0.061
28.0	3.32	3.32	0.111
29.0	3.37	3.36	0.131
30.0	3.43	3.40	0.152
32.0	3.48	3.48	0.280
34.0	3.56	3.56	0.236
36.0	3.64	3.63	0.293
38.0	3.69	3.69	0.415
40.0	3.73	3.75	0.514

On the other hand, except for path E67 which clearly exhibits lower values, the rest of the dispersion curves show similar velocities at periods greater than about 30 sec. Also, for periods less than about 17 sec path E67 shows lower values than E84. As for the first higher-mode velocities, they exhibit less, but consistent, variation throughout their period range. Therefore, in comparison, this pattern of group velocity variation is apparently more pronounced than previously observed among TAB and SHI stations data, and seems to suggest little variation in the average velocity structure of the region at greater depths.

3.3.4 JER Station Data

Again, on the basis of similarity in group velocity dispersion behavior, JER station data seem to fall into four groups. These are J54, J89, J127 and J147. Their mean paths are displayed in Figure 3.16, while their corresponding average Rayleigh wave group velocities along with their weighted standard deviations are illustrated in Figures 3.34-3.37, and given in Tables 3.16 through 3.19. In many aspects JER dispersion curves are remarkably analogous to those of EIL station. First, it is observed that the fundamental-mode data, measured between 3-59 sec, also exhibit significant variation in velocity at periods less than about 46 sec. Since both J147 and J127 traverse the southwestern portion of the plate and sample different parts of the Arabian shield, the highest group velocities are observed along these paths. The lowest velocities are associated with path J89 which, as does E84, traverses the region in an E-W direction. Furthermore, at periods less than about 30s, path J54, which samples the northern portion of the plate, shows slightly higher velocities than J89. Second, as
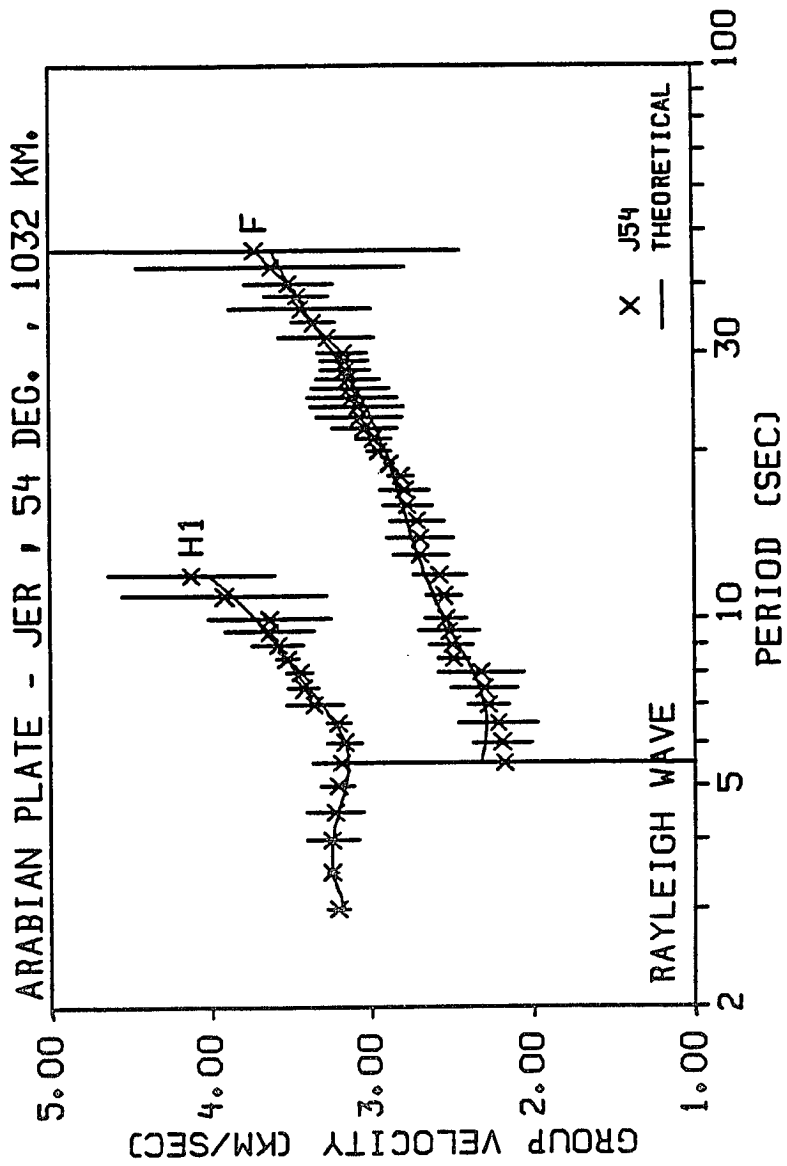
Figure 3.34. Averaged fundamental and first higher-mode Rayleigh wave dispersion curves with weighted standard deviations for path J54.

- 88 -

Table 3.16. Average Rayleigh wave group velocity dispersion data for path J54.

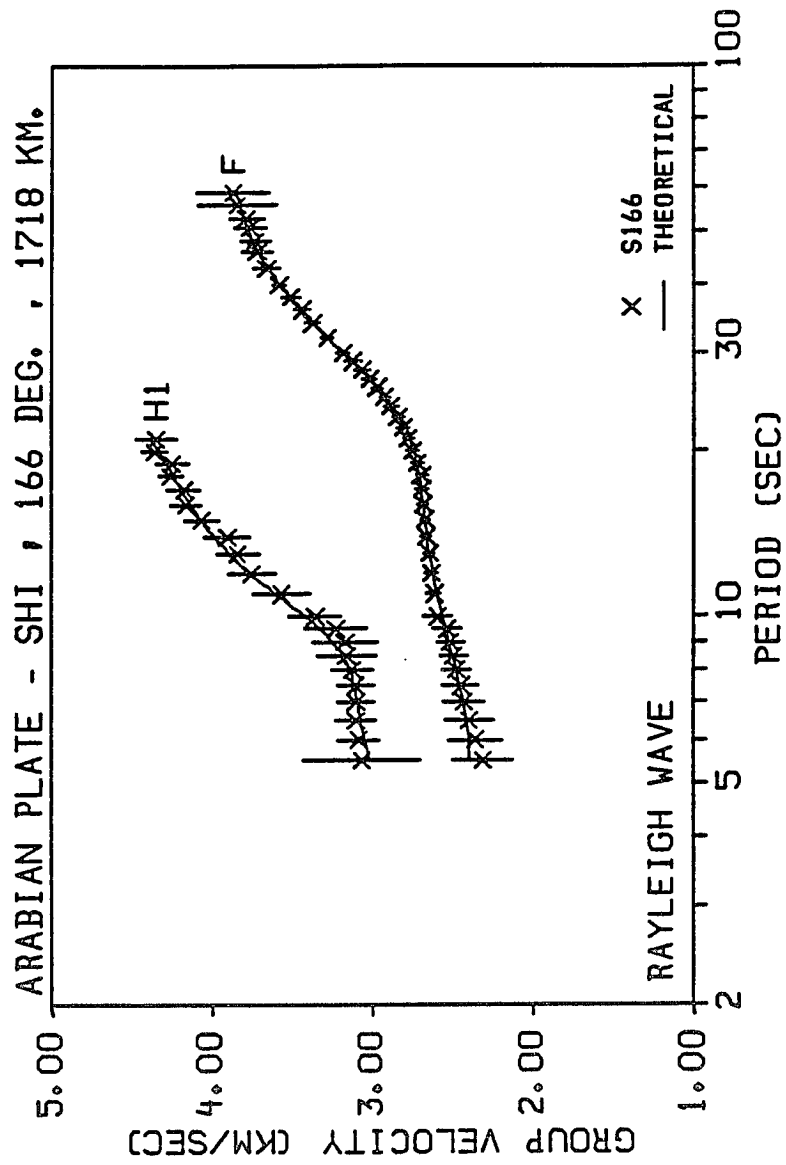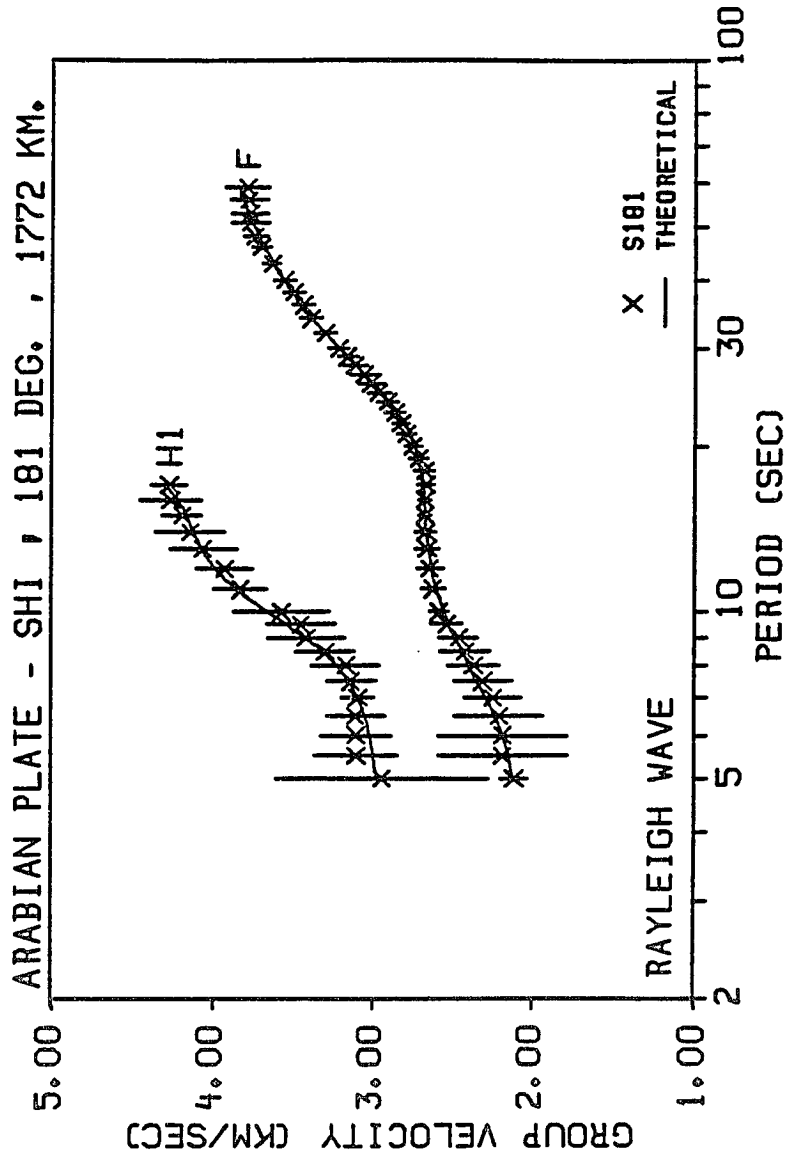|	Fundamental-Mode			Higher-Mode		
Period (sec)	Observed Velocity (km/sec)	Theoretical Velocity (km/sec)	Standard Deviation (km/sec)	Observed Velocity (km/sec)	Theoretical Velocity (km/sec)	Standard Deviation (km/sec)
3.0				3.20	3.17	0.068
3.5				3.24	3.25	0.035
4.0				3.24	3.24	0.157
4.5				3.22	3.20	0.173
5.0				3.21	3.16	0.104
5.5	2.18	2.33	1.179	3.19	3.15	0.081
6.0	2.19	2.30	0.182	3.17	3.17	0.109
6.5	2.22	2.30	0.246	3.20	3.23	0.070
7.0	2.28	2.31	0.130	3.36	3.31	0.178
7.5	2.31	2.33	0.202	3.42	3.39	0.099
8.0	2.33	2.37	0.269	3.44	3.46	0.082
8.5	2.49	2.42	0.098	3.52	3.53	0.068
9.0	2.50	2.46	0.136	3.58	3.59	0.161
9.5	2.52	2.51	0.182	3.63	3.65	0.278
10.0	2.54	2.55	0.128	3.63	3.71	0.386
11.0	2.55	2.62	0.105	3.91	3.86	0.640
12.0	2.58	2.67	0.159	4.12	4.01	0.521
13.0	2.69	2.71	0.174			
14.0	2.70	2.75	0.207			
15.0	2.71	2.78	0.165			
16.0	2.77	2.81	0.151			
17.0	2.79	2.83	0.155			
18.0	2.81	2.86	0.081			
19.0	2.88	2.88	0.028			
20.0	2.95	2.91	0.071			
21.0	2.98	2.94	0.107			
22.0	3.03	2.97	0.203			
23.0	3.07	3.00	0.262			
24.0	3.08	3.03	0.290			
25.0	3.11	3.06	0.282			
26.0	3.13	3.09	0.239			
27.0	3.14	3.12	0.196			
28.0	3.15	3.16	0.156			
29.0	3.16	3.19	0.148			
30.0	3.17	3.22	0.150			
32.0	3.27	3.29	0.301			
34.0	3.35	3.35	0.136			
36.0	3.43	3.41	0.445			
38.0	3.45	3.46	0.196			
40.0	3.51	3.50	0.280			
43.0	3.62	3.56	0.835			
46.0	3.72	3.61	1.280			
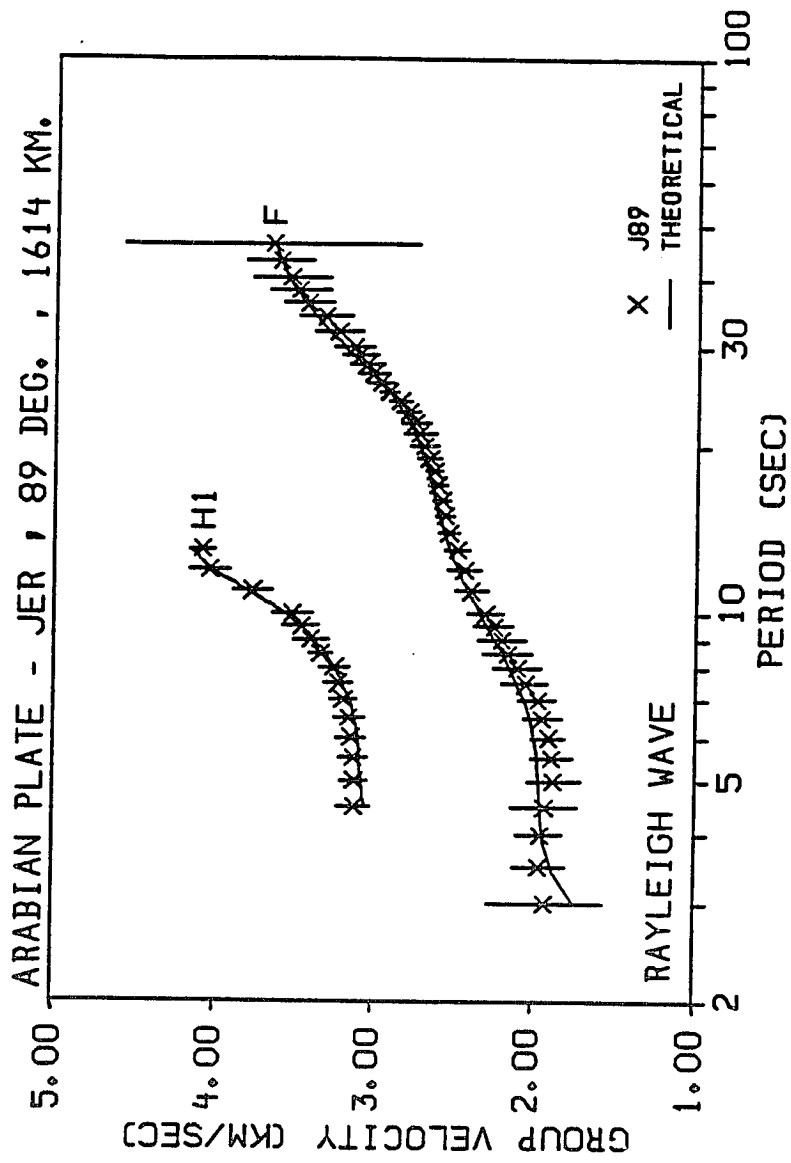
Figure 3.35. Averaged fundamental and first higher-mode Rayleigh wave dispersion curves with weighted standard deviations for path J89.

Table 3.17. Average Rayleigh wave group velocity dispersion data for path J89.

	Fundamental-Mode			Higher-Mode		
Period (sec)	Observed Velocity (km/sec)	Theoretical Velocity (km/sec)	Standard Deviation (km/sec)	Observed Velocity (km/sec)	Theoretical Velocity (km/sec)	Standard Deviation (km/sec)
3.0	1.92	1.75	0.356			
3.5	1.96	1.89	0.162			
4.0	1.96	1.95	0.142			
4.5	1.93	1.96	0.198	3.12	3.06	0.102
5.0	1.87	1.97	0.158	3.12	3.08	0.087
5.5	1.88	1.98	0.126	3.13	3.09	0.091
6.0	1.91	2.00	0.102	3.14	3.10	0.094
6.5	1.95	2.02	0.117	3.15	3.12	0.090
7.0	1.97	2.06	0.113	3.19	3.15	0.081
7.5	2.05	2.10	0.142	3.23	3.20	0.085
8.0	2.10	2.15	0.147	3.25	3.25	0.092
8.5	2.16	2.20	0.150	3.34	3.31	0.076
9.0	2.20	2.24	0.146	3.40	3.38	0.115
9.5	2.25	2.29	0.124	3.46	3.46	0.115
10.0	2.30	2.34	0.112	3.52	3.56	0.129
11.0	2.39	2.41	0.104	3.77	3.80	0.126
12.0	2.44	2.48	0.100	4.04	4.02	0.129
13.0	2.48	2.53	0.080	4.08	4.16	0.077
14.0	2.53	2.57	0.068			
15.0	2.56	2.60	0.057			
16.0	2.58	2.63	0.056			
17.0	2.61	2.65	0.060			
18.0	2.63	2.68	0.054			
19.0	2.66	2.70	0.070			
20.0	2.69	2.73	0.090			
21.0	2.72	2.76	0.101			
22.0	2.75	2.79	0.093			
23.0	2.80	2.83	0.076			
24.0	2.85	2.88	0.075			
25.0	2.92	2.93	0.060			
26.0	2.97	2.98	0.083			
27.0	3.02	3.04	0.099			
28.0	3.06	3.09	0.109			
29.0	3.11	3.15	0.112			
30.0	3.14	3.20	0.125			
32.0	3.24	3.30	0.153			
34.0	3.32	3.38	0.165			
36.0	3.43	3.45	0.160			
38.0	3.49	3.51	0.190			
40.0	3.54	3.56	0.244			
43.0	3.61	3.61	0.209			
46.0	3.66	3.65	0.924			
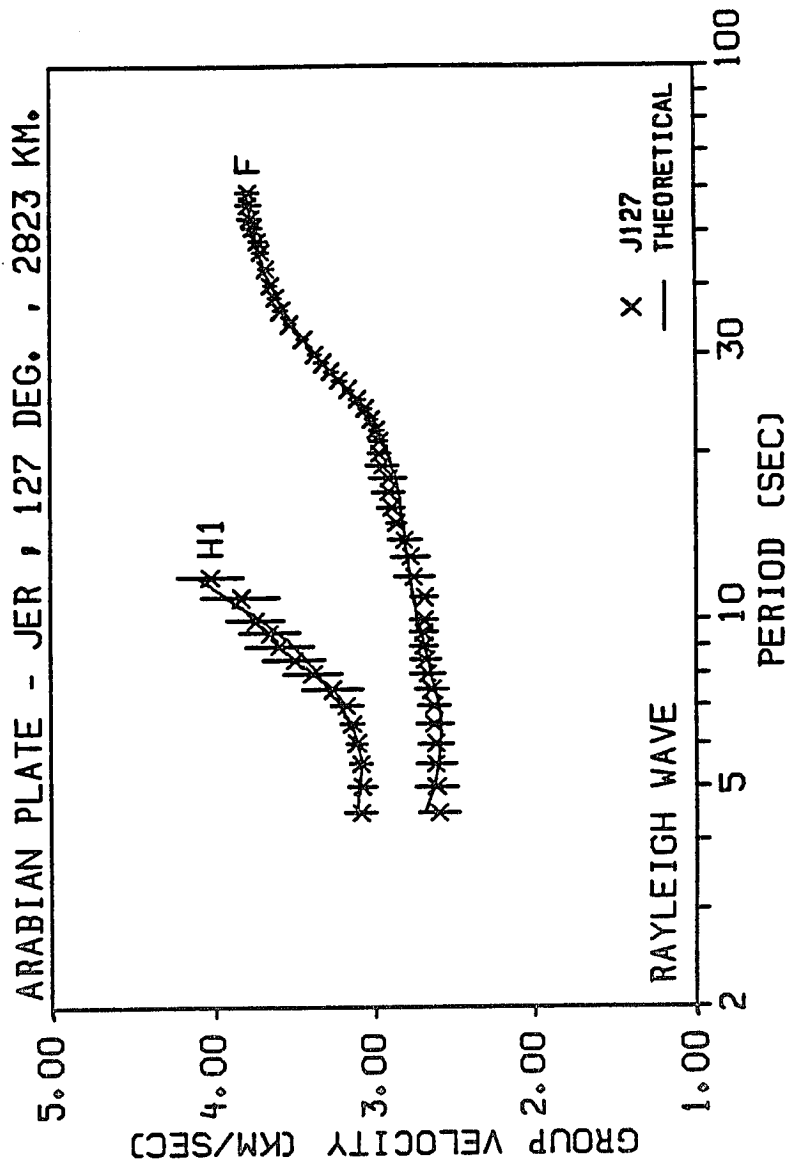
Figure 3.36. Averaged fundamental and first higher-mode Rayleigh wave dispersion curves with weighted standard deviations for path J127.

- 92 -

Table 3.18. Average Rayleigh wave group velocity dispersion data for path J127.

Period (sec)	Fundamental-Mode			Higher-Mode		
	Observed Velocity (km/sec)	Theoretical Velocity (km/sec)	Standard Deviation (km/sec)	Observed Velocity (km/sec)	Theoretical Velocity (km/sec)	Standard Deviation (km/sec)
4.5	2.60	2.68	0.125	3.09	3.12	0.096
5.0	2.61	2.63	0.133	3.08	3.10	0.085
5.5	2.62	2.60	0.121	3.09	3.09	0.069
6.0	2.62	2.59	0.110	3.11	3.11	0.060
6.5	2.62	2.59	0.115	3.14	3.16	0.069
7.0	2.63	2.60	0.095	3.18	3.22	0.096
7.5	2.64	2.62	0.103	3.26	3.29	0.186
8.0	2.67	2.64	0.105	3.39	3.35	0.181
8.5	2.68	2.67	0.097	3.50	3.43	0.191
9.0	2.69	2.69	0.086	3.59	3.51	0.208
9.5	2.69	2.71	0.087	3.65	3.60	0.189
10.0	2.69	2.73	0.083	3.74	3.70	0.173
11.0	2.69	2.76	0.084	3.83	3.92	0.241
12.0	2.75	2.78	0.118	4.02	4.10	0.201
13.0	2.77	2.80	0.118			
14.0	2.81	2.81	0.106			
15.0	2.87	2.82	0.059			
16.0	2.90	2.84	0.081			
17.0	2.91	2.85	0.098			
18.0	2.92	2.87	0.114			
19.0	2.95	2.89	0.099			
20.0	2.97	2.92	0.068			
21.0	2.97	2.95	0.053			
22.0	2.99	2.99	0.046			
23.0	3.02	3.04	0.039			
24.0	3.06	3.08	0.039			
25.0	3.11	3.13	0.050			
26.0	3.16	3.18	0.036			
27.0	3.22	3.23	0.044			
28.0	3.27	3.28	0.044			
29.0	3.32	3.32	0.042			
30.0	3.37	3.36	0.040			

Table 3.18. Continued.

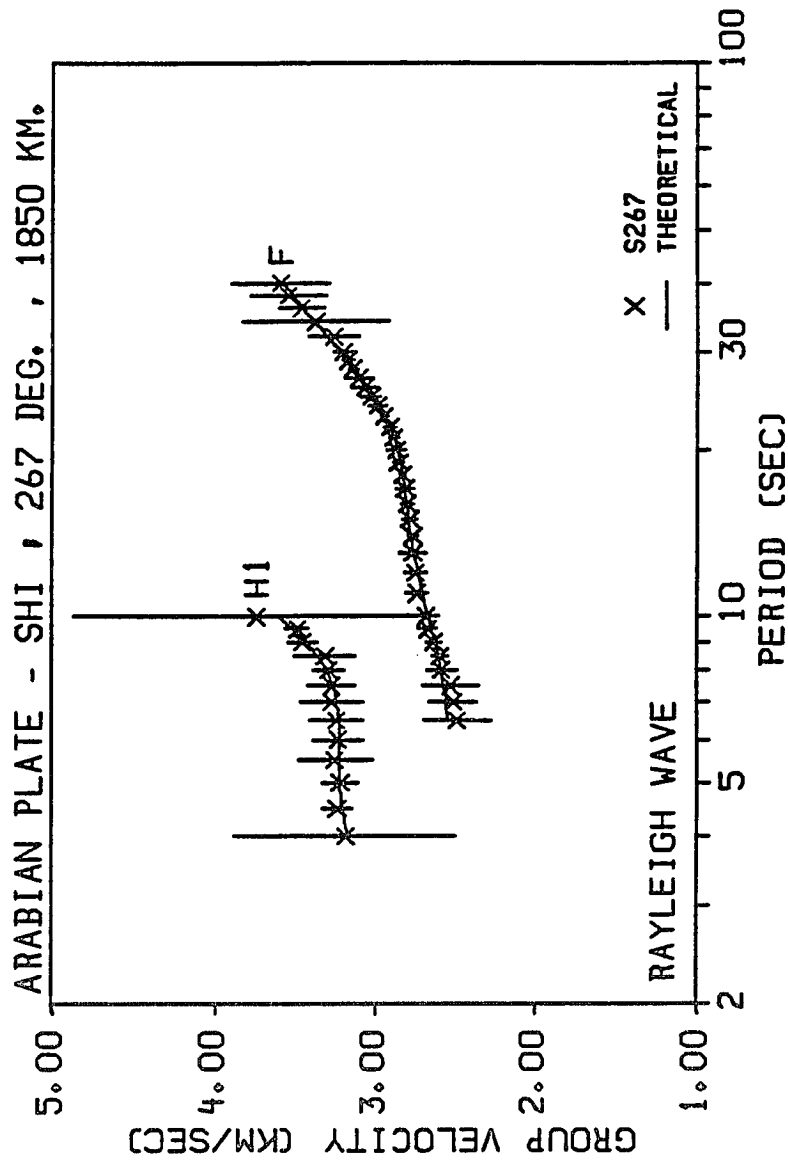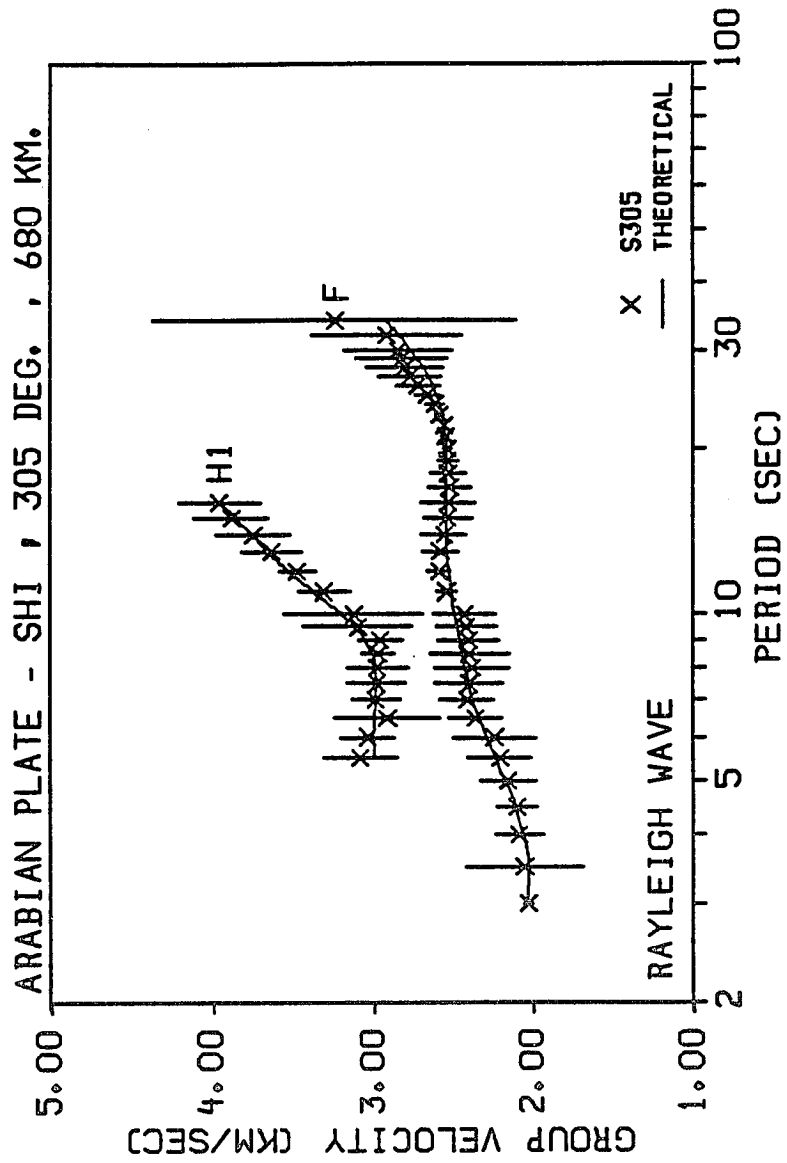|	Fundamental-Mode			Higher-Mode		
Period (sec)	Observed Velocity (km/sec)	Theoretical Velocity (km/sec)	Standard Deviation (km/sec)	Observed Velocity (km/sec)	Theoretical Velocity (km/sec)	Standard Deviation (km/sec)
32.0	3.44	3.44	0.032			
34.0	3.53	3.51	0.035			
36.0	3.58	3.56	0.043			
38.0	3.62	3.61	0.039			
40.0	3.64	3.64	0.039			
43.0	3.67	3.69	0.046			
46.0	3.71	3.72	0.051			
48.0	3.72	3.74	0.054			
51.0	3.75	3.76	0.059			
53.0	3.77	3.77	0.069			
56.0	3.78	3.78	0.070			
59.0	3.78	3.79	0.070			
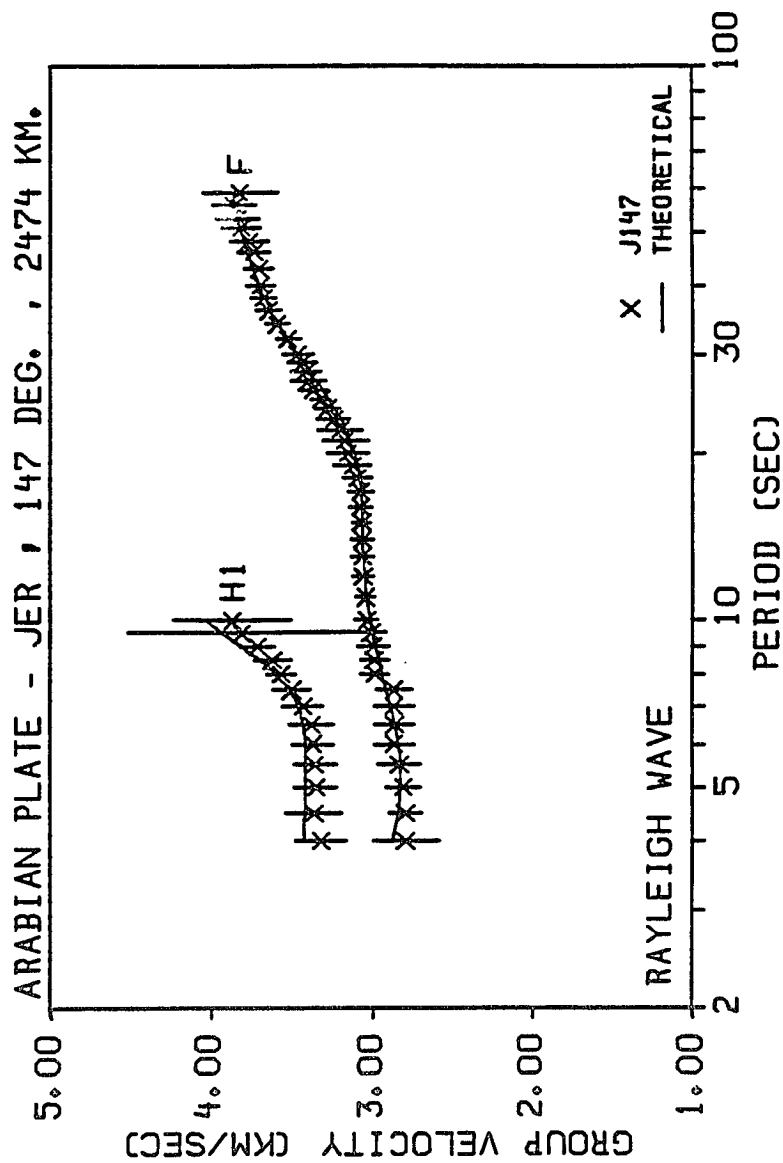
Figure 3.37. Averaged fundamental and first higher-mode Rayleigh wave dispersion curves with weighted standard deviations for path J147.

- 95 -

Table 3.19. Average Rayleigh wave group velocity dispersion data for path J147.

	Fundamental-Mode			Higher-Mode		
Period (sec)	Observed Velocity (km/sec)	Theoretical Velocity (km/sec)	Standard Deviation (km/sec)	Observed Velocity (km/sec)	Theoretical Velocity (km/sec)	Standard Deviation (km/sec)
4.0	2.80	2.88	0.206	3.32	3.43	0.155
4.5	2.80	2.85	0.102	3.37	3.42	0.172
5.0	2.81	2.83	0.109	3.36	3.42	0.130
5.5	2.84	2.83	0.132	3.36	3.42	0.133
6.0	2.87	2.85	0.121	3.37	3.42	0.126
6.5	2.87	2.87	0.120	3.38	3.43	0.135
7.0	2.87	2.89	0.121	3.43	3.46	0.121
7.5	2.87	2.92	0.112	3.50	3.51	0.115
8.0	2.99	2.94	0.088	3.56	3.59	0.090
8.5	2.99	2.96	0.088	3.62	3.70	0.109
9.0	3.00	2.99	0.096	3.72	3.82	0.106
9.5	3.01	3.00	0.092	3.81	3.93	0.702
10.0	3.04	3.02	0.074	3.87	4.03	0.364
11.0	3.05	3.04	0.059			
12.0	3.06	3.06	0.066			
13.0	3.07	3.06	0.069			
14.0	3.07	3.07	0.069			
15.0	3.07	3.07	0.059			
16.0	3.08	3.07	0.068			
17.0	3.08	3.08	0.080			
18.0	3.10	3.08	0.087			
19.0	3.13	3.10	0.110			
20.0	3.16	3.12	0.124			
21.0	3.17	3.14	0.141			
22.0	3.21	3.17	0.133			
23.0	3.25	3.20	0.102			
24.0	3.28	3.24	0.080			
25.0	3.32	3.28	0.065			
26.0	3.37	3.32	0.089			
27.0	3.40	3.36	0.106			
28.0	3.42	3.40	0.091			
29.0	3.44	3.43	0.087			

Table 3.19. Continued.

	Fundamental-Mode			Higher-Mode		
Period (sec)	Observed Velocity (km/sec)	Theoretical Velocity (km/sec)	Standard Deviation (km/sec)	Observed Velocity (km/sec)	Theoretical Velocity (km/sec)	Standard Deviation (km/sec)
30.0	3.47	3.47	0.094			
32.0	3.53	3.53	0.073			
34.0	3.60	3.59	0.073			
36.0	3.64	3.63	0.076			
38.0	3.68	3.67	0.080			
40.0	3.70	3.71	0.089			
43.0	3.71	3.75	0.089			
46.0	3.73	3.78	0.093			
48.0	3.76	3.80	0.114			
51.0	3.81	3.82	0.121			
53.0	3.83	3.83	0.129			
56.0	3.86	3.85	0.134			
59.0	3.82	3.86	0.230			

in the case of EIL station data, it is observed that paths characterized by high velocity fundamental modes also have corresponding high velocity first higher modes. In addition, the higher-mode dispersion of paths J54, J89 and J147 also exhibit less pronounced but consistent variation throughout their 3-13 seconds period range. This resemblance in the characteristics between JER and EIL dispersion curves is concluded to be due to: (1) the proximity of these stations to each other, and (2) the location of both stations along the northwestern boundary of the Arabian plate.

CHAPTER 4

SEISMIC VELOCITY STRUCTURE

The inversion of surface wave dispersion curves to model the Earth's seismic velocity structure is a firmly established method in seismology. In this chapter, the results of using two such inversion techniques to estimate the vertical and lateral variations of shear velocity structure of the Arabian plate are presented. These models are the first of their kind in terms of details and coverage of this region.

4.1 Inversion Procedures

Detailed reviews of linear least-squares inversion clearly demonstrate the powerful role this method plays in extracting information about the earth's structure and other physical parameters (Jupp and Vozoff, 1975; Lines and Treitel, 1984). The recent literature includes many efforts that have been directed toward the development and diverse application of geo-physical inversion techniques. Unlike the forward approach to geophysical data interpretation in which a model is assumed, the purpose of inversion is to extract information which involves the estimation of the parameters of a postulated model from a set of observations. This method of evaluating the forward problem to determine how well a current model fits the data, also includes an estimate of the model resolution and variance which assist in improving the interpretation of results.

Typically, the linear least-squares problem is presented according to the following formulation,

$$y = Ax + \varepsilon \tag{4.1}$$

where $y_{m \times 1}$ represents a vector of observed data, $A_{m \times n}$ is a coefficients or kernel matrix relating the model parameters to observation, $x_{n \times 1}$ is an unknown solution vector of the model parameters, and $\varepsilon_{m \times 1}$ is a vector of residuals that compensates for the differences between observed and theoretical values. A solution to the above inverse problem may be written as

$$x = (A^T A + \gamma^2 I)^{-1} A^T y.$$

The superscript T indicates the transpose of A, the I is an identity matrix, and the damping factor γ is a scalar variable to control the instability of poorly constrained problems due to the presence of singular values that approach zero. In practice, solving the above equation is simplified by using the Singular Value Decomposition (SVD) of the A matrix (Lawson and Hanson, 1974). Assuming $V^T V = I$ and $UU^T = I$, the orthogonal transformation of the coefficients matrix can be expressed in terms of eigenvalues and eigenvectors as

$$A = USV^T.$$

$U_{m \times m}$ and $V_{n \times n}$ are two orthogonal matrices, and $S_{m \times n}$ is an upper left diagonal matrix whose s_{ii}, $i = 1, ..., k$ elements, where $k = \min[m,n]$, are the singular values of A. The number of nonzero singular values determines the rank of the matrix A. Since the inverse of the coefficient matrix is $A^{-1} = VS^{-1}U^T$, a solution to the least squares problems can be expressed as follows

$$x = VS^{-1}U^T y.$$

Furthermore, the resolution matrix for the above solution is

$$R = VS^{-1}SV^{T},$$

and the scaled covariance matrix expression for the solution vector of the least squares problem is

$$C = \sigma^2 VS^{-2}V^{T}$$

where the scalar factor σ^2 represents the data variance.

As a computational approach to inversion, the stochastic (Franklin, 1970) and differential (Claerbout, 1976; Twomey, 1977; Russell, 1987) techniques are usually used to control the instability problem. To demonstrate the difference between the two techniques, consider the following generalized expression for the damped linear least-squares method,

$$\begin{bmatrix} y \\ 0 \end{bmatrix} = \begin{bmatrix} A \\ \gamma F \end{bmatrix} x + \begin{bmatrix} \varepsilon \\ \varepsilon_\gamma \end{bmatrix} \tag{4.2}$$

where $F_{n \times n}$ is an arbitrary matrix appended to the original least-squares expression.

If $F = I$, as in stochastic inversion, equal weights are given to the elements of x in order to constrain the norm of the solution vector, and minimize the function $|y - Ax|^2 + \gamma^2 |x|^2$.

In the case of differential inversion, F is constructed as an upper bidiagonal matrix to constraint the norm of the solution vector gradient. A form of this first-order difference weighting matrix is

$$F = \begin{bmatrix} 1 & -1 & 0 & 0 & . & 0 \\ 0 & 1 & -1 & 0 & . & 0 \\ 0 & 0 & 1 & -1 & . & 0 \\ . & . & . & . & . & 0 \\ . & . & . & . & 1 & -1 \\ 0 & 0 & 0 & 0 & 0 & 1 \end{bmatrix} .$$

The inverse of F is an upper triangular unity matrix, and the minimization function is $|y - Ax|^2 + \gamma^2 |Fx|^2$. Furthermore, the differential operator F can be modified to include a diagonal weighting matrix $W_{n \times n}$, and $F_W = W \, F$ may be substituted in expression (4.2). If $W = I$, no weight is applied, but if a certain element of W is assigned a value of $w_{ii} < 1$ or $w_{ii} > 1$, where $i = 1, ..., n$, the constraint on the difference between that solution element and the one below it is either decreased or increased, respectively. The only exception to this rule is that, applying weight on the last column of the last row of F will result in directly constraining the last element of the solution vector.

The inversion of surface wave dispersion for the estimation of shear velocity models has evolved from the treatments to the complete general inverse problem developed by Backus and Gilbert (1967, 1968, 1970) and extended by Jackson (1972, 1979). Thorough discussions on surface wave inversion procedures are given by Der and Landisman (1970, 1972), Wiggins (1972), Knopoff (1972), Kovach (1978), and most recently by Russell (1980, 1987).

Setting up the linearized surface waves inversion problem involves perturbing Rayleigh and Love waves shear velocity β, phase velocity c, compressional velocity α, and media density ρ relative to the shear velocities of an assumed plane layered velocity model. Since α and β are related by Poisson's ratio (Bullen and Bolt, 1985), and α and ρ are related empirically for rocks (Talwani et al., 1959; Birch, 1964), an iterative approach can be used to invert for β then the corresponding values of α and ρ can be calculated. In discrete form the surface wave inversion problem in terms of phase velocities is expressed as

$$\delta c_i = \sum_{j=1}^{n} A_{ij} \, \delta \beta_j + \varepsilon_i \qquad (4.3)$$

where $i = 1, ..., m$ is the number of frequency observations, $j = 1, ..., n$ is the number of shear velocity layers, and at a given layer thickness or depth z the kernel A is the Rayleigh or Love wave expression defined by

$$A_{ij} = \int_{z_j}^{z_{j+1}} A_i(z) \, dz \quad .$$

Detailed derivation for the above integral expression of $A(\omega,z)$ for Rayleigh and Love wave equations can be found in Wang (1981), Herrmann (1985) and Russell (1987).

It should be evident that expression (4.3) is equivalent to the least-squares problem (4.1), and can be expressed in matrix form as

$$\delta c = A \, \delta \beta + \varepsilon \quad .$$

However, in order to estimate the change in β relative to changes in phase velocity, a starting shear velocity model $\beta_j^o (j = 1, n)$ is used, such that

$$\delta c_i = c_i^m - c_i^o$$

would reflect the corresponding change of measured phase velocity c_i^m at a given frequency relative to the initial c_i^o. Furthermore, the estimated shear velocity model can be updated after each iteration ($\beta = \beta^o + \delta\beta$), and the A matrix is recalculated according to the new β values. Therefore, the perturbation relationship of phase velocity as a function of shear velocity can be expressed as follows

$$c_i^m = c_i(\beta) + \varepsilon_i$$

and can be expanded in a Taylor series about β^o as

$$c_i^m = c_i(\beta^o) + \sum_{j=1}^{n} \frac{\partial c_i}{\partial \beta_j} \delta\beta_j + \varepsilon_i.$$

A similar expression for group velocity measurements can also be written by substituting c_i with U_i. Finally, since the phase velocity partial derivative in the above expression is equivalent to the wave equation integral, the perturbation problem of surface wave inversion can be directly set up in terms of these derivatives. Wang (1981) provides an analytical solution to the phase velocity partial derivatives, and Rodi *et al.* (1975) gives a stable approximation to the group velocity partial derivatives.

4.2 Shear Velocity Models

There are very few published studies on the deep velocity structure of the Arabian plate. As mentioned in Chapter 2, Niazi (1968) and Arkhangel'skaya *et al.* (1974) deduced their velocity structures from Rayleigh wave phase and group velocity measurements by selecting a grossly simplified theoretical model whose calculated dispersion curve matched their observed values. Knopoff and Fouda (1975), on the other hand, constructed an average model by using the Hedgehog technique. Since none of these models are detailed enough to reflect any variation in the structure of the plate, a completely independent starting model is selected for use with the surface wave inversion program "SURF" developed by David R. Russell and published in volume IV of Herrmann's (1985) *Computer Programs in Seismology* manuals.

In the absence of well established *a priori* information suitable for stochastic inversion, a starting shear velocity model consisting of a single layer over half space is selected for use with non-linear differential inver-

sion. The half space is comprised of several layers with identical, but higher, velocities than the overlying layer. After experimenting with a number of starting model configurations in order to evaluate the resolution of the dispersion data obtained in this study, the selected model consists of 26 layers with a total thickness of 100.0 km. The first two were 0.5 km thick, followed by five 1.0 km, four 2.0, 4.0, and 5.0 km, five 6.0 km, and two 10.0 km thick layers. The top, presumably sedimentary, layer shear velocity was set to 4.9 km/sec, and a constant 5.2 km/sec is assigned to the half space layers. A Poisson ratio of 0.25 is used for the crustal layers, and a constant value of 0.27 for the upper mantle layers.

In the inversion process, Poisson ratios, layer thicknesses and differential operator layer weights are kept fixed. Although, no discontinuity weights are used in this study, a weight of 0.2 is assigned to the bottom layer of the half space model to allow it to move freely. The shear velocities, compressional velocities, and layer densities are allowed to vary with each iteration. A high damping factor was also decreased gradually with each iteration until physically reasonable shear velocity models, velocity residuals, resolving kernels, and a good match between the observed and theoretical dispersion curves are obtained.

Results of the inversion of mixed-path averaged dispersion curves are discussed in the following sections. Figures 4.1 through 4.19 show the estimated shear velocity models and their resolving kernels at 0.8, 2.5, 4.5, 7.0, 11.0, 16.0, 24.0, 32.5, 42.5, 53.0, 65.0 and 77.0 km depths. The resolving kernels in those figures correspond to models (e.g., E30h) obtained from the combined inversion of fundamental and higher modes dispersion curves. However, in the absence of higher modes, the resolving

kernels correspond to the fundamental-mode models, e.g., T190f. Also, in these figures the individual resolving kernel amplitudes are scaled independently, i.e. normalized, in order to accentuate the position and width of the peaks with respect to the depths of the layers of the velocity models. The layer depths and thicknesses (measured from the surface to the center of the layers), compressional and shear velocities, layers density, and shear velocity standard deviations values are listed in Tables 4.1 through 4.32. Finally, the theoretical dispersion curves calculated from the inverted models are listed along with the observed data in Tables 3.1-3.19, and represented by solid lines in Figures 3.19-3.37.

The most distinguishing feature common among some of the estimated models are the effects of including higher-mode dispersion curves in the inversion process. The first effect is observed in the form of an apparent shallow low-velocity layer caused by mismatch between the fundamental and higher modes dispersion curves. This discrepancy is usually due to the difficulty of identifying and picking higher-mode group velocities at short periods. For this reason, both the fundamental- and higher-mode models are used to interpret and discuss the characteristics of each velocity structure. The second effect is a positive one, because the presence of higher modes plays a role in improving the inverted model resolution with increasing depth. Higher modes are known to have deeper penetration at a given period than fundamental modes. Hence, the physically unreasonable shear velocity increase or decrease observed in the upper mantle layers are better constrained with higher modes (e.g., TAB versus SHI models).

4.2.1 TAB Station Models

Among all the dispersion curves obtained for the Arabian plate, station TAB data represent an average of the region. The paths traverse the northern, central and eastern portions of the plate, and sample most of the major tectonic provinces of the plate. Figures 4.1-4.3 show the estimated shear velocity models and their resolving kernels for paths T164, T190 and T228, respectively. The parameters for these models are presented in Tables 4.1 through 4.3. Inspection of the data in those tables indicate significant lateral variation in the velocity structure of the plate.

Model T164f, shown in Figure 4.1, reflects the velocity structure of the eastern portion of the Arabian plate. Due to the sources and TAB station locations, this model samples a good portion of the Zagros continental collision zone and the N-S trending section of the Mesopotamian foredeep. In general, the model shows a gradual increase in shear velocity from 2.70 km/sec near the surface to 4.49 km/sec at about 70.0 km depth. The apparent decrease in shear velocity below 80.0 km is probably due to the diminishing resolution of the model at that depth. The velocity varies between 2.70-3.16 km/sec within the top 12.0 kilometers, and shows a slight increase from 3.06 km/sec to 3.1 km/sec at approximately 5.0 km depth. Two other velocity gradients are observed in this model. The first occurs around 20.0 km, where the velocity increases from 3.44 to 3.61 km/sec, and the second is around 45.0 km depth, where the velocity increases from 3.64 to 4.34 km/sec. These velocity gradients at 12.0, 20.0 and 45.0 km seem to indicate the depths to the top of the crystalline basement, the Conrad and Moho discontinuities within this region of the Arabian plate, respectively. In other words, this indicates that this part of the
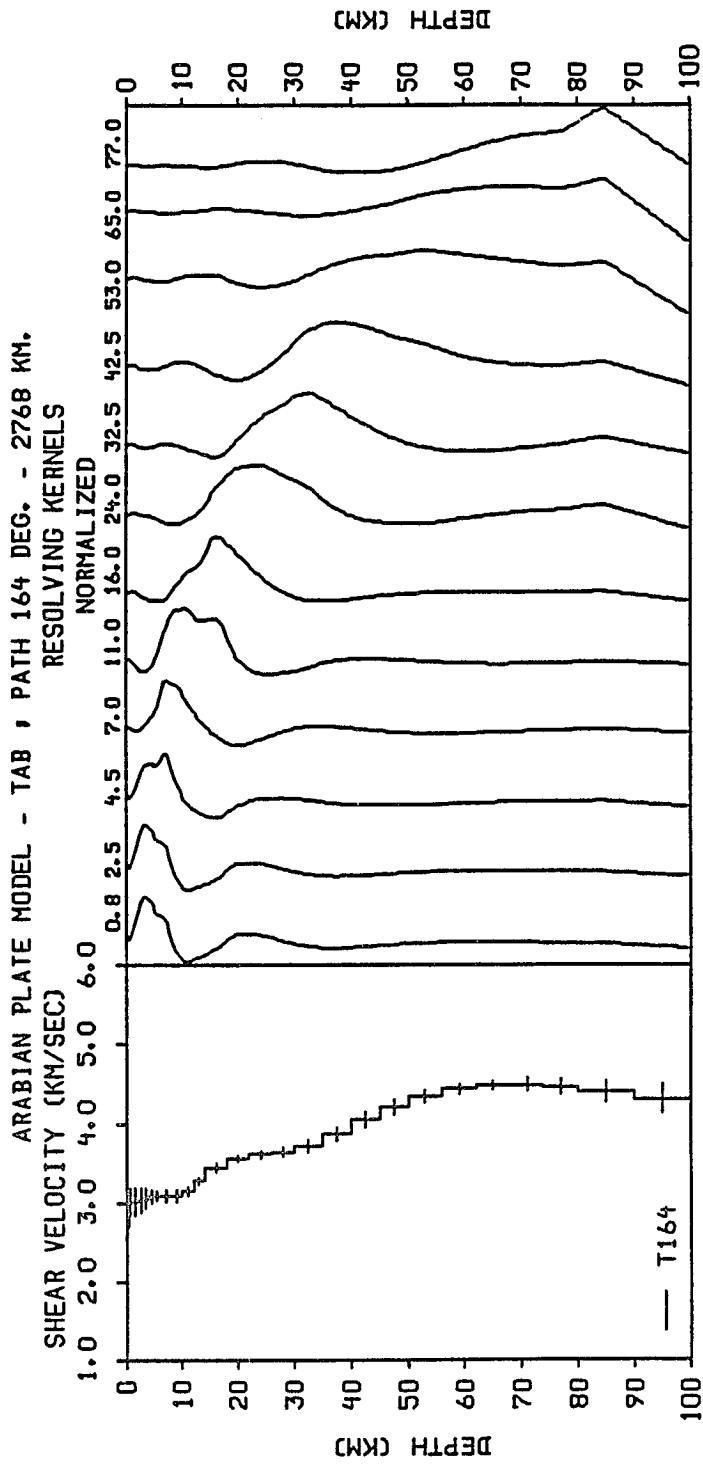
Figure 4.1. Shear velocity model T164f and resolving kernels estimated from fundamental-mode Rayleigh waves.

- 108 -

Table 4.1. Crustal velocity structure of the Arabian plate along path T164, derived from fundamental-mode data.

			Velocity Model T164f			
Layer Number	Layer Depth* (km)	Layer Thickness (km)	Compressional Velocity (km/sec)	Shear Velocity (km/sec)	Density (gm/cc)	Standard Deviation (km/sec)
1	0.2	0.5	4.68	2.70	2.430	0.178
2	0.8	0.5	5.21	3.01	2.541	0.176
3	1.5	1.0	5.21	3.01	2.543	0.174
4	2.5	1.0	5.25	3.03	2.549	0.161
5	3.5	1.0	5.30	3.06	2.560	0.127
6	4.5	1.0	5.34	3.08	2.568	0.085
7	5.5	1.0	5.36	3.09	2.572	0.060
8	7.0	2.0	5.35	3.09	2.571	0.074
9	9.0	2.0	5.36	3.10	2.572	0.075
10	11.0	2.0	5.47	3.16	2.593	0.061
11	13.0	2.0	5.68	3.28	2.637	0.053
12	16.0	4.0	5.96	3.44	2.692	0.055
13	20.0	4.0	6.17	3.56	2.751	0.044
14	24.0	4.0	6.25	3.61	2.776	0.048
15	28.0	4.0	6.31	3.64	2.794	0.060
16	32.5	5.0	6.45	3.72	2.834	0.073
17	37.5	5.0	6.70	3.87	2.902	0.088
18	42.5	5.0	7.20	4.04	3.045	0.100
19	47.5	5.0	7.50	4.21	3.140	0.098
20	53.0	6.0	7.74	4.34	3.221	0.082
21	59.0	6.0	7.90	4.43	3.276	0.063
22	65.0	6.0	7.98	4.48	3.304	0.064
23	71.0	6.0	8.00	4.49	3.309	0.081
24	77.0	6.0	7.95	4.46	3.292	0.105
25	85.0	10.0	7.84	4.40	3.256	0.138
26	95.0	10.0	7.68	4.31	3.202	0.194

* from the surface to the middle of the layers.
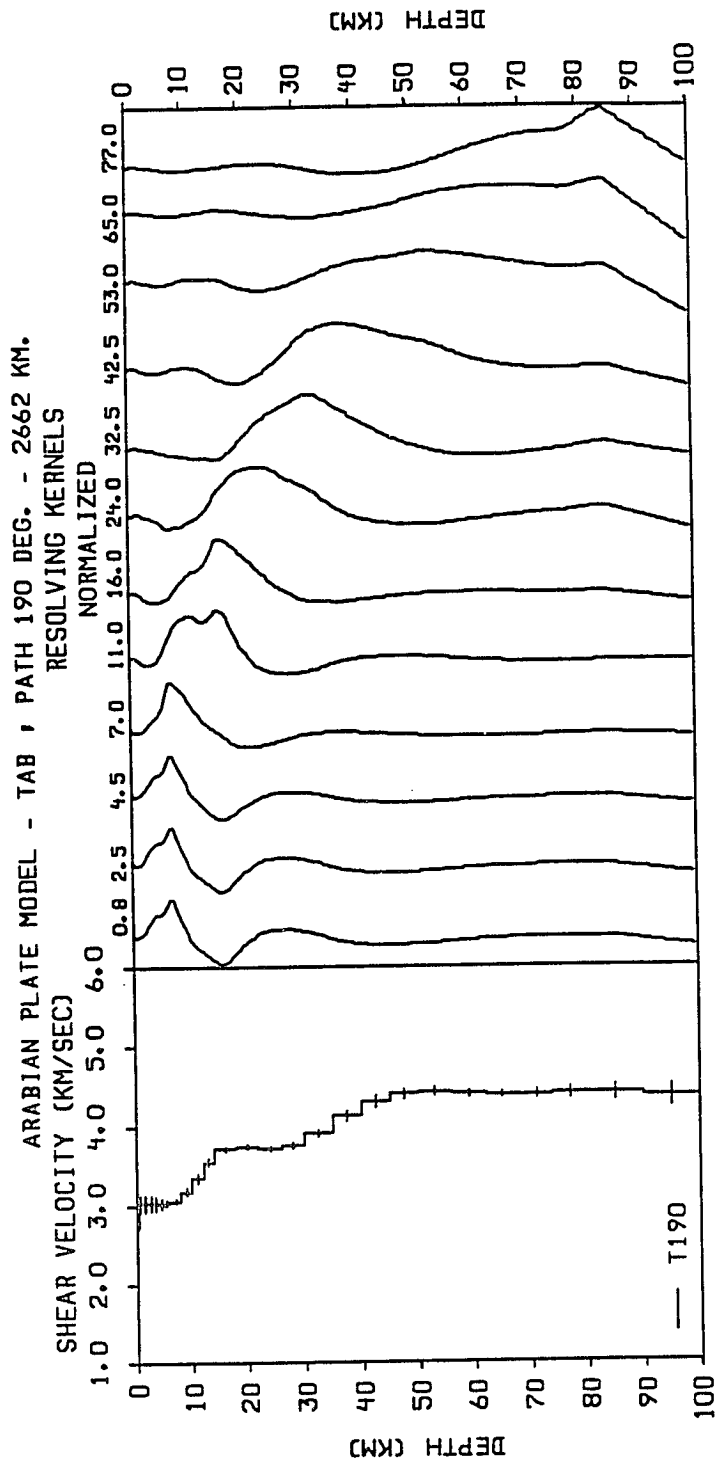
Figure 4.2. Shear velocity model T190f and resolving kernels estimated from fundamental-mode Rayleigh waves.

- 110 -

Table 4.2. Crustal velocity structure of the Arabian plate along path T190, derived from fundamental-mode data.

	Velocity Model T190f					
Layer Number	Layer Depth* (km)	Layer Thickness (km)	Compressional Velocity (km/sec)	Shear Velocity (km/sec)	Density (gm/cc)	Standard Deviation (km/sec)
1	0.2	0.5	4.71	2.72	2.437	0.108
2	0.8	0.5	5.24	3.03	2.548	0.107
3	1.5	1.0	5.25	3.03	2.550	0.106
4	2.5	1.0	5.25	3.03	2.550	0.103
5	3.5	1.0	5.24	3.03	2.548	0.091
6	4.5	1.0	5.23	3.02	2.546	0.069
7	5.5	1.0	5.24	3.03	2.548	0.041
8	7.0	2.0	5.30	3.06	2.560	0.029
9	9.0	2.0	5.50	3.17	2.599	0.049
10	11.0	2.0	5.81	3.35	2.661	0.058
11	13.0	2.0	6.14	3.55	2.743	0.048
12	16.0	4.0	6.42	3.71	2.827	0.034
13	20.0	4.0	6.48	3.74	2.843	0.029
14	24.0	4.0	6.44	3.72	2.831	0.031
15	28.0	4.0	6.51	3.76	2.853	0.037
16	32.5	5.0	6.77	3.91	2.920	0.054
17	37.5	5.0	7.14	4.12	3.024	0.069
18	42.5	5.0	7.66	4.30	3.194	0.076
19	47.5	5.0	7.83	4.40	3.253	0.073
20	53.0	6.0	7.87	4.42	3.267	0.061
21	59.0	6.0	7.84	4.40	3.254	0.044
22	65.0	6.0	7.80	4.38	3.243	0.041
23	71.0	6.0	7.81	4.38	3.245	0.056
24	77.0	6.0	7.84	4.40	3.254	0.074
25	85.0	10.0	7.85	4.41	3.260	0.097
26	95.0	10.0	7.78	4.37	3.236	0.136

* from the surface to the middle of the layers.
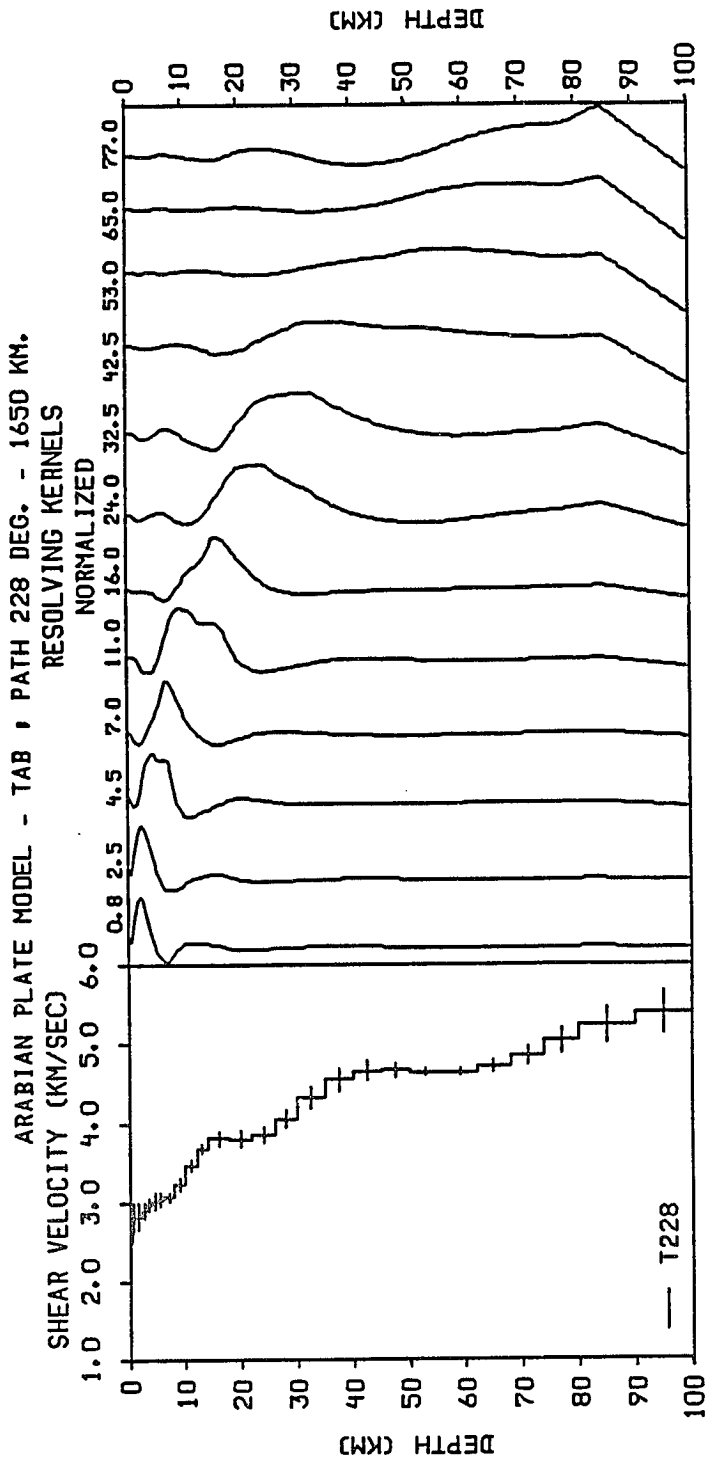
Figure 4.3. Shear velocity model T228f and resolving kernels estimated from fundamental-mode Rayleigh waves.

- 112 -

Table 4.3. Crustal velocity structure of the Arabian plate along path T228, derived from fundamental-mode data.

			Velocity Model T228f			
Layer Number	Layer Depth* (km)	Layer Thickness (km)	Compressional Velocity (km/sec)	Shear Velocity (km/sec)	Density (gm/cc)	Standard Deviation (km/sec)
1	0.2	0.5	4.33	2.50	2.365	0.187
2	0.8	0.5	4.86	2.80	2.469	0.184
3	1.5	1.0	4.89	2.82	2.476	0.171
4	2.5	1.0	5.01	2.89	2.502	0.101
5	3.5	1.0	5.14	2.97	2.529	0.076
6	4.5	1.0	5.23	3.02	2.545	0.106
7	5.5	1.0	5.27	3.04	2.553	0.087
8	7.0	2.0	5.33	3.08	2.567	0.056
9	9.0	2.0	5.60	3.23	2.619	0.073
10	11.0	2.0	6.01	3.47	2.702	0.071
11	13.0	2.0	6.38	3.68	2.814	0.060
12	16.0	4.0	6.60	3.81	2.875	0.086
13	20.0	4.0	6.58	3.80	2.871	0.106
14	24.0	4.0	6.68	3.85	2.896	0.105
15	28.0	4.0	7.02	4.05	2.987	0.105
16	32.5	5.0	7.49	4.33	3.138	0.132
17	37.5	5.0	7.88	4.55	3.270	0.145
18	42.5	5.0	8.30	4.66	3.418	0.128
19	47.5	5.0	8.32	4.67	3.426	0.090
20	53.0	6.0	8.27	4.64	3.409	0.054
21	59.0	6.0	8.27	4.64	3.409	0.049
22	65.0	6.0	8.40	4.71	3.454	0.074
23	71.0	6.0	8.65	4.86	3.542	0.114
24	77.0	6.0	8.98	5.04	3.655	0.166
25	85.0	10.0	9.33	5.24	3.794	0.225
26	95.0	10.0	9.61	5.39	3.900	0.272

* from the surface to the middle of the layers.

plate is characterized by a deep Moho, a thin basement, and a thick sedimentary layer.

Model T190f, whose path traverses a significant portion of the Arabian shield, portrays a slightly different velocity structure for the plate. Figure 4.2 shows that the shear velocity varies from 2.72 km/sec near the surface to 4.42. km/sec at about 53.0 km depth. Within the top 8.0 kilometers, the velocity is almost constant, and the difference between the layers does not exceed 0.03 km/sec. Similarly, at depths between 16.0 and 30.0 km the velocity changes by only 0.05 km/sec. These two groups of layers are separated by a velocity gradient that varies from 3.17 km/sec at 9.0 km to 3.55 km/sec at 13.0 km depth. A second velocity gradient is observed between 32.5 km and 42.5 km depth. The velocity within these layers increases from 3.91 km/sec to 4.30 km/sec. Apparently this model indicates that the sedimentary cover is about 8.0 km thick, the Conrad discontinuity is about 14.0 km deep, and the Moho discontinuity is at approximately 37.0 km depth.

Model T228f is presented in Figure 4.3. As expected, this model illustrates a different velocity structure for the plate. The path of this model mainly traverses the Zagros, the Mesopotamian foredeep and Arabian platform. The shear velocity of this model varies from 2.50 km/sec near the surface to 4.67 km/sec at approximately 47.0 km depth. From the surface to a depth of about 7.0 km the velocity increases gradually to 3.08 km/sec. A velocity gradient is observed between 10.0 km and 14.0 km depth, where the velocity varies from 3.23 km/sec to 3.68 km/sec. A second velocity gradient of 4.05-4.55 km/sec is observed between about 30.0 km and 40.0 km. Below 40.0 km the shear velocity averages 4.65 km/sec, whereas

the velocity increase at depths greater than 70.0 km is simply due to the lack of resolution caused by the limited period range of the dispersion curve for this path. It is evident that, unlike the two previous velocity structures, this model places the average top of the crystalline basement at about 5.5 km, the Conrad discontinuity at a relatively shallow depth of 14.0 km, and the Moho discontinuity around 35-37 km.

4.2.2 SHI Station Models

SHI station data provided seven shear velocity models for various regions of the Arabian plate. Figures 4.4 through 4.10 show the fundamental-mode and combined fundamental- and higher-mode models obtained for paths S166, S181, S212, S267, S305, S310 and S316, respectively. The parameters for these models are listed in Tables 4.4-4.16. Note that, the observed low velocity at shallow depth is, as indicated earlier, caused by mismatch between the fundamental- and higher-mode dispersion curves.

Models S166h and S166f, shown in Figure 4.4, sample the eastern portion of the plate, and similar to model T164f they reflect an almost gradual increase in shear velocity from 2.36 km/sec near the surface to 4.57 km/sec at about 60.0 km depth. Below this depth the velocity increases by only 0.14 km/sec. A observed increase in the shear velocity from 2.90 km/sec to 3.22 km/sec at about 9.0 km depth seems to mark the top of the crystalline basement, and the velocity gradient around 20.0 km depth indicates the depth to the Conrad discontinuity. The velocity between 20-35 km depth does not seem to change very much, and the velocity gradient that follows it indicates that the Moho discontinuity is about 45.0 km deep.

Figure 4.4. Shear velocity model S166h and resolving kernels estimated from the fundamental and first higher-mode Rayleigh waves. The dotted line model S166f is estimated from the fundamental-mode only.

- 116 -

Table 4.4. Crustal velocity structure of the Arabian plate along path S166, derived from fundamental- and higher-mode data.

	Velocity Model S166h					
Layer Number	Layer Depth* (km)	Layer Thickness (km)	Compressional Velocity (km/sec)	Shear Velocity (km/sec)	Density (gm/cc)	Standard Deviation (km/sec)
1	0.2	0.5	5.98	3.45	2.696	0.231
2	0.8	0.5	6.03	3.48	2.708	0.194
3	1.5	1.0	5.21	3.01	2.541	0.146
4	2.5	1.0	4.48	2.59	2.388	0.104
5	3.5	1.0	4.34	2.50	2.367	0.067
6	4.5	1.0	4.61	2.66	2.415	0.059
7	5.5	1.0	5.02	2.90	2.504	0.069
8	7.0	2.0	5.40	3.12	2.580	0.072
9	9.0	2.0	5.55	3.21	2.611	0.061
10	11.0	2.0	5.58	3.22	2.616	0.053
11	13.0	2.0	5.68	3.28	2.636	0.047
12	16.0	4.0	5.95	3.44	2.691	0.058
13	20.0	4.0	6.31	3.64	2.793	0.060
14	24.0	4.0	6.43	3.71	2.830	0.064
15	28.0	4.0	6.48	3.74	2.843	0.065
16	32.5	5.0	6.72	3.88	2.907	0.067
17	37.5	5.0	7.20	4.16	3.044	0.076
18	42.5	5.0	7.85	4.41	3.259	0.085
19	47.5	5.0	8.08	4.54	3.340	0.091
20	53.0	6.0	8.15	4.57	3.363	0.098
21	59.0	6.0	8.14	4.57	3.360	0.103
22	65.0	6.0	8.16	4.58	3.369	0.109
23	71.0	6.0	8.24	4.63	3.397	0.119
24	77.0	6.0	8.34	4.68	3.432	0.132
25	85.0	10.0	8.41	4.72	3.458	0.144
26	95.0	10.0	8.39	4.71	3.450	0.149
27	112.5	25.0	8.28	4.65	3.410	0.159
28	137.5	25.0	8.17	4.59	3.371	0.175
29	162.5	25.0	8.25	4.63	3.398	0.177
30	187.5	25.0	8.50	4.77	3.490	0.188

* from the surface to the middle of the layers.

Table 4.5. Crustal velocity structure of the Arabian plate along path S166, derived from fundamental-mode data.

Velocity Model S166f						
Layer Number	Layer Depth* (km)	Layer Thickness (km)	Compressional Velocity (km/sec)	Shear Velocity (km/sec)	Density (gm/cc)	Standard Deviation (km/sec)
1	0.2	0.5	4.09	2.36	2.333	0.154
2	0.8	0.5	4.62	2.67	2.417	0.153
3	1.5	1.0	4.63	2.68	2.420	0.151
4	2.5	1.0	4.67	2.70	2.428	0.135
5	3.5	1.0	4.77	2.75	2.450	0.097
6	4.5	1.0	4.93	2.85	2.484	0.057
7	5.5	1.0	5.13	2.96	2.527	0.055
8	7.0	2.0	5.37	3.10	2.575	0.076
9	9.0	2.0	5.63	3.25	2.625	0.065
10	11.0	2.0	5.84	3.37	2.668	0.054
11	13.0	2.0	5.99	3.46	2.698	0.054
12	16.0	4.0	6.09	3.51	2.726	0.052
13	20.0	4.0	6.17	3.56	2.752	0.050
14	24.0	4.0	6.36	3.67	2.809	0.064
15	28.0	4.0	6.64	3.84	2.887	0.074
16	32.5	5.0	6.94	4.01	2.965	0.090
17	37.5	5.0	7.19	4.15	3.042	0.107
18	42.5	5.0	7.61	4.27	3.176	0.115
19	47.5	5.0	7.78	4.37	3.237	0.109
20	53.0	6.0	7.95	4.47	3.295	0.095
21	59.0	6.0	8.11	4.55	3.348	0.090
22	65.0	6.0	8.21	4.61	3.387	0.104
23	71.0	6.0	8.25	4.63	3.400	0.132
24	77.0	6.0	8.21	4.61	3.385	0.166
25	85.0	10.0	8.10	4.55	3.345	0.208
26	95.0	10.0	7.91	4.44	3.281	0.259

* from the surface to the middle of the layers.
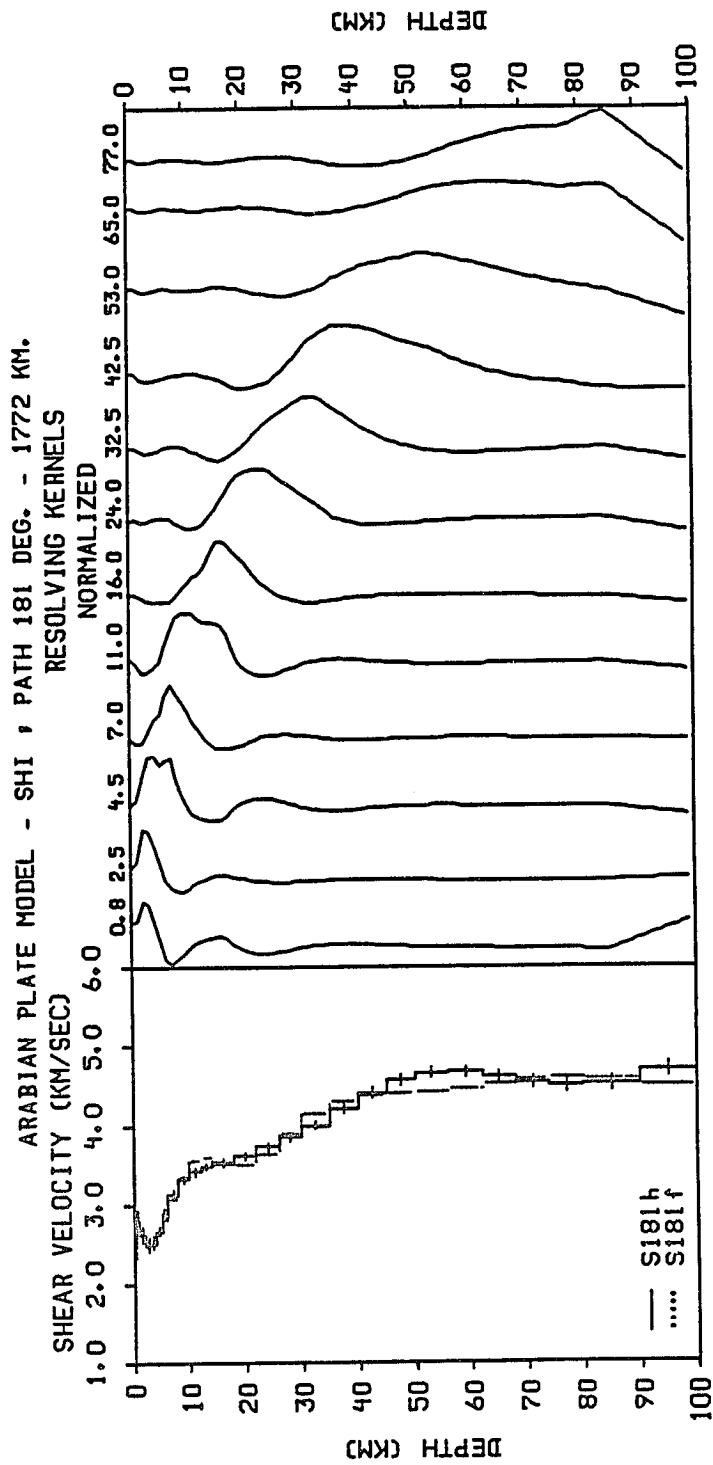
Figure 4.5. Shear velocity model S181h and resolving kernels estimated from the fundamental and first higher-mode Rayleigh waves. The dotted line model S181f is estimated from the fundamental-mode only.

Table 4.6. Crustal velocity structure of the Arabian plate along path S181, derived from fundamental- and higher-mode data.

			Velocity Model S181h			
Layer Number	Layer Depth* (km)	Layer Thickness (km)	Compressional Velocity (km/sec)	Shear Velocity (km/sec)	Density (gm/cc)	Standard Deviation (km/sec)
1	0.2	0.5	4.51	2.61	2.393	0.156
2	0.8	0.5	4.85	2.80	2.467	0.131
3	1.5	1.0	4.54	2.62	2.398	0.100
4	2.5	1.0	4.29	2.48	2.361	0.075
5	3.5	1.0	4.34	2.51	2.367	0.056
6	4.5	1.0	4.62	2.67	2.417	0.053
7	5.5	1.0	5.01	2.90	2.503	0.056
8	7.0	2.0	5.43	3.13	2.586	0.054
9	9.0	2.0	5.74	3.32	2.649	0.047
10	11.0	2.0	5.92	3.42	2.685	0.048
11	13.0	2.0	6.03	3.48	2.708	0.044
12	16.0	4.0	6.11	3.53	2.734	0.044
13	20.0	4.0	6.27	3.62	2.780	0.047
14	24.0	4.0	6.46	3.73	2.839	0.051
15	28.0	4.0	6.67	3.85	2.895	0.052
16	32.5	5.0	6.93	4.00	2.962	0.057
17	37.5	5.0	7.28	4.20	3.069	0.059
18	42.5	5.0	7.85	4.41	3.260	0.062
19	47.5	5.0	8.14	4.57	3.361	0.068
20	53.0	6.0	8.31	4.66	3.420	0.071
21	59.0	6.0	8.32	4.67	3.424	0.067
22	65.0	6.0	8.22	4.61	3.389	0.068
23	71.0	6.0	8.09	4.54	3.342	0.081
24	77.0	6.0	8.01	4.49	3.313	0.096
25	85.0	10.0	8.04	4.51	3.325	0.101
26	95.0	10.0	8.37	4.70	3.444	0.096

* from the surface to the middle of the layers.

Table 4.7. Crustal velocity structure of the Arabian plate along path S181, derived from fundamental-mode data.

			Velocity Model S181f			
Layer Number	Layer Depth* (km)	Layer Thickness (km)	Compressional Velocity (km/sec)	Shear Velocity (km/sec)	Density (gm/cc)	Standard Deviation (km/sec)
1	0.2	0.5	3.98	2.30	2.316	0.111
2	0.8	0.5	4.50	2.60	2.391	0.109
3	1.5	1.0	4.51	2.60	2.391	0.105
4	2.5	1.0	4.49	2.59	2.388	0.087
5	3.5	1.0	4.50	2.60	2.390	0.061
6	4.5	1.0	4.62	2.67	2.416	0.058
7	5.5	1.0	4.89	2.82	2.476	0.066
8	7.0	2.0	5.30	3.06	2.561	0.065
9	9.0	2.0	5.81	3.36	2.663	0.053
10	11.0	2.0	6.16	3.55	2.747	0.057
11	13.0	2.0	6.24	3.60	2.772	0.053
12	16.0	4.0	6.13	3.54	2.740	0.045
13	20.0	4.0	6.05	3.50	2.716	0.047
14	24.0	4.0	6.29	3.63	2.788	0.060
15	28.0	4.0	6.73	3.89	2.910	0.072
16	32.5	5.0	7.17	4.14	3.034	0.084
17	37.5	5.0	7.45	4.30	3.124	0.092
18	42.5	5.0	7.80	4.38	3.240	0.093
19	47.5	5.0	7.84	4.40	3.257	0.085
20	53.0	6.0	7.88	4.42	3.270	0.074
21	59.0	6.0	7.95	4.46	3.295	0.074
22	65.0	6.0	8.05	4.52	3.329	0.091
23	71.0	6.0	8.15	4.57	3.362	0.116
24	77.0	6.0	8.19	4.60	3.379	0.146
25	85.0	10.0	8.17	4.58	3.370	0.181
26	95.0	10.0	8.01	4.50	3.314	0.222

* from the surface to the middle of the layers.
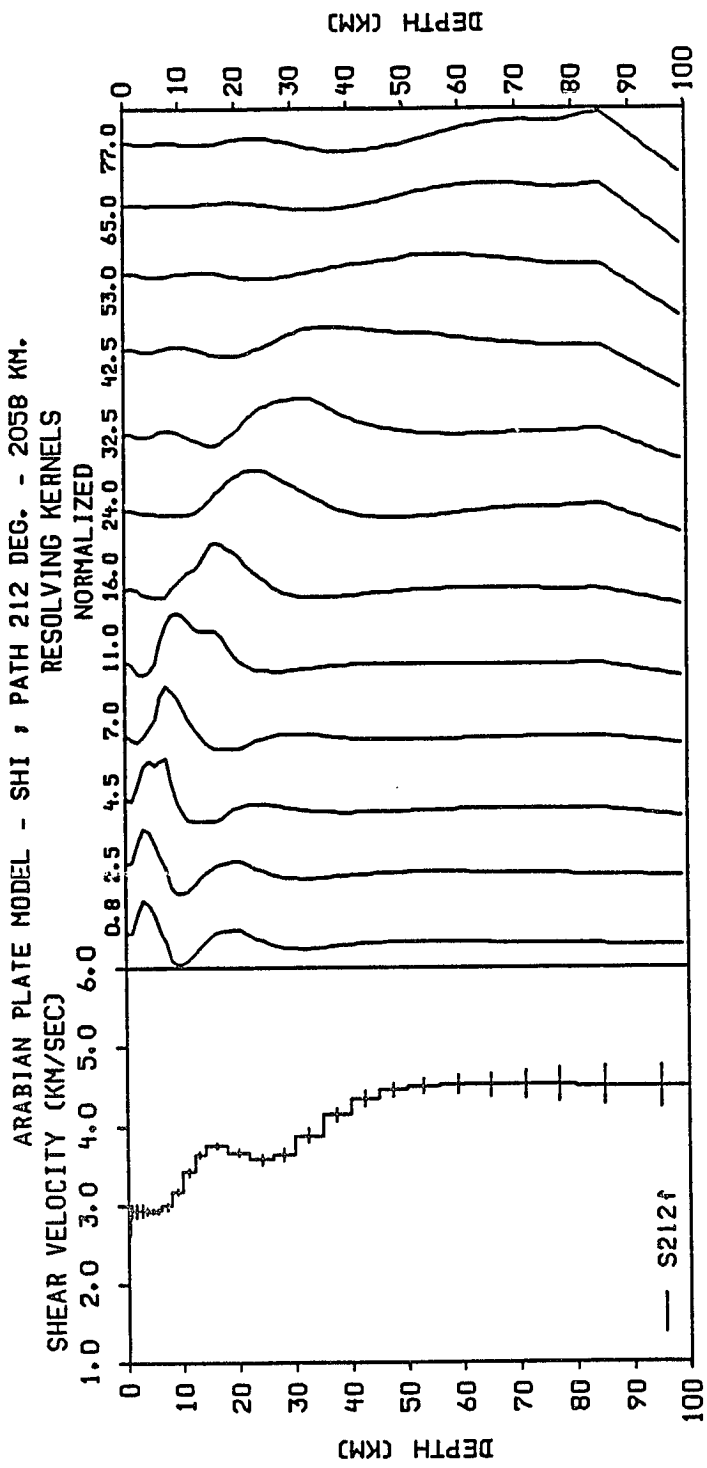
Figure 4.6. Shear velocity model S212 and resolving kernels estimated from fundamental-mode Rayleigh waves.

- 122 -

Table 4.8. Crustal velocity structure of the Arabian plate along path S212, derived from fundamental-mode data.

Layer Number	Layer Depth* (km)	Layer Thickness (km)	Compressional Velocity (km/sec)	Shear Velocity (km/sec)	Density (gm/cc)	Standard Deviation (km/sec)
Velocity Model S212f						
1	0.2	0.5	4.55	2.63	2.400	0.089
2	0.8	0.5	5.07	2.93	2.514	0.088
3	1.5	1.0	5.08	2.93	2.516	0.086
4	2.5	1.0	5.08	2.93	2.516	0.076
5	3.5	1.0	5.07	2.93	2.514	0.052
6	4.5	1.0	5.06	2.92	2.512	0.027
7	5.5	1.0	5.08	2.93	2.516	0.029
8	7.0	2.0	5.18	2.99	2.536	0.044
9	9.0	2.0	5.48	3.17	2.597	0.041
10	11.0	2.0	5.92	3.42	2.683	0.042
11	13.0	2.0	6.30	3.64	2.791	0.046
12	16.0	4.0	6.51	3.76	2.853	0.043
13	20.0	4.0	6.35	3.67	2.805	0.044
14	24.0	4.0	6.19	3.57	2.757	0.064
15	28.0	4.0	6.32	3.65	2.796	0.078
16	32.5	5.0	6.71	3.88	2.905	0.088
17	37.5	5.0	7.17	4.14	3.036	0.093
18	42.5	5.0	7.74	4.34	3.220	0.093
19	47.5	5.0	7.94	4.45	3.288	0.090
20	53.0	6.0	8.02	4.50	3.318	0.095
21	59.0	6.0	8.04	4.51	3.325	0.115
22	65.0	6.0	8.05	4.52	3.326	0.147
23	71.0	6.0	8.05	4.52	3.327	0.182
24	77.0	6.0	8.05	4.52	3.326	0.215
25	85.0	10.0	8.03	4.51	3.322	0.243
26	95.0	10.0	8.01	4.49	3.312	0.258

* from the surface to the middle of the layers.
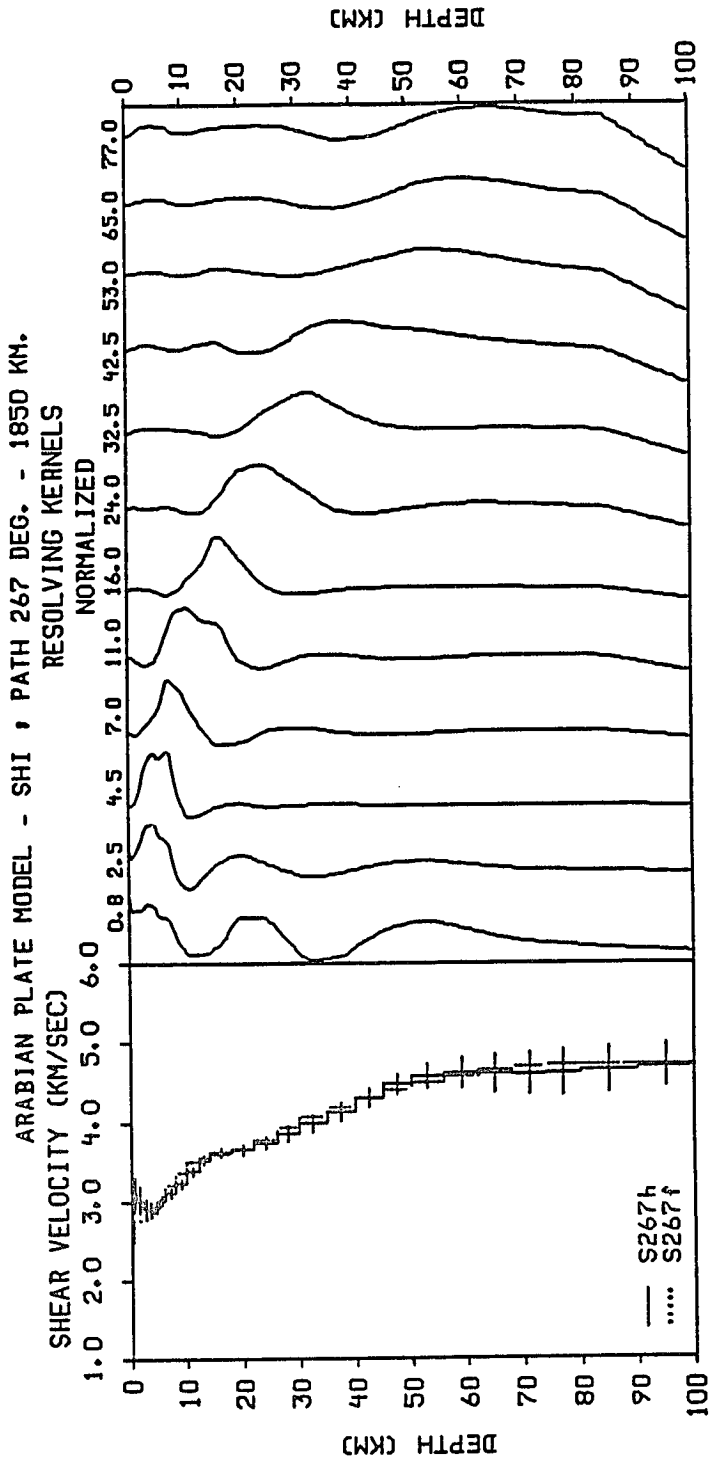
Figure 4.7. Shear velocity model S267h and resolving kernels estimated from the fundamental and first higher-mode Rayleigh waves. The dotted line model S267f is estimated from the fundamental-mode only.

- 124 -

Table 4.9. Crustal velocity structure of the Arabian plate along path S267, derived from fundamental- and higher-mode data.

Layer Number	Layer Depth* (km)	Layer Thickness (km)	Compressional Velocity (km/sec)	Shear Velocity (km/sec)	Density (gm/cc)	Standard Deviation (km/sec)
			Velocity Model S267h			
1	0.2	0.5	4.94	2.85	2.487	0.221
2	0.8	0.5	5.39	3.11	2.578	0.196
3	1.5	1.0	5.24	3.02	2.547	0.158
4	2.5	1.0	5.06	2.92	2.512	0.121
5	3.5	1.0	5.01	2.89	2.501	0.096
6	4.5	1.0	5.07	2.93	2.515	0.075
7	5.5	1.0	5.21	3.01	2.542	0.057
8	7.0	2.0	5.38	3.10	2.576	0.060
9	9.0	2.0	5.59	3.23	2.618	0.066
10	11.0	2.0	5.86	3.38	2.671	0.061
11	13.0	2.0	6.11	3.53	2.732	0.060
12	16.0	4.0	6.27	3.62	2.781	0.065
13	20.0	4.0	6.33	3.65	2.799	0.066
14	24.0	4.0	6.48	3.74	2.843	0.084
15	28.0	4.0	6.68	3.86	2.898	0.098
16	32.5	5.0	6.90	3.98	2.954	0.109
17	37.5	5.0	7.16	4.13	3.031	0.113
18	42.5	5.0	7.68	4.31	3.202	0.117
19	47.5	5.0	7.97	4.47	3.300	0.131
20	53.0	6.0	8.16	4.58	3.368	0.162
21	59.0	6.0	8.22	4.62	3.391	0.202
22	65.0	6.0	8.22	4.61	3.388	0.242
23	71.0	6.0	8.21	4.61	3.385	0.273
24	77.0	6.0	8.23	4.62	3.394	0.290
25	85.0	10.0	8.30	4.66	3.418	0.293
26	95.0	10.0	8.40	4.72	3.454	0.273

* from the surface to the middle of the layers.

Table 4.10. Crustal velocity structure of the Arabian plate along path
S267, derived from fundamental-mode data.

Velocity Model S267f						
Layer Number	Layer Depth* (km)	Layer Thickness (km)	Compressional Velocity (km/sec)	Shear Velocity (km/sec)	Density (gm/cc)	Standard Deviation (km/sec)
1	0.2	0.5	4.24	2.45	2.354	0.143
2	0.8	0.5	4.77	2.76	2.450	0.142
3	1.5	1.0	4.79	2.76	2.453	0.142
4	2.5	1.0	4.81	2.78	2.459	0.135
5	3.5	1.0	4.89	2.82	2.476	0.114
6	4.5	1.0	5.04	2.91	2.509	0.078
7	5.5	1.0	5.27	3.04	2.554	0.043
8	7.0	2.0	5.55	3.20	2.609	0.050
9	9.0	2.0	5.84	3.37	2.668	0.068
10	11.0	2.0	6.06	3.50	2.717	0.065
11	13.0	2.0	6.18	3.57	2.753	0.052
12	16.0	4.0	6.24	3.60	2.771	0.051
13	20.0	4.0	6.33	3.66	2.800	0.066
14	24.0	4.0	6.54	3.78	2.861	0.087
15	28.0	4.0	6.81	3.93	2.929	0.099
16	32.5	5.0	7.05	4.07	2.997	0.102
17	37.5	5.0	7.26	4.19	3.062	0.101
18	42.5	5.0	7.65	4.30	3.192	0.108
19	47.5	5.0	7.84	4.40	3.254	0.131
20	53.0	6.0	8.01	4.50	3.315	0.168
21	59.0	6.0	8.17	4.59	3.371	0.211
22	65.0	6.0	8.29	4.65	3.414	0.250
23	71.0	6.0	8.36	4.70	3.441	0.279
24	77.0	6.0	8.40	4.71	3.454	0.295
25	85.0	10.0	8.40	4.71	3.454	0.296
26	95.0	10.0	8.36	4.69	3.440	0.274

* from the surface to the middle of the layers.

Figure 4.8. Shear velocity model S305h and resolving kernels estimated from the fundamental and first higher-mode Rayleigh waves. The dotted line model S305f is estimated from the fundamental-mode only.

- 127 -

Table 4.11. Crustal velocity structure of the Arabian plate along path S305, derived from fundamental- and higher-mode data.

Velocity Model S305h						
Layer Number	Layer Depth* (km)	Layer Thickness (km)	Compressional Velocity (km/sec)	Shear Velocity (km/sec)	Density (gm/cc)	Standard Deviation (km/sec)
1	0.2	0.5	4.34	2.51	2.368	0.068
2	0.8	0.5	4.53	2.61	2.396	0.053
3	1.5	1.0	4.04	2.33	2.325	0.034
4	2.5	1.0	4.09	2.36	2.333	0.050
5	3.5	1.0	4.52	2.61	2.394	0.075
6	4.5	1.0	4.92	2.84	2.481	0.071
7	5.5	1.0	5.17	2.98	2.534	0.063
8	7.0	2.0	5.30	3.06	2.561	0.066
9	9.0	2.0	5.30	3.06	2.561	0.062
10	11.0	2.0	5.31	3.06	2.561	0.066
11	13.0	2.0	5.41	3.13	2.583	0.067
12	16.0	4.0	5.64	3.26	2.628	0.071
13	20.0	4.0	5.85	3.38	2.671	0.085
14	24.0	4.0	5.87	3.39	2.675	0.103
15	28.0	4.0	5.86	3.39	2.673	0.118
16	32.5	5.0	6.06	3.50	2.717	0.130
17	37.5	5.0	6.49	3.75	2.847	0.148
18	42.5	5.0	7.10	3.99	3.013	0.180
19	47.5	5.0	7.35	4.12	3.091	0.219
20	53.0	6.0	7.42	4.16	3.113	0.254
21	59.0	6.0	7.40	4.15	3.107	0.279
22	65.0	6.0	7.39	4.15	3.104	0.293
23	71.0	6.0	7.41	4.16	3.112	0.296
24	77.0	6.0	7.45	4.18	3.124	0.295
25	85.0	10.0	7.46	4.19	3.128	0.293
26	95.0	10.0	7.34	4.12	3.088	0.302

* from the surface to the middle of the layers.

Table 4.12. Crustal velocity structure of the Arabian plate along path S305, derived from fundamental-mode data.

Velocity Model S305f						
Layer Number	Layer Depth* (km)	Layer Thickness (km)	Compressional Velocity (km/sec)	Shear Velocity (km/sec)	Density (gm/cc)	Standard Deviation (km/sec)
1	0.2	0.5	3.61	2.09	2.250	0.056
2	0.8	0.5	4.15	2.40	2.341	0.053
3	1.5	1.0	4.19	2.42	2.347	0.039
4	2.5	1.0	4.36	2.52	2.371	0.049
5	3.5	1.0	4.63	2.67	2.419	0.084
6	4.5	1.0	4.91	2.83	2.480	0.081
7	5.5	1.0	5.14	2.97	2.527	0.070
8	7.0	2.0	5.30	3.06	2.560	0.071
9	9.0	2.0	5.41	3.13	2.583	0.065
10	11.0	2.0	5.56	3.21	2.612	0.073
11	13.0	2.0	5.71	3.30	2.642	0.080
12	16.0	4.0	5.80	3.35	2.660	0.080
13	20.0	4.0	5.75	3.32	2.651	0.066
14	24.0	4.0	5.78	3.34	2.657	0.063
15	28.0	4.0	6.02	3.48	2.706	0.082
16	32.5	5.0	6.42	3.71	2.826	0.117
17	37.5	5.0	6.85	3.95	2.941	0.156
18	42.5	5.0	7.39	4.15	3.104	0.191
19	47.5	5.0	7.59	4.26	3.170	0.219
20	53.0	6.0	7.66	4.30	3.194	0.233
21	59.0	6.0	7.62	4.28	3.182	0.231
22	65.0	6.0	7.54	4.23	3.155	0.214
23	71.0	6.0	7.46	4.19	3.126	0.188
24	77.0	6.0	7.39	4.15	3.105	0.157
25	85.0	10.0	7.36	4.13	3.094	0.125
26	95.0	10.0	7.37	4.14	3.098	0.099

* from the surface to the middle of the layers.

Figure 4.9. Shear velocity model S310h and resolving kernels estimated from the fundamental and first higher-mode Rayleigh waves. The dotted line model S310f is estimated from the fundamental-mode only.

- 130 -

Table 4.13. Crustal velocity structure of the Arabian plate along path S310, derived from fundamental- and higher-mode data.

	Velocity Model S310h					
Layer Number	Layer Depth* (km)	Layer Thickness (km)	Compressional Velocity (km/sec)	Shear Velocity (km/sec)	Density (gm/cc)	Standard Deviation (km/sec)
1	0.2	0.5	4.54	2.62	2.400	0.121
2	0.8	0.5	4.82	2.78	2.460	0.104
3	1.5	1.0	4.47	2.58	2.386	0.086
4	2.5	1.0	4.28	2.47	2.359	0.067
5	3.5	1.0	4.45	2.57	2.383	0.037
6	4.5	1.0	4.92	2.84	2.483	0.029
7	5.5	1.0	5.50	3.18	2.600	0.061
8	7.0	2.0	5.98	3.46	2.697	0.087
9	9.0	2.0	6.06	3.50	2.718	0.087
10	11.0	2.0	5.91	3.41	2.682	0.078
11	13.0	2.0	5.80	3.35	2.661	0.069
12	16.0	4.0	5.86	3.38	2.671	0.067
13	20.0	4.0	6.10	3.52	2.730	0.076
14	24.0	4.0	6.21	3.59	2.764	0.090
15	28.0	4.0	6.20	3.58	2.761	0.103
16	32.5	5.0	6.33	3.65	2.798	0.117
17	37.5	5.0	6.72	3.88	2.908	0.135
18	42.5	5.0	7.37	4.14	3.098	0.168
19	47.5	5.0	7.66	4.30	3.194	0.208
20	53.0	6.0	7.76	4.35	3.227	0.241
21	59.0	6.0	7.71	4.33	3.211	0.264
22	65.0	6.0	7.60	4.27	3.175	0.275
23	71.0	6.0	7.50	4.21	3.139	0.277
24	77.0	6.0	7.41	4.16	3.110	0.271
25	85.0	10.0	7.34	4.12	3.088	0.259
26	95.0	10.0	7.30	4.10	3.077	0.241

* from the surface to the middle of the layers.

Table 4.14. Crustal velocity structure of the Arabian plate along path S310, derived from fundamental-mode data.

	Velocity Model S310f					
Layer Number	Layer Depth* (km)	Layer Thickness (km)	Compressional Velocity (km/sec)	Shear Velocity (km/sec)	Density (gm/cc)	Standard Deviation (km/sec)
1	0.2	0.5	4.02	2.32	2.323	0.085
2	0.8	0.5	4.55	2.63	2.401	0.085
3	1.5	1.0	4.56	2.63	2.403	0.085
4	2.5	1.0	4.60	2.66	2.413	0.074
5	3.5	1.0	4.75	2.74	2.444	0.045
6	4.5	1.0	5.01	2.89	2.502	0.017
7	5.5	1.0	5.37	3.10	2.573	0.048
8	7.0	2.0	5.76	3.33	2.652	0.081
9	9.0	2.0	6.07	3.51	2.722	0.088
10	11.0	2.0	6.19	3.57	2.757	0.085
11	13.0	2.0	6.14	3.54	2.741	0.086
12	16.0	4.0	6.00	3.46	2.700	0.091
13	20.0	4.0	5.95	3.43	2.690	0.080
14	24.0	4.0	6.08	3.51	2.724	0.078
15	28.0	4.0	6.33	3.66	2.800	0.087
16	32.5	5.0	6.64	3.83	2.886	0.107
17	37.5	5.0	6.94	4.01	2.964	0.137
18	42.5	5.0	7.40	4.15	3.106	0.172
19	47.5	5.0	7.59	4.26	3.170	0.208
20	53.0	6.0	7.72	4.33	3.213	0.238
21	59.0	6.0	7.77	4.36	3.232	0.256
22	65.0	6.0	7.78	4.36	3.234	0.262
23	71.0	6.0	7.75	4.35	3.224	0.255
24	77.0	6.0	7.71	4.33	3.210	0.238
25	85.0	10.0	7.66	4.30	3.195	0.214
26	95.0	10.0	7.63	4.28	3.185	0.183

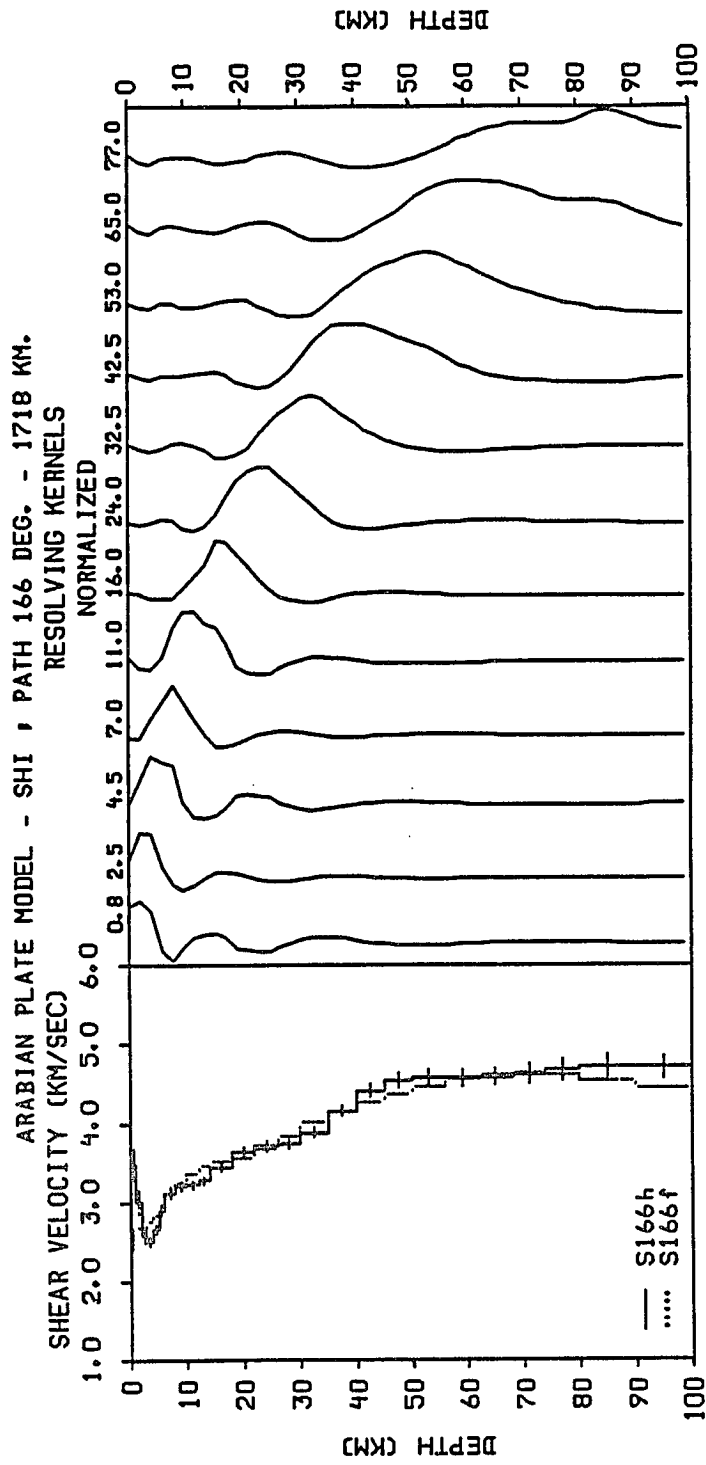* from the surface to the middle of the layers.

- 132 -

Figure 4.10. Shear velocity model S316h and resolving kernels estimated from the fundamental and first higher-mode Rayleigh waves. The dotted line model S316f is estimated from the fundamental-mode only.

- 133 -

Table 4.15. Crustal velocity structure of the Arabian plate along path S316, derived from fundamental- and higher-mode data.

			Velocity Model S316h			
Layer Number	Layer Depth* (km)	Layer Thickness (km)	Compressional Velocity (km/sec)	Shear Velocity (km/sec)	Density (gm/cc)	Standard Deviation (km/sec)
1	0.2	0.5	3.83	2.21	2.289	0.101
2	0.8	0.5	4.38	2.53	2.374	0.095
3	1.5	1.0	4.44	2.56	2.381	0.085
4	2.5	1.0	4.54	2.62	2.399	0.069
5	3.5	1.0	4.74	2.74	2.443	0.043
6	4.5	1.0	5.05	2.91	2.510	0.023
7	5.5	1.0	5.42	3.13	2.585	0.049
8	7.0	2.0	5.81	3.36	2.663	0.082
9	9.0	2.0	6.10	3.52	2.730	0.094
10	11.0	2.0	6.19	3.57	2.756	0.089
11	13.0	2.0	6.10	3.52	2.730	0.082
12	16.0	4.0	5.93	3.42	2.686	0.081
13	20.0	4.0	5.83	3.36	2.666	0.083
14	24.0	4.0	5.90	3.41	2.680	0.097
15	28.0	4.0	6.09	3.52	2.728	0.111
16	32.5	5.0	6.36	3.67	2.809	0.124
17	37.5	5.0	6.68	3.86	2.897	0.139
18	42.5	5.0	7.16	4.02	3.032	0.163
19	47.5	5.0	7.35	4.12	3.091	0.193
20	53.0	6.0	7.41	4.16	3.110	0.224
21	59.0	6.0	7.36	4.13	3.096	0.248
22	65.0	6.0	7.28	4.09	3.071	0.262
23	71.0	6.0	7.22	4.05	3.049	0.265
24	77.0	6.0	7.19	4.03	3.040	0.258
25	85.0	10.0	7.21	4.05	3.047	0.243
26	95.0	10.0	7.30	4.10	3.076	0.222

* from the surface to the middle of the layers.

Table 4.16. Crustal velocity structure of the Arabian plate along path S316, derived from fundamental-mode data.

			Velocity Model S316f			
Layer Number	Layer Depth* (km)	Layer Thickness (km)	Compressional Velocity (km/sec)	Shear Velocity (km/sec)	Density (gm/cc)	Standard Deviation (km/sec)
1	0.2	0.5	4.02	2.32	2.323	0.082
2	0.8	0.5	4.55	2.63	2.402	0.082
3	1.5	1.0	4.56	2.63	2.403	0.083
4	2.5	1.0	4.60	2.65	2.411	0.073
5	3.5	1.0	4.73	2.73	2.440	0.047
6	4.5	1.0	4.97	2.87	2.494	0.019
7	5.5	1.0	5.32	3.07	2.564	0.051
8	7.0	2.0	5.72	3.30	2.643	0.088
9	9.0	2.0	6.05	.3.50	2.716	0.099
10	11.0	2.0	6.18	3.57	2.755	0.094
11	13.0	2.0	6.09	3.52	2.728	0.091
12	16.0	4.0	5.85	3.38	2.670	0.094
13	20.0	4.0	5.64	3.25	2.627	0.086
14	24.0	4.0	5.69	3.28	2.637	0.086
15	28.0	4.0	5.98	3.45	2.696	0.101
16	32.5	5.0	6.38	3.68	2.813	0.124
17	37.5	5.0	6.74	3.89	2.911	0.150
18	42.5	5.0	7.16	4.02	3.030	0.179
19	47.5	5.0	7.23	4.06	3.054	0.209
20	53.0	6.0	7.19	4.03	3.039	0.235
21	59.0	6.0	7.06	3.96	2.999	0.254
22	65.0	6.0	6.93	3.89	2.961	0.261
23	71.0	6.0	6.83	3.83	2.935	0.256
24	77.0	6.0	6.79	3.81	2.925	0.241
25	85.0	10.0	6.81	3.82	2.931	0.218
26	95.0	10.0	6.92	3.89	2.960	0.188

* from the surface to the middle of the layers.

- 135 -

The velocity in the upper mantle seems to increase from 4.54 km/sec to 4.71 km/sec at 100.0 km depth.

Models S181h and S181f, shown in Figure 4.5, also traverse the eastern portion of the Arabian plate. The 2.30 km/sec shear velocity near the surface seems to increase rapidly to 3.32 km/sec and 3.48 km/sec at depths of 9.0 and 13.0 km, respectively. Thus, marking the top of the crystalline basement below along this path. The velocity between 13.0 km and 53.0 km shows a very gradual increase within which two gradients can be distinguished. The first marks the Conrad discontinuity at a depth of about 20 km, and the second marks the Moho discontinuity at a depth of about 45.0 km. The shear velocity within the upper crust seems to vary between 3.48-3.62 km/sec, while the velocity range within the lower crust is 3.73-4.41 km/sec. The upper mantle velocity increases from 4.57 km/sec to 4.70 km/sec.

Model S212f, shown in Figure 4.6, is the only SHI station velocity structure exclusively derived from fundamental-mode dispersion data. Although, this model samples the southern end of the Arabian shield region, a significant portion of its path traverses the Mesopotamian foredeep and Arabian platform. This is clearly reflected by the existence of about 6.0 km of sediments overlaying the basement. The velocity within this ranges from 2.63 km/sec near the surface to 2.93 km/sec at the bottom. The gradual increase in velocity from 2.99 km/sec to 3.64 km/sec seems to place the Conrad discontinuity at a shallow depth of about 12.0 km. Below this depth the velocity decreases to 3.57 km/sec at 24.0 km, and gradually increases to 4.34 km/sec at 42.5 km, and seems to indicated that Moho is about 40.0 km deep. The observed low-velocity layer within the lower

crust, on the other hand, can easily be attributed to the rapid change in velocity within the depth range, and the inversion process attempts to fit the observed data. The velocity in the upper mantle seems to change very little, and it averages around 4.51 km/sec.

Models S267h and S267f are presented in Figure 4.7. These models show that the sedimentary layer thickness is about 11.0 km, within which the shear velocity increases from 2.45 km/sec near the surface to 3.38 km/sec at the top of the crystalline basement. The Conrad discontinuity inferred from the change in velocity with depth appears to be located at about 20.0-22.0 km depth. The velocity within the upper crust varies from 3.53 km/sec to 3.65 km/sec. A gradual increase in velocity from 3.74 km/sec to 4.47 km/sec characterizes the lower crust. Below the Moho discontinuity, which seems to be located at 45.0 km depth, the shear velocity range is 4.58-4.72 km/sec.

Models S305h and S305f path exclusively traverses the Zagros mountain belt folded zone. Figure 4.8 shows that the boundaries of the major crustal layers are well defined by relatively rapid change in shear velocity. The higher-mode data seem to have contributed significantly to the refinement of model S305h. A remarkable feature of this model is the low (4.12-4.19 km/sec) upper mantle shear velocity. Also, the sedimentary layer seems to abruptly end at about 6.0 km depth. The velocity within this layer increases from 2.09 km/sec near the surface to 2.98 km/sec at the top of the crystalline basement. Again, the apparent low-velocity layer near the surface is most likely due to a discrepancy between the fundamental and higher modes at short periods. The upper crust is marked by an almost constant velocity between 8.0 km and the Conrad discontinuity at 18.0 km

depth. Within this layer the velocity increases from 3.06 km/sec by a mere 0.2 km/sec. In the lower crust the shear velocity also seems to be almost constant, because it varies between 3.38 km/sec and 3.75 km/sec at about 37.0 km depth, where the Moho discontinuity is identified.

Models S310h and S310f path also traverses the Zagros mountain belt and its folded belt. However, Figure 4.9 shows that the major layers of these models are not as sharply defined as S305h. However, it also shows that the sedimentary layer ends abruptly at a depth of about 5.0 km, where the shear velocity is 2.84 km/sec, and that the upper mantle exhibits low shear velocities that varies between 4.14-4.35 km/sec. Note that, the the decrease in velocity within the upper mantle, which is observed in model S310h but not in S310f, is most likely due to the limited period range of the dispersion curves along this path. In addition, a mismatch between the fundamental- and higher-mode dispersion data is responsible for the apparent low-velocity layer near the surface. As for the Conrad and Moho discontinuities, they also seem to be located at depths of about 18.0 km and 37.0 km, respectively. The velocity within the upper crust varies between 3.18-3.38 km/sec, and the velocity within the lower crust varies from 3.52 km/sec to 3.88 km/sec.

Models S316h and S316f are shown in Figure 4.10. Again, the path of these models also traverses the Zagros mountain belt and its folded belt. The major layers in this case are not as well defined as either those in models S305h or S310h. Nevertheless, the upper mantle still exhibits low velocities that vary between 4.02-4.16 km/sec. The Moho is also observed at about 37.0 km depth, but the Conrad discontinuity is difficult to identify due to the higher velocities observed between about 8.0-18.0 km. The

velocities above the Moho increase from 3.36 km/sec at 20.0 km depth to 3.86 km/sec. Finally, the observed 2.21 km/sec shear velocity near the surface seems to increase gradually within the sedimentary layers of this model to 2.91 km/sec at 5.0 km depth.

4.2.3 EIL Station Models

Figures 4.11 through 4.15 show the five models obtained from the inversion of EIL station averaged dispersion curves. The parameters for these models are presented in Tables 4.17-4.24. The velocity structures along paths E30, E67 and E84 are estimated from the fundamental and higher-mode dispersion data, while the models along paths E123 and E131 are estimated from the fundamental-mode only. In the following discussion, both the fundamental- and higher-mode models are used to interpret the velocity structures, and identify discrepancies between the dispersion data.

Models E30h and E30f are presented in Figure 4.11. The path for these models traverses the northwestern region of the Arabian plate. The shear velocity near the surface seems to increase gradually to a depth of 3.0 km, but varies very little between 3.0-9.0 km. Within these depths the velocity ranges are 1.98-2.97 km/sec, and 3.11-3.37 km/sec, respectively. The upper crustal structure is also characterized by a gradual increase in velocity from 3.5 km/sec to 3.62 km/sec at about 18.0 km depth, where the Conrad discontinuity is identified. Below this depth, the velocity changes slowly from 3.78 km/sec to 4.09 km/sec near the Moho discontinuity at about 37.0 km depth. Although, the upper mantle structure is difficult to ascertain, because of a mismatch between the fundamental and higher modes dispersion data at longer periods, the shear velocities below the
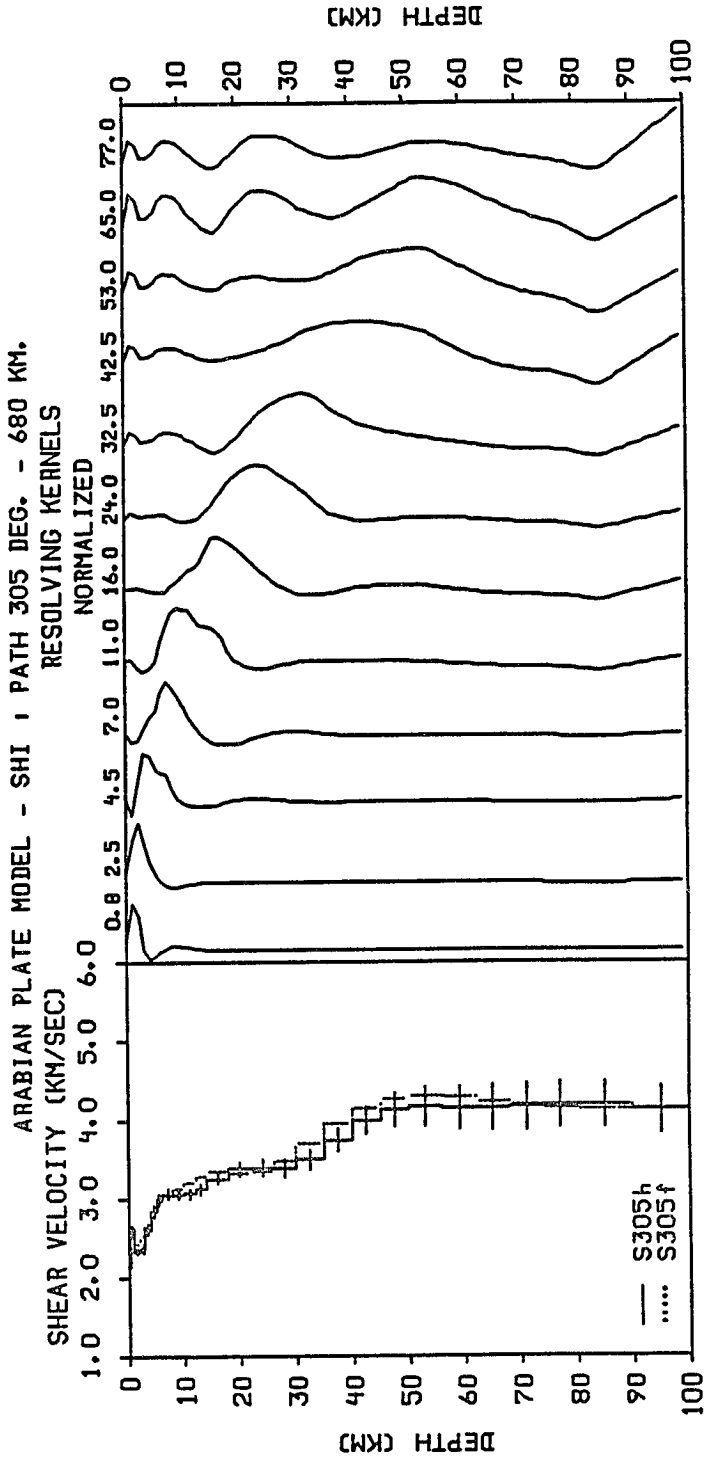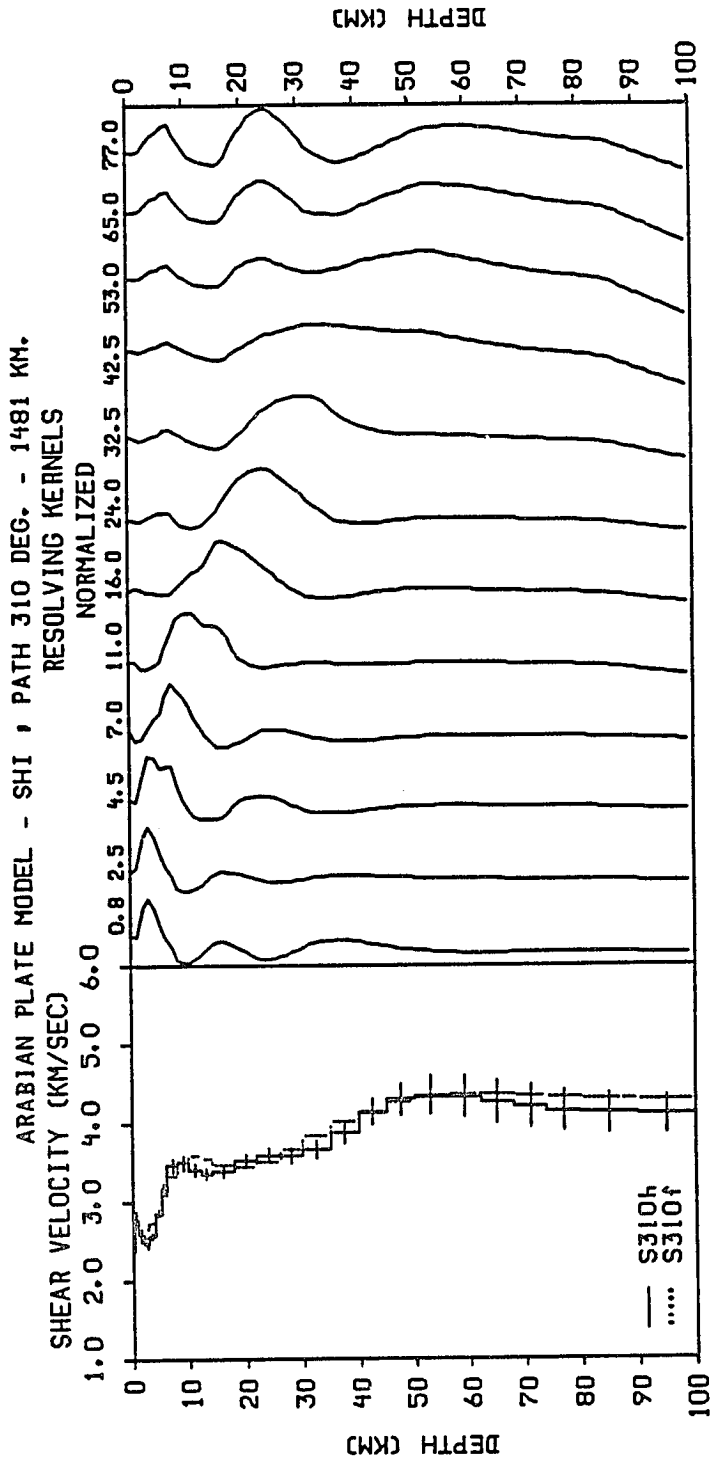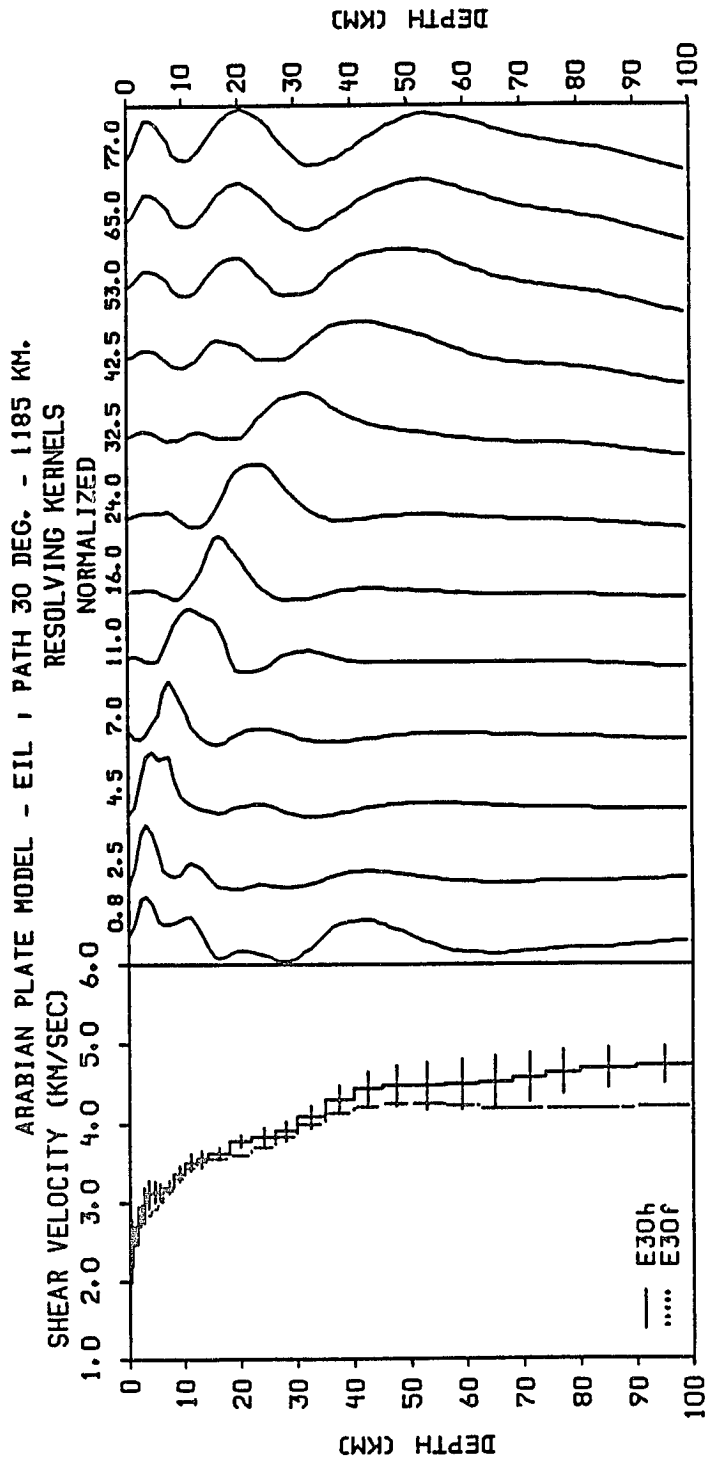
Figure 4.11. Shear velocity model E30h and resolving kernels estimated from the fundamental and first higher-mode Rayleigh waves. The dotted line model E30f is estimated from the fundamental-mode only.

- 140 -

Table 4.17. Crustal velocity structure of the Arabian plate along path E30, derived from fundamental- and higher-mode data.

Velocity Model E30h						
Layer Number	Layer Depth* (km)	Layer Thickness (km)	Compressional Velocity (km/sec)	Shear Velocity (km/sec)	Density (gm/cc)	Standard Deviation (km/sec)
1	0.2	0.5	3.42	1.98	2.218	0.270
2	0.8	0.5	4.23	2.44	2.352	0.257
3	1.5	1.0	4.69	2.71	2.432	0.244
4	2.5	1.0	5.15	2.97	2.529	0.226
5	3.5	1.0	5.38	3.11	2.576	0.188
6	4.5	1.0	5.43	3.13	2.586	0.138
7	5.5	1.0	5.44	3.14	2.588	0.099
8	7.0	2.0	5.54	3.20	2.608	0.093
9	9.0	2.0	5.84	3.37	2.668	0.096
10	11.0	2.0	6.07	3.50	2.721	0.107
11	13.0	2.0	6.16	3.56	2.747	0.103
12	16.0	4.0	6.27	3.62	2.782	0.082
13	20.0	4.0	6.54	3.78	2.861	0.071
14	24.0	4.0	6.65	3.84	2.890	0.105
15	28.0	4.0	6.76	3.90	2.918	0.132
16	32.5	5.0	7.08	4.09	3.004	0.146
17	37.5	5.0	7.47	4.31	3.130	0.168
18	42.5	5.0	7.91	4.44	3.280	0.213
19	47.5	5.0	7.97	4.48	3.301	0.263
20	53.0	6.0	7.97	4.48	3.301	0.305
21	59.0	6.0	8.00	4.49	3.310	0.328
22	65.0	6.0	8.07	4.53	3.335	0.329
23	71.0	6.0	8.17	4.58	3.370	0.314
24	77.0	6.0	8.27	4.64	3.408	0.289
25	85.0	10.0	8.37	4.70	3.444	0.260
26	95.0	10.0	8.44	4.74	3.470	0.232

* from the surface to the middle of the layers.

Table 4.18. Crustal velocity structure of the Arabian plate along path E30, derived from fundamental-mode data.

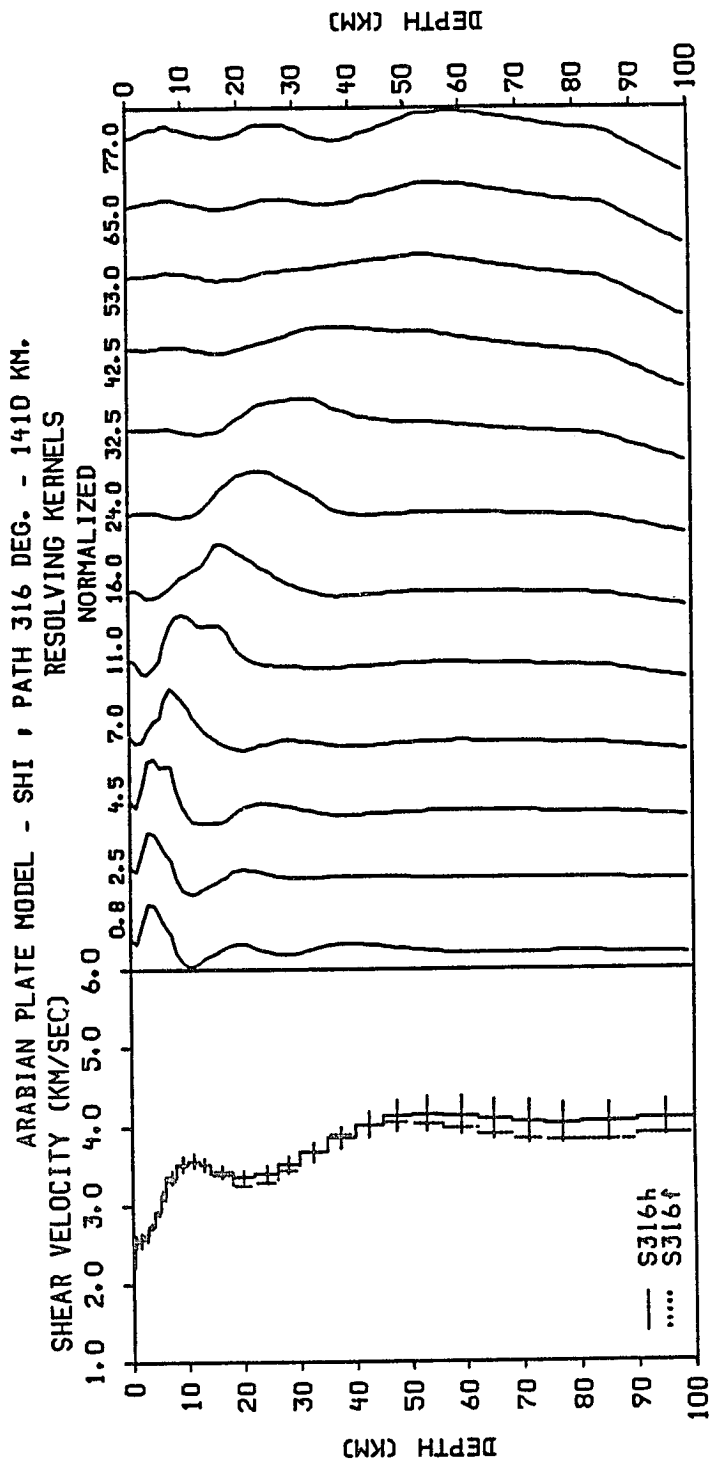|			Velocity Model E30f			
Layer Number	Layer Depth* (km)	Layer Thickness (km)	Compressional Velocity (km/sec)	Shear Velocity (km/sec)	Density (gm/cc)	Standard Deviation (km/sec)
1	0.2	0.5	4.30	2.48	2.362	0.134
2	0.8	0.5	4.83	2.79	2.462	0.133
3	1.5	1.0	4.84	2.79	2.465	0.133
4	2.5	1.0	4.86	2.81	2.469	0.131
5	3.5	1.0	4.92	2.84	2.483	0.122
6	4.5	1.0	5.04	2.91	2.509	0.103
7	5.5	1.0	5.23	3.02	2.546	0.075
8	7.0	2.0	5.46	3.15	2.592	0.053
9	9.0	2.0	5.73	3.31	2.646	0.061
10	11.0	2.0	5.95	3.43	2.690	0.079
11	13.0	2.0	6.09	3.52	2.727	0.083
12	16.0	4.0	6.17	3.56	2.750	0.073
13	20.0	4.0	6.23	3.60	2.769	0.051
14	24.0	4.0	6.39	3.69	2.816	0.048
15	28.0	4.0	6.64	3.83	2.886	0.073
16	32.5	5.0	6.92	4.00	2.959	0.111
17	37.5	5.0	7.15	4.13	3.029	0.148
18	42.5	5.0	7.50	4.21	3.140	0.178
19	47.5	5.0	7.56	4.24	3.159	0.197
20	53.0	6.0	7.55	4.24	3.157	0.204
21	59.0	6.0	7.51	4.22	3.144	0.199
22	65.0	6.0	7.47	4.19	3.131	0.184
23	71.0	6.0	7.45	4.18	3.124	0.162
24	77.0	6.0	7.45	4.18	3.123	0.137
25	85.0	10.0	7.47	4.19	3.129	0.112
26	95.0	10.0	7.51	4.21	3.143	0.090

* from the surface to the middle of the layers.

- 142 -
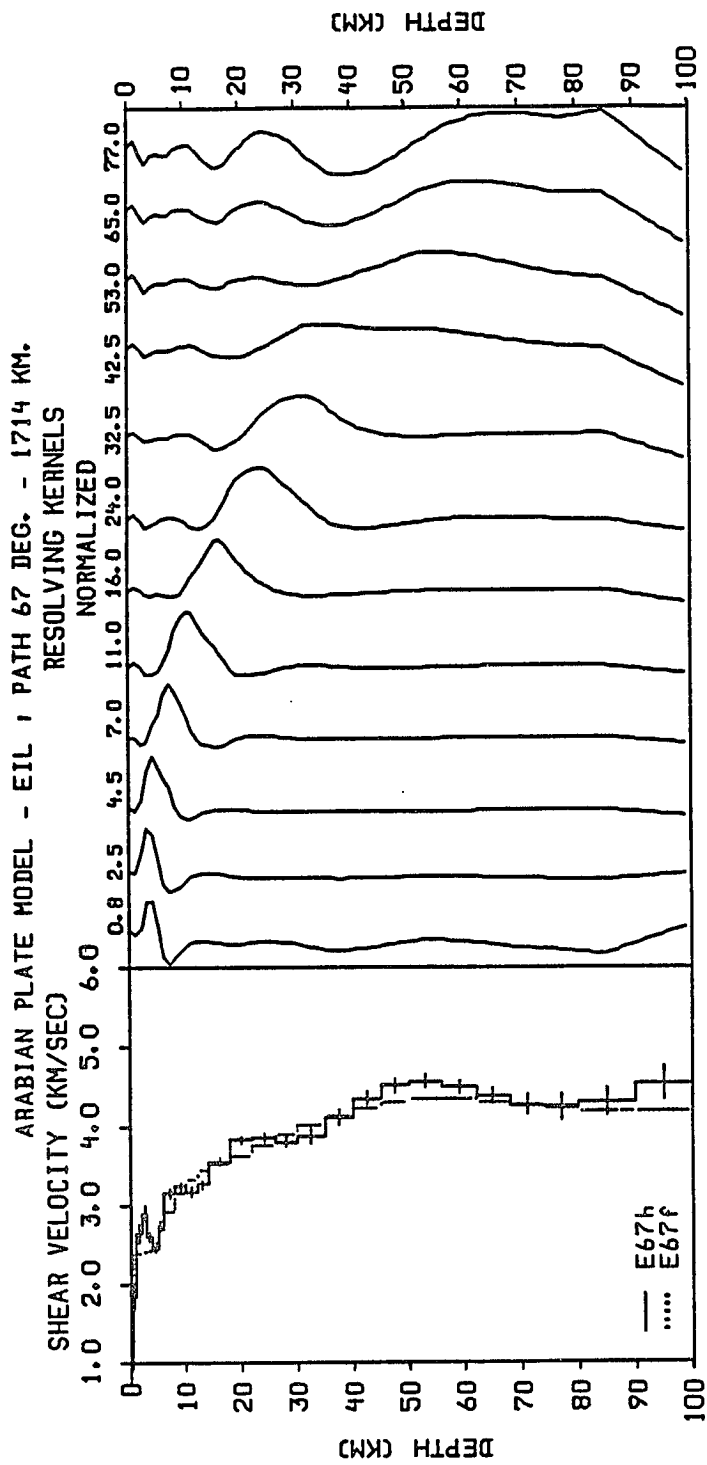
Figure 4.12. Shear velocity model E67h and resolving kernels estimated from the fundamental and first higher-mode Rayleigh waves. The dotted line model E67f is estimated from the fundamental-mode only.

- 143 -

Table 4.19. Crustal velocity structure of the Arabian plate along path E67, derived from fundamental- and higher-mode data.

	Velocity Model E67h					
Layer Number	Layer Depth* (km)	Layer Thickness (km)	Compressional Velocity (km/sec)	Shear Velocity (km/sec)	Density (gm/cc)	Standard Deviation (km/sec)
1	0.2	0.5	1.61	0.93	1.694	0.188
2	0.8	0.5	3.19	1.84	2.181	0.163
3	1.5	1.0	4.58	2.64	2.407	0.126
4	2.5	1.0	5.03	2.90	2.506	0.097
5	3.5	1.0	4.52	2.61	2.395	0.061
6	4.5	1.0	4.24	2.45	2.354	0.038
7	5.5	1.0	4.74	2.74	2.442	0.061
8	7.0	2.0	5.46	3.15	2.591	0.063
9	9.0	2.0	5.61	3.24	2.622	0.053
10	11.0	2.0	5.50	3.17	2.600	0.056
11	13.0	2.0	5.65	3.26	2.629	0.056
12	16.0	4.0	6.15	3.55	2.745	0.058
13	20.0	4.0	6.63	3.83	2.885	0.051
14	24.0	4.0	6.67	3.85	2.894	0.057
15	28.0	4.0	6.59	3.80	2.873	0.073
16	32.5	5.0	6.72	3.88	2.908	0.096
17	37.5	5.0	7.12	4.11	3.018	0.099
18	42.5	5.0	7.75	4.35	3.226	0.093
19	47.5	5.0	8.04	4.51	3.323	0.092
20	53.0	6.0	8.13	4.56	3.356	0.091
21	59.0	6.0	8.02	4.50	3.316	0.088
22	65.0	6.0	7.80	4.38	3.243	0.101
23	71.0	6.0	7.61	4.27	3.179	0.129
24	77.0	6.0	7.55	4.24	3.158	0.160
25	85.0	10.0	7.67	4.30	3.197	0.185
26	95.0	10.0	8.08	4.53	3.338	0.210

* from the surface to the middle of the layers.

Table 4.20. Crustal velocity structure of the Arabian plate along path E67, derived from fundamental-mode data.

			Velocity Model E67f			
Layer Number	Layer Depth* (km)	Layer Thickness (km)	Compressional Velocity (km/sec)	Shear Velocity (km/sec)	Density (gm/cc)	Standard Deviation (km/sec)
1	0.2	0.5	3.61	2.08	2.249	0.097
2	0.8	0.5	4.14	2.39	2.339	0.094
3	1.5	1.0	4.15	2.39	2.340	0.091
4	2.5	1.0	4.15	2.40	2.342	0.068
5	3.5	1.0	4.21	2.43	2.350	0.034
6	4.5	1.0	4.38	2.53	2.373	0.041
7	5.5	1.0	4.66	2.69	2.426	0.057
8	7.0	2.0	5.04	2.91	2.507	0.055
9	9.0	2.0	5.44	3.14	2.588	0.045
10	11.0	2.0	5.75	3.32	2.649	0.052
11	13.0	2.0	5.95	3.43	2.690	0.049
12	16.0	4.0	6.10	3.52	2.731	0.051
13	20.0	4.0	6.28	3.63	2.785	0.063
14	24.0	4.0	6.51	3.76	2.852	0.079
15	28.0	4.0	6.73	3.89	2.911	0.094
16	32.5	5.0	6.94	4.01	2.965	0.105
17	37.5	5.0	7.13	4.12	3.023	0.105
18	42.5	5.0	7.51	4.22	3.145	0.102
19	47.5	5.0	7.65	4.30	3.192	0.107
20	53.0	6.0	7.73	4.34	3.219	0.125
21	59.0	6.0	7.74	4.34	3.221	0.153
22	65.0	6.0	7.68	4.31	3.203	0.186
23	71.0	6.0	7.60	4.27	3.175	0.218
24	77.0	6.0	7.52	4.22	3.148	0.247
25	85.0	10.0	7.47	4.19	3.130	0.270
26	95.0	10.0	7.47	4.20	3.132	0.275

* from the surface to the middle of the layers.

Figure 4.13. Shear velocity model E84h and resolving kernels estimated from the fundamental and first higher-mode Rayleigh waves. The dotted line model E84f is estimated from the fundamental-mode only.

- 146 -

Table 4.21. Crustal velocity structure of the Arabian plate along path E84, derived from fundamental- and higher-mode data.

	Velocity Model E84h					
Layer Number	Layer Depth* (km)	Layer Thickness (km)	Compressional Velocity (km/sec)	Shear Velocity (km/sec)	Density (gm/cc)	Standard Deviation (km/sec)
1	0.2	0.5	3.13	1.80	2.170	0.185
2	0.8	0.5	4.01	2.32	2.322	0.149
3	1.5	1.0	4.58	2.65	2.408	0.104
4	2.5	1.0	5.00	2.89	2.500	0.071
5	3.5	1.0	5.07	2.92	2.513	0.045
6	4.5	1.0	4.99	2.88	2.498	0.044
7	5.5	1.0	5.04	2.91	2.508	0.054
8	7.0	2.0	5.32	3.07	2.565	0.056
9	9.0	2.0	5.78	3.34	2.656	0.051
10	11.0	2.0	6.00	3.47	2.701	0.059
11	13.0	2.0	6.03	3.48	2.710	0.058
12	16.0	4.0	6.09	3.51	2.726	0.068
13	20.0	4.0	6.45	3.72	2.835	0.057
14	24.0	4.0	6.81	3.93	2.929	0.056
15	28.0	4.0	6.94	4.01	2.964	0.075
16	32.5	5.0	7.05	4.07	2.997	0.099
17	37.5	5.0	7.42	4.29	3.116	0.110
18	42.5	5.0	8.19	4.60	3.380	0.119
19	47.5	5.0	8.69	4.88	3.553	0.139
20	53.0	6.0	8.98	5.04	3.654	0.169
21	59.0	6.0	9.06	5.09	3.684	0.204
22	65.0	6.0	9.02	5.07	3.669	0.236
23	71.0	6.0	8.97	5.04	3.650	0.260
24	77.0	6.0	8.96	5.03	3.646	0.273
25	85.0	10.0	9.00	5.05	3.661	0.276
26	95.0	10.0	9.12	5.12	3.708	0.270

* from the surface to the middle of the layers.

Table 4.22. Crustal velocity structure of the Arabian plate along path E84, derived from fundamental-mode data.

			Velocity Model E84f			
Layer Number	Layer Depth* (km)	Layer Thickness (km)	Compressional Velocity (km/sec)	Shear Velocity (km/sec)	Density (gm/cc)	Standard Deviation (km/sec)
1	0.2	0.5	4.08	2.36	2.332	0.095
2	0.8	0.5	4.61	2.66	2.415	0.093
3	1.5	1.0	4.63	2.67	2.418	0.089
4	2.5	1.0	4.66	2.69	2.425	0.058
5	3.5	1.0	4.73	2.73	2.440	0.023
6	4.5	1.0	4.85	2.80	2.467	0.050
7	5.5	1.0	5.02	2.90	2.504	0.069
8	7.0	2.0	5.23	3.02	2.546	0.069
9	9.0	2.0	5.51	3.18	2.601	0.057
10	11.0	2.0	5.80	3.35	2.661	0.058
11	13.0	2.0	6.06	3.50	2.717	0.053
12	16.0	4.0	6.22	3.59	2.767	0.055
13	20.0	4.0	6.26	3.61	2.778	0.070
14	24.0	4.0	6.37	3.68	2.812	0.081
15	28.0	4.0	6.66	3.84	2.891	0.080
16	32.5	5.0	7.06	4.08	2.999	0.078
17	37.5	5.0	7.47	4.32	3.132	0.084
18	42.5	5.0	8.04	4.51	3.325	0.104
19	47.5	5.0	8.31	4.66	3.420	0.134
20	53.0	6.0	8.49	4.76	3.486	0.170
21	59.0	6.0	8.59	4.82	3.520	0.205
22	65.0	6.0	8.62	4.84	3.530	0.232
23	71.0	6.0	8.59	4.82	3.520	0.245
24	77.0	6.0	8.51	4.78	3.494	0.245
25	85.0	10.0	8.40	4.72	3.454	0.232
26	95.0	10.0	8.26	4.64	3.405	0.202

* from the surface to the middle of the layers.
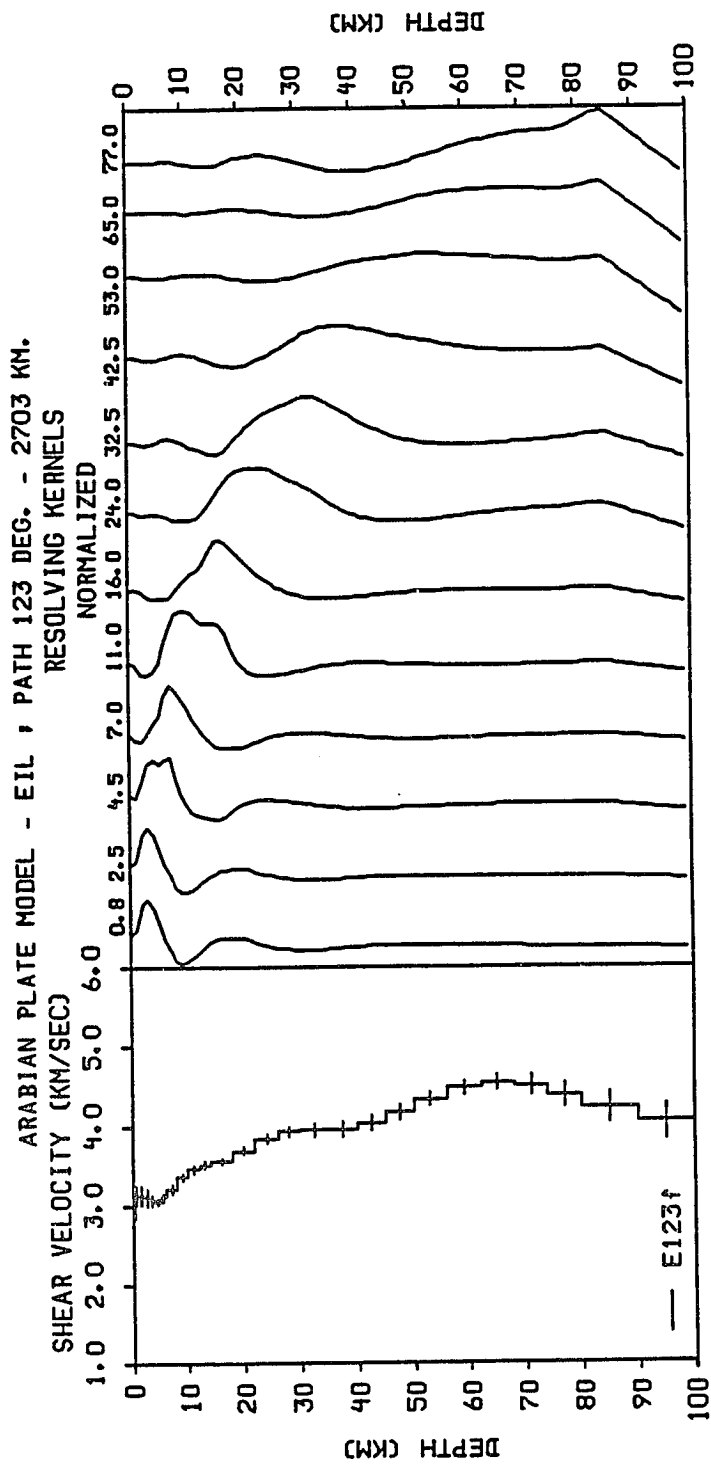
Figure 4.14. Shear velocity model E123f and resolving kernels estimated from fundamental-mode Rayleigh waves.

- 149 -

Table 4.23. Crustal velocity structure of the Arabian plate along path E123, derived from fundamental-mode data.

Layer Number	Layer Depth* (km)	Layer Thickness (km)	Compressional Velocity (km/sec)	Shear Velocity (km/sec)	Density (gm/cc)	Standard Deviation (km/sec)
1	0.2	0.5	4.90	2.83	2.478	0.125
2	0.8	0.5	5.43	3.13	2.585	0.124
3	1.5	1.0	5.42	3.13	2.585	0.120
4	2.5	1.0	5.37	3.10	2.575	0.102
5	3.5	1.0	5.31	3.06	2.561	0.067
6	4.5	1.0	5.29	3.06	2.559	0.044
7	5.5	1.0	5.38	3.11	2.577	0.050
8	7.0	2.0	5.57	3.22	2.614	0.060
9	9.0	2.0	5.82	3.36	2.663	0.050
10	11.0	2.0	5.98	3.46	2.697	0.049
11	13.0	2.0	6.07	3.51	2.722	0.049
12	16.0	4.0	6.16	3.56	2.748	0.044
13	20.0	4.0	6.38	3.69	2.815	0.043
14	24.0	4.0	6.65	3.84	2.889	0.058
15	28.0	4.0	6.81	3.93	2.929	0.072
16	32.5	5.0	6.84	3.95	2.939	0.087
17	37.5	5.0	6.86	3.96	2.943	0.099
18	42.5	5.0	7.18	4.03	3.036	0.101
19	47.5	5.0	7.42	4.16	3.114	0.092
20	53.0	6.0	7.72	4.33	3.214	0.082
21	59.0	6.0	7.97	4.47	3.299	0.084
22	65.0	6.0	8.08	4.53	3.338	0.101
23	71.0	6.0	8.02	4.50	3.318	0.126
24	77.0	6.0	7.82	4.39	3.250	0.157
25	85.0	10.0	7.53	4.23	3.151	0.192
26	95.0	10.0	7.21	4.05	3.046	0.230

* from the surface to the middle of the layers.
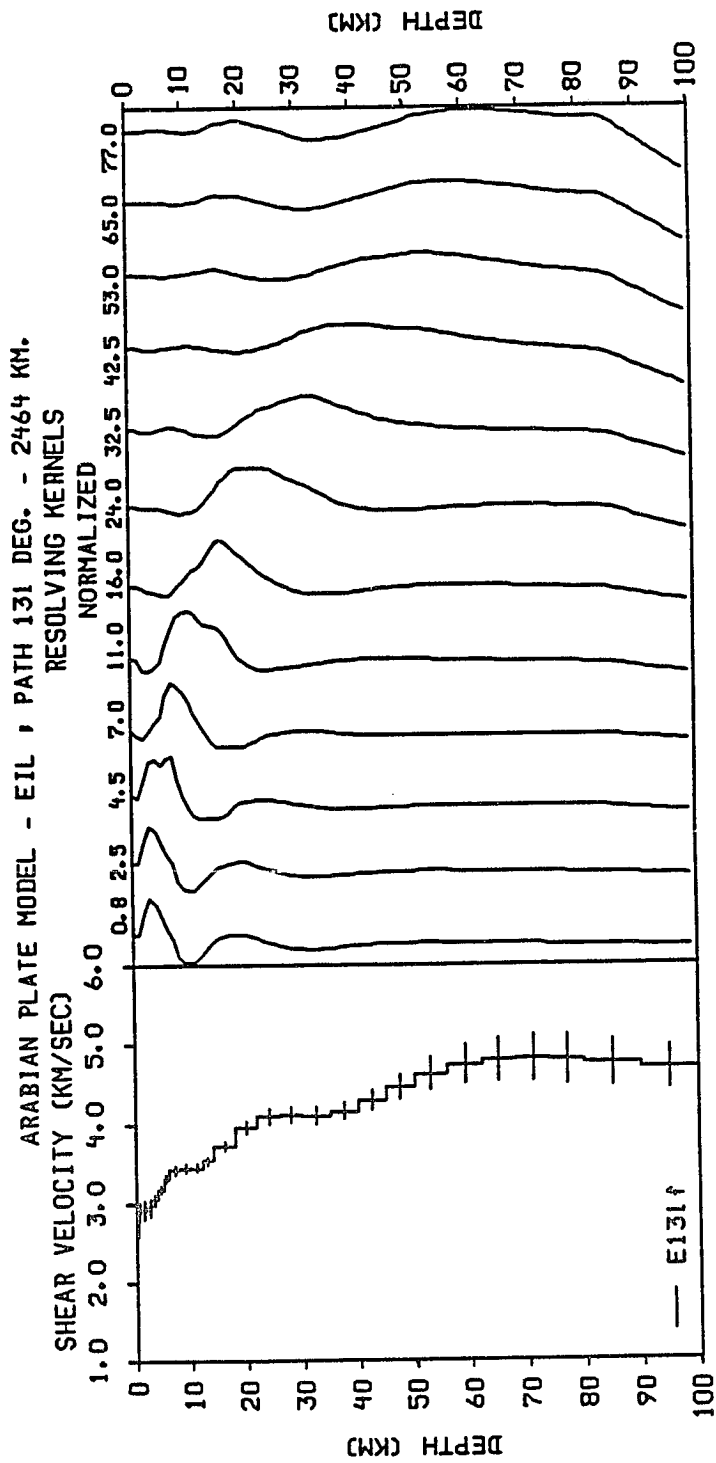
Figure 4.15. Shear velocity model E131f and resolving kernels estimated from fundamental-mode Rayleigh waves.

- 151 -

Table 4.24. Crustal velocity structure of the Arabian plate along path E131, derived from fundamental-mode data.

	Velocity Model E131f					
Layer Number	Layer Depth* (km)	Layer Thickness (km)	Compressional Velocity (km/sec)	Shear Velocity (km/sec)	Density (gm/cc)	Standard Deviation (km/sec)
1	0.2	0.5	4.49	2.59	2.388	0.119
2	0.8	0.5	5.02	2.90	2.504	0.118
3	1.5	1.0	5.04	2.91	2.507	0.117
4	2.5	1.0	5.11	2.95	2.522	0.104
5	3.5	1.0	5.27	3.05	2.555	0.074
6	4.5	1.0	5.51	3.18	2.601	0.045
7	5.5	1.0	5.74	3.31	2.648	0.046
8	7.0	2.0	5.92	3.42	2.685	0.062
9	9.0	2.0	5.96	3.44	2.693	0.055
10	11.0	2.0	5.98	3.45	2.696	0.049
11	13.0	2.0	6.12	3.53	2.737	0.052
12	16.0	4.0	6.43	3.71	2.829	0.058
13	20.0	4.0	6.86	3.96	2.943	0.075
14	24.0	4.0	7.09	4.09	3.009	0.097
15	28.0	4.0	7.12	4.11	3.017	0.107
16	32.5	5.0	7.10	4.10	3.011	0.107
17	37.5	5.0	7.19	4.15	3.041	0.109
18	42.5	5.0	7.64	4.29	3.188	0.125
19	47.5	5.0	7.95	4.46	3.294	0.157
20	53.0	6.0	8.24	4.63	3.397	0.198
21	59.0	6.0	8.45	4.74	3.471	0.240
22	65.0	6.0	8.55	4.80	3.507	0.274
23	71.0	6.0	8.57	4.81	3.514	0.297
24	77.0	6.0	8.54	4.79	3.503	0.306
25	85.0	10.0	8.47	4.75	3.480	0.300
26	95.0	10.0	8.38	4.70	3.447	0.274

* from the surface to the middle of the layers.

Moho seems to be low. According to model E30f, the velocity at the top of the upper mantle is about 4.02 km/sec, which is slightly lower than that obtained for model E30h. The actual velocity structure within the upper mantle probably resembles that of the fundamental-mode model.

Models E67h and E67f, shown in Figure 4.12, sample the north central region of the plate. Its path mostly traverses the Arabian platform and Mesopotamian foredeep, and runs roughly parallel to T228. A clear difference between the two models is that, E67h exhibits sharper boundaries due to the inclusion of higher-mode data in the inversion process. Models E67f and T228, on the other hand, show similar gradual increase of velocity with depth. According to model E67h, the crystalline basement, the Conrad and Moho discontinuities are located at depths of 6.0, 18.0 and 40.0 km, respectively. The shear velocity within the upper and lower crust varies very little. In the upper crust the velocity range is 3.15-3.55 km/sec, and in the lower crust it is 3.83-4.35 km/sec. The upper mantle velocity varies between 4.24-4.56 km/sec. Also, model E67f indicates that the sedimentary layer velocity seems to increase from 2.08 km/sec near the surface to about 2.74 km/sec at the top of the basement.

Models E84h and E84f, shown in Figure 4.13, also sample the north central region of the plate in an almost E-W direction. The path for these models almost coincides with S267. Although, the fundamental-mode models (i.e., E84f and S267f) show very similar gradual increase of velocity with depth, including higher-mode data in the inversion of model E84h seems to enhance the definition of crustal layers, but exaggerates the upper mantle velocities. This increase of velocity in the upper mantle is due to the limited period range of higher-mode data. Model E84f shows the shear

velocity in the upper mantle to vary between 8.04 km/sec and 8.62 km/sec. According to model E84h, the basement is overlain by about 8.0 km of sediments, whereas the Conrad and Moho discontinuities are located at about 20.0 km and 40-45 km depth, respectively. The velocity of the sedimentary layer increases from a very low 1.80 km/sec to 2.91 km/sec. Within the upper crust the shear velocity range is 3.07-3.72 km/sec, and in the lower crust the velocity range is 3.93-4.60 km/sec.

Model E123f, presented in Figure 4.14, is one of the few models whose path traverses the Arabian shield and platform, but not the Mesopotamian foredeep. It is unfortunate that no reliable higher-mode data are available along this path. Nevertheless, the fundamental-mode data seem to show subtle variation between the major layers of the model. The sedimentary layer does not seem to exceed 5.0 km depth, and the shear velocity within this layer is markedly higher, 2.83-3.06 km/sec, than previously seen in other models. The upper crust is characterized by a gradual increase in velocity from 3.11 km/sec to 3.69 km/sec at the top of the Conrad discontinuity, which is observed at 18.0 km depth. In contrast, the lower crust exhibits an almost constant velocity, it varies between 3.84-3.96 km/sec. Below the Moho discontinuity, which is observed at depth of about 37.0-40 km, the velocity increases from a relatively low 4.03 km/sec to a maximum of 4.53 km/sec. The apparent low-velocity layer within the upper mantle is probably questionable, and it may be due to low resolution at that depth.

Model E131f is presented in Figure 4.15. This is another of those models whose path traverses a significant portion of the Arabian shield and a smaller region of the Arabian platform. A thin layer of sediments, whose

thickness does not seem to exceed 3.0 km, is observed in this model. The velocity in this layer increases from 2.59 km/sec near the surface to 2.95 km/sec. The top of the crystalline basement is marked a gradual increase in velocity from 3.05 km/sec to 3.31 km/sec at depth of about 5.0 km. Below this depth the upper crust velocity changes very little. It increases from 3.42 km/sec to 3.96 km/sec at 20.0 km, where the Conrad discontinuity is observed. Within the lower crust the velocity also changes very little. The shear velocity range in this layer is 4.09-4.46 km/sec, which places the Moho discontinuity at about 40.0-45.0 km depth. In contrast with model E123f, the velocities in the upper mantle increase from 4.63 km/sec to 4.81 km/sec, and shows no conclusive evidence for the existence of a low-velocity layer at this depth.

4.2.4 JER Station Models

The shear velocity models along paths J54, J89, J127 and J147 are presented in Figures 4.16 through 4.19, and the parameters for these models are listed in Tables 4.25-4.32. Although, the quality of JER station data is lower than that of the other stations, the major discontinuities and characteristics of the shear velocity structures along each path can still be estimated from the models.

Models J54h and J54f are presented in Figure 4.16. Similar to E30 and E67, the path for these models traverses the north part of the Arabian plate, including the Arabian platform and Mesopotamian foredeep. The models obtained from inversion seem to indicate that the basement is covered by about 6.0-7.0 km of sediments, where the velocity increases with depth from 1.93 km/sec to 2.83 km/sec. The Conrad and Moho
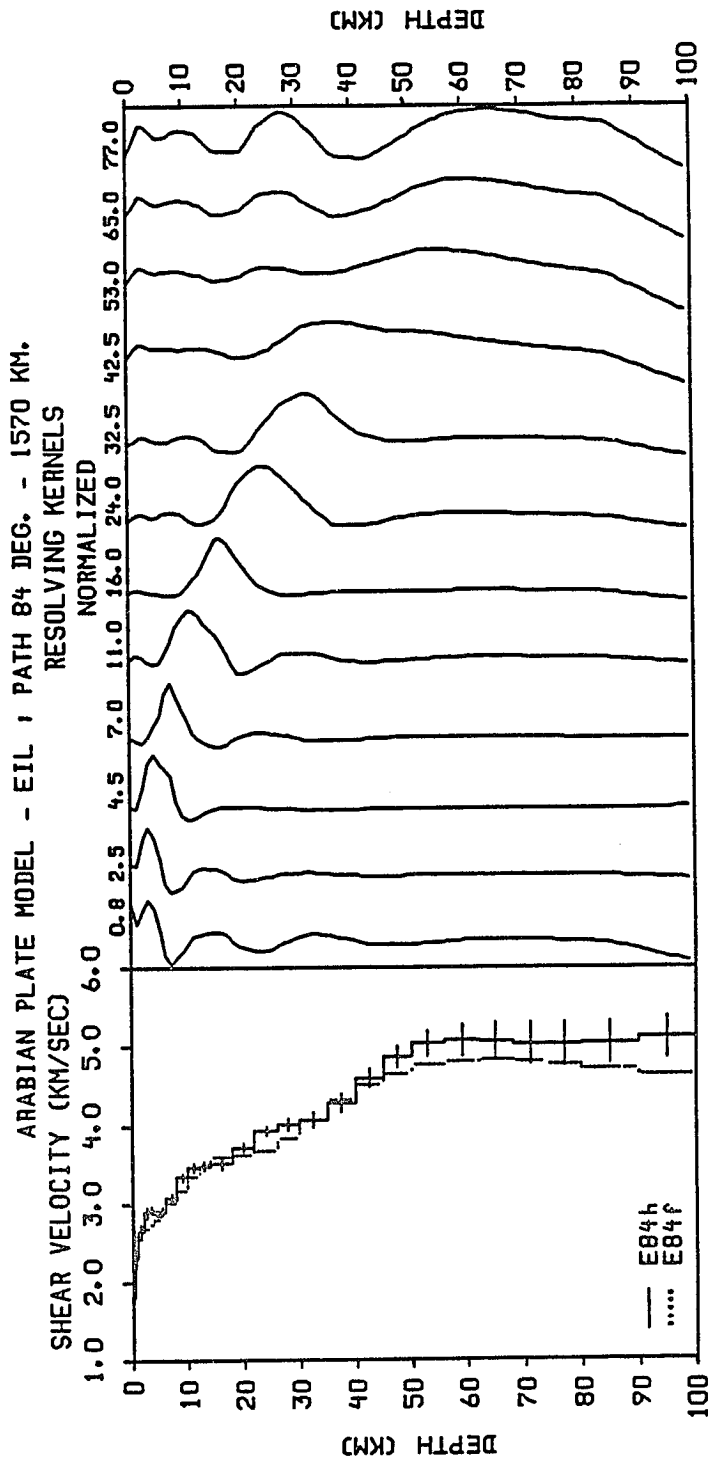
Figure 4.16. Shear velocity model J54h and resolving kernels estimated from the fundamental and first higher-mode Rayleigh waves. The dotted line model J54f is estimated from the fundamental-mode only.

- 156 -

Table 4.25. Crustal velocity structure of the Arabian plate along path J54, derived from fundamental- and higher-mode data.

Velocity Model J54h						
Layer Number	Layer Depth* (km)	Layer Thickness (km)	Compressional Velocity (km/sec)	Shear Velocity (km/sec)	Density (gm/cc)	Standard Deviation (km/sec)
1	0.2	0.5	3.34	1.93	2.204	0.191
2	0.8	0.5	4.26	2.46	2.356	0.173
3	1.5	1.0	4.84	2.80	2.466	0.149
4	2.5	1.0	5.29	3.05	2.557	0.126
5	3.5	1.0	5.32	3.07	2.563	0.100
6	4.5	1.0	5.04	2.91	2.507	0.068
7	5.5	1.0	4.77	2.76	2.450	0.052
8	7.0	2.0	4.90	2.83	2.477	0.064
9	9.0	2.0	5.85	3.38	2.669	0.061
10	11.0	2.0	6.44	3.72	2.832	0.061
11	13.0	2.0	6.38	3.68	2.814	0.058
12	16.0	4.0	6.11	3.53	2.733	0.064
13	20.0	4.0	6.26	3.61	2.777	0.073
14	24.0	4.0	6.61	3.82	2.878	0.092
15	28.0	4.0	6.85	3.95	2.941	0.104
16	32.5	5.0	6.96	4.02	2.970	0.113
17	37.5	5.0	7.03	4.06	2.988	0.126
18	42.5	5.0	7.34	4.12	3.088	0.142
19	47.5	5.0	7.50	4.21	3.141	0.161
20	53.0	6.0	7.68	4.31	3.202	0.185
21	59.0	6.0	7.83	4.39	3.251	0.210
22	65.0	6.0	7.91	4.44	3.279	0.234
23	71.0	6.0	7.93	4.45	3.285	0.253
24	77.0	6.0	7.90	4.43	3.276	0.268
25	85.0	10.0	7.84	4.40	3.257	0.282
26	95.0	10.0	7.77	4.36	3.231	0.296

* from the surface to the middle of the layers.

Table 4.26. Crustal velocity structure of the Arabian plate along path J54, derived from fundamental-mode data.

Velocity Model J54f						
Layer Number	Layer Depth* (km)	Layer Thickness (km)	Compressional Velocity (km/sec)	Shear Velocity (km/sec)	Density (gm/cc)	Standard Deviation (km/sec)
1	0.2	0.5	3.68	2.13	2.263	0.142
2	0.8	0.5	4.22	2.43	2.350	0.142
3	1.5	1.0	4.23	2.44	2.353	0.142
4	2.5	1.0	4.29	2.48	2.361	0.135
5	3.5	1.0	4.47	2.58	2.386	0.110
6	4.5	1.0	4.79	2.76	2.453	0.076
7	5.5	1.0	5.20	3.00	2.539	0.058
8	7.0	2.0	5.63	3.25	2.625	0.073
9	9.0	2.0	5.93	3.43	2.687	0.081
10	11.0	2.0	6.06	3.50	2.718	0.079
11	13.0	2.0	6.10	3.52	2.731	0.076
12	16.0	4.0	6.19	3.57	2.757	0.076
13	20.0	4.0	6.50	3.75	2.851	0.076
14	24.0	4.0	6.91	3.99	2.956	0.088
15	28.0	4.0	7.22	4.17	3.049	0.099
16	32.5	5.0	7.38	4.26	3.101	0.104
17	37.5	5.0	7.40	4.27	3.109	0.111
18	42.5	5.0	7.61	4.27	3.179	0.130
19	47.5	5.0	7.66	4.30	3.195	0.163
20	53.0	6.0	7.79	4.37	3.238	0.202
21	59.0	6.0	7.99	4.48	3.307	0.241
22	65.0	6.0	8.22	4.62	3.390	0.270
23	71.0	6.0	8.43	4.73	3.466	0.288
24	77.0	6.0	8.59	4.82	3.521	0.292
25	85.0	10.0	8.68	4.87	3.551	0.284
26	95.0	10.0	8.66	4.86	3.543	0.259

* from the surface to the middle of the layers.

- 158 -

Figure 4.17. Shear velocity model J89h and resolving kernels estimated from the fundamental and first higher-mode Rayleigh waves. The dotted line model J89f is estimated from the fundamental-mode only.

- 159 -

Table 4.27. Crustal velocity structure of the Arabian plate along path J89,
derived from fundamental- and higher-mode data.

Velocity Model J89h						
Layer Number	Layer Depth* (km)	Layer Thickness (km)	Compressional Velocity (km/sec)	Shear Velocity (km/sec)	Density (gm/cc)	Standard Deviation (km/sec)
1	0.2	0.5	1.68	0.97	1.723	0.135
2	0.8	0.5	2.48	1.43	2.043	0.107
3	1.5	1.0	4.12	2.38	2.336	0.090
4	2.5	1.0	5.30	3.06	2.559	0.084
5	3.5	1.0	4.86	2.80	2.469	0.081
6	4.5	1.0	4.34	2.51	2.367	0.061
7	5.5	1.0	4.73	2.73	2.440	0.052
8	7.0	2.0	5.34	3.08	2.567	0.059
9	9.0	2.0	5.52	3.18	2.603	0.057
10	11.0	2.0	5.72	3.30	2.643	0.060
11	13.0	2.0	6.01	3.47	2.704	0.055
12	16.0	4.0	6.19	3.57	2.757	0.051
13	20.0	4.0	6.17	3.56	2.752	0.052
14	24.0	4.0	6.40	3.70	2.820	0.058
15	28.0	4.0	6.73	3.89	2.910	0.063
16	32.5	5.0	6.92	4.00	2.960	0.069
17	37.5	5.0	7.01	4.05	2.984	0.071
18	42.5	5.0	7.45	4.18	3.124	0.076
19	47.5	5.0	7.87	4.42	3.265	0.088
20	53.0	6.0	8.27	4.64	3.407	0.106
21	59.0	6.0	8.42	4.73	3.460	0.127
22	65.0	6.0	8.29	4.65	3.415	0.149
23	71.0	6.0	8.05	4.52	3.329	0.161
24	77.0	6.0	7.88	4.42	3.269	0.155
25	85.0	10.0	7.83	4.39	3.251	0.124
26	95.0	10.0	7.78	4.37	3.236	0.071

* from the surface to the middle of the layers.

Table 4.28. Crustal velocity structure of the Arabian plate along path J89, derived from fundamental-mode data.

Velocity Model J89f						
Layer Number	Layer Depth* (km)	Layer Thickness (km)	Compressional Velocity (km/sec)	Shear Velocity (km/sec)	Density (gm/cc)	Standard Deviation (km/sec)
1	0.2	0.5	3.52	2.03	2.234	0.117
2	0.8	0.5	4.05	2.34	2.327	0.114
3	1.5	1.0	4.08	2.35	2.331	0.101
4	2.5	1.0	4.09	2.36	2.333	0.060
5	3.5	1.0	4.14	2.39	2.340	0.061
6	4.5	1.0	4.33	2.50	2.366	0.070
7	5.5	1.0	4.69	2.71	2.431	0.064
8	7.0	2.0	5.14	2.97	2.529	0.066
9	9.0	2.0	5.56	3.21	2.613	0.065
10	11.0	2.0	5.84	3.37	2.669	0.062
11	13.0	2.0	6.03	3.48	2.708	0.059
12	16.0	4.0	6.17	3.56	2.751	0.066
13	20.0	4.0	6.32	3.65	2.796	0.079
14	24.0	4.0	6.51	3.76	2.852	0.094
15	28.0	4.0	6.75	3.89	2.914	0.101
16	32.5	5.0	7.02	4.05	2.986	0.103
17	37.5	5.0	7.30	4.22	3.076	0.107
18	42.5	5.0	7.76	4.36	3.229	0.122
19	47.5	5.0	7.95	4.46	3.294	0.147
20	53.0	6.0	8.08	4.54	3.339	0.181
21	59.0	6.0	8.15	4.57	3.363	0.219
22	65.0	6.0	8.18	4.59	3.373	0.253
23	71.0	6.0	8.18	4.59	3.374	0.279
24	77.0	6.0	8.17	4.58	3.370	0.294
25	85.0	10.0	8.15	4.57	3.363	0.297
26	95.0	10.0	8.12	4.56	3.352	0.279

* from the surface to the middle of the layers.

- 161 -
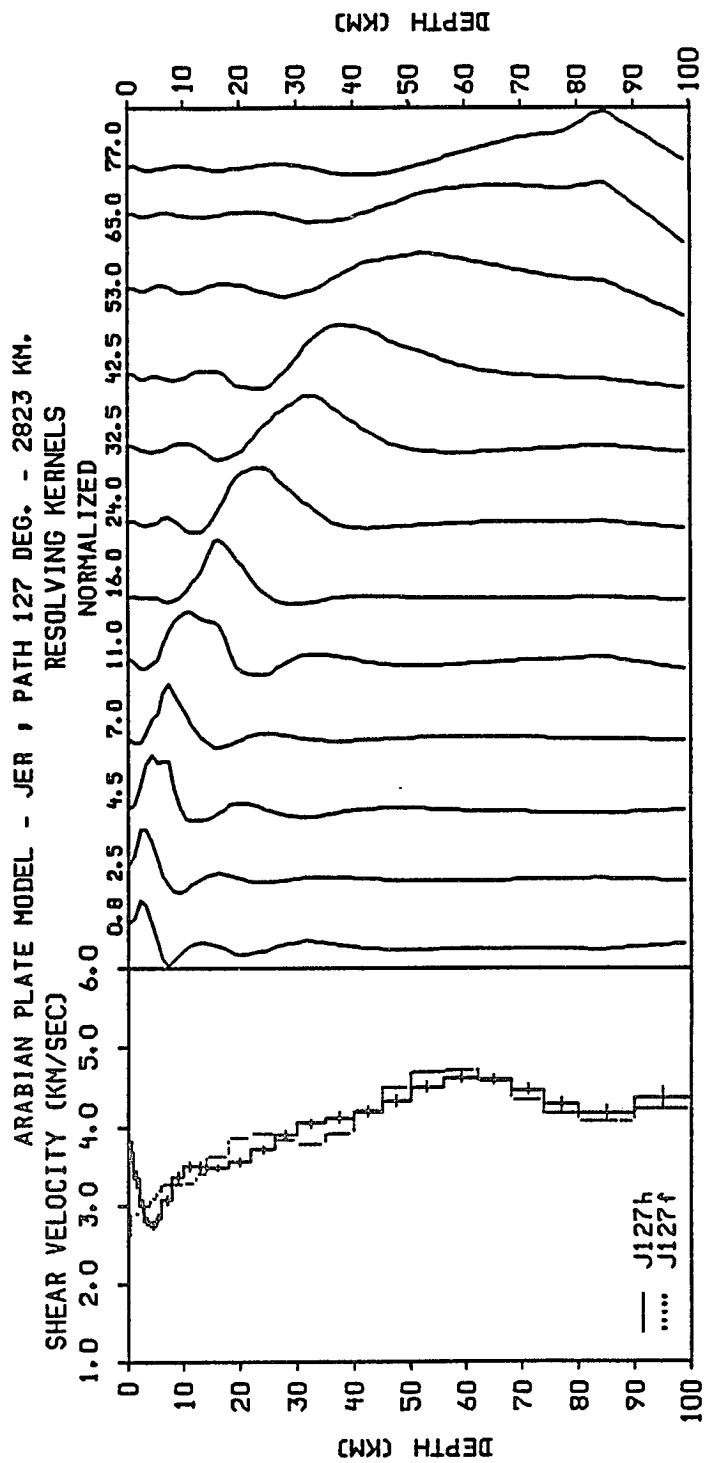
Figure 4.18. Shear velocity model J127h and resolving kernels estimated from the fundamental and first higher-mode Rayleigh waves. The dotted line model J127f is estimated from the fundamental-mode only.

- 162 -

Table 4.29. Crustal velocity structure of the Arabian plate along path J127, derived from fundamental- and higher-mode data.

	Velocity Model J127h					
Layer Number	Layer Depth* (km)	Layer Thickness (km)	Compressional Velocity (km/sec)	Shear Velocity (km/sec)	Density (gm/cc)	Standard Deviation (km/sec)
1	0.2	0.5	6.22	3.59	2.765	0.153
2	0.8	0.5	6.37	3.68	2.812	0.132
3	1.5	1.0	5.78	3.34	2.656	0.104
4	2.5	1.0	5.20	3.00	2.540	0.072
5	3.5	1.0	4.85	2.80	2.467	0.049
6	4.5	1.0	4.76	2.75	2.446	0.050
7	5.5	1.0	4.92	2.84	2.483	0.053
8	7.0	2.0	5.32	3.07	2.564	0.056
9	9.0	2.0	5.82	3.36	2.664	0.057
10	11.0	2.0	6.05	3.50	2.716	0.058
11	13.0	2.0	6.07	3.50	2.720	0.053
12	16.0	4.0	6.03	3.48	2.710	0.047
13	20.0	4.0	6.15	3.55	2.746	0.044
14	24.0	4.0	6.43	3.71	2.828	0.049
15	28.0	4.0	6.75	3.90	2.915	0.051
16	32.5	5.0	7.00	4.04	2.980	0.056
17	37.5	5.0	7.13	4.11	3.020	0.065
18	42.5	5.0	7.47	4.19	3.131	0.073
19	47.5	5.0	7.72	4.33	3.215	0.074
20	53.0	6.0	8.02	4.50	3.317	0.070
21	59.0	6.0	8.22	4.62	3.390	0.061
22	65.0	6.0	8.20	4.60	3.382	0.058
23	71.0	6.0	7.96	4.47	3.296	0.067
24	77.0	6.0	7.63	4.29	3.186	0.082
25	85.0	10.0	7.42	4.17	3.115	0.097
26	95.0	10.0	7.78	4.37	3.237	0.128

* from the surface to the middle of the layers.

Table 4.30. Crustal velocity structure of the Arabian plate along path J127, derived from fundamental-mode data.

Velocity Model J127f						
Layer Number	Layer Depth* (km)	Layer Thickness (km)	Compressional Velocity (km/sec)	Shear Velocity (km/sec)	Density (gm/cc)	Standard Deviation (km/sec)
1	0.2	0.5	4.46	2.58	2.385	0.136
2	0.8	0.5	4.99	2.88	2.498	0.134
3	1.5	1.0	5.00	2.89	2.500	0.130
4	2.5	1.0	5.05	2.92	2.511	0.106
5	3.5	1.0	5.19	2.99	2.537	0.065
6	4.5	1.0	5.37	3.10	2.573	0.053
7	5.5	1.0	5.53	3.19	2.607	0.071
8	7.0	2.0	5.65	3.26	2.630	0.077
9	9.0	2.0	5.66	3.27	2.633	0.060
10	11.0	2.0	5.71	3.30	2.642	0.064
11	13.0	2.0	5.91	3.41	2.682	0.063
12	16.0	4.0	6.28	3.63	2.785	0.060
13	20.0	4.0	6.68	3.85	2.896	0.060
14	24.0	4.0	6.77	3.91	2.920	0.065
15	28.0	4.0	6.63	3.83	2.885	0.070
16	32.5	5.0	6.55	3.78	2.862	0.084
17	37.5	5.0	6.78	3.91	2.922	0.099
18	42.5	5.0	7.48	4.20	3.134	0.104
19	47.5	5.0	8.02	4.50	3.317	0.096
20	53.0	6.0	8.38	4.70	3.446	0.079
21	59.0	6.0	8.40	4.71	3.454	0.063
22	65.0	6.0	8.14	4.57	3.360	0.067
23	71.0	6.0	7.75	4.35	3.225	0.086
24	77.0	6.0	7.41	4.16	3.112	0.113
25	85.0	10.0	7.26	4.07	3.063	0.153
26	95.0	10.0	7.51	4.22	3.144	0.209

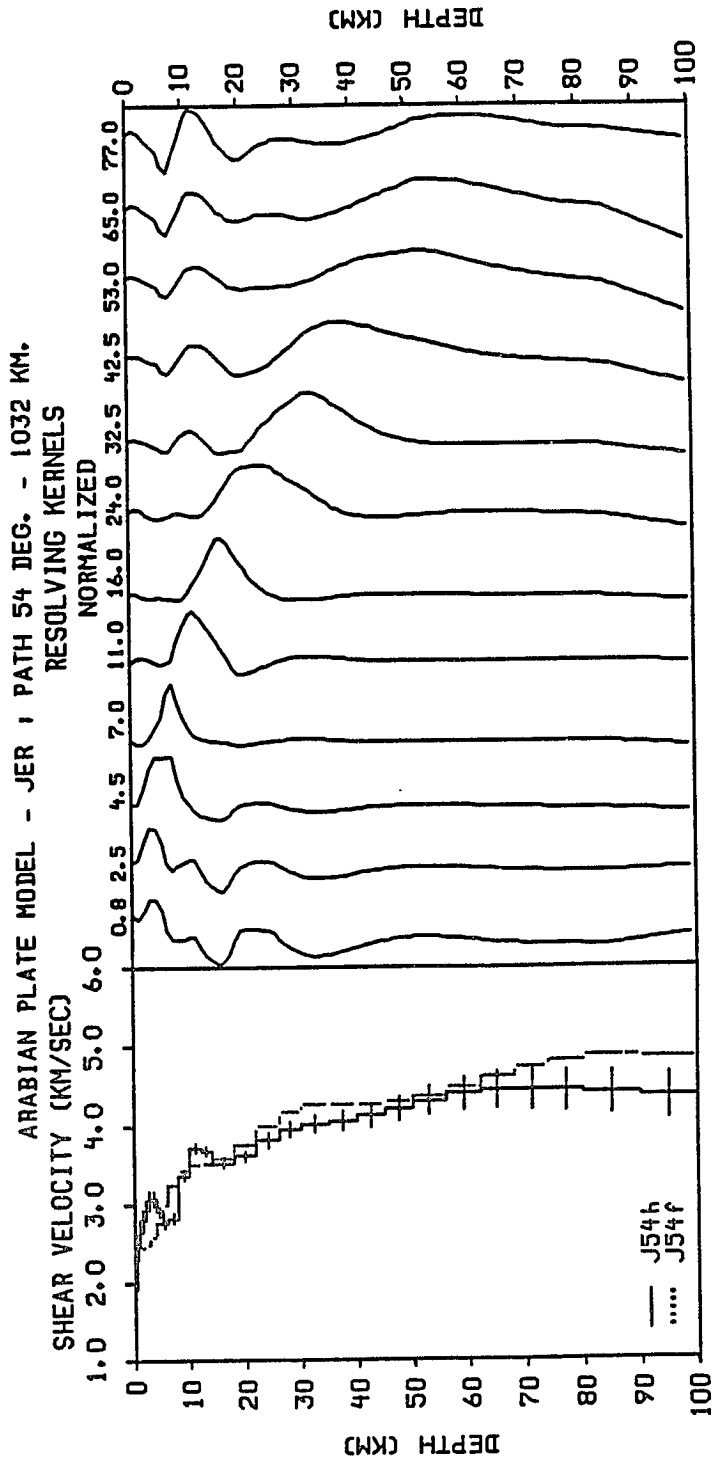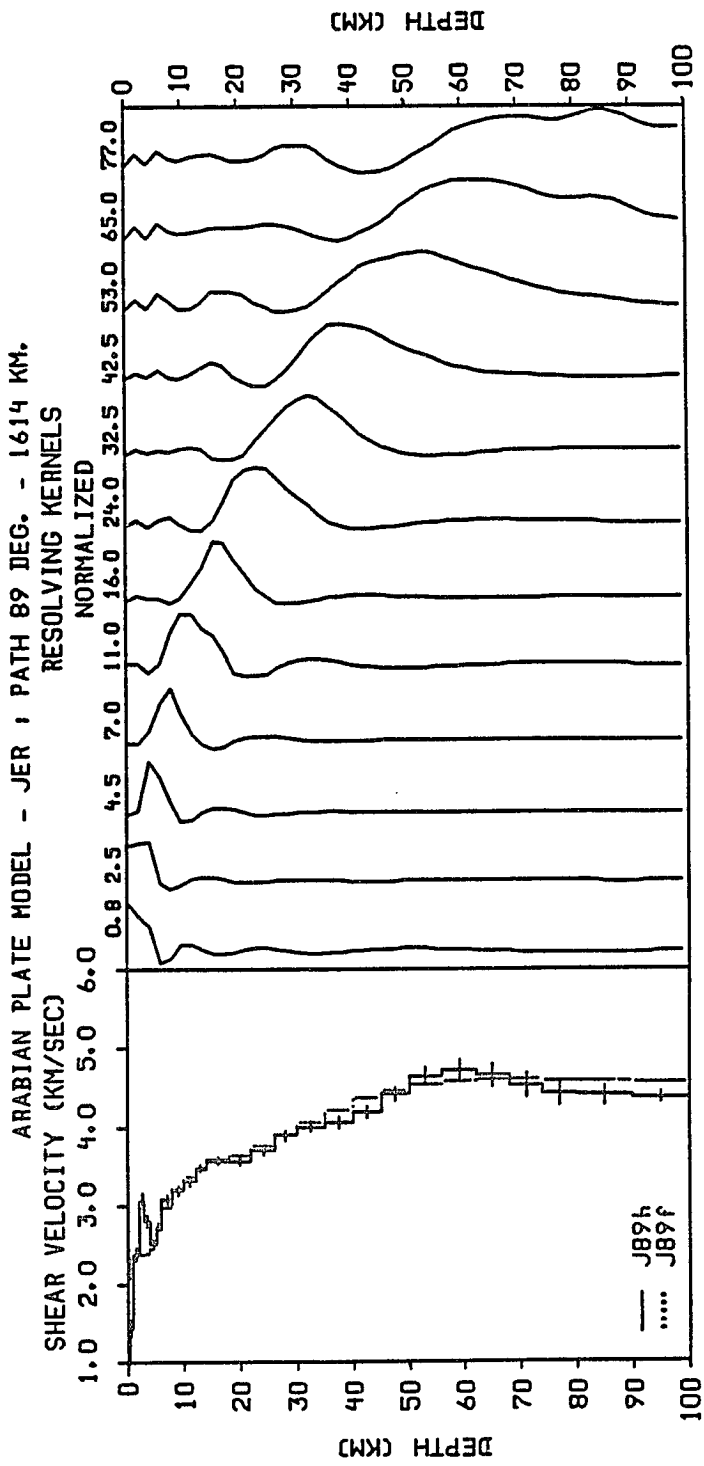* from the surface to the middle of the layers.
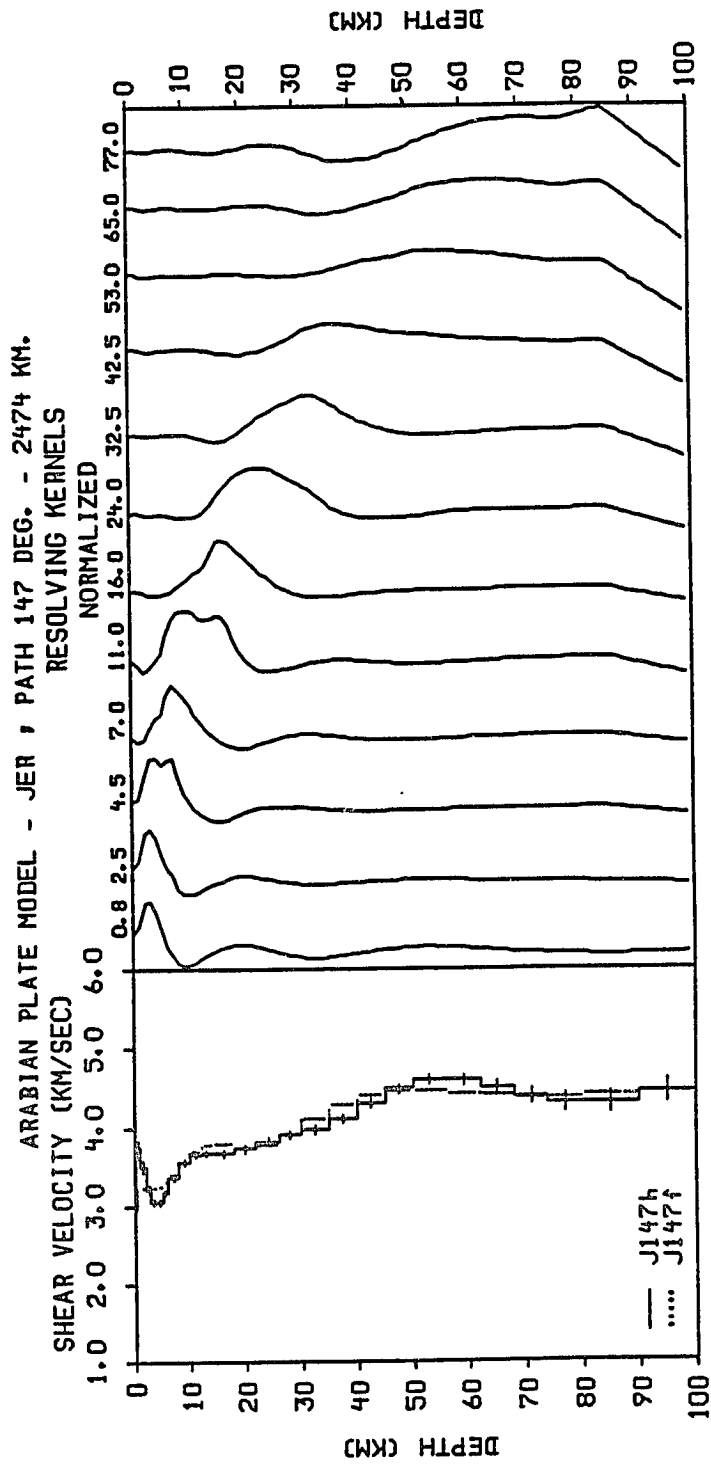
Figure 4.19. Shear velocity model J147h and resolving kernels estimated from the fundamental and first higher-mode Rayleigh waves. The dotted line model J147f is estimated from the fundamental-mode only.

- 165 -

Table 4.31. Crustal velocity structure of the Arabian plate along path J147, derived from fundamental- and higher-mode data.

			Velocity Model J147h			
Layer Number	Layer Depth* (km)	Layer Thickness (km)	Compressional Velocity (km/sec)	Shear Velocity (km/sec)	Density (gm/cc)	Standard Deviation (km/sec)
1	0.2	0.5	6.24	3.60	2.771	0.092
2	0.8	0.5	6.51	3.76	2.853	0.086
3	1.5	1.0	6.07	3.50	2.720	0.076
4	2.5	1.0	5.56	3.21	2.613	0.061
5	3.5	1.0	5.28	3.05	2.556	0.045
6	4.5	1.0	5.28	3.05	2.556	0.036
7	5.5	1.0	5.49	3.17	2.598	0.038
8	7.0	2.0	5.83	3.37	2.666	0.044
9	9.0	2.0	6.16	3.56	2.749	0.042
10	11.0	2.0	6.33	3.65	2.799	0.040
11	13.0	2.0	6.36	3.67	2.809	0.040
12	16.0	4.0	6.36	3.67	2.808	0.042
13	20.0	4.0	6.46	3.73	2.837	0.043
14	24.0	4.0	6.62	3.82	2.882	0.048
15	28.0	4.0	6.76	3.91	2.919	0.053
16	32.5	5.0	6.90	3.98	2.953	0.059
17	37.5	5.0	7.12	4.11	3.019	0.061
18	42.5	5.0	7.67	4.30	3.197	0.060
19	47.5	5.0	8.00	4.49	3.310	0.059
20	53.0	6.0	8.20	4.60	3.381	0.064
21	59.0	6.0	8.18	4.59	3.374	0.073
22	65.0	6.0	8.00	4.49	3.312	0.086
23	71.0	6.0	7.80	4.38	3.243	0.102
24	77.0	6.0	7.68	4.31	3.200	0.120
25	85.0	10.0	7.68	4.31	3.203	0.136
26	95.0	10.0	7.93	4.45	3.286	0.147

* from the surface to the middle of the layers.

Table 4.32. Crustal velocity structure of the Arabian plate along path J147,
derived from fundamental-mode data.

Velocity Model J147f						
Layer Number	Layer Depth* (km)	Layer Thickness (km)	Compressional Velocity (km/sec)	Shear Velocity (km/sec)	Density (gm/cc)	Standard Deviation (km/sec)
1	0.2	0.5	5.05	2.91	2.509	0.113
2	0.8	0.5	5.57	3.22	2.614	0.111
3	1.5	1.0	5.58	3.22	2.616	0.108
4	2.5	1.0	5.58	3.22	2.616	0.090
5	3.5	1.0	5.59	3.23	2.618	0.059
6	4.5	1.0	5.63	3.25	2.626	0.047
7	5.5	1.0	5.73	3.31	2.647	0.060
8	7.0	2.0	5.90	3.41	2.680	0.068
9	9.0	2.0	6.16	3.56	2.749	0.056
10	11.0	2.0	6.40	3.70	2.821	0.053
11	13.0	2.0	6.54	3.78	2.861	0.054
12	16.0	4.0	6.56	3.79	2.865	0.053
13	20.0	4.0	6.49	3.75	2.847	0.058
14	24.0	4.0	6.55	3.78	2.863	0.076
15	28.0	4.0	6.79	3.92	2.924	0.088
16	32.5	5.0	7.11	4.11	3.016	0.096
17	37.5	5.0	7.42	4.28	3.114	0.097
18	42.5	5.0	7.84	4.40	3.256	0.091
19	47.5	5.0	7.93	4.45	3.288	0.082
20	53.0	6.0	7.94	4.46	3.289	0.079
21	59.0	6.0	7.89	4.43	3.272	0.090
22	65.0	6.0	7.83	4.39	3.252	0.113
23	71.0	6.0	7.79	4.37	3.239	0.142
24	77.0	6.0	7.79	4.37	3.239	0.176
25	85.0	10.0	7.83	4.40	3.253	0.213
26	95.0	10.0	7.92	4.45	3.284	0.248

* from the surface to the middle of the layers.

discontinuities can be identified at depths of about 20.0 km and 40.0 km, respectively. The velocity variation within the upper crust is about 3.38-3.61 km/sec, whereas the velocity variation in the lower crust is more gradual and it changes from 3.82-4.06 km/sec. Below the Moho, the shear velocity range is 4.12-4.45 km/sec, and seems to be better controlled by the higher-mode data than previously observed with either E30h and E67h models.

Models J89h and J89f are shown in Figures 4.17. The path for these models closely coincides with E84. Hence, it is not surprising that their crustal velocity structures are very similar to E84 models. According to J89f, the near surface shear velocity of the sedimentary layer is about 2.03 km/sec. The depth of this layer is about 8.0 km, where the velocity range is 2.97-3.08 km/sec. In the upper crust the velocity increases gradually from 3.18 km/sec to 3.70 km/sec at 24.0 depth, where the Conrad discontinuity is identified. The shear velocity within the lower crust also varies gradually. It increases from 3.89 km/sec to 4.42 km/sec at the Moho discontinuity at about 40-45 km depth. In contrast with E84 models, the upper mantle velocity structure is better constrained, and shows an average velocity of about 4.52 km/sec.

Models J127h and J127f are presented in Figures 4.18. Because path J127 also traverses the Arabian shield and platform, but not the Mesopotamian foredeep, these models show a velocity structure that is very similar to E123. According to model J127f the crystalline basement is overlain by about 6.0 km thick sediments with a velocity range of 2.58-3.19 km/sec. The upper crust seems to be better defined by the higher-mode data, and shows that the Conrad discontinuity is about 20.0 km deep. The average

velocity within this layer is about 3.48 km/sec. As for the lower crust, the higher-mode and fundamental-mode models seem to present two contrasting velocity structures. Model J127h shows the shear velocity to gradually increase from 3.71 km/sec to 4.19 km/sec at about 40.0-45.0 km depth, where the Moho discontinuity is located. Model J127f, on the other hand, indicates that the shear velocity in the lower crust changes very little with depth, and exhibits an average of 3.93 km/sec. Below the Moho, the upper mantle velocity decreases from 4.50 km/sec to 4.07 km/sec with depth.

Models J147h and J147f shown in Figures 4.19. The path for these models is similar to E131. It traverses a significant portion of the Arabian shield and a small region of the Arabian platform. Model J147f shows that a layer of sediments, about 5.0 km thick, overlays the basement. The velocity within the sediments increases with depth from 2.91 km/sec near the surface to 3.25 km/sec. Both Models indicate that the upper crustal velocity exhibits an average of about 3.55 km/sec, and changes very little with depth. Within the lower crust the velocity variation is gradual, and it increases from 3.82 km/sec to 4.11 km/sec. According to these models the Conrad and Moho discontinuities are located at about 20.0 km and 40.0 km depth, respectively. The shear velocity within the upper mantle seems to slightly decrease with increasing depth from 4.60 km/sec to 4.31 km/sec.

4.2.5 Comparison with Other Models

Niazi (1968), Arkhangel'skaya et al. (1974), Knopoff and Fouda (1975) and Mooney et al. (1985) have all presented velocity models along various paths across the Arabian plate. Comparisons between their models and some of the velocity structures of this study are discussed in this sec-

tion. However, due to the similarity between Arkhangel'skaya *et al.* (1974) and Niazi (1968) velocity structures, only the latter is referenced in the following comparison.

For comparisons with Niazi (1968) and Knopoff and Fouda (1975) velocity structures, models T190f, S267f, S267h, E84f, E84h, J89f and J89h are selected, because they either parallel or closely coincide with their SHI-HLW, JER-SHI and SHI-AAE two stations paths. Figures 4.20 and 4.21 show an overlay of all models. The solid and dotted lines represent the higher-mode and fundamental-mode models obtained in this study, while the solid lines with symbols represent models obtained by previous studies. Also, in these figures Knopoff and Fouda (1975) high/low velocity crust and high/low velocity mantle structures are referred to as HH, HL, LH and LL models.

In general, Figures 4.20-4.21 show that the shear velocity models obtained in this study are in good agreement with those of Knopoff and Fouda (1975) and Niazi (1968). This is due, in particular, to the wide range of velocities predicted by Knopoff and Fouda (1975), since the models along paths T190, S267, E84 and J89 all fall within the velocity limits of the HH, HL, LH and LL models. However, this result indirectly confirms Knopoff and Fouda (1975) conclusion regarding the relatively low velocities that characterize the Arabian stable shelf (roughly equivalent to the Arabian platform region) when compared with the Canadian shield region. The most important differences between the models are reflected in the features of the sedimentary layer and depth of the Moho discontinuity. Unlike the results obtained in this study, both Knopoff and Fouda (1975) and Niazi (1968) show a thinner sedimentary layer with relatively higher
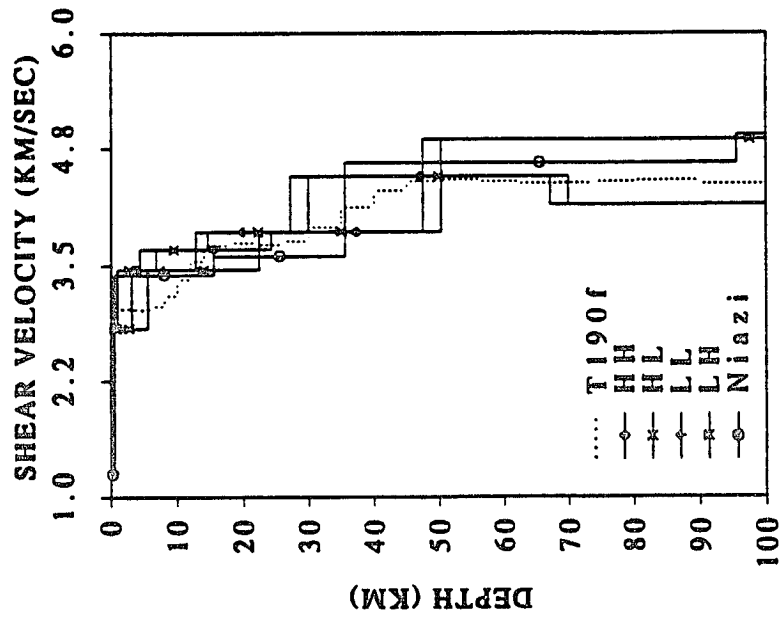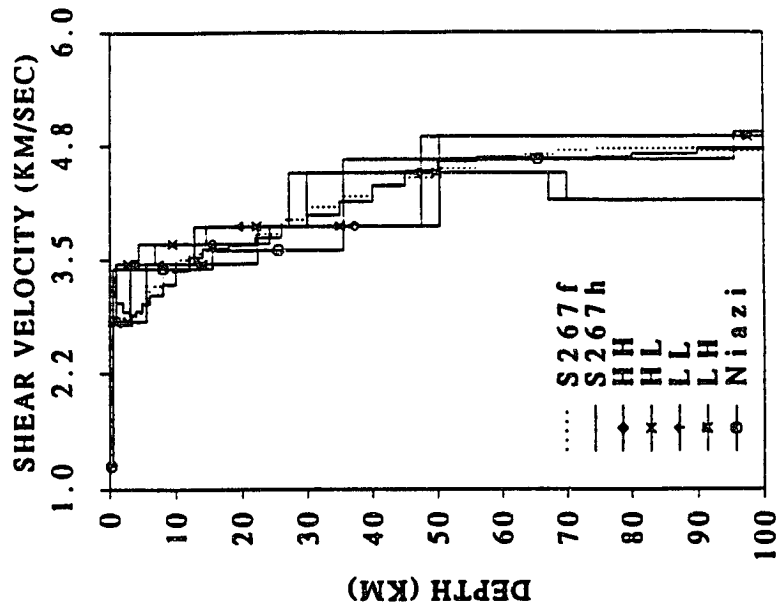
Figure 4.20. Plots comparing the seismic velocity models T190f, S267f and S267h with those obtained by Knopoff and Fouda (1975) and Niazi (1968). The latter models are denoted by HH, HL, LL, LH and Niazi, respectively.

- 171 -
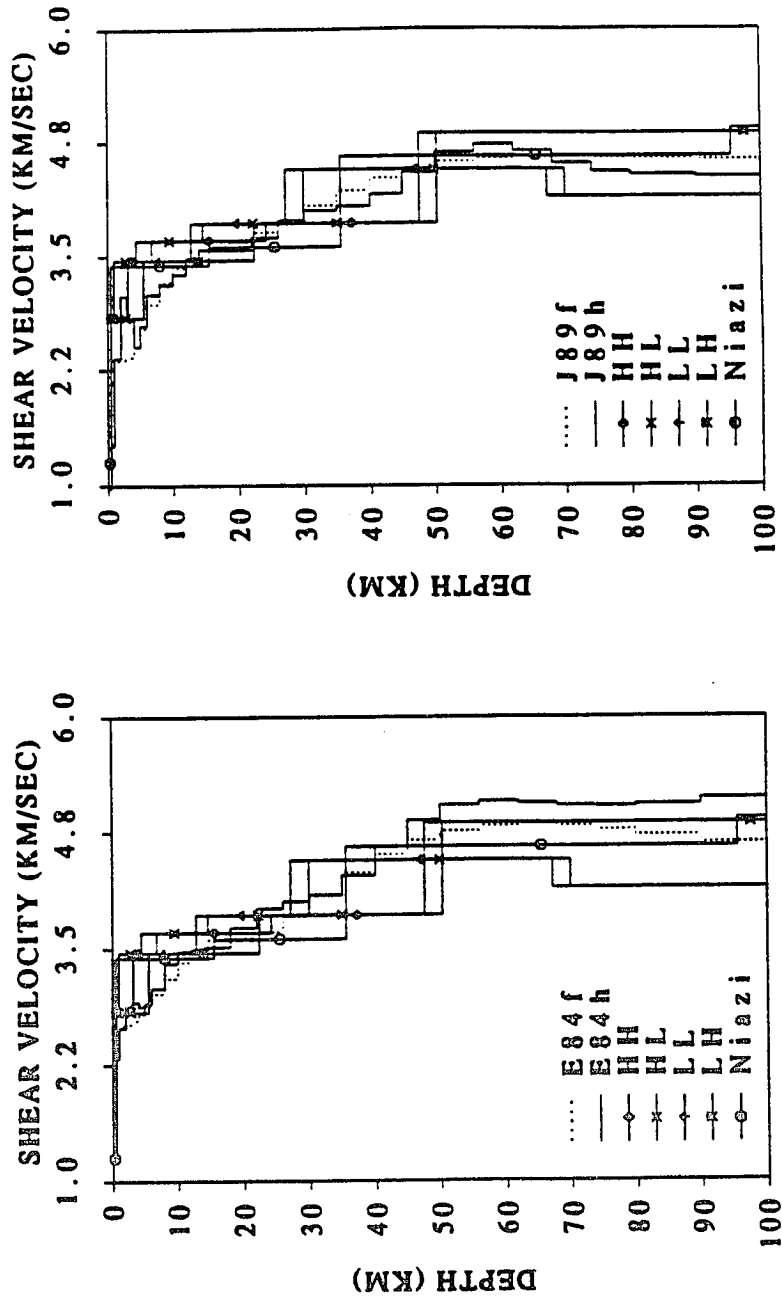
Figure 4.21. Plots comparing the seismic velocity models E84f, E84h, J89f and J89h with those obtained by Knopoff and Fouda (1975) and Niazi (1968). The latter models are denoted by HH, HL, LL, LH and Niazi, respectively.

- 172 -

shear velocity, and a Moho that is approximately 35.0 km deep. The most likely reasons for these discrepancies are that Niazi (1968) relied on an assumed theoretical model to fit his observed dispersion curves velocities, and that Knopoff and Fouda (1975) results are influenced by their wide range of velocity models for the region.

Similarly, to compare with the Mooney *et al.* (1985) refraction models, Figures 4.22 and 4.23 show a composite of all models in terms of compressional rather than shear velocities. The solid and dotted lines represent the higher-mode and fundamental-mode models obtained in this study along paths T190, S212, E131 and J147. The solid lines with symbols represent the models inferred from the Saudi Arabia seismic deep-refraction data. Models SARL1-2, SARL2-3, SARL4 and SARL4-5 correspond to the velocity structures between the five shot points along the refraction line. In Figures 3.13-3.16 the location of these shot points is marked by asterisks.

Considering that the surface wave models represent an average velocity structure over a much longer path than the refraction line, a remarkable correlation between the models shown in Figures 4.22-4.23 is evident. Except for the top sedimentary layers, the velocity gradients and range in the surface-wave models are in good agreement with the refraction velocity structures. This is especially clear in case of the models along paths E131 and J147 which mainly traverse the Arabian shield. The models along paths T190 and S212 show lower and higher upper mantle velocities, respectively, because they both traverse significant portions of the Arabian platform and Mesopotamian foredeep. A more important result of this comparison is the excellent agreement between all models regarding the depth
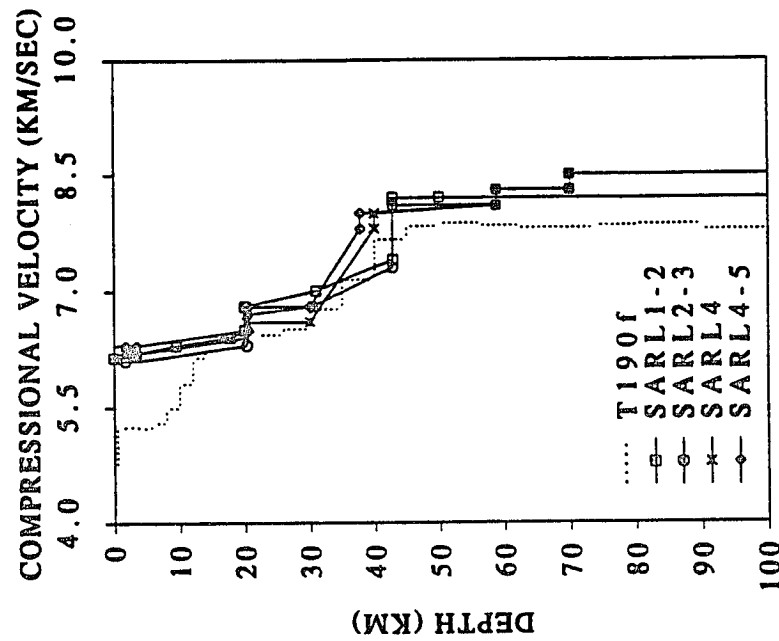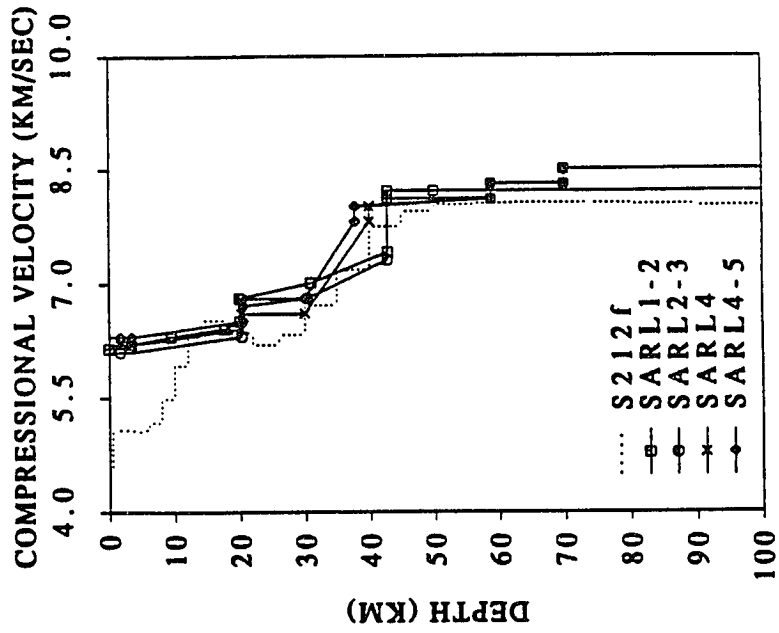
Figure 4.22. Plots comparing the seismic velocity models T190f and S212f with those obtained from the Saudi Arabian deep-refraction profile by Mooney *et al.* (1985). The refraction models are denoted by SARL1-2, SARL2-3, SARL4 and SARL4-5.

- 174 -
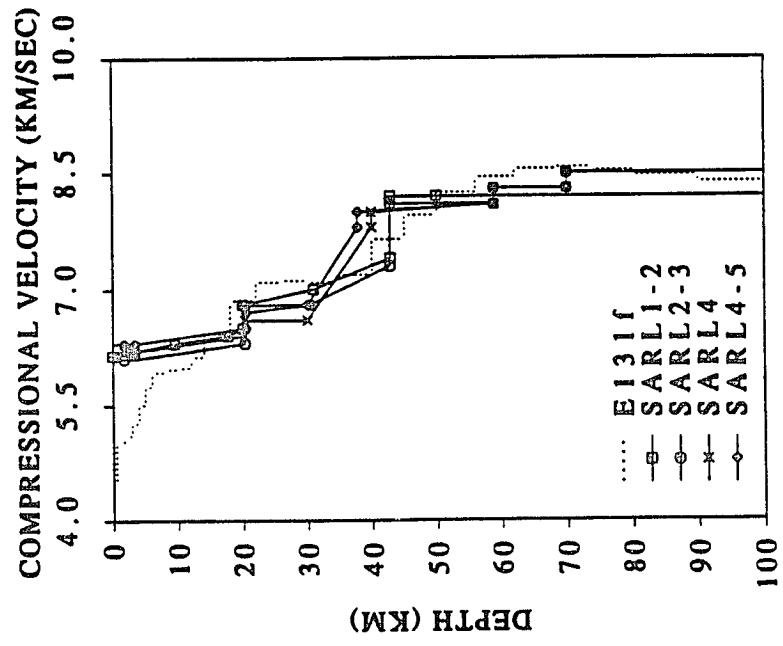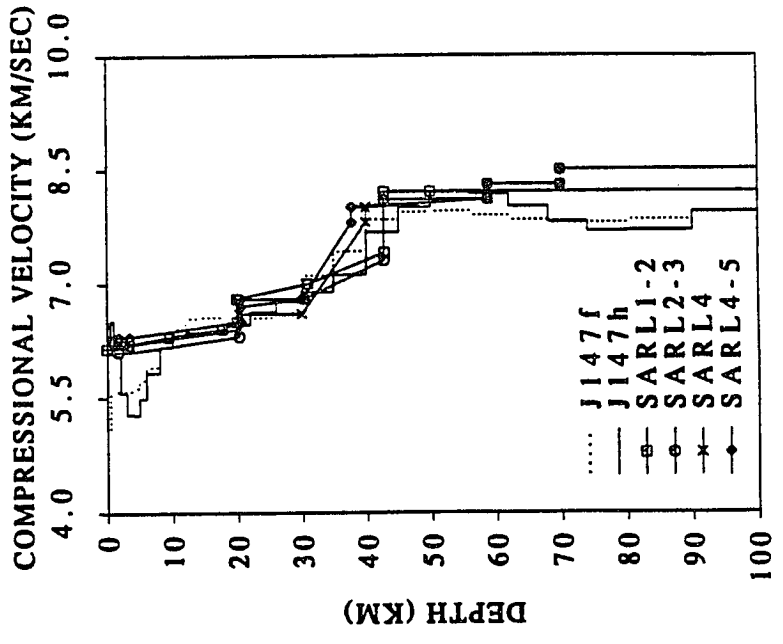
Figure 4.23. Plots comparing the seismic velocity models E131f, J147f and J147h with those obtained from the Saudi Arabian deep-refraction profile by Mooney *et al.* (1985). The refraction models are denoted by SARL1-2, SARL2-3, SARL4 and SARL4-5.

- 175 -

of the Conrad and Moho discontinuities. Similar to the refraction velocity structures, the surface-wave models also place the Conrad at about 20.0 km depth, and the Moho at 37.0-45.0 km depth. In summary, with more and higher quality data, and denser station coverage the entire plate velocity structure can be mapped with an unprecedented degree of accuracy.

4.3 Three-Dimensional Velocity Model

Even though the shear velocity models derived from mixed-paths show significant variation, those models do not demonstrate the detailed crustal an upper mantle structure that is important to understanding the tectonics of the Arabian plate. In order to provide a quantitative description of the lateral heterogeneity in the region, a surface-wave regionalization method is used to estimate pure-path dispersion curves and present a three-dimensional model for the plate.

The grid-dispersion inversion used in this study was introduced by Feng and Teng (1983). The objective of this stochastic inversion method is to represent an observed set of dispersion curves as the sum of group delays within grid elements. The basic regionalization principle from which the method has evolved can be expressed as follows,

$$\frac{1}{V_i(T)} = \sum_{j=1}^{n} \frac{d_{ij}}{D_i} \frac{1}{v_j(T)} \qquad (4.4)$$

where, $V_i(T)$ is the mixed-path group velocity, d_{ij} is the pure-path distance within each grid element, D_i is the dispersion curve mixed-path distance, $v_j(T)$ is the grid element group velocity, and T is the reference period at which V_i and v_j are calculated. The subscripts i, where i = 1, ..., m, and j, where j = 1, ..., n, indicate the total number of dispersion curves and

number of grid elements, respectively. To provide stability to the inversion of (4.4), the grid-dispersion problem can be expressed in terms of the deviations of grid elements delays from a reference dispersion curve as follows,

$$\frac{1}{U_i(T)} - \frac{1}{V_i(T)} = \sum_{j=1}^{n} \frac{d_{ij}}{D_i}\left[\frac{1}{u_j(T)} - \frac{1}{v_j(T)}\right]$$ (4.5)

where, $U_i(T)$ is the measured mixed-path dispersion curve group velocity at a given period, and $u_j(T)$ is the calculated grid velocity at that period. Therefore, in order to solve (4.5) iteratively for $u_j(T)$, equation (4.4) is used to determine the theoretical mixed-path delays with respect to a hypothetical starting group velocity model. During the initial iteration the average of all mixed-path dispersion curves is used as a pure-path starting model, whereas for subsequent iterations prior values of $u_j(T)$ are used to refine the calculated pure-path grid velocities. Expanding the grid-dispersion expression (4.5) in matrix form yields,

$$\begin{bmatrix} \frac{1}{U_1(T)} - \frac{1}{V_1(T)} \\ \cdot \\ \cdot \\ \cdot \\ \cdot \\ \frac{1}{U_m(T)} - \frac{1}{V_m(T)} \end{bmatrix} = \begin{bmatrix} \frac{d_{11}}{D_1} & \cdots & \frac{d_{1n}}{D_1} \\ \cdot & \cdots & \cdot \\ \cdot & \cdots & \cdot \\ \cdot & \cdots & \cdot \\ \cdot & \cdots & \cdot \\ \frac{d_{m1}}{D_m} & \cdots & \frac{d_{mn}}{D_m} \end{bmatrix} \begin{bmatrix} \frac{1}{u_1(T)} - \frac{1}{v_1(T)} \\ \cdot \\ \cdot \\ \cdot \\ \frac{1}{u_n(T)} - \frac{1}{v_n(T)} \end{bmatrix}.$$ (4.6)

The left hand side of (4.6) represent the amount of change, i.e. $\delta y_{m \times n}$, in measured velocities with respect to a set of theoretical mixed-path velocities, whereas the right hand side represent the difference, i.e. $\delta x_{n \times 1}$, between calculated pure-path velocities and the hypothetical starting model. If the sum of normalized grid element distances for each dispersion curve

path is represented by a matrix $A_{m \times n}$, equation (4.5) can then be written in vector-matrix form as

$$\delta y = A\, \delta x \ .$$

This is a standard iterative least-squares problem equivalent to (4.1), operating on the perturbation of δx, and requires stochastic damping to constraint the solution to physically reasonable values. In this case, the solution to this problem is

$$\delta x = (A^T A + \gamma^2 I)^{-1} A^T \, \delta y \ ,$$

where, γ is the damping factor, I is an identity matrix, and the superscript T is the transpose of a matrix. The SVD solution can be written as

$$\delta x = V S^{-1} U^T \, \delta y.$$

Considering that the grid dispersion curves are estimated over a range of periods, and that the kernel matrix does not require updating after every perturbation, Lawson and Hanson (1974) describes a very efficient computational approach for applying SVD to this type of least squares problem. The approach does not only provide the numerical stability that is characteristic of orthogonal transformations, but also the means to operate on all vectors of measured and theoretical data simultaneously. Hence, reducing the problem to a simple algebraic computation of solution vectors, resolution and covariance matrices for each period.

Among the advantages of grid-dispersion inversion are, the grid element size mainly depends on the dispersion information density, and that the method requires no *a priori* assumption regarding either the surface or subsurface geology of a region. In formulating the inversion procedure,

grids with various element sizes were implemented to test the coverage and resolution of the 152 dispersion curve paths shown in Figures 4.24. The adopted grid is presented in Figure 4.25. It divides the Arabian plate region into 100 equal area elements. The dimensions of each element is 3×3 degrees. The pure-path distances within the individual grid elements d_{ij} are then determined and normalized by their corresponding mixed-path distances D_i to produce the $A_{m \times n}$ kernel matrix. To formulate the vector $y_{m \times n}$ at each period in (4.6), the starting group velocity values $v_j(T)$ for each element are assumed to be the average of all group velocity measurements $U_i(T)$, and the theoretical slowness $1/V_i(T)$ values are then calculated using equation (4.4). Subsequently, the initial dispersion curve for the individual grid elements are updated by the solution from the preceding iteration.

Figures 4.26-4.33 show examples of the pure-path group velocity dispersion curves obtained from the grid-dispersion inversion method after three iterations. Increasing the number of iterations showed no significant improvement in the estimated dispersion curves over the period range of 6-59 sec. In these figures the symbols represent the estimated pure-path group velocities, and the solid lines represent the theoretical dispersion curves obtained from the inversion of each grid element dispersion data. As expected, the most striking variations are observed among grid elements 42-47, 53-58, 63-69 and 74-79, because these elements extend from the Arabian Shield, through the Mesopotamian foreland, to the Mesopotamian foredeep. For example, Figures 4.29 and 4.30 show the shield dispersion curves having higher group velocities than those for the foredeep. In comparison, the dispersion curves for grid elements 54, 55, 64, 65, 75 and 76 which cover the Arabian shield show higher velocities than elements 46,
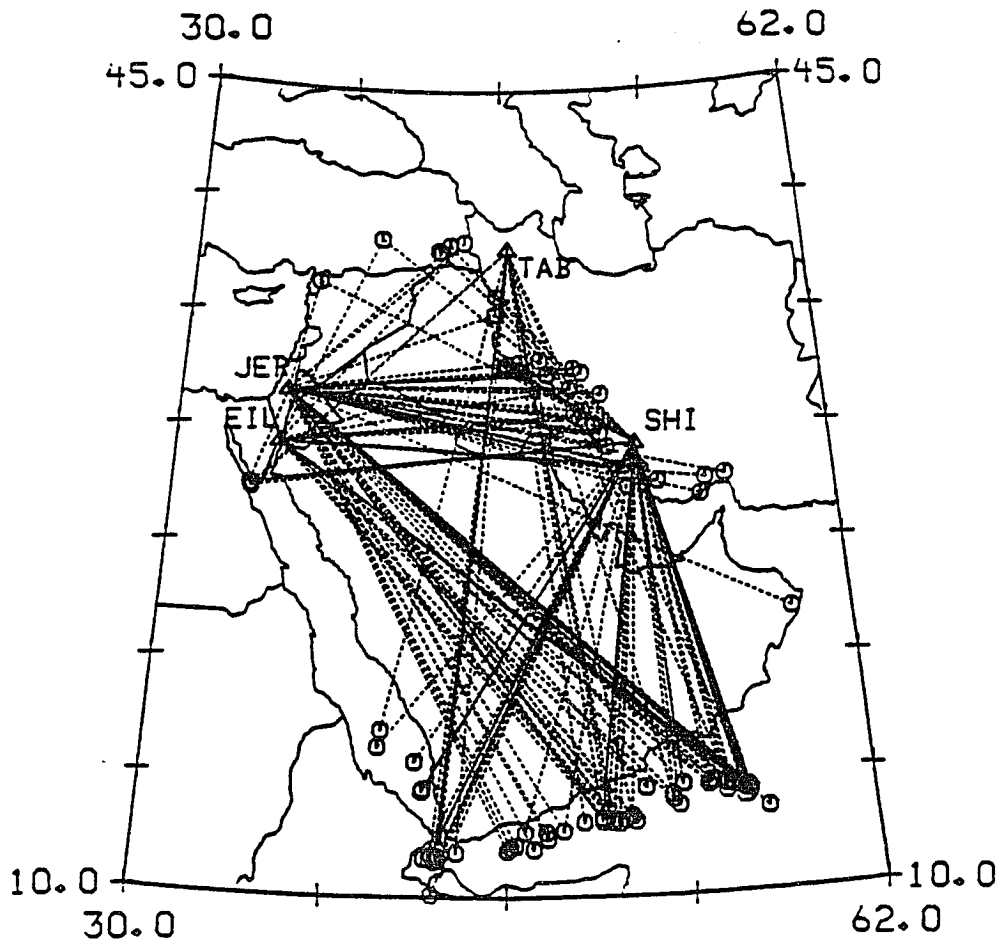
Figure 4.24. A composite of Rayleigh wave propagation paths for stations TAB, SHI, EIL and JER.

- 180 -
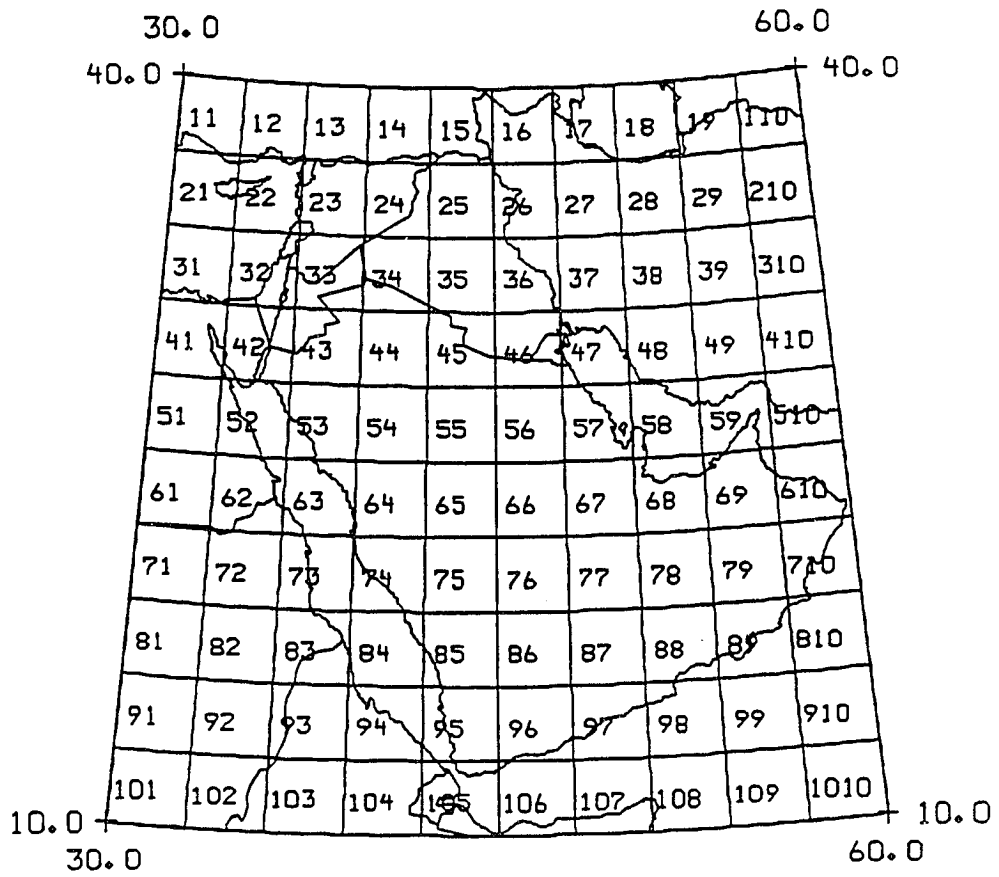
Figure 4.25. The 3 X 3 degrees grid used in the grid-dispersion inversion.

- 181 -
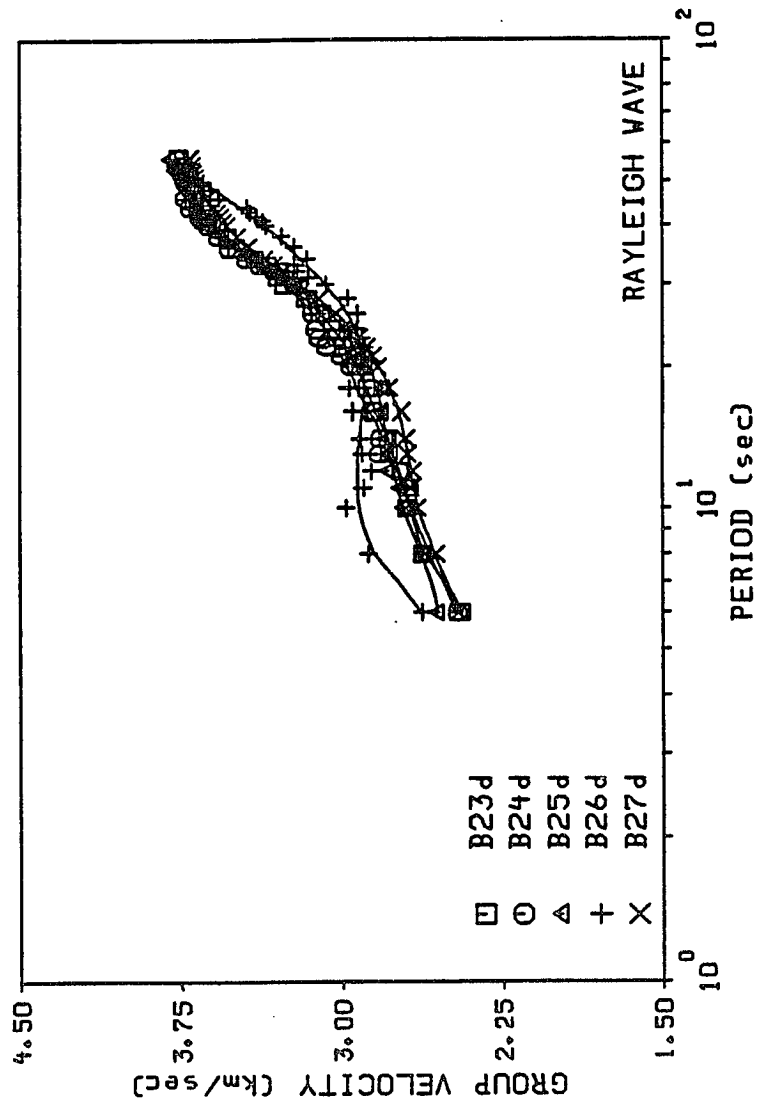
Figure 4.26. Estimated pure-path dispersion curves for grid elements 23, 24, 25, 26 and 27.

- 182 -
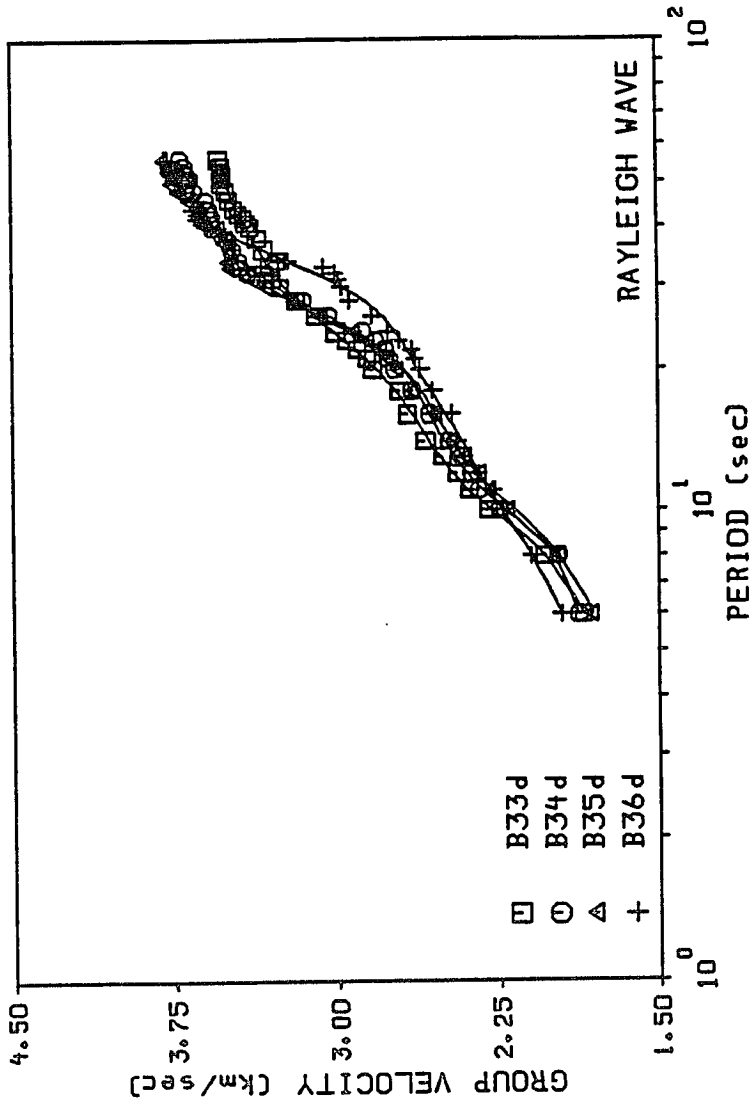
Figure 4.27. Estimated pure-path dispersion curves for grid elements 33, 34, 35 and 36.

- 183 -
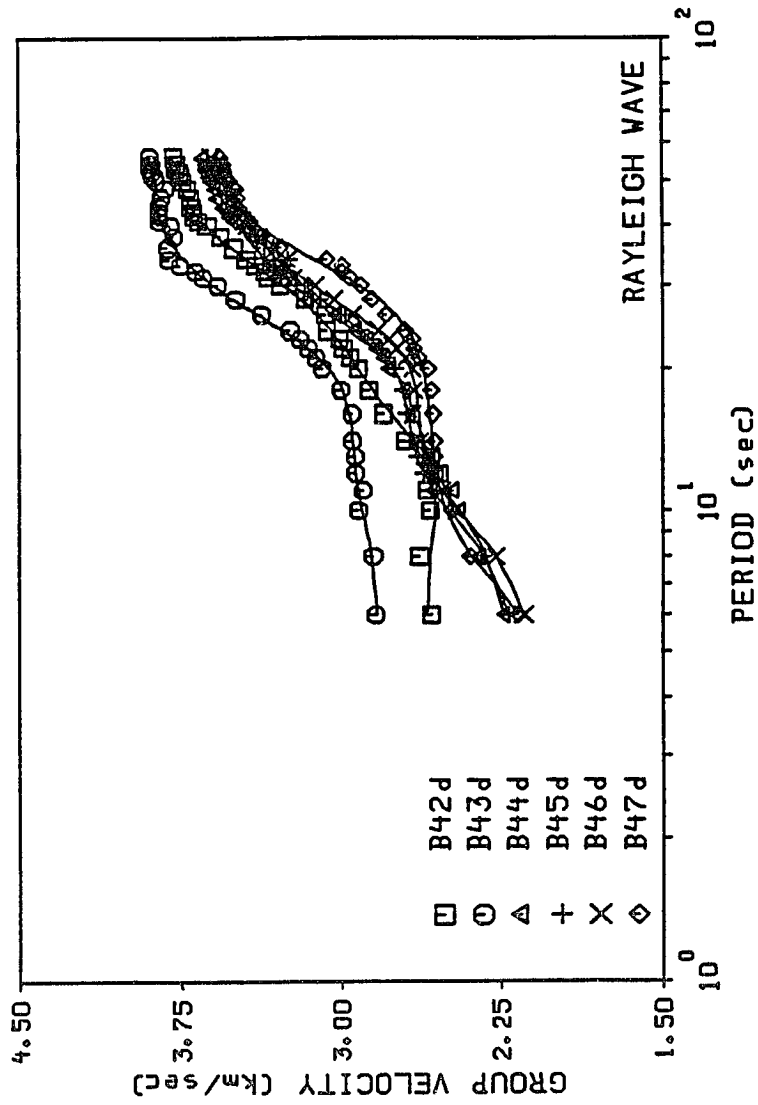
Figure 4.28. Estimated pure-path dispersion curves for grid elements 42, 43, 44, 45, 46 and 47.

- 184 -
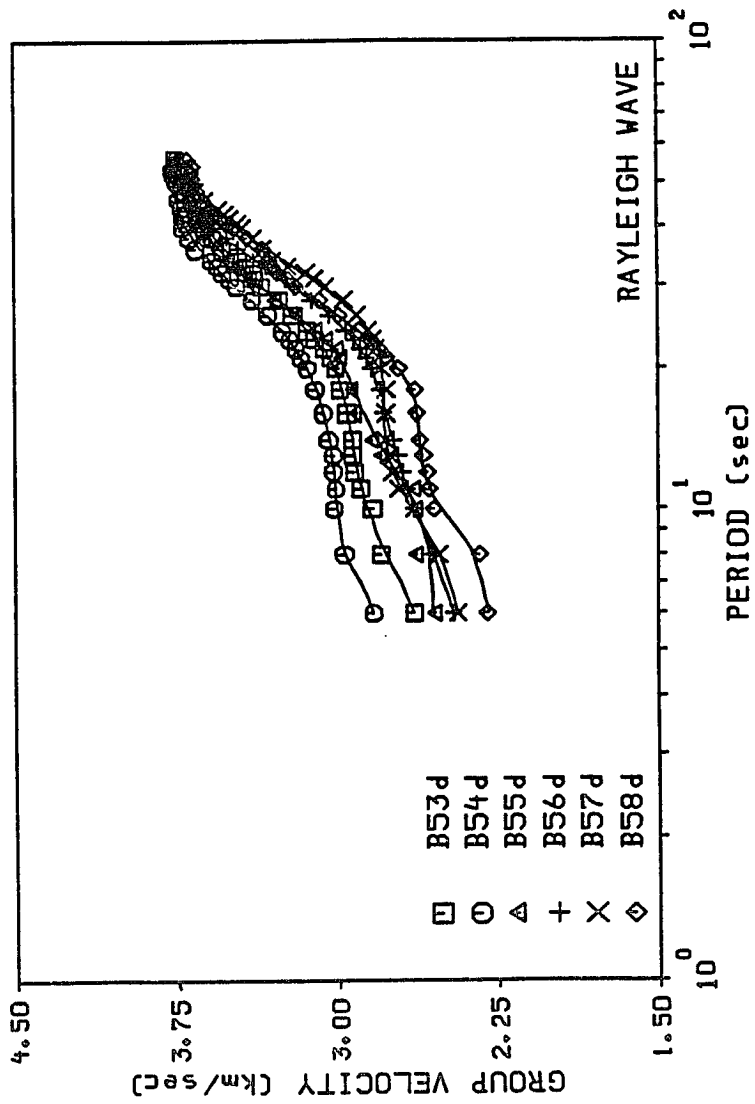
Figure 4.29. Estimated pure-path dispersion curves for grid elements 53, 54, 55, 56, 57 and 58.

- 185 -
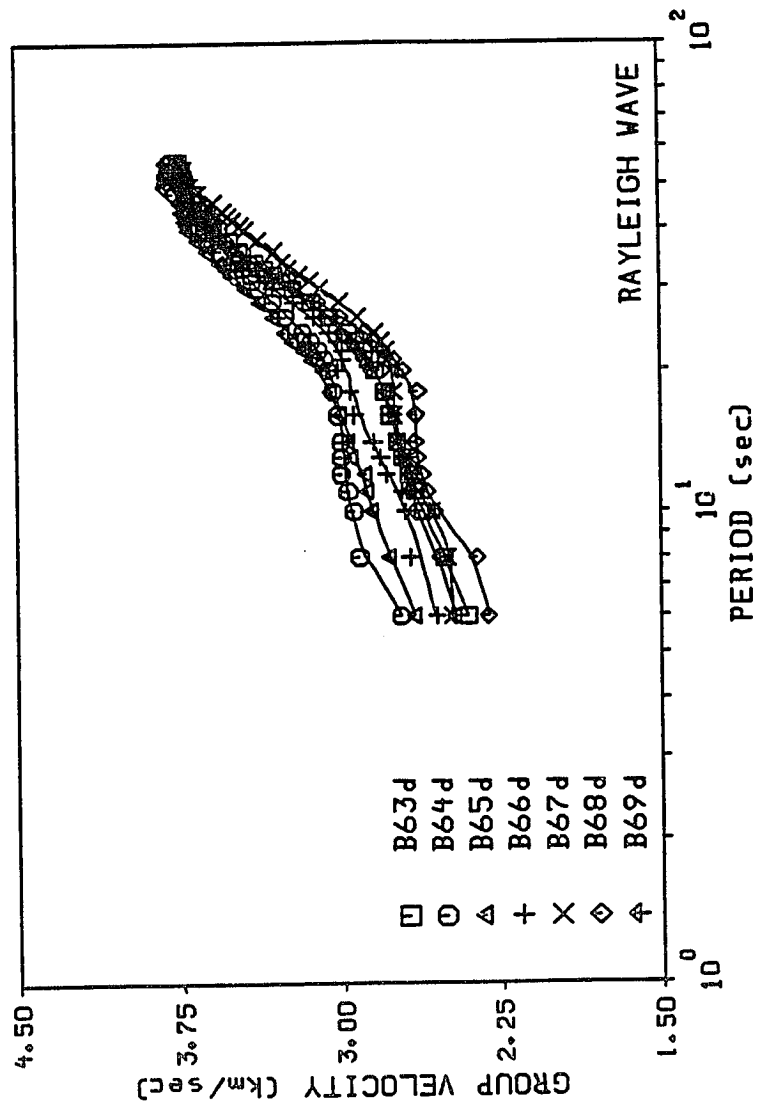
Figure 4.30. Estimated pure-path dispersion curves for grid elements 63, 64, 65, 66, 67, 68 and 69.

- 186 -
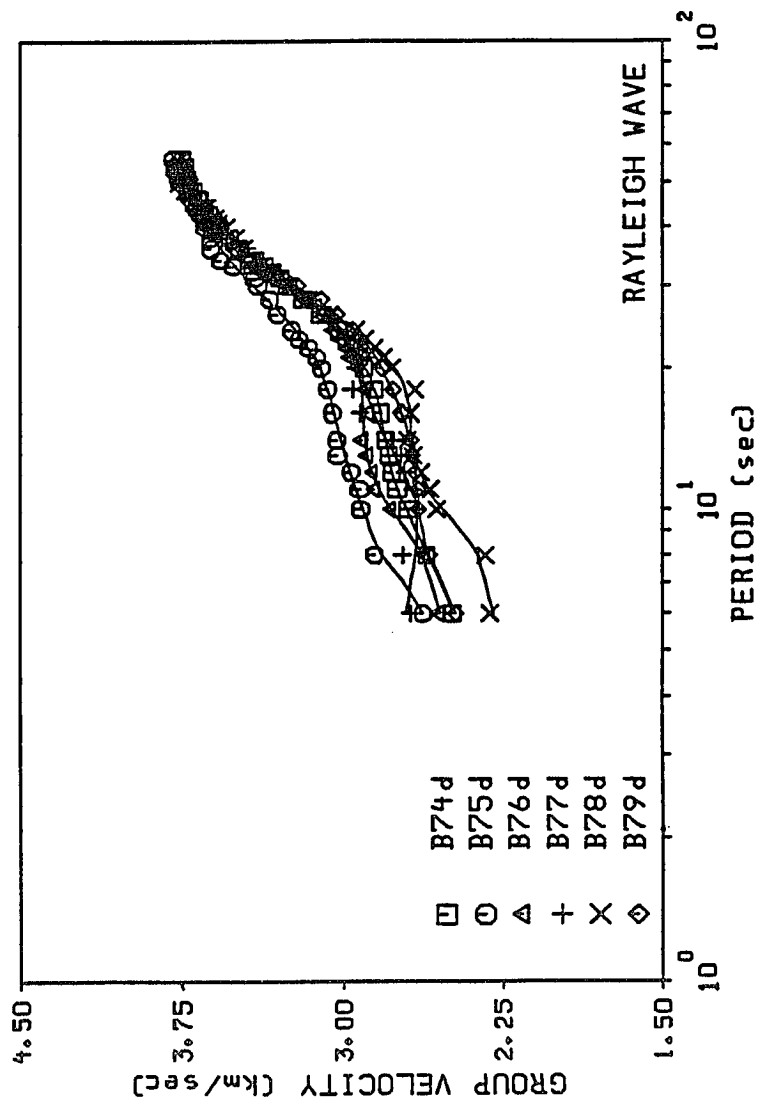
Figure 4.31. Estimated pure-path dispersion curves for grid elements 74, 75, 76, 77, 78 and 79.

- 187 -
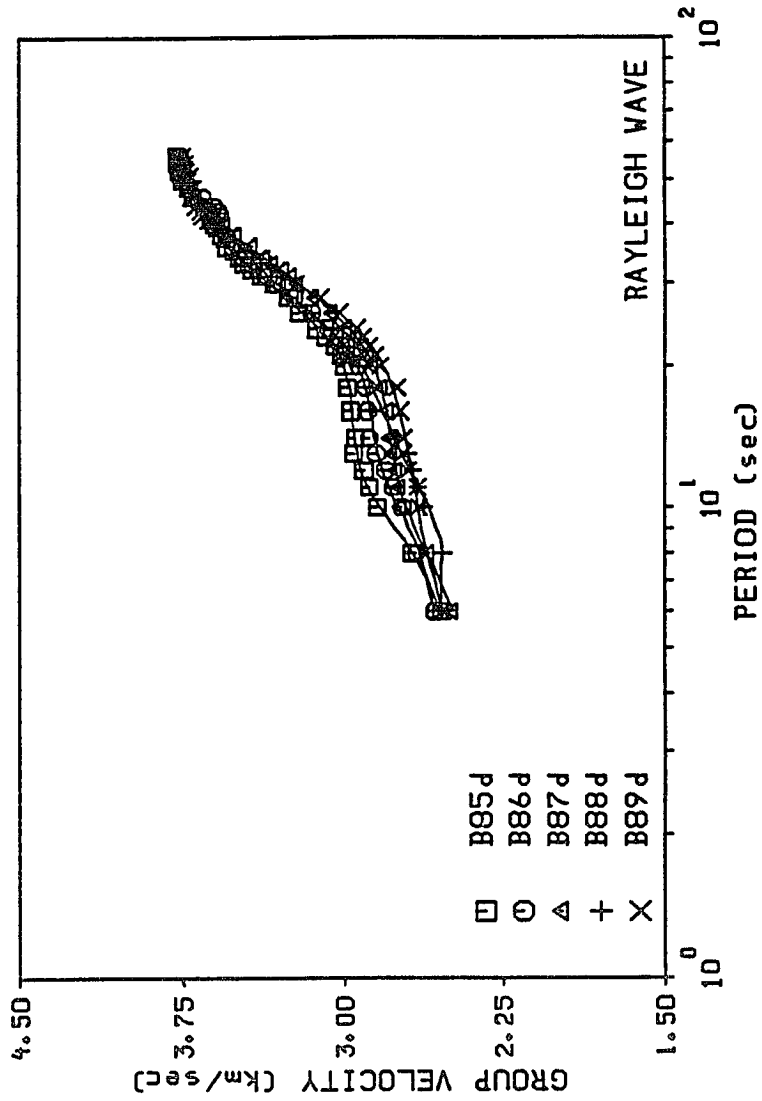
Figure 4.32. Estimated pure-path dispersion curves for grid elements 85, 86, 87, 88 and 89.
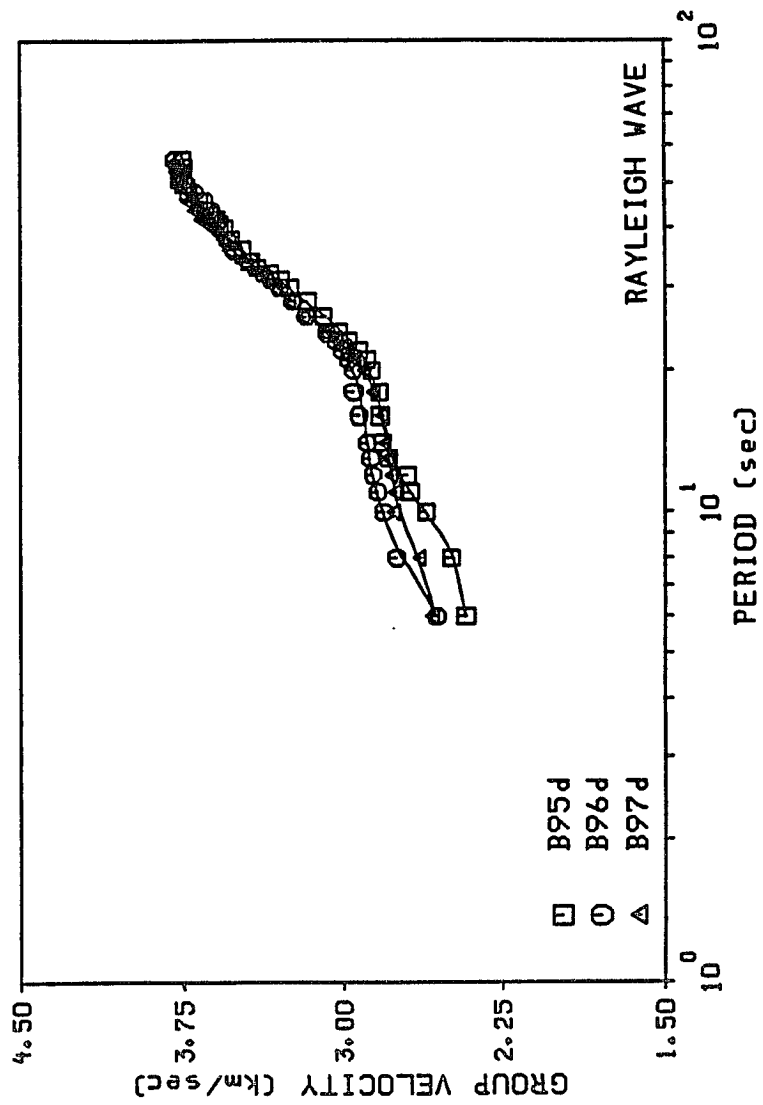
Figure 4.33. Estimated pure-path dispersion curves for grid elements 95, 96 and 97.

- 189 -

56, 57, 67, 68, 77, 78 and 88 within the Mesopotamian foredeep.

Finally, the pure-path fundamental mode dispersion curves of all grid elements, which are located within the Arabian plate, are inverted individually. Similar to the mixed-path average dispersion curves analysis, the same single layer over a half space starting model and differential inversion technique are used for estimating the pure-path shear velocity structures to a depth of 100.0 km.

4.3.1 Spatial Velocity Variation

The three-dimensional shear velocity structure of the Arabian plate is presented in Figures 4.34 through 4.38. These illustrations depict the lateral velocity heterogeneity at depths of 5.0 km to 80.0 km, in 5.0 km intervals. The isodepth surfaces are derived from the pure-path shear velocity models of the grid elements covering the plate. The surfaces are smoothed using a two-dimensional cubic spline interpolation scheme, while grid elements outside the plate region are assigned constant velocity values that correspond to the starting shear velocity model. Relative to the average model of the plate, the troughs and peaks of these surfaces represent regions of low and high velocities, respectively. To provide a better perspective of the lateral variation, the surfaces are plotted in a northwesterly direction that is roughly parallel to the trend of the Zagros mountain belt and the extension of the plate. The most striking feature of these illustrations is the continuous change in the distribution and location of the troughs and peaks of shear velocity at various depths. For instance, the velocity lows that are associated with the Mesopotamian foredeep seems to persist to about 30.0 km depth. Also, the influence of surface geology on
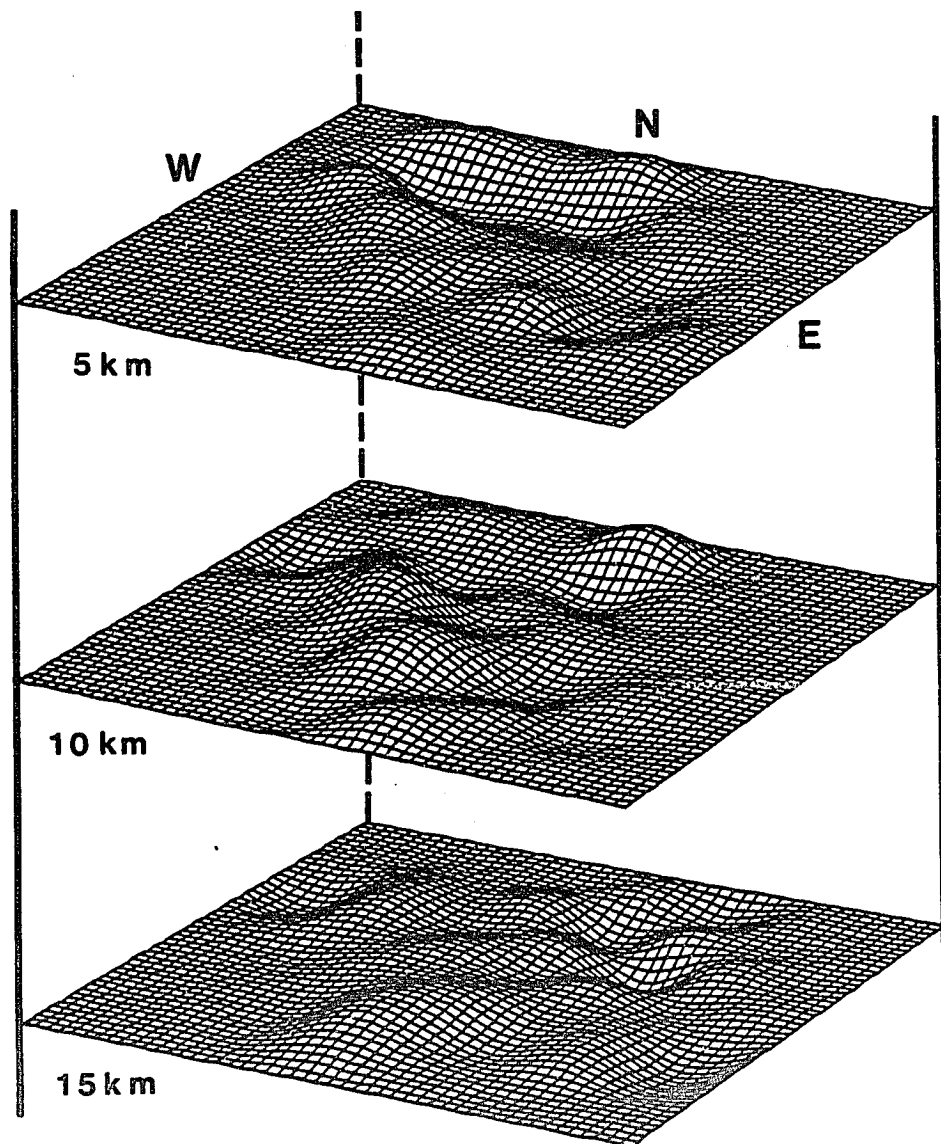
Figure 4.34. A three-dimensional illustration of the shear velocity struc-
ture variation of the Arabian plate at depths of 5, 10 and
15 km.
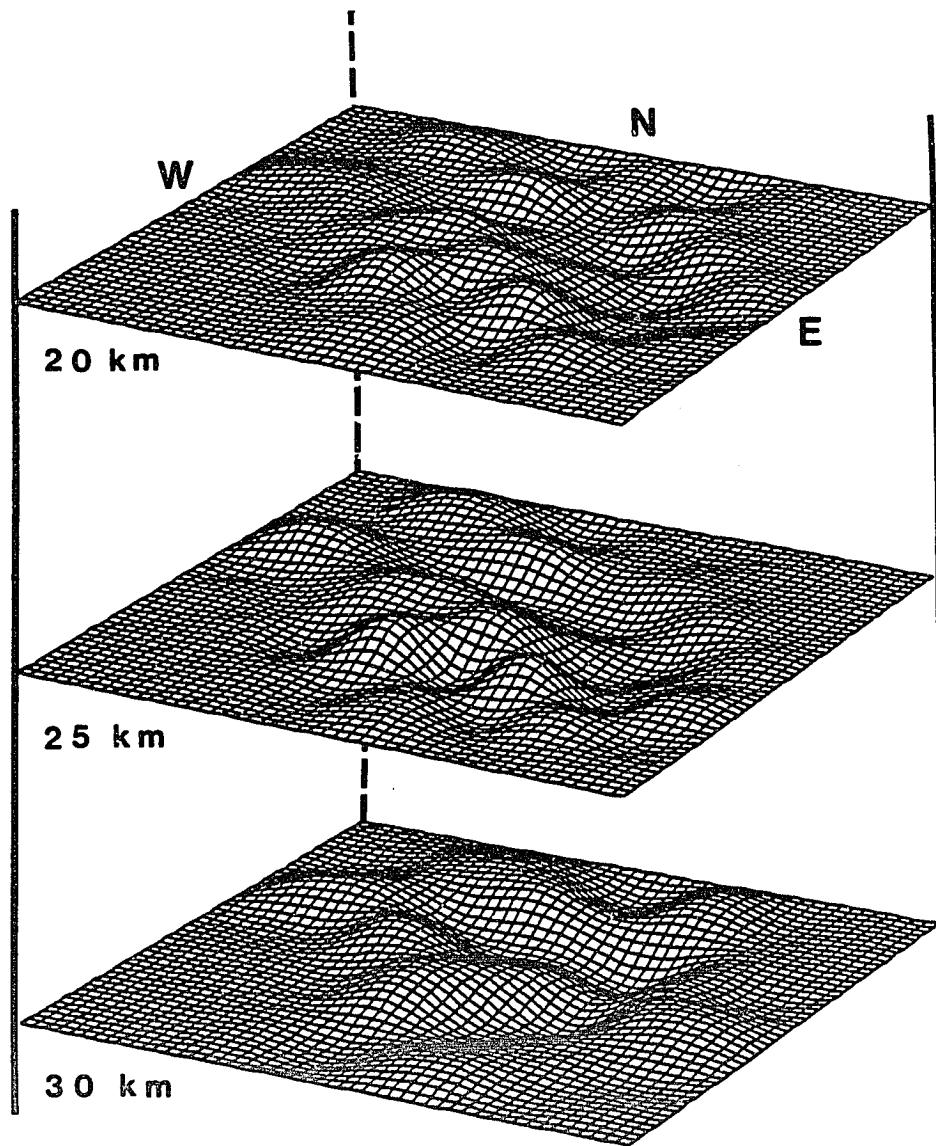
Figure 4.35. A three-dimensional illustration of the shear velocity structure variation of the Arabian plate at depths of 20, 25 and 30 km.
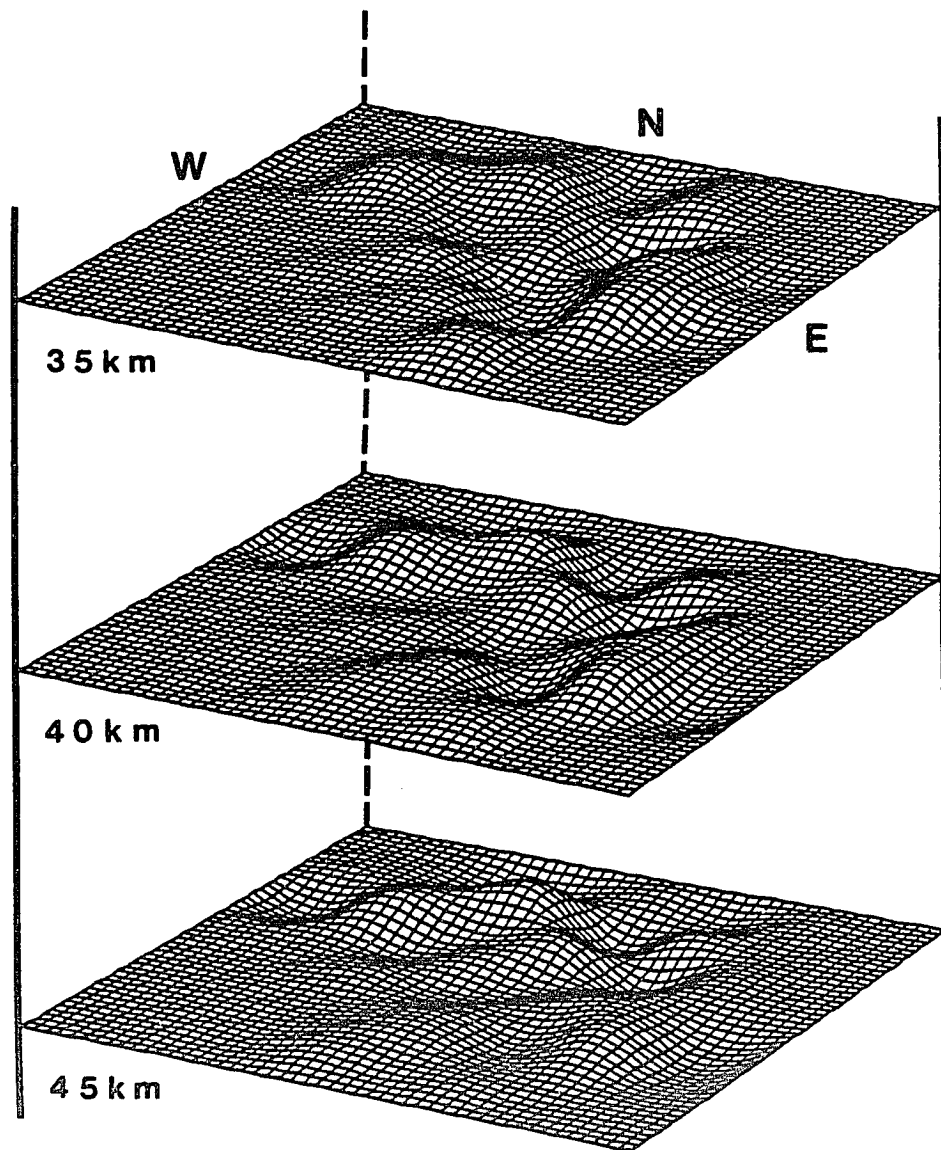
Figure 4.36. A three-dimensional illustration of the shear velocity structure variation of the Arabian plate at depths of 35, 40 and 45 km.
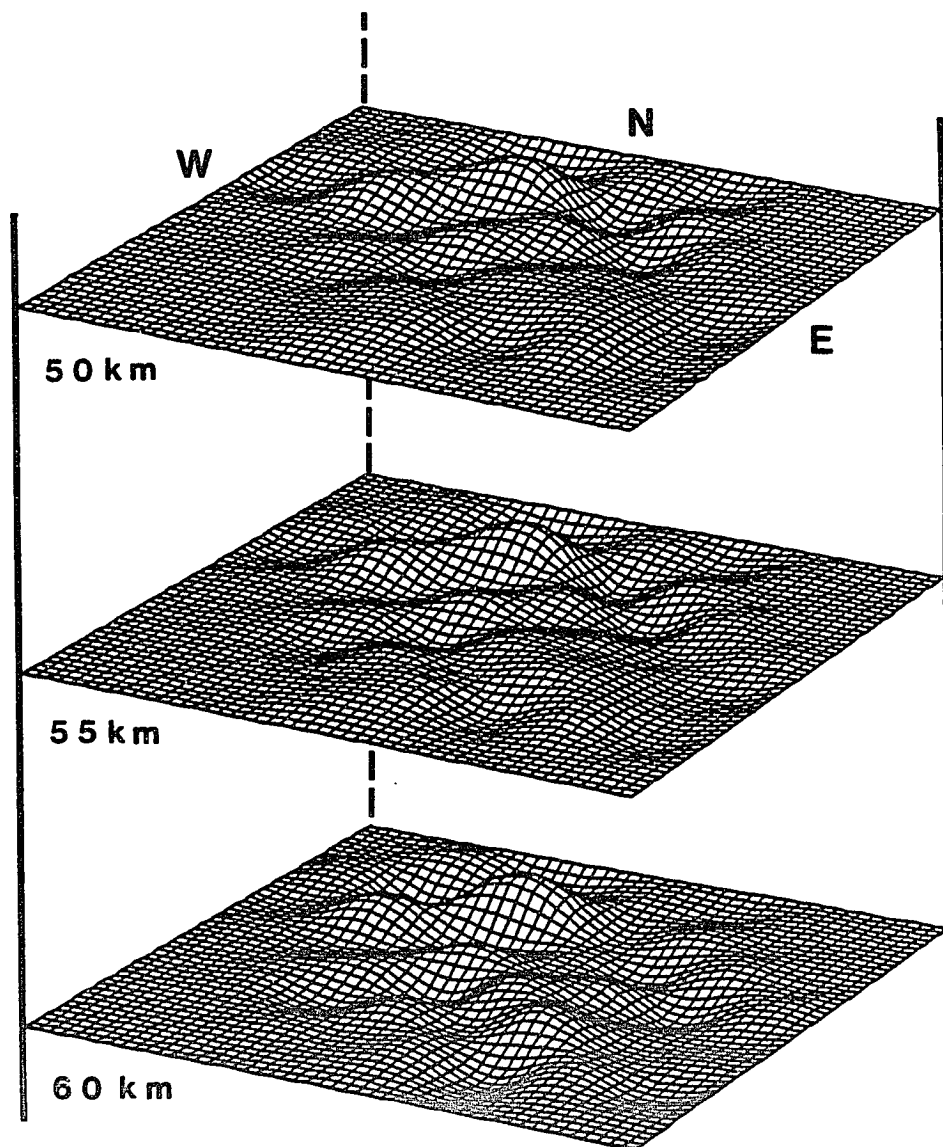
Figure 4.37. A three-dimensional illustration of the shear velocity structure variation of the Arabian plate at depths of 50, 55 and 60 km.

- 194 -
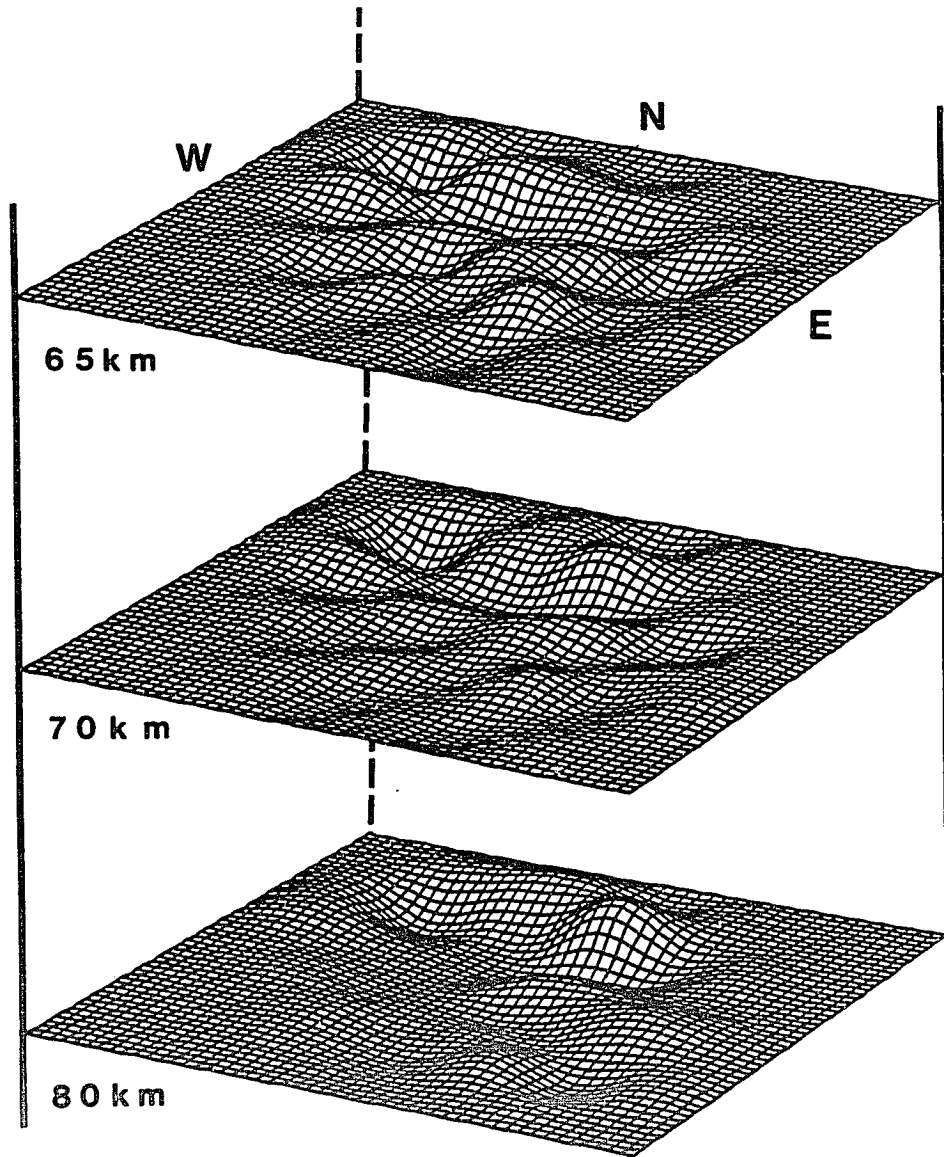
Figure 4.38. A three-dimensional illustration of the shear velocity struc-
ture variation of the Arabian plate at depths of 65, 70 and
80 km.

the subsurface structure of the plate slowly diminishes with increasing depth.

To facilitate interpreting the three-dimensional model, shear velocity contour maps of the isodepth surfaces are presented in Figures 4.39 through 4.52. Because the geographic boundaries of the Arabian plate are also included in these figures, the contour maps provide significantly better perspective of the lateral and vertical velocity variations. It should be evident that, these contour maps clearly reflect the surface manifestations and subsurface velocity heterogeneity of the region.

The first important result of this analysis can be observed in Figures 4.39 and 4.40. That is, the remarkable delineation of the Arabian shield and Mesopotamian foredeep by the shear velocity contours at 5.0 km and 10.0 km depths. The shape and extension of the contours closely correlate with the physiographic boundaries and surface geology of these major tectonic units. The contours clearly show that the shield area is confined to the west and southwestern part of the plate, whereas the Mesopotamian foredeep exhibits a northern, northwestern and western trends that are parallel to Zagros mountain belt. At 5.0 km depth, the velocity within the shield reaches a high of 3.2 km/sec, and drops to a low 2.6-2.7 km/sec within the thick sedimentary column of the foredeep. At 10.0 km depth, the velocity high is 3.7 km/sec in the shield, and velocity low is 3.2 km/sec in the foredeep. Also, Figures 4.39 and 4.40 show that the shear velocity of the shield area decreases rapidly toward the north and northeast, and decreases gradually towards the east and south. The implication of this result is that, the observed velocity variation is in very good agreement with the pattern of Brown's (1972) depth contours to the top of the
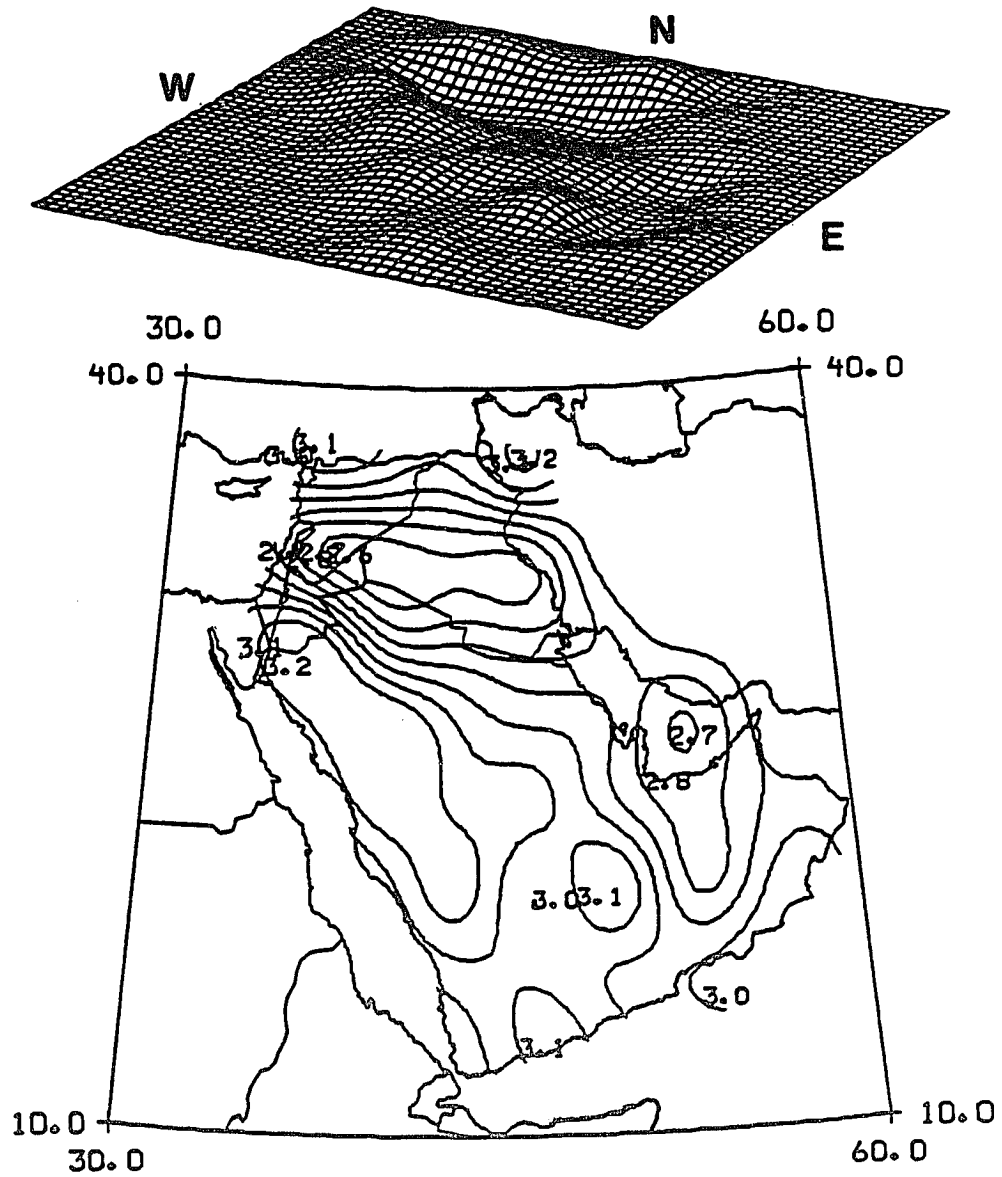
Figure 4.39. Lateral variation of shear velocity in the Arabian plate at depth of 5 km. The contour values are in km/sec.
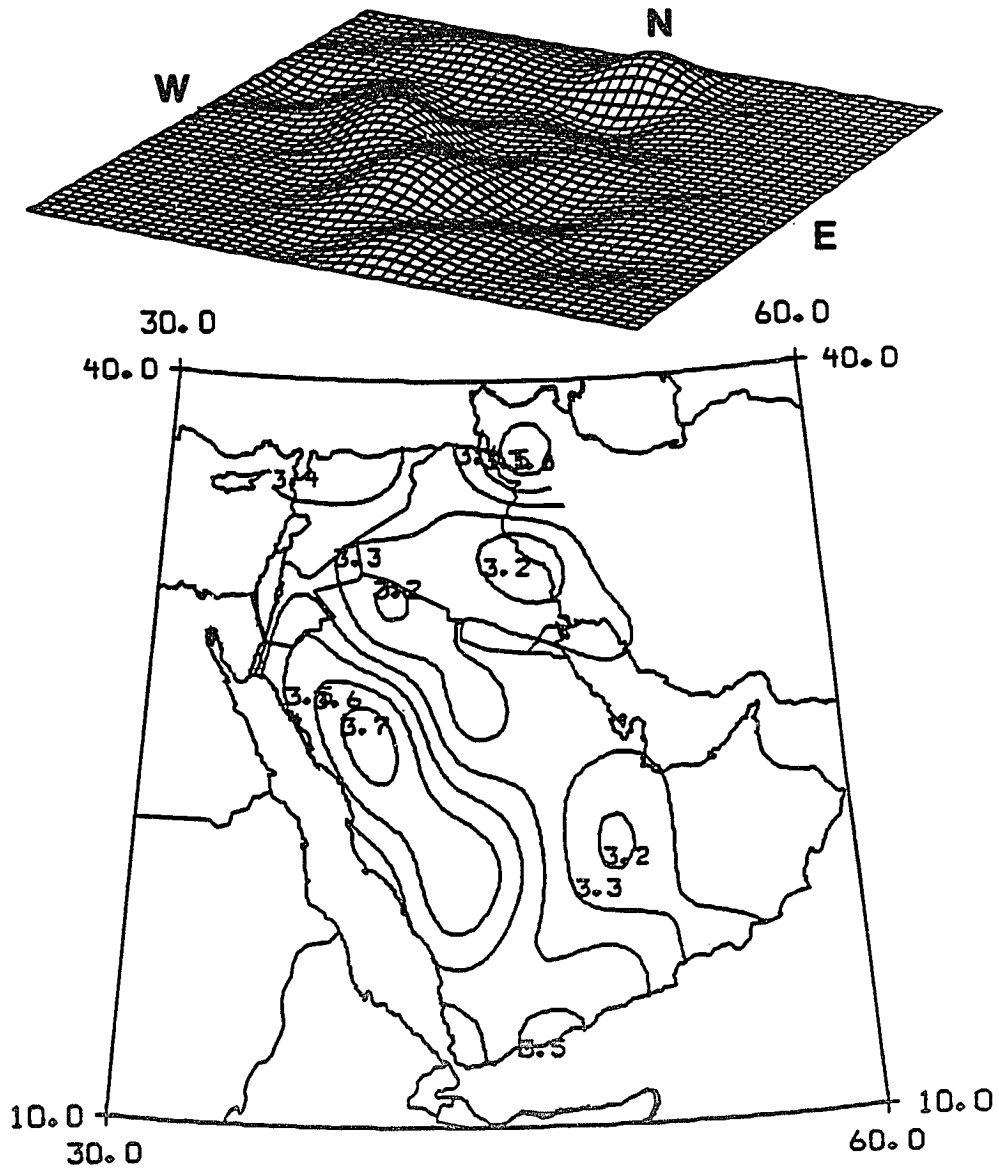
Figure 4.40. Lateral variation of shear velocity in the Arabian plate at depth of 10 km. The contour values are in km/sec.
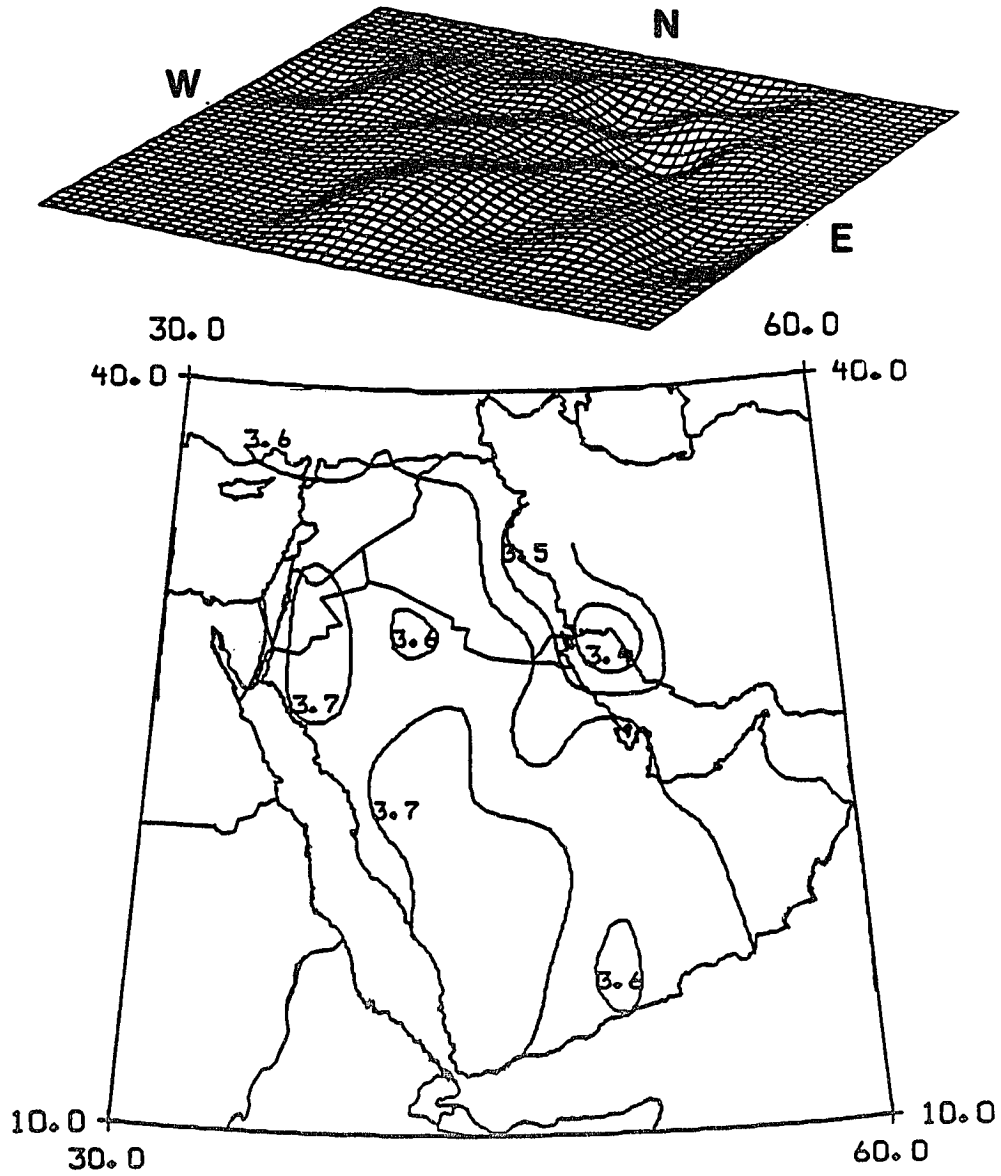
Figure 4.41. Lateral variation of shear velocity in the Arabian plate
at depth of 15 km. The contour values are in km/sec.
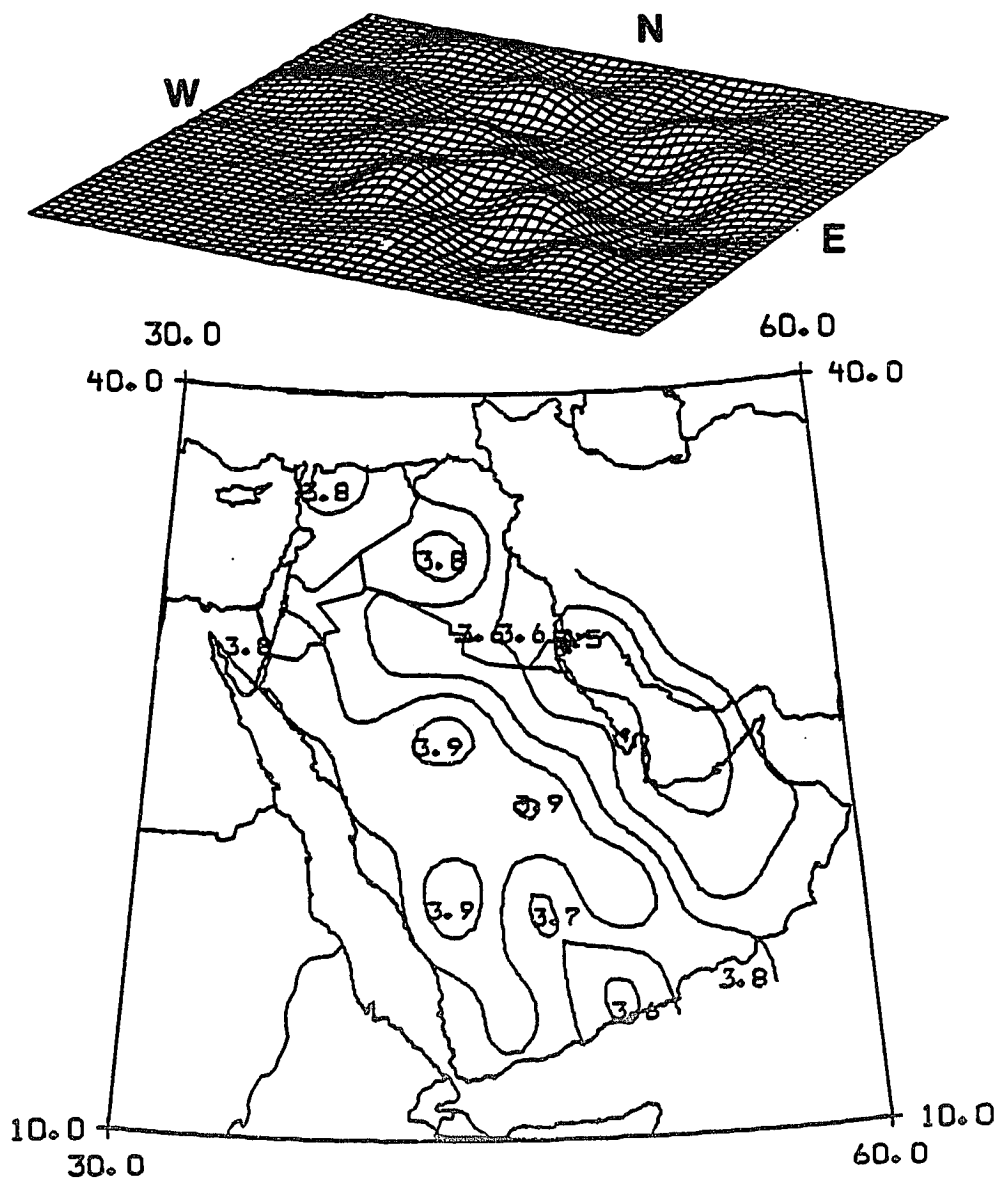
Figure 4.42. Lateral variation of shear velocity in the Arabian plate at depth of 20 km. The contour values are in km/sec.

- 200 -
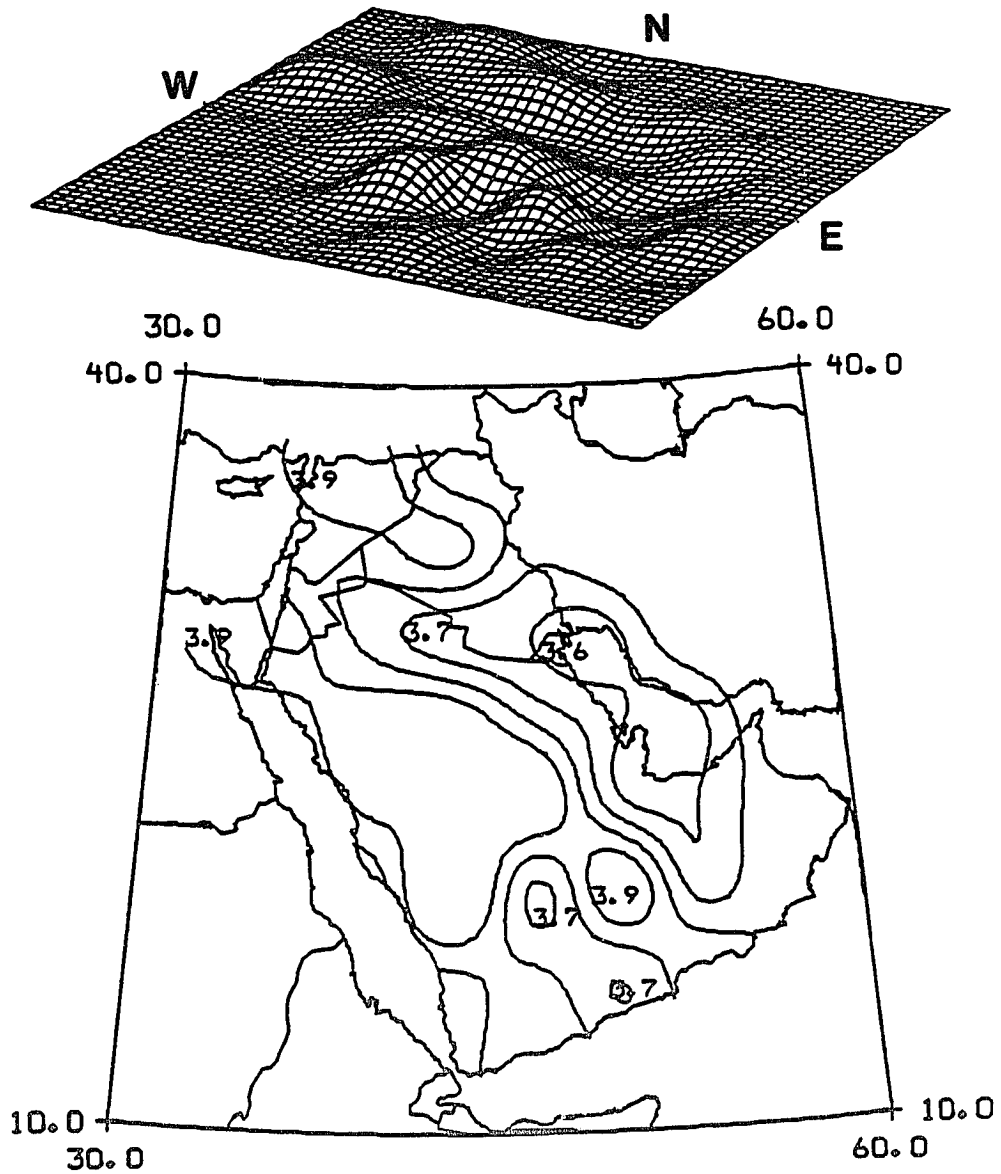
Figure 4.43. Lateral variation of shear velocity in the Arabian plate at depth of 25 km. The contour values are in km/sec.
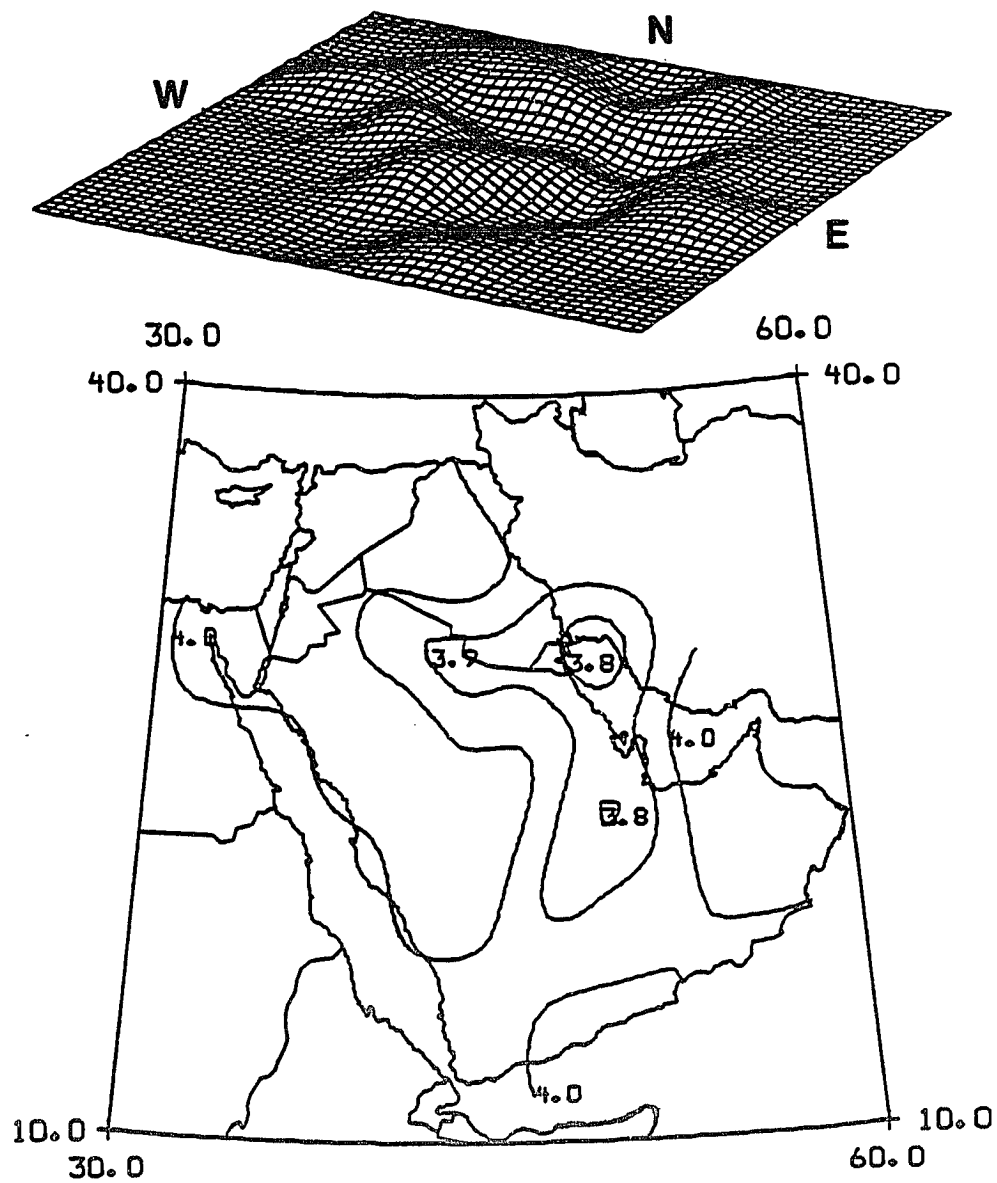
Figure 4.44. Lateral variation of shear velocity in the Arabian plate at depth of 30 km. The contour values are in km/sec.

- 202 -
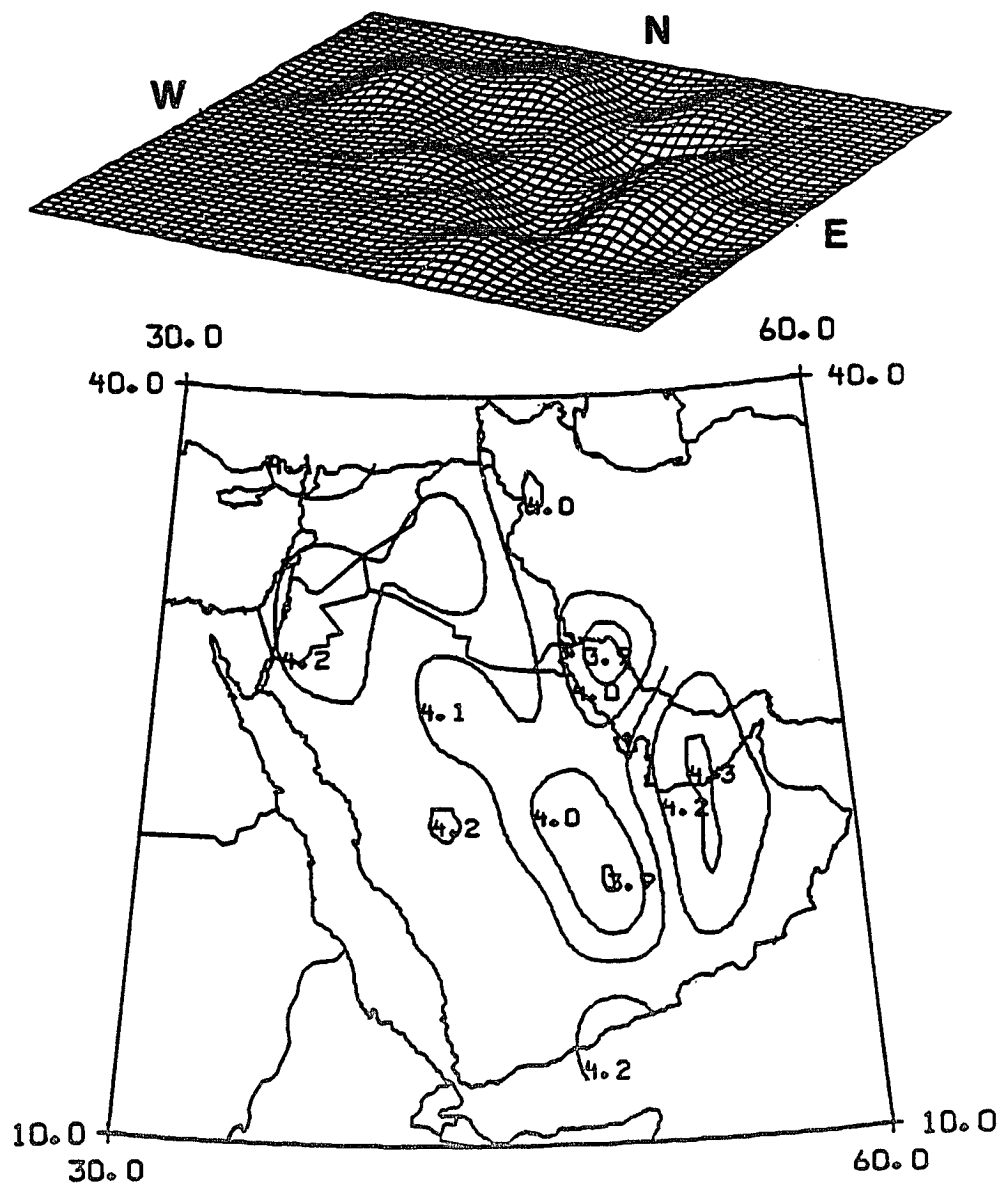
Figure 4.45. Lateral variation of shear velocity in the Arabian plate at depth of 35 km. The contour values are in km/sec.
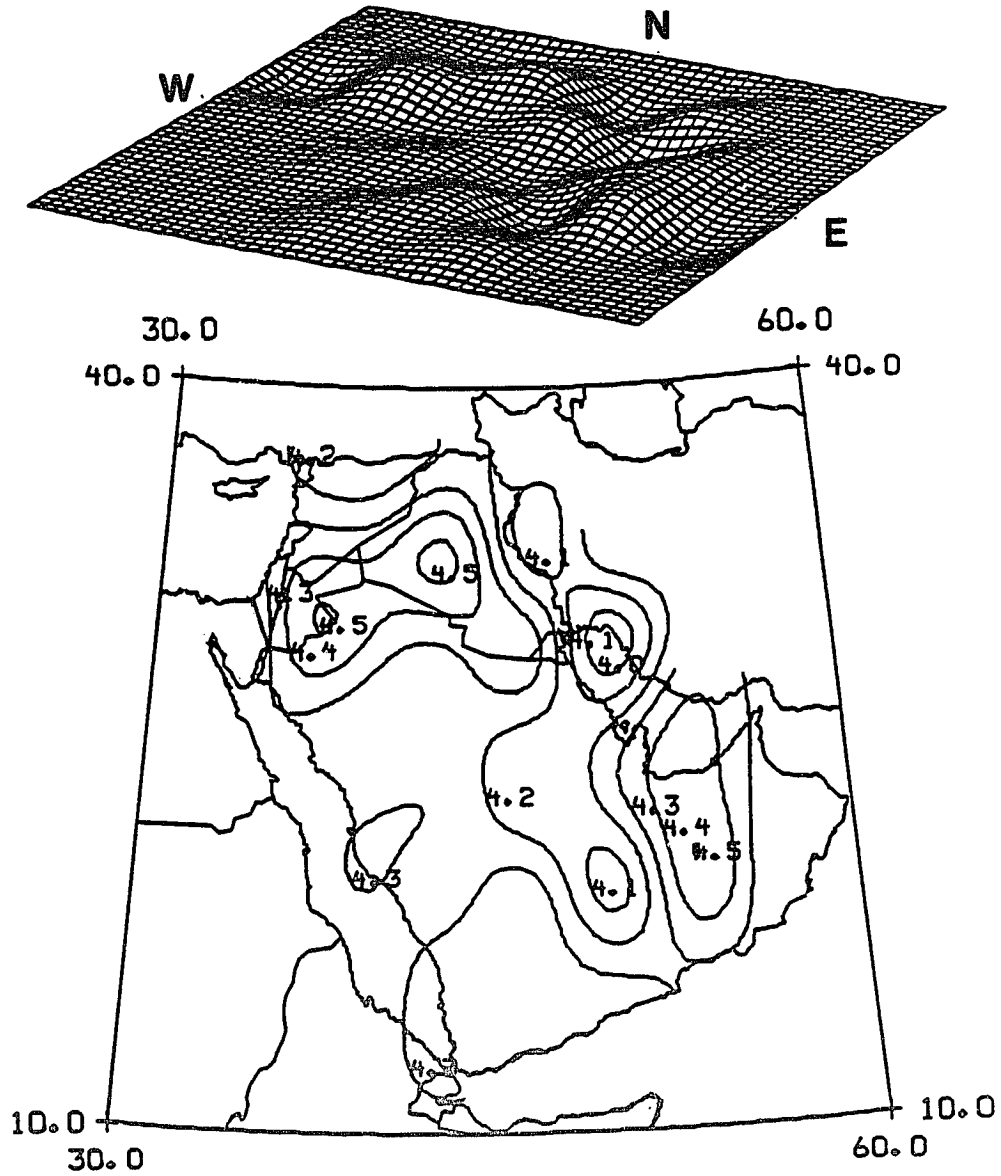
Figure 4.46. Lateral variation of shear velocity in the Arabian plate at depth of 40 km. The contour values are in km/sec.

- 204 -
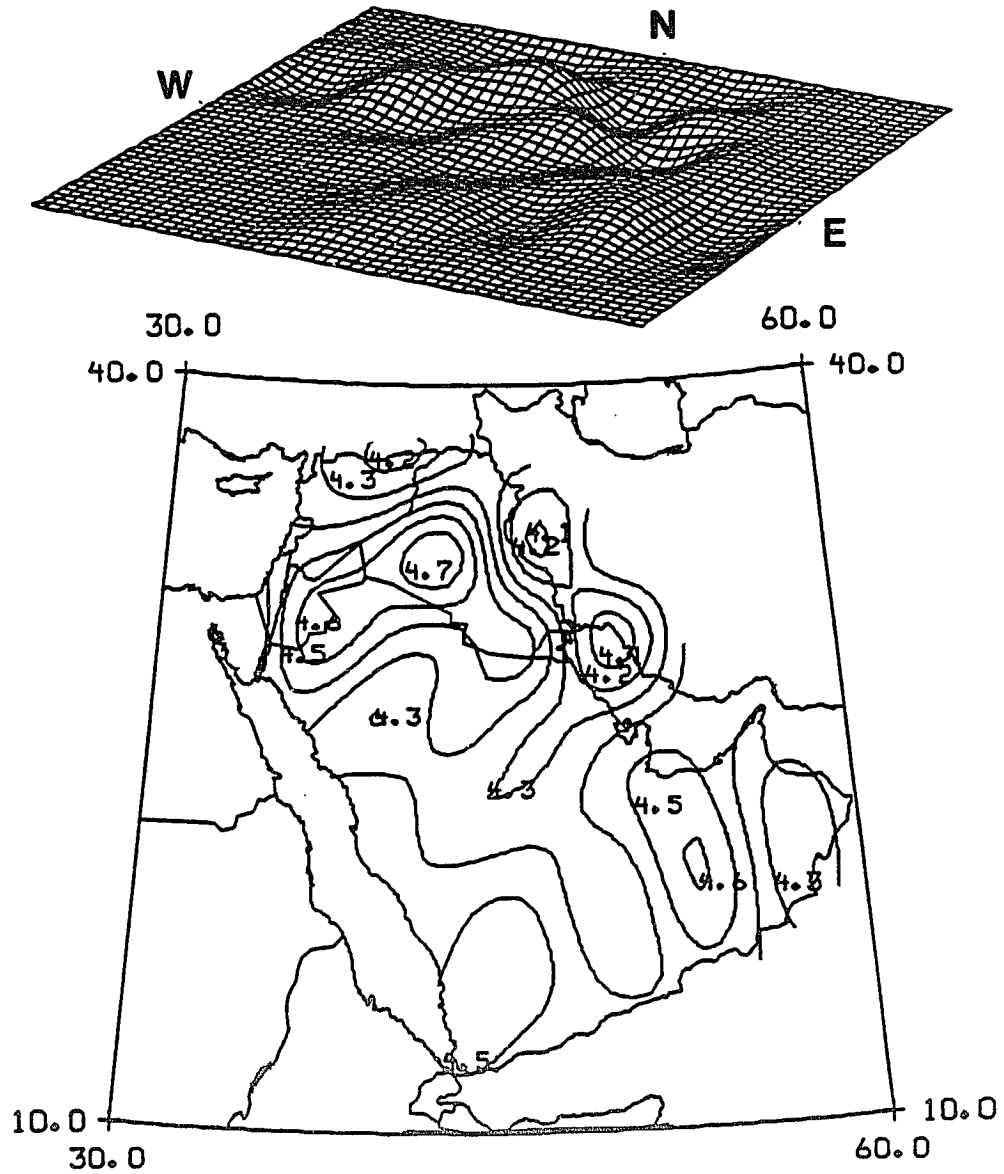
Figure 4.47. Lateral variation of shear velocity in the Arabian plate at depth of 45 km. The contour values are in km/sec.
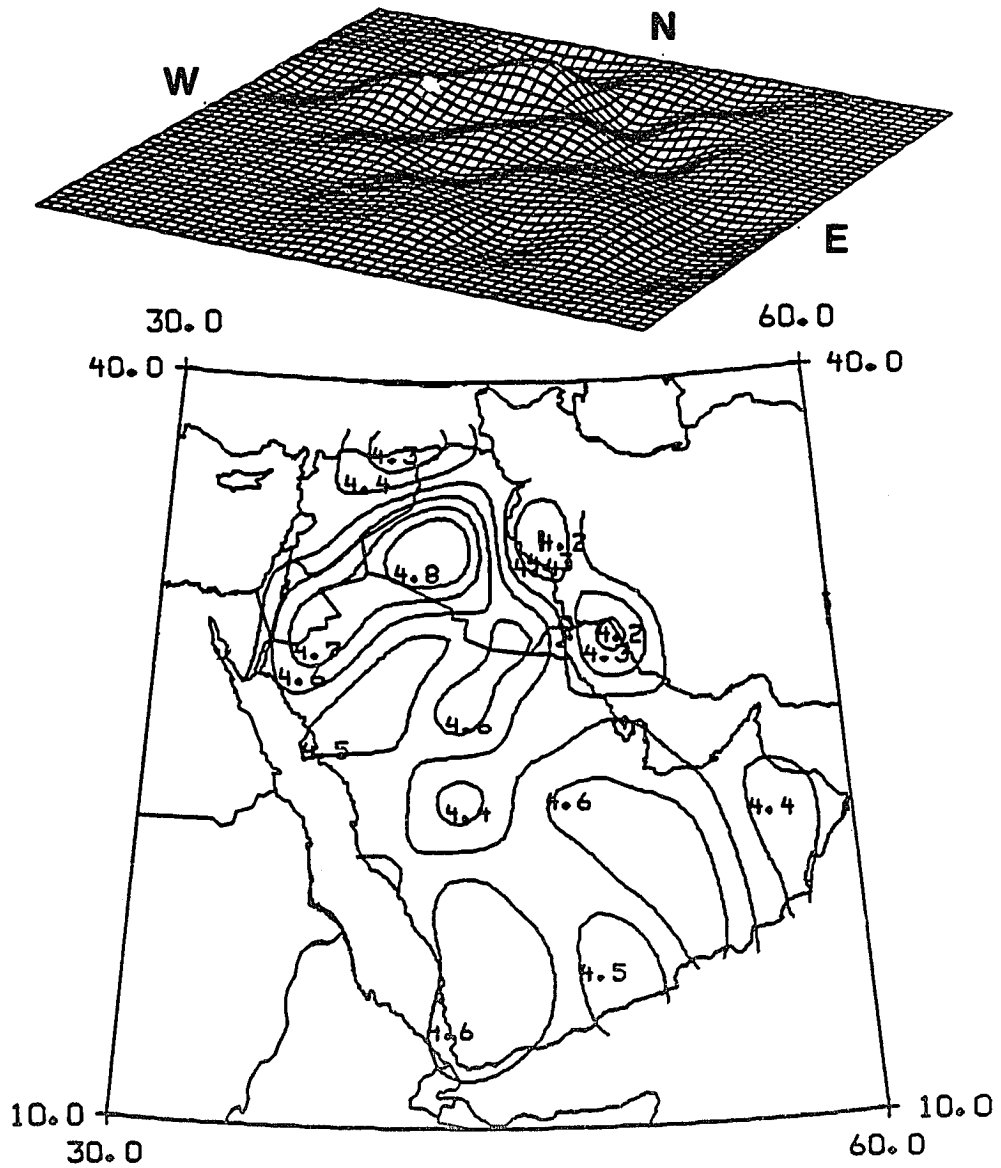
Figure 4.48. Lateral variation of shear velocity in the Arabian plate
at depth of 50 km. The contour values are in km/sec.

- 206 -
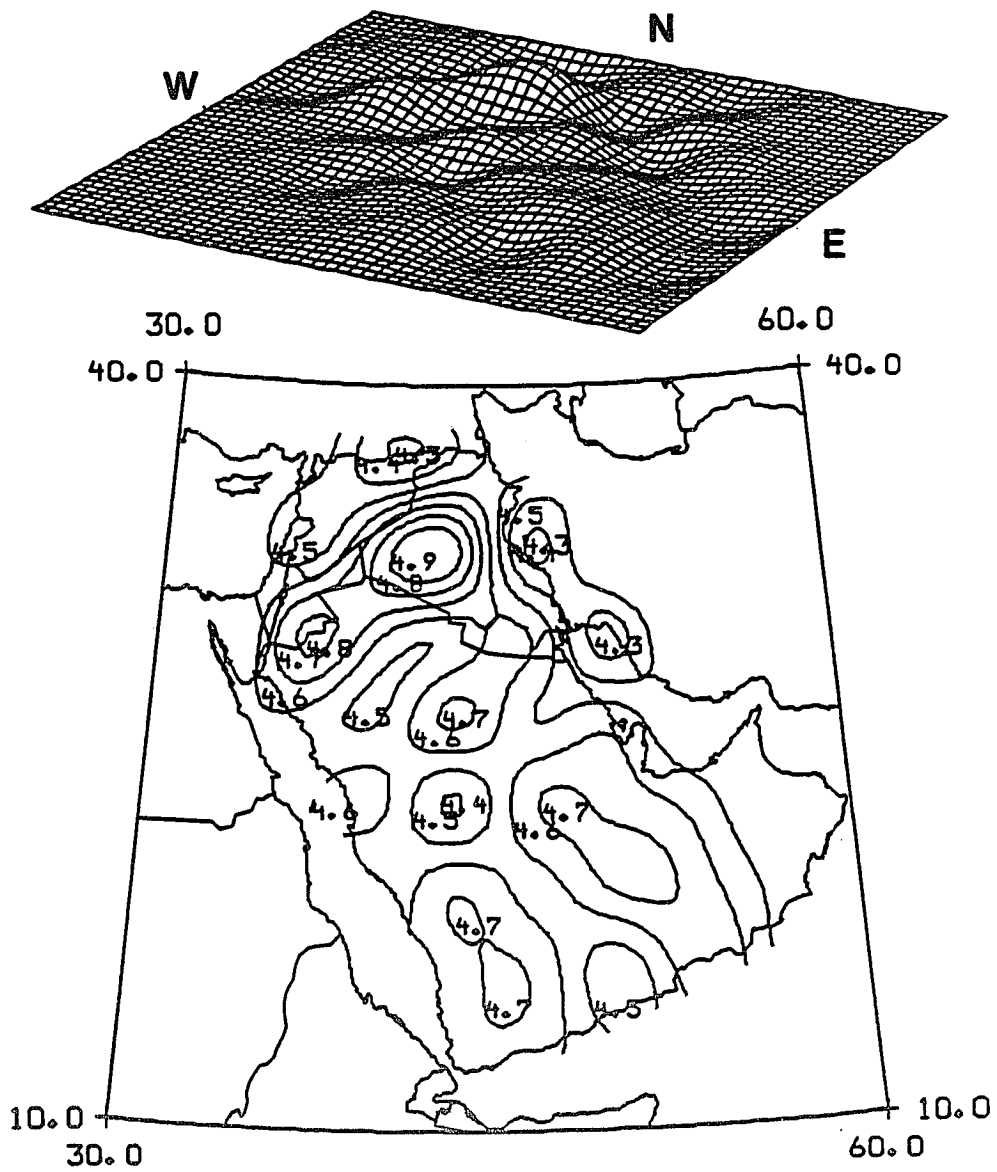
Figure 4.49. Lateral variation of shear velocity in the Arabian plate at depth of 55 km. The contour values are in km/sec.
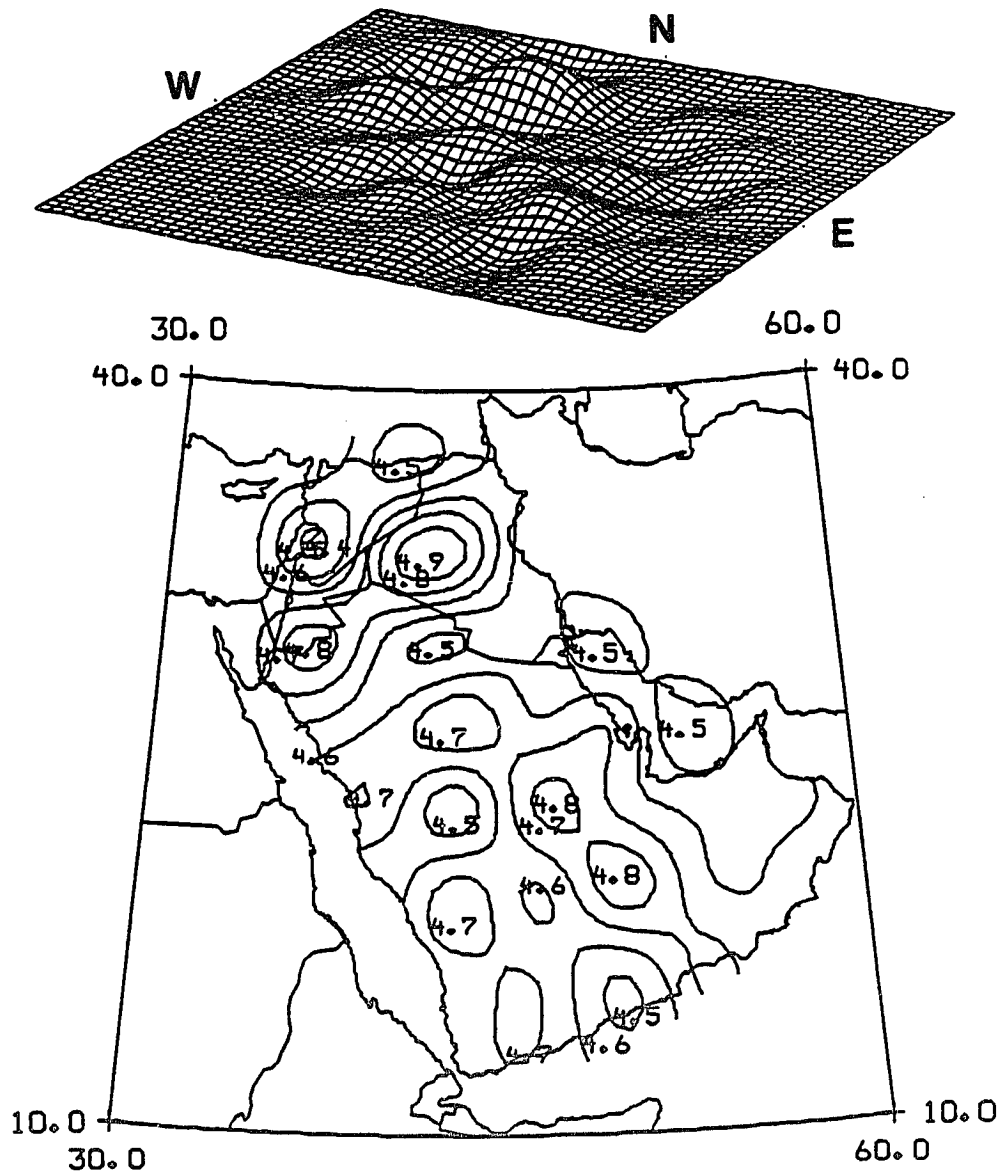
Figure 4.50. Lateral variation of shear velocity in the Arabian plate at depth of 60 km. The contour values are in km/sec.
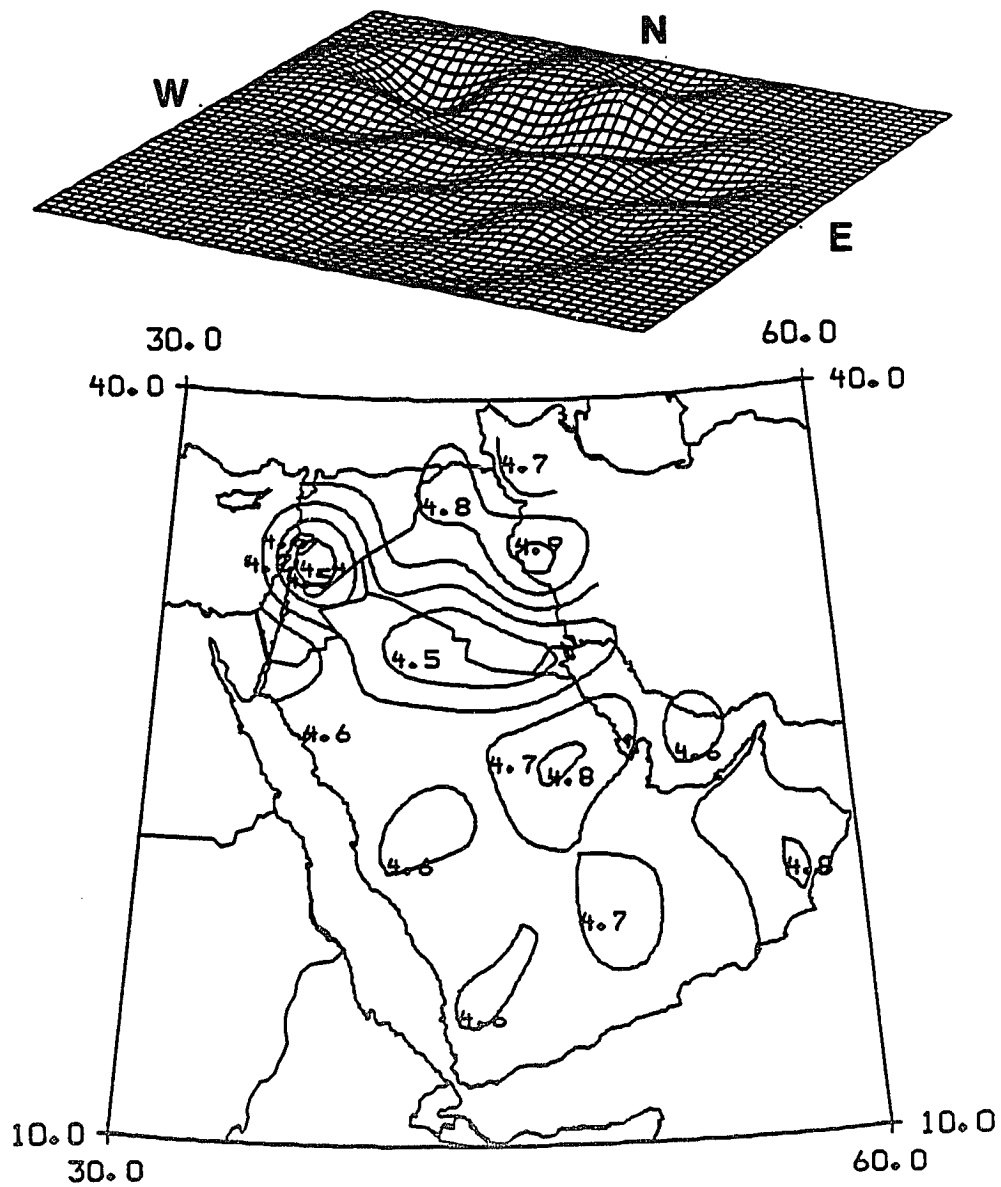
Figure 4.51. Lateral variation of shear velocity in the Arabian plate at depth of 70 km. The contour values are in km/sec.
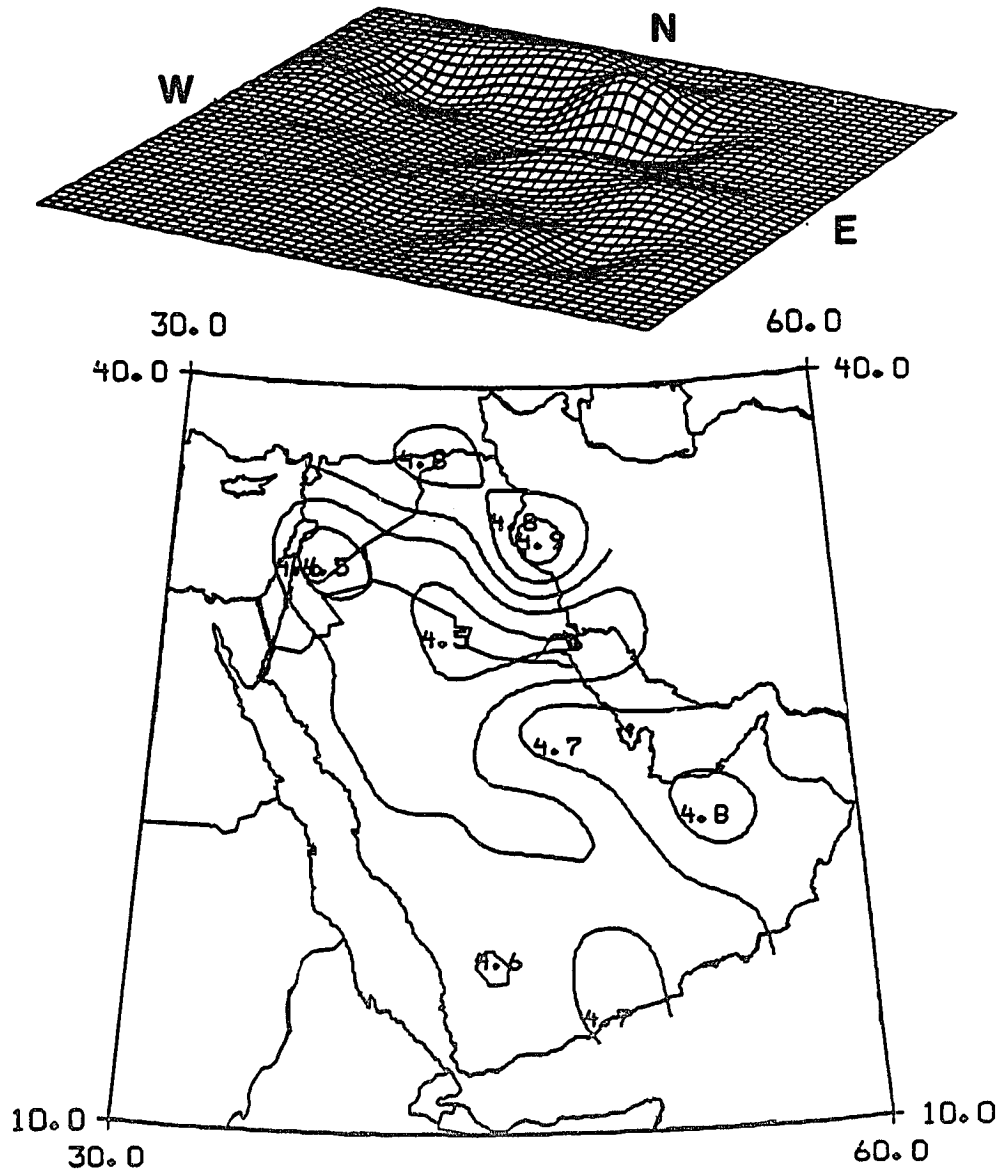
Figure 4.52. Lateral variation of shear velocity in the Arabian plate at depth of 80 km. The contour values are in km/sec.

basement in the region.

The second important result of this analysis involves the shear velocity variation within the upper crust, lower crust, and effect of the Mesopotamian sedimentary layer on the structure of the plate. Figures 4.41 and 4.43 show that, at 15.0-25.0 km depth, the differences in shear velocity between the various tectonic regions decreases to approximately 0.3 km/sec. The higher velocities are observed under the shield, and the lower velocities are under the foredeep. Although, this lateral velocity distribution is familiar, because it simply follows that of the shallower layers which are influenced by the configuration of the shield and foredeep structures, it is the depth at which this pattern can be observed that is interesting. Figures 4.44-4.45 show the effect of the exceptionally thick sedimentary column of the foredeep can be observed to a depth of at least 30.0 km. In addition, the lateral velocity variation within the lower crust seems to increase from 0.3 km/sec to 0.4 km/sec at 40.0-45.0 km depth. Figures 4.46 and 4.47 also show that the velocity under shield is no longer higher than that under the foredeep. Instead, the highest shear velocities are observed beneath the northern and western regions of the plate. This marks a significant change in the lateral velocity heterogeneity of the Arabian plate structure.

The third important result of this analysis is the observed change in shear velocity variation pattern with increasing depth. As indicated earlier, the shear velocity under the Arabian shield is higher than that under the Mesopotamian foredeep. This is evidently the case within the crust of the Arabian plate only, because below 40.0 km the isodepth contour maps presented in Figures 4.46-4.52 show a remarkable reversal in the pattern of shear velocity variation. In these figures, the contours indicate that the

velocity under the shield region is significantly lower than the rest of the plate, and that the upper mantle velocity variation is approximately 0.3-0.5 km/sec. This result supports and extends Woodhouse and Dziewonski (1984) conclusion regarding the possible existence of a low velocity anomalies along the western and southwestern Arabian plate.

4.3.2 Spatial Depth Variation

Similar to the isodepth surfaces and contour maps presented in the previous section, Figure 4.53 shows a three-dimensional model of equal velocity surfaces also derived from the grid-dispersion inversion. Based on the selected velocities of 3.0, 3.5 and 4.0 km/sec, the model shown in this figure is that of the crust of the Arabian plate. Comparison between these surfaces, clearly show significant velocity variation with depth throughout the region. Also, the pattern of observed velocity heterogeneity correlates very well with the major tectonic features. This observation is better demonstrated by the equal velocity contour maps shown in Figures 4.54-4.56. According to these figures, the contours primarily follow the structure and trend of the Arabian shield and Mesopotamian foredeep. Therefore, it is not surprising to see that the 3.0, 3.5 and 4.0 km/sec velocities are located at shallower depth within the shield and at greater depths within the foredeep. This lateral velocity distribution is undoubtedly controlled by the structural configuration of the thick sedimentary column of the foredeep.

Finally, it is important to mention that, the shield depth contours in Figure 4.54 show steeper gradient towards the north and northeast, and a gradual gradient to the east and southeast. This indicates a good agreement
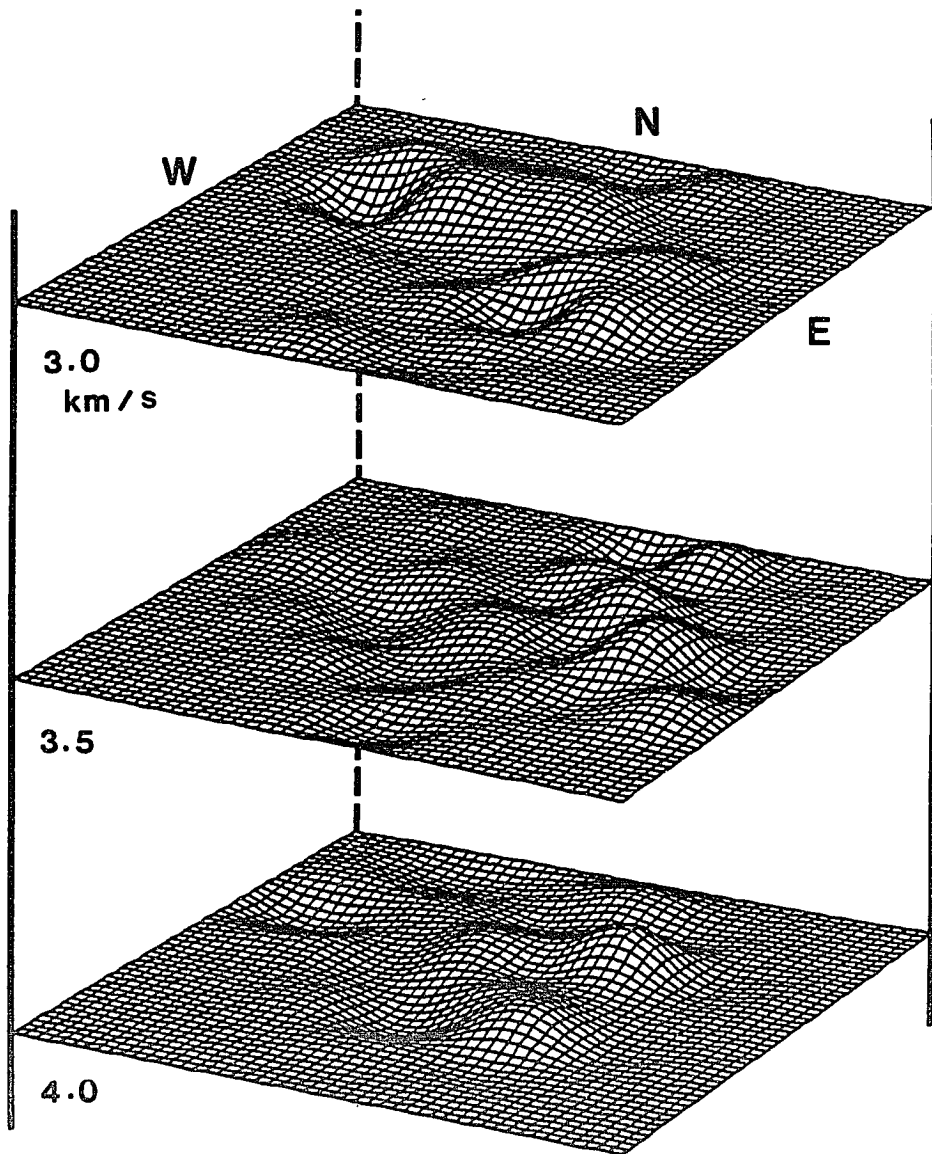
Figure 4.53. A three-dimensional illustration of the variation of 3.0, 3.5 and 4.0 km/sec shear velocities with depth in the Arabian plate.
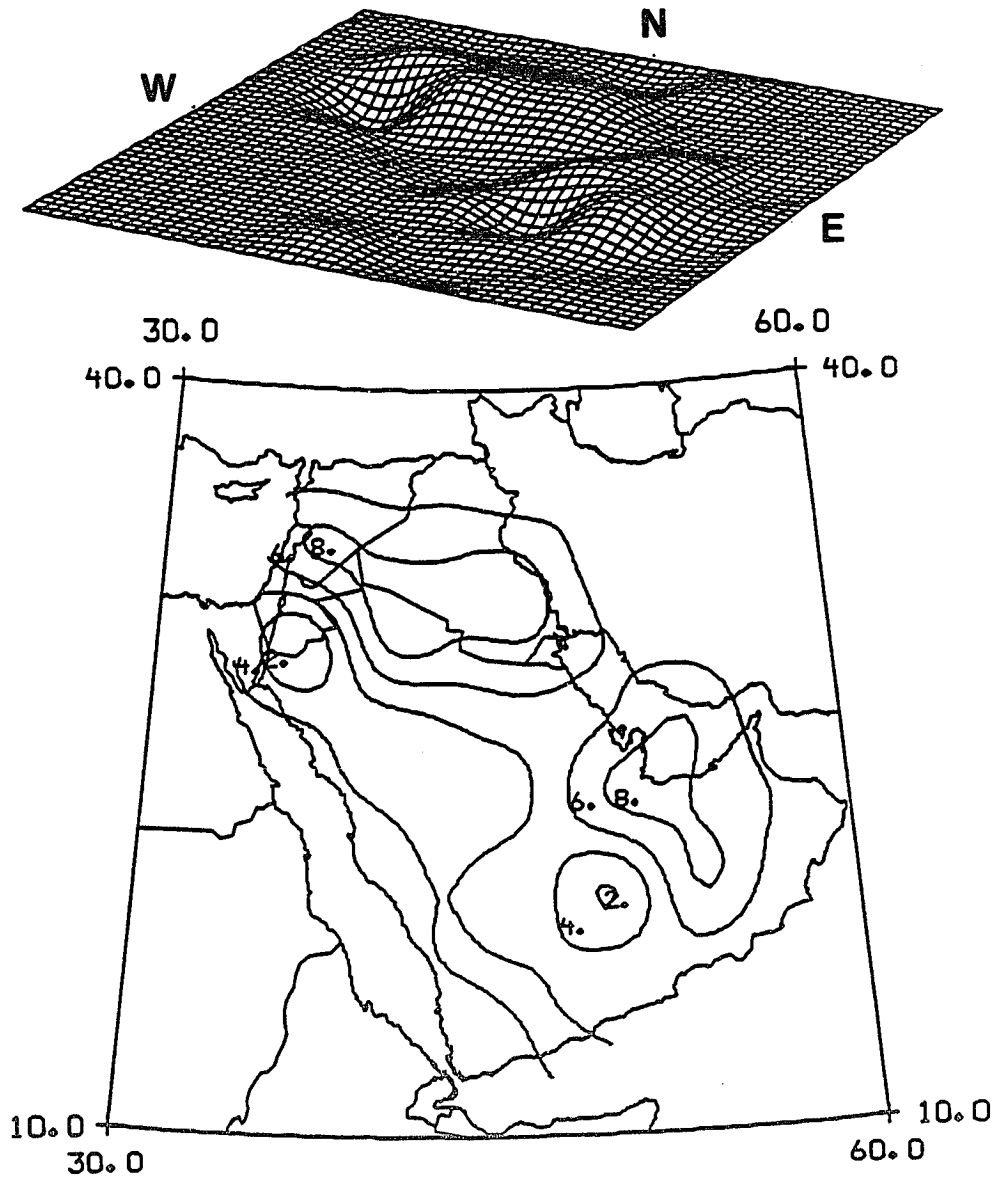
Figure 4.54. Variation of 3.0 km/sec shear velocity with depth in the Arabian plate. The contour values are in kilometers.
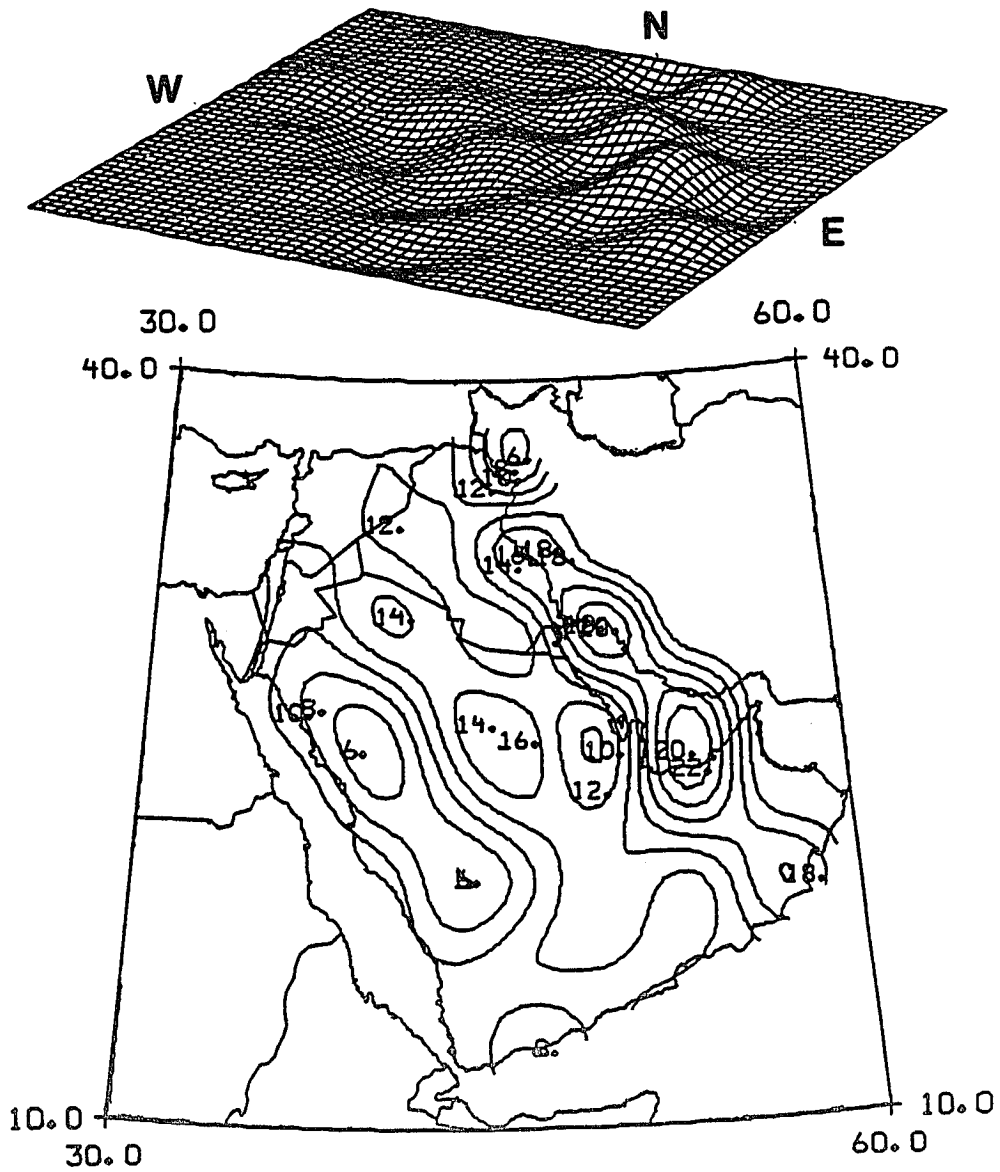
Figure 4.55. Variation of 3.5 km/sec shear velocity with depth in the Arabian plate. The contour values are in kilometers.

- 215 -
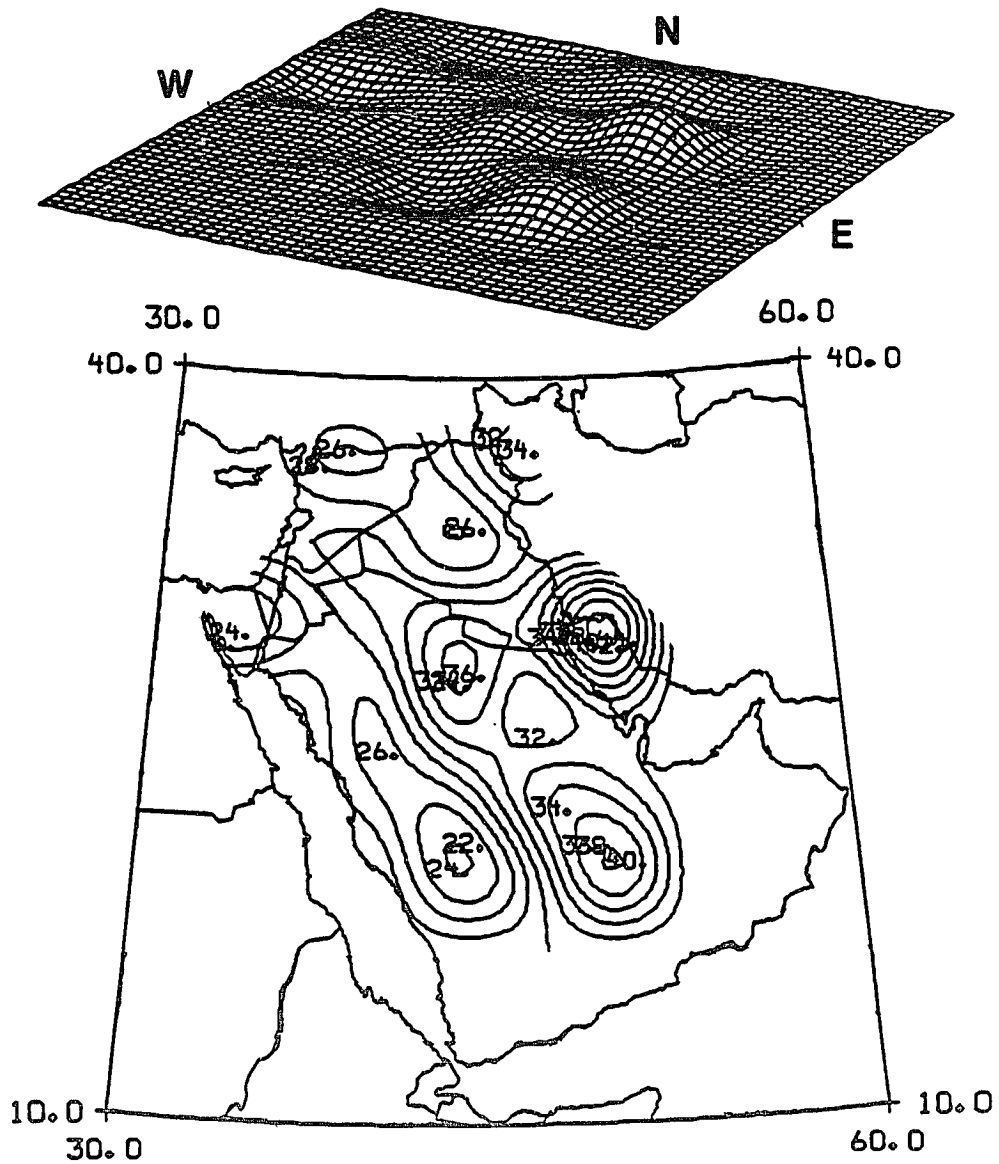
Figure 4.56. Variation of 4.0 km/sec shear velocity with depth in the Arabian plate. The contour values are in kilometers.

- 216 -

with Brown's (1972) depth contours to the top of the basement. Also, inspection of the depth contours in Figure 4.56 seems to indicate that the crustal structure of the Arabian plate increases in thickness towards the north, northeast, east and southeast as the distance from the shield increases. In other words, the crust is thicker under the foredeep and thinner under the shield.

4.4 Upper Mantle Structure

Until now all the discussion has been focused on the crustal structure of the Arabian plate. The limited range of dispersion curve periods determined in this study has obviously restricted the inverted models to the current depth of 100.0 km. Attempts to estimate the structure of the upper mantle using this data resulted in unacceptable degradation of resolution with increasing depth. Also, as mentioned earlier, no single-station phase velocities are determined in this study, because until recently the number of of published reliable focal mechanism solutions has been scarce, and the waveforms for these events were not available for analysis. Therefore, in order to derive deep shear velocity model, as well as compare the estimated dispersion curves, the mixed-path data is augmented with other Rayleigh wave group and phase velocity dispersion curves from previous studies.

Tables 4.33, 4.34 and 4.35 show the phase and group velocity dispersion data estimated by Knopoff and Fouda (1975), Niazi (1968) and Arkhangel'skaya et al. (1974), respectively. The Knopoff and Fouda (1975) two-station phase velocities are the most comprehensive, because of their long period range of 22.7-166.7 sec, and the three different paths that

Table 4.33. Knopoff and Fouda (1975) two-station dispersion data for various paths across the Arabian plate.

| Period (sec) | Rayleigh Wave Fundamental-Mode Phase Velocity | | | |
	SHI - HLW Velocity (km/sec)	JER - SHI Velocity (km/sec)	SHI - AAE Velocity (km/sec)	AR Velocity (km/sec)
22.7	3.74	3.85	3.57	3.74
30.1	3.94	3.93	3.80	3.94
35.2	4.00	3.97	3.92	4.00
41.0	4.02	4.00	3.98	4.02
50.0	4.04	4.03	4.01	4.04
65.8	4.06	4.05	4.02	4.06
78.1	4.08	4.08	4.04	4.08
89.3	4.10	4.11	4.05	4.11
100.0	4.12	4.14	4.07	4.14
113.6	4.17	4.19	4.10	4.19
131.6	4.25	4.25	4.14	4.25
147.1	4.33	4.30	4.19	4.30
166.7	4.43	4.38	4.25	4.38

Table 4.34. Niazi (1968) two-station dispersion data across the Arabian plate.

Rayleigh Wave Fundamental-Mode SHI - AAE		
Period (sec)	Phase Velocity (km/sec)	Group Velocity (km/sec)
20.0	3.46	2.79
25.0	3.67	2.94
30.0	3.82	3.17
35.0	3.93	3.36
40.0	4.05	3.54
45.0	4.12	3.66

Table 4.35. Arkhangel'skaya et al. (1974) regionalized dispersion data for path II across the Arabian plate.

Group Velocity Fundamental-Mode - Path II		
Period (sec)	Rayleigh Wave Velocity (km/sec)	Love Wave Velocity (km/sec)
15.0	2.89	3.31
20.0	2.94	3.36
25.0	3.11	3.46
30.0	3.35	3.54
35.0	3.51	3.69
40.0	—	3.83

connect between stations SHI-HLW (29.8583° N, 31.3417° E), JER-SHI and SHI-AAE (9.0292° N, 38.7656° E). The AR path in Table 4.33, represents Knopoff and Fouda (1975) average dispersion curve for the entire plate. The Niazi (1968) two-station data cover a limited period range, and extend over a path between SHI-AAE stations. Arkhangel'skaya et al. (1974) regionalized Rayleigh wave dispersion data are even more limited, and cover a path that runs in north-south direction parallel to northwestern boundary of the Arabian plate. Their Love wave dispersion data is listed in Table 4.35 for completeness, but not used for either inversion or comparison. The azimuths of both Knopoff and Fouda (1975) and Niazi (1968) paths roughly coincide with those of S212, S267, E84 and J89 shown in Figure 3.13-3.16.

Figure 4.57 through 4.64 show examples of the combined Rayleigh wave group and phase velocity dispersion curves. Also, the nomenclature used to identify the augmented data sets consist of two letters referring to the source of previous study and the station path name used in this study. For example, ARS212 refers to the average dispersion data (AR) listed in Table 4.33, and station SHI path S212, whereas JSJ89 stands for Knopoff and Fouda (1975) JER-SHI path and station JER path J89. Also, in these figures the group velocity fundamental (GF) and first higher (GH1) modes are from this study. The fundamental-mode phase velocity curves (PF) are interpolated from Knopoff and Fouda (1975) data. The circles, which are labeled NSA, represent Niazi (1968) fundamental-mode group and phase velocities. The solid line in these figures represents the theoretical dispersion curves derived from the inverted models. Note that, according to Figure 4.57, Niazi's (1968) group and phase velocities seem to correlate better
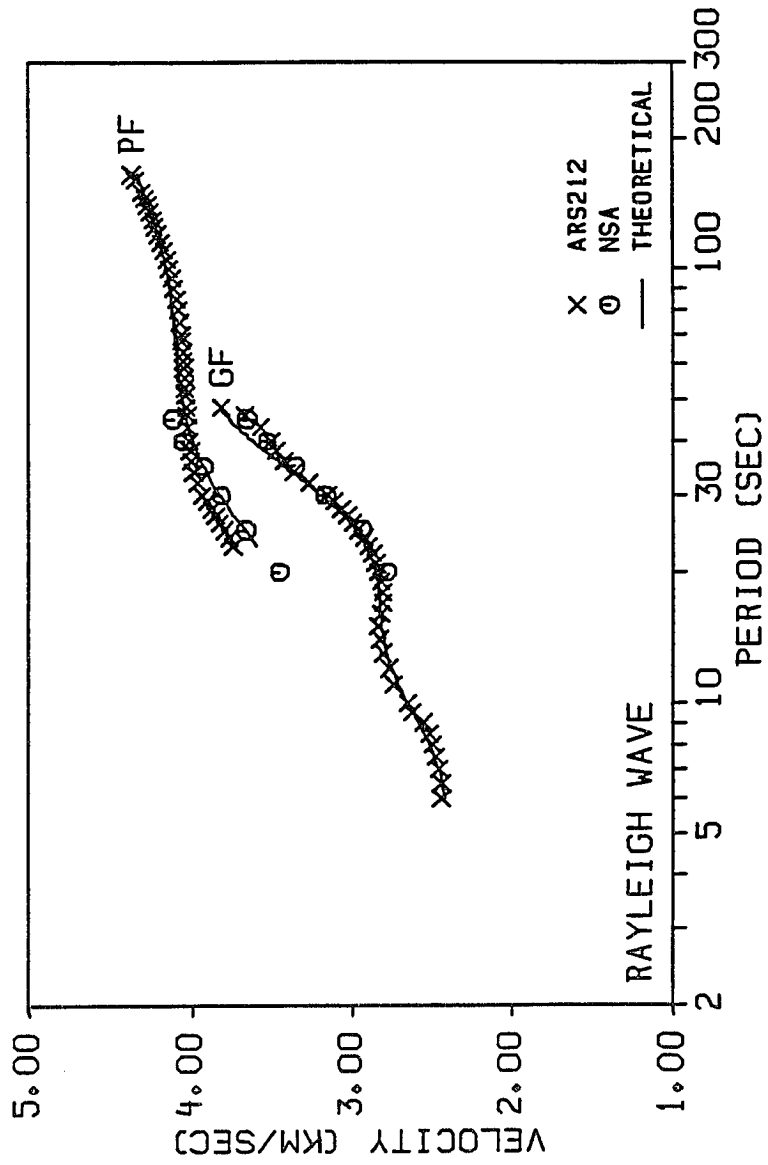
Figure 4.57. An example of augmented group and phase velocity dispersion curves used to estimate the deep velocity structure of the Arabian plate. The group velocities (GF and GHI) are those obtained in this study for path S212 and by Niazi (1968). The AR phase velocities (PF) are calculated by Knopoff and Fouda (1975).

- 221 -
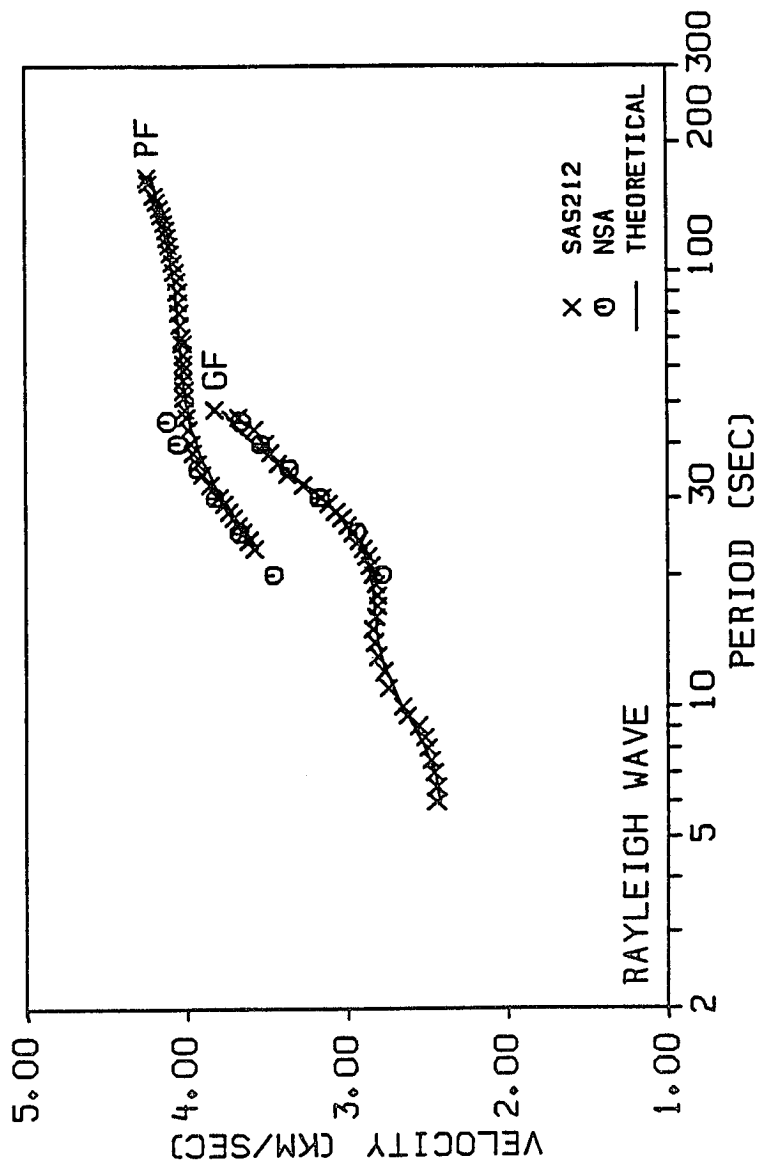
Figure 4.58. An example of augmented group and phase velocity dispersion curves used to estimate the deep velocity structure of the Arabian plate. The group velocities (GF and GH1) are those obtained in this study for path S212 and by Niazi (1968). The SHI-AAE phase velocities (PF) are calculated by Knopoff and Fouda (1975).

- 222 -
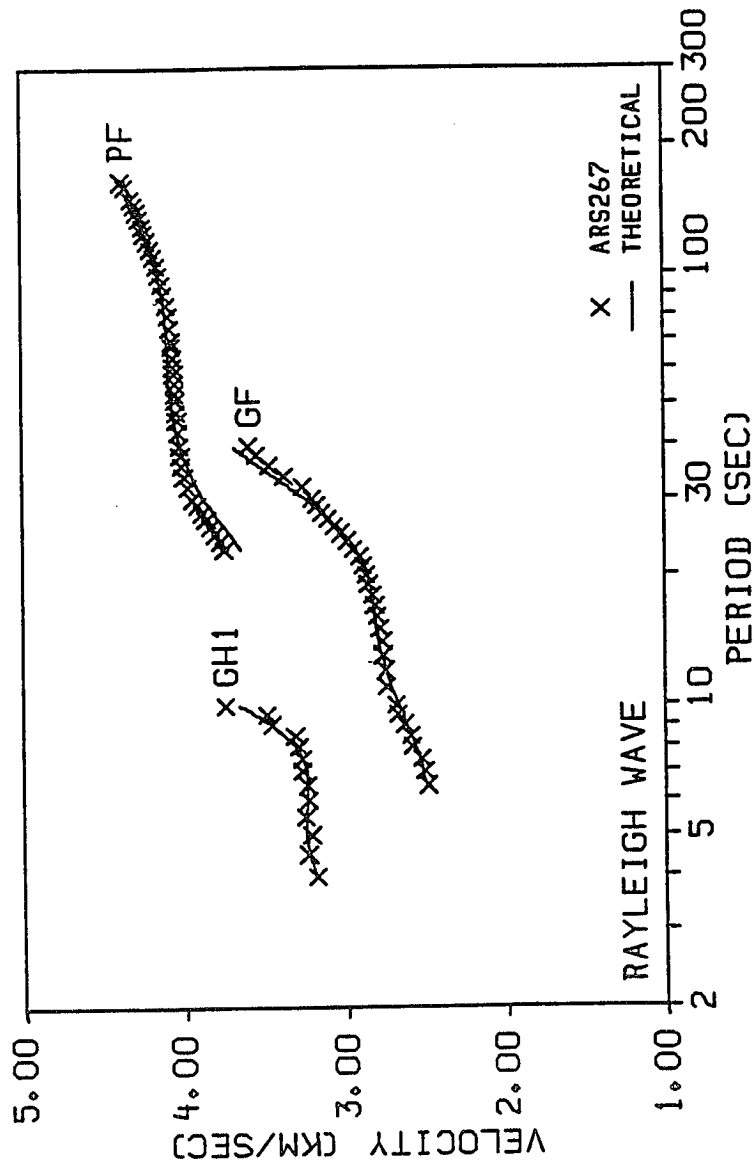
Figure 4.59. An example of augmented group and phase velocity dispersion curves used to estimate the deep velocity structure of the Arabian plate. The group velocities (GF and GH1) are those obtained in this study for path S267, and AR phase velocities (PF) are calculated by Knopoff and Fouda (1975).

- 223 -
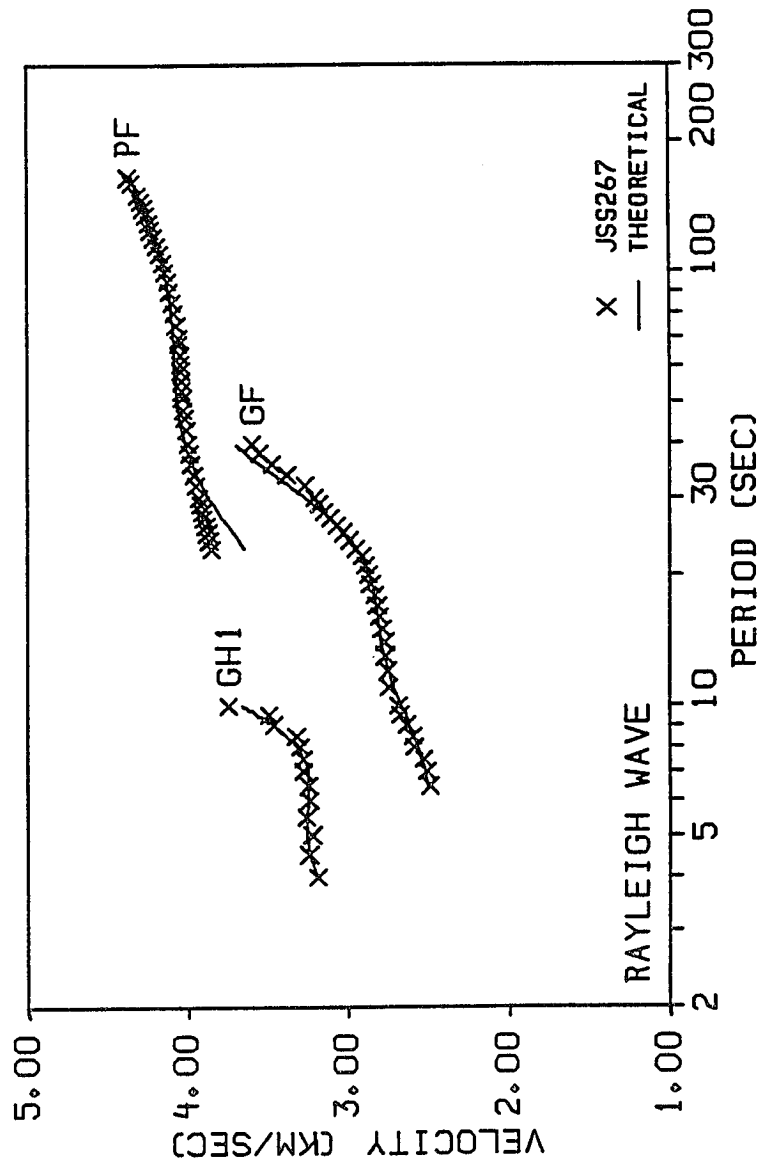
Figure 4.60. An example of augmented group and phase velocity dispersion curves used to estimate the deep velocity structure of the Arabian plate. The group velocities (GF and GH1) are those obtained in this study for path S267, and JER-SHI phase velocities (PF) are calculated by Knopoff and Fouda (1975). Fouda (1975).
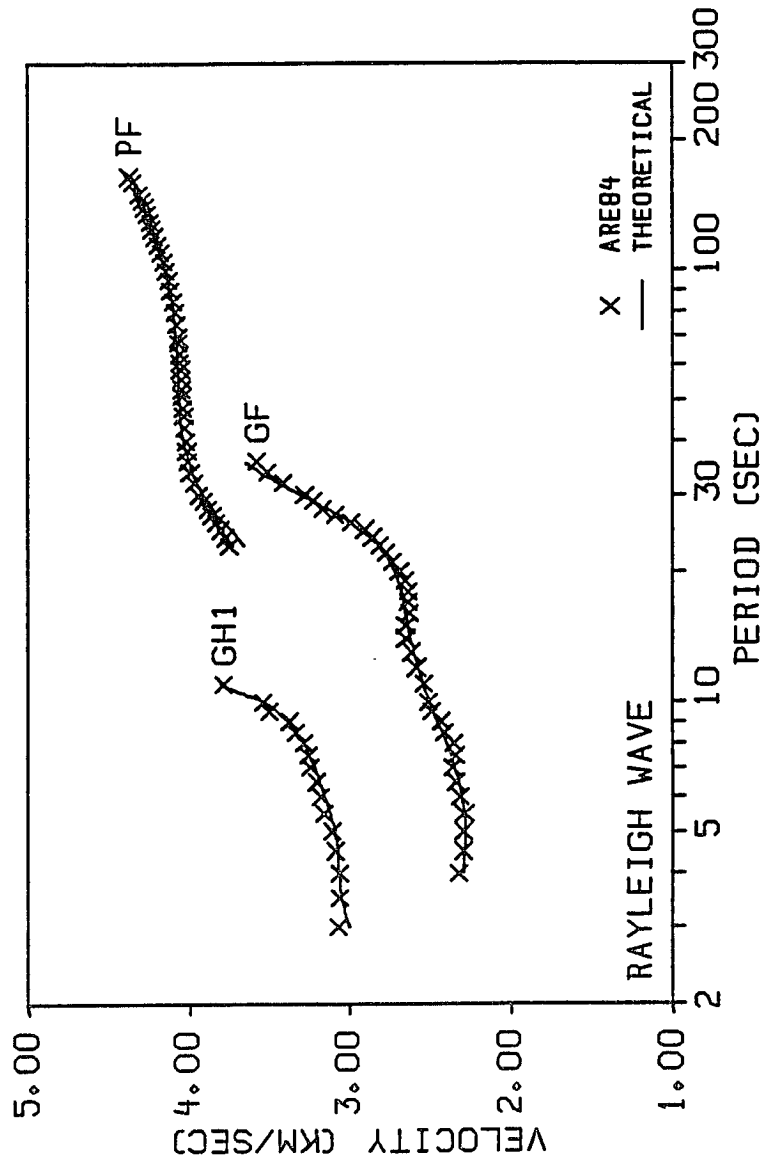
Figure 4.61. An example of augmented group and phase velocity dispersion curves used to estimate the deep velocity structure of the Arabian plate. The group velocities (GF and GH1) are those obtained in this study for path E84, and AR phase velocities (PF) are calculated by Knopoff and Fouda (1975).
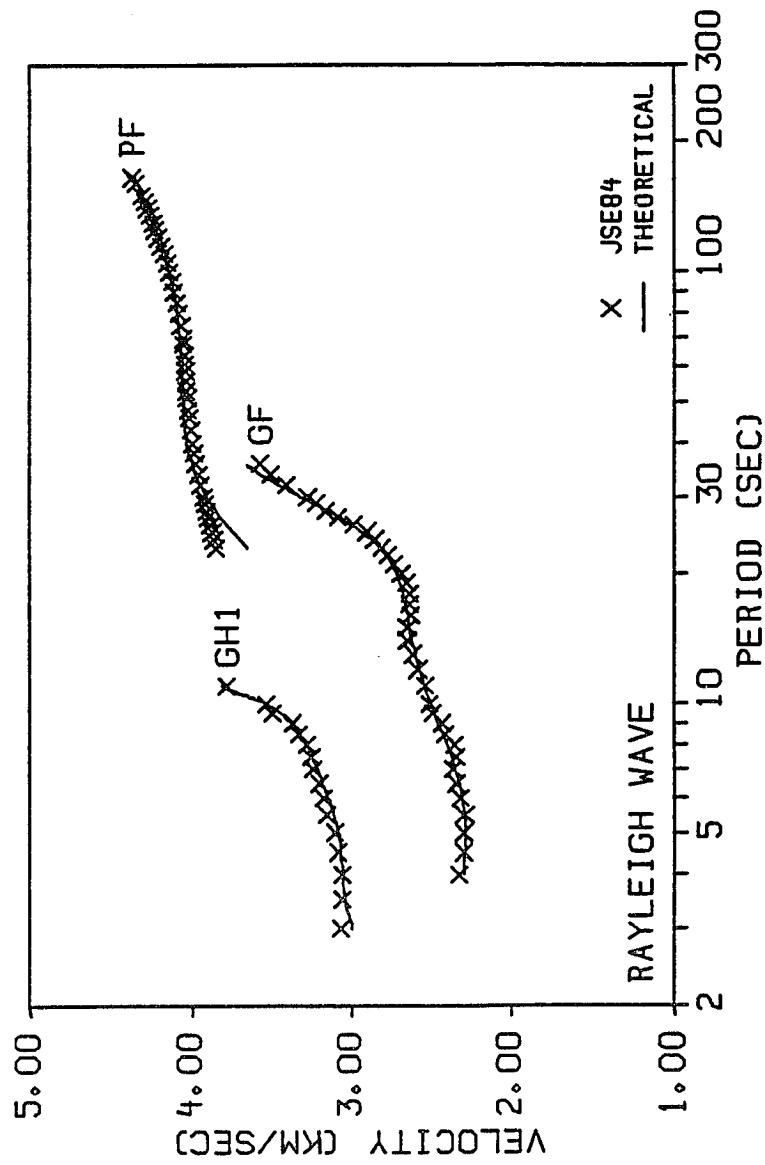
Figure 4.62. An example of augmented group and phase velocity dispersion curves used to estimate the deep velocity structure of the Arabian plate. The group velocities (GF and GF1) are those obtained in this study for path E84, and JER-SHI phase velocities (PF) are calculated by Knopoff and Fouda (1975).
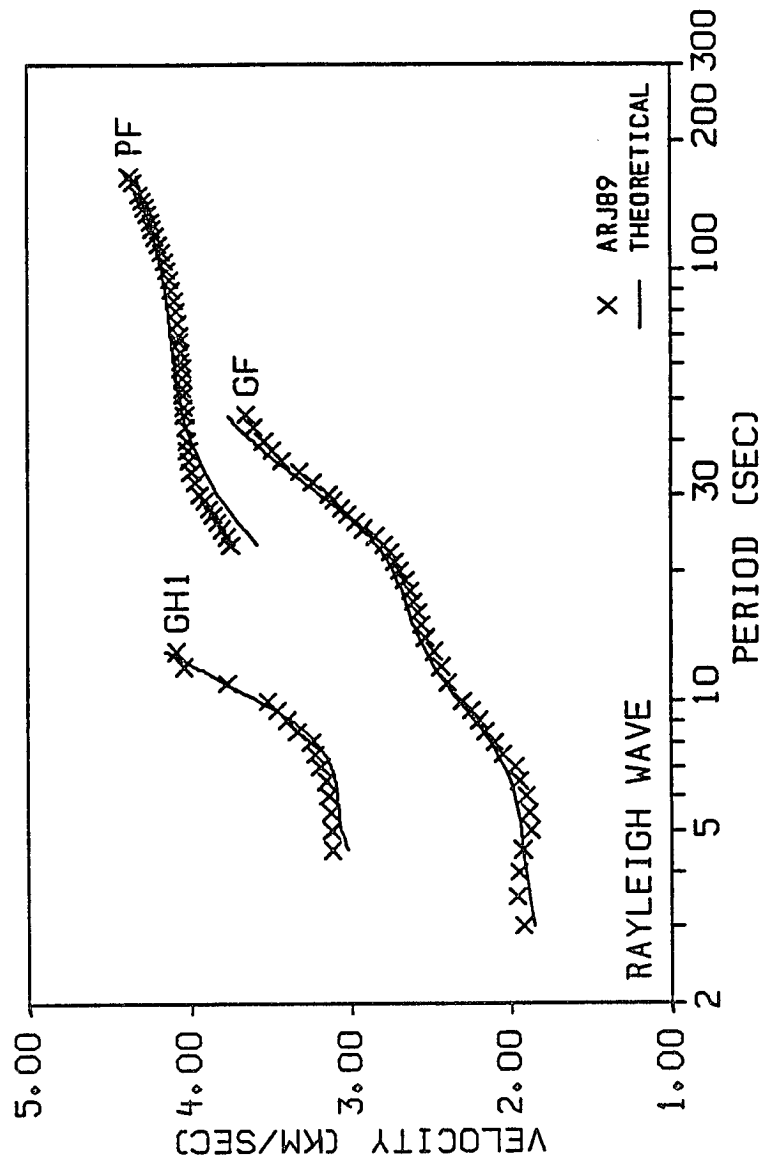
Figure 4.63. An example of augmented group and phase velocity dispersion curves used to estimate the deep velocity structure of the Arabian plate. The group velocities (GF and GH1) are those obtained in this study for path J89, and AR phase velocities (PF) are calculated by Knopoff and

- 227 -
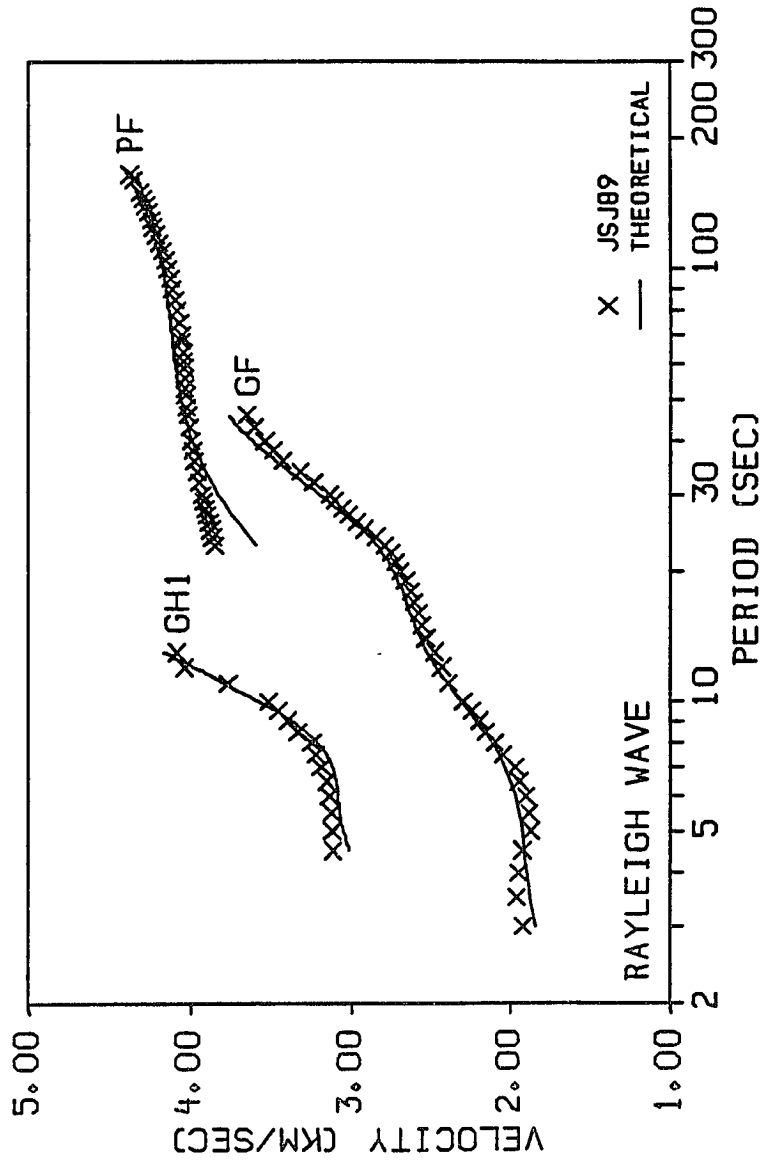
Figure 4.64. An example of augmented group and phase velocity dispersion curves used to estimate the deep velocity structure of the Arabian plate. The group velocities (GF and GF1) are those obtained in this study for path J89, and JER-SHI phase velocities (PF) are calculated by Knopoff and Fouda (1975).

- 228 -

with path S212 group velocities and the theoretical dispersion curve than with Knopoff and Fouda (1975) phase velocities. However, in Figure 4.57 all data seem to correlate very well. Furthermore, the Knopoff and Fouda (1975) average phase velocities (AR) seem to be more consistent with the theoretical and group velocities estimated in this study.

The shear velocity models obtained from the inversion of augmented data are shown in Figures 4.65-4.68, and the parameters for these models are listed in Tables 4.36 through 4.46. The resolving kernels shown in these figures correspond to the models that are plotted in solid lines. The starting model used for obtaining these models consists of a single layer over a half space, that extends to a depth of 300.0 km. Common among the inverted models is that they all show the thickness of the crust is approximately 40.0 km, and gradual increase in velocity marks the location of the major discontinuities. They also show a sedimentary layer that is about 8.0 km thick. Below the Moho discontinuity, the models along paths S212, S267 and J89 all show a high-velocity layer that is approximately 100.0 km thick. Although, this finding is in contrast with Knopoff and Fouda (1975), who proposed the existence of a low-velocity channel throughout the region at a depth of 100-140 km, the models along path E84 surprisingly show the high-velocity layer to be much thinner, and ends at about 100 km depth. Instead, the top of a pronounced low-velocity channel, according to the models along paths S212, S267 and J89, starts at depth of 120.0 km and extends to a possible depth of 270.0 km. However, it should be noted that, the resolution at 270.0 km is poor, and this low-velocity layer may extend to greater depths.

Figure 4.65. Deep shear velocity model and resolving kernels estimated from the fundamental and first higher-mode group velocity for path S212, and the fundamental-mode phase velocity for AR and SHI-AAE paths obtained by Knopoff and Fouda (1975).

Table 4.36. Crustal and upper mantle velocity structure of the Arabian plate obtained from the simultaneous inversion of AR and S212 dispersion curves.

			Velocity Model ARS212			
Layer Number	Layer Depth* (km)	Layer Thickness (km)	Compressional Velocity (km/sec)	Shear Velocity (km/sec)	Density (gm/cc)	Standard Deviation (km/sec)
1	0.2	0.5	4.42	2.55	2.378	0.052
2	0.8	0.5	4.95	2.86	2.488	0.051
3	1.5	1.0	4.96	2.86	2.490	0.051
4	2.5	1.0	4.96	2.86	2.491	0.047
5	3.5	1.0	4.97	2.87	2.494	0.037
6	4.5	1.0	5.02	2.90	2.504	0.024
7	5.5	1.0	5.14	2.97	2.528	0.018
8	7.0	2.0	5.33	3.08	2.567	0.027
9	9.0	2.0	5.66	3.27	2.632	0.031
10	11.0	2.0	6.00	3.47	2.701	0.028
11	13.0	2.0	6.27	3.62	2.780	0.026
12	16.0	4.0	6.41	3.70	2.823	0.027
13	20.0	4.0	6.38	3.69	2.815	0.024
14	24.0	4.0	6.39	3.69	2.818	0.024
15	28.0	4.0	6.56	3.79	2.865	0.026
16	32.5	5.0	6.86	3.96	2.944	0.027
17	37.5	5.0	7.23	4.17	3.052	0.028
18	42.5	5.0	7.76	4.36	3.229	0.028
19	47.5	5.0	8.00	4.49	3.309	0.029
20	53.0	6.0	8.14	4.57	3.360	0.030
21	59.0	6.0	8.20	4.60	3.383	0.031
22	65.0	6.0	8.23	4.62	3.393	0.031
23	71.0	6.0	8.26	4.63	3.402	0.032
24	77.0	6.0	8.30	4.66	3.417	0.035
25	85.0	10.0	8.36	4.69	3.438	0.038
26	95.0	10.0	8.42	4.73	3.463	0.039
27	105.0	10.0	8.47	4.75	3.479	0.039
28	115.0	10.0	8.47	4.75	3.478	0.039
29	125.0	10.0	8.41	4.72	3.457	0.039
30	135.0	10.0	8.30	4.66	3.418	0.039
31	145.0	10.0	8.16	4.58	3.367	0.040
32	155.0	10.0	8.01	4.49	3.312	0.041
33	165.0	10.0	7.86	4.41	3.264	0.041
34	175.0	10.0	7.75	4.35	3.225	0.041
35	190.0	20.0	7.68	4.31	3.200	0.040
36	210.0	20.0	7.71	4.33	3.211	0.037
37	230.0	20.0	7.84	4.40	3.257	0.032
38	250.0	20.0	8.06	4.53	3.333	0.032
39	270.0	20.0	8.34	4.68	3.433	0.040
40	290.0	20.0	8.65	4.86	3.541	0.053

* from the surface to the middle of the layers.

Table 4.37. Crustal and upper mantle velocity structure of the Arabian plate obtained from the simultaneous inversion of SA and S212 dispersion curves.

			Velocity Model SAS212			
Layer Number	Layer Depth* (km)	Layer Thickness (km)	Compressional Velocity (km/sec)	Shear Velocity (km/sec)	Density (gm/cc)	Standard Deviation (km/sec)
1	0.2	0.5	4.40	2.54	2.377	0.023
2	0.8	0.5	4.93	2.85	2.485	0.022
3	1.5	1.0	4.94	2.85	2.487	0.022
4	2.5	1.0	4.95	2.86	2.488	0.021
5	3.5	1.0	4.96	2.86	2.492	0.016
6	4.5	1.0	5.02	2.90	2.503	0.011
7	5.5	1.0	5.14	2.96	2.527	0.008
8	7.0	2.0	5.33	3.08	2.566	0.012
9	9.0	2.0	5.65	3.26	2.629	0.013
10	11.0	2.0	5.98	3.45	2.696	0.012
11	13.0	2.0	6.23	3.60	2.770	0.011
12	16.0	4.0	6.37	3.68	2.812	0.012
13	20.0	4.0	6.35	3.67	2.806	0.011
14	24.0	4.0	6.36	3.67	2.809	0.010
15	28.0	4.0	6.51	3.76	2.853	0.011
16	32.5	5.0	6.78	3.91	2.923	0.012
17	37.5	5.0	7.11	4.10	3.015	0.012
18	42.5	5.0	7.62	4.28	3.181	0.012
19	47.5	5.0	7.86	4.41	3.262	0.013
20	53.0	6.0	8.02	4.50	3.317	0.013
21	59.0	6.0	8.11	4.55	3.349	0.013
22	65.0	6.0	8.16	4.58	3.366	0.014
23	71.0	6.0	8.19	4.60	3.378	0.014
24	77.0	6.0	8.22	4.61	3.388	0.015
25	85.0	10.0	8.25	4.63	3.399	0.017
26	95.0	10.0	8.27	4.64	3.408	0.017
27	105.0	10.0	8.28	4.65	3.409	0.017
28	115.0	10.0	8.25	4.63	3.398	0.017
29	125.0	10.0	8.18	4.59	3.375	0.017
30	135.0	10.0	8.09	4.54	3.343	0.017
31	145.0	10.0	7.98	4.48	3.304	0.018
32	155.0	10.0	7.88	4.42	3.268	0.018
33	165.0	10.0	7.78	4.37	3.235	0.018
34	175.0	10.0	7.70	4.32	3.209	0.018
35	190.0	20.0	7.66	4.30	3.193	0.018
36	210.0	20.0	7.68	4.31	3.200	0.016
37	230.0	20.0	7.76	4.36	3.229	0.014
38	250.0	20.0	7.90	4.44	3.277	0.014
39	270.0	20.0	8.08	4.54	3.340	0.018
40	290.0	20.0	8.28	4.65	3.412	0.023

* from the surface to the middle of the layers.
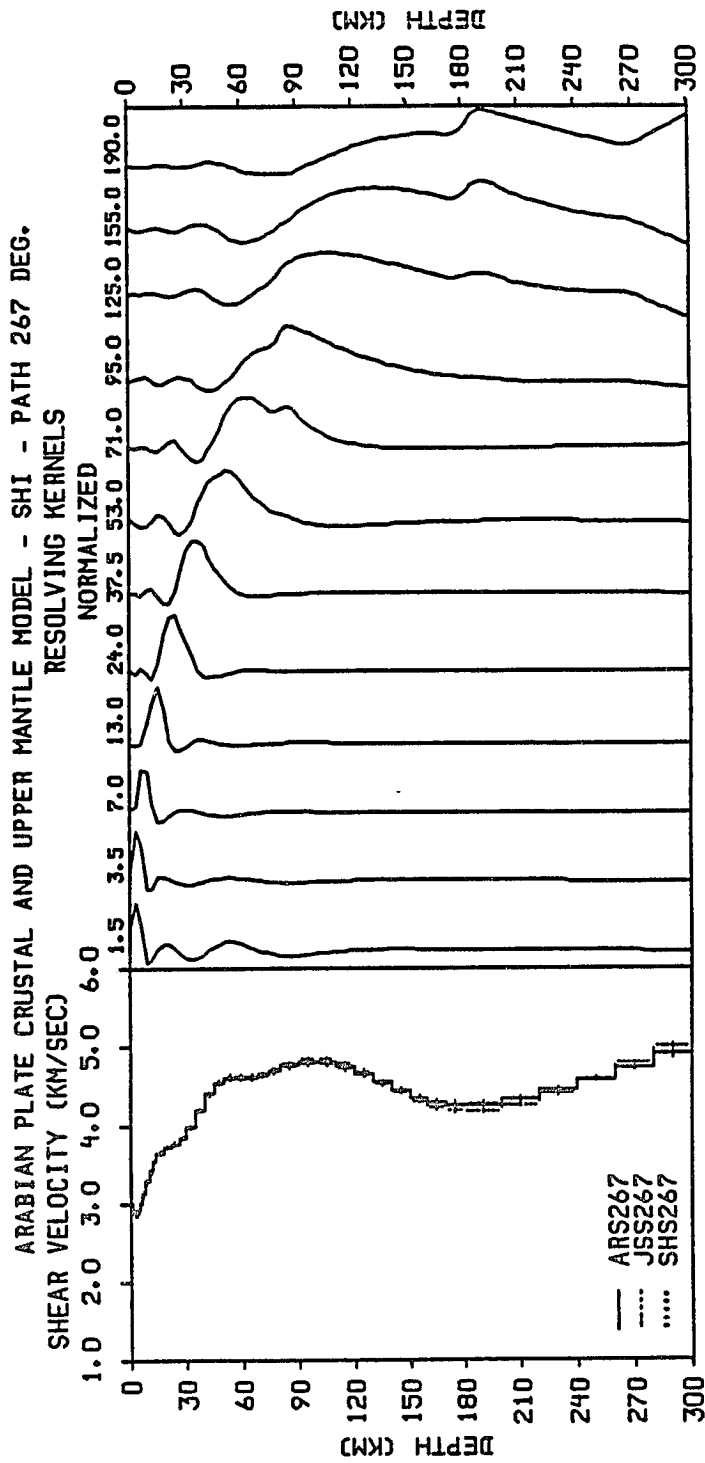
Figure 4.66. Deep shear velocity model and resolving kernels estimated from the fundamental and first higher-mode group velocity for path S267, and the fundamental-mode phase velocity for AR, JER-SHI and SHI-HLW paths obtained by Knopoff and Fouda (1975).

- 233 -

Table 4.38. Crustal and upper mantle velocity structure of the Arabian plate obtained from the simultaneous inversion of AR and S267 dispersion curves.

			Velocity Model ARS267			
Layer Number	Layer Depth* (km)	Layer Thickness (km)	Compressional Velocity (km/sec)	Shear Velocity (km/sec)	Density (gm/cc)	Standard Deviation (km/sec)
1	0.2	0.5	4.68	2.70	2.431	0.066
2	0.8	0.5	5.16	2.98	2.532	0.059
3	1.5	1.0	5.08	2.93	2.516	0.049
4	2.5	1.0	5.00	2.89	2.499	0.039
5	3.5	1.0	4.98	2.87	2.495	0.031
6	4.5	1.0	5.04	2.91	2.509	0.022
7	5.5	1.0	5.20	3.00	2.540	0.017
8	7.0	2.0	5.42	3.13	2.584	0.021
9	9.0	2.0	5.69	3.28	2.637	0.022
10	11.0	2.0	5.93	3.42	2.686	0.022
11	13.0	2.0	6.14	3.54	2.741	0.020
12	16.0	4.0	6.31	3.64	2.793	0.019
13	20.0	4.0	6.43	3.71	2.829	0.018
14	24.0	4.0	6.52	3.76	2.854	0.018
15	28.0	4.0	6.64	3.83	2.886	0.018
16	32.5	5.0	6.88	3.97	2.948	0.018
17	37.5	5.0	7.25	4.18	3.059	0.020
18	42.5	5.0	7.83	4.40	3.252	0.022
19	47.5	5.0	8.09	4.54	3.341	0.023
20	53.0	6.0	8.20	4.60	3.381	0.024
21	59.0	6.0	8.21	4.61	3.387	0.025
22	65.0	6.0	8.22	4.62	3.391	0.027
23	71.0	6.0	8.28	4.65	3.411	0.028
24	77.0	6.0	8.38	4.70	3.447	0.029
25	85.0	10.0	8.50	4.77	3.490	0.030
26	95.0	10.0	8.58	4.82	3.517	0.030
27	105.0	10.0	8.57	4.81	3.515	0.030
28	115.0	10.0	8.48	4.76	3.482	0.029
29	125.0	10.0	8.31	4.67	3.422	0.029
30	135.0	10.0	8.11	4.55	3.351	0.029
31	145.0	10.0	7.92	4.44	3.282	0.030
32	155.0	10.0	7.75	4.35	3.225	0.030
33	165.0	10.0	7.63	4.28	3.185	0.031
34	175.0	10.0	7.57	4.25	3.165	0.031
35	190.0	20.0	7.58	4.25	3.166	0.031
36	210.0	20.0	7.69	4.32	3.206	0.028
37	230.0	20.0	7.90	4.43	3.275	0.024
38	250.0	20.0	8.16	4.58	3.367	0.024
39	270.0	20.0	8.44	4.74	3.470	0.030
40	290.0	20.0	8.74	4.91	3.571	0.040

* from the surface to the middle of the layers.

Table 4.39. Crustal and upper mantle velocity structure of the Arabian plate obtained from the simultaneous inversion of JS and S267 dispersion curves.

Velocity Model JSS267						
Layer Number	Layer Depth* (km)	Layer Thickness (km)	Compressional Velocity (km/sec)	Shear Velocity (km/sec)	Density (gm/cc)	Standard Deviation (km/sec)
1	0.2	0.5	4.70	2.72	2.435	0.088
2	0.8	0.5	5.18	2.99	2.535	0.078
3	1.5	1.0	5.09	2.94	2.519	0.065
4	2.5	1.0	5.00	2.89	2.501	0.052
5	3.5	1.0	4.98	2.87	2.495	0.041
6	4.5	1.0	5.04	2.91	2.509	0.030
7	5.5	1.0	5.20	3.00	2.539	0.023
8	7.0	2.0	5.41	3.13	2.583	0.028
9	9.0	2.0	5.68	3.28	2.637	0.030
10	11.0	2.0	5.93	3.42	2.686	0.029
11	13.0	2.0	6.14	3.54	2.741	0.027
12	16.0	4.0	6.31	3.64	2.794	0.026
13	20.0	4.0	6.44	3.72	2.831	0.024
14	24.0	4.0	6.53	3.77	2.856	0.024
15	28.0	4.0	6.65	3.84	2.889	0.024
16	32.5	5.0	6.89	3.98	2.950	0.024
17	37.5	5.0	7.25	4.19	3.061	0.026
18	42.5	5.0	7.84	4.40	3.256	0.030
19	47.5	5.0	8.10	4.55	3.347	0.031
20	53.0	6.0	8.22	4.62	3.390	0.032
21	59.0	6.0	8.24	4.62	3.395	0.034
22	65.0	6.0	8.24	4.62	3.395	0.036
23	71.0	6.0	8.28	4.65	3.410	0.037
24	77.0	6.0	8.36	4.69	3.441	0.039
25	85.0	10.0	8.47	4.75	3.479	0.040
26	95.0	10.0	8.54	4.80	3.505	0.040
27	105.0	10.0	8.54	4.79	3.503	0.039
28	115.0	10.0	8.44	4.74	3.470	0.039
29	125.0	10.0	8.29	4.65	3.413	0.038
30	135.0	10.0	8.09	4.54	3.344	0.039
31	145.0	10.0	7.91	4.44	3.278	0.040
32	155.0	10.0	7.75	4.35	3.223	0.041
33	165.0	10.0	7.63	4.28	3.185	0.042
34	175.0	10.0	7.58	4.25	3.167	0.042
35	190.0	20.0	7.58	4.26	3.169	0.041
36	210.0	20.0	7.70	4.32	3.209	0.037
37	230.0	20.0	7.91	4.44	3.279	0.033
38	250.0	20.0	8.17	4.58	3.369	0.032
39	270.0	20.0	8.45	4.74	3.471	0.040
40	290.0	20.0	8.74	4.90	3.570	0.054

* from the surface to the middle of the layers.

Table 4.40. Crustal and upper mantle velocity structure of the Arabian plate obtained from the simultaneous inversion of SH and S267 dispersion curves.

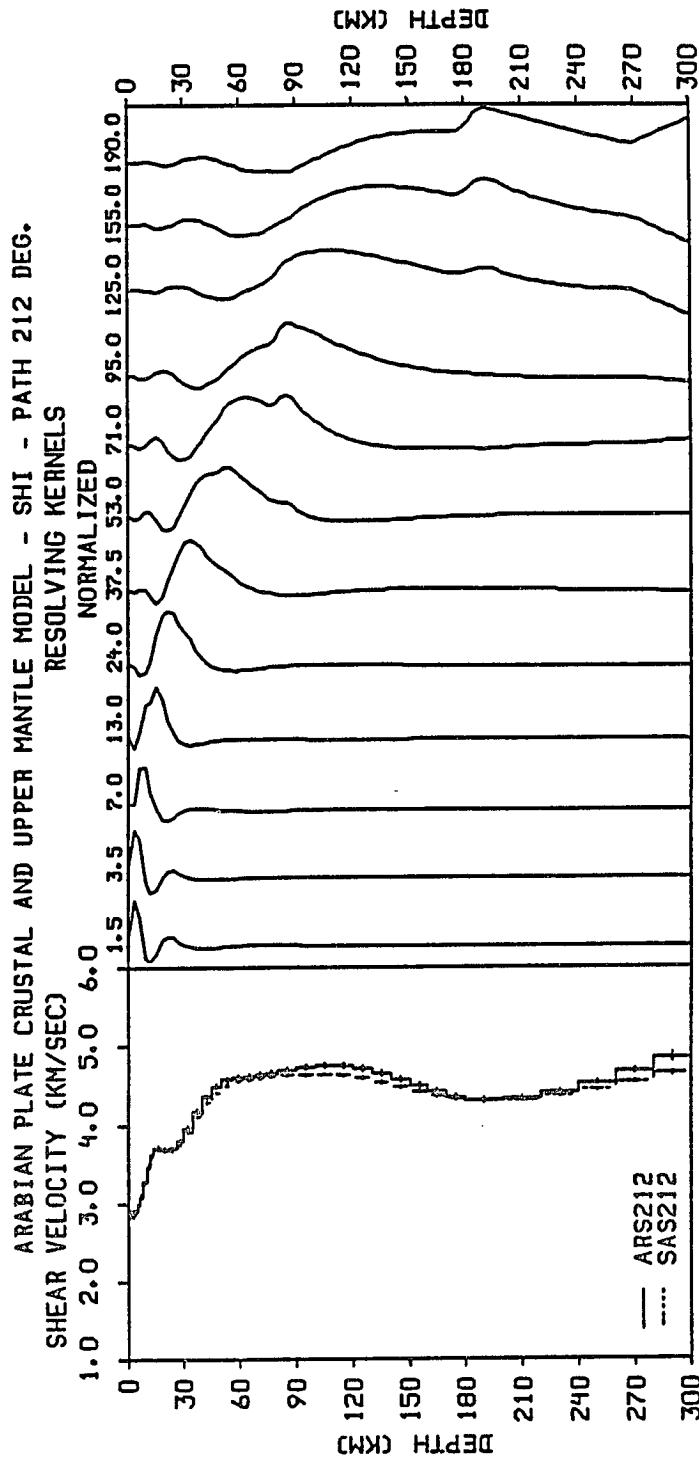|			Velocity Model SHS267			
Layer Number	Layer Depth* (km)	Layer Thickness (km)	Compressional Velocity (km/sec)	Shear Velocity (km/sec)	Density (gm/cc)	Standard Deviation (km/sec)
1	0.2	0.5	4.70	2.71	2.433	0.066
2	0.8	0.5	5.17	2.99	2.534	0.059
3	1.5	1.0	5.09	2.94	2.518	0.049
4	2.5	1.0	5.00	2.89	2.501	0.039
5	3.5	1.0	4.98	2.87	2.495	0.031
6	4.5	1.0	5.04	2.91	2.509	0.022
7	5.5	1.0	5.20	3.00	2.539	0.017
8	7.0	2.0	5.41	3.13	2.583	0.021
9	9.0	2.0	5.68	3.28	2.636	0.022
10	11.0	2.0	5.93	3.42	2.686	0.022
11	13.0	2.0	6.14	3.54	2.741	0.020
12	16.0	4.0	6.31	3.64	2.793	0.019
13	20.0	4.0	6.43	3.71	2.829	0.018
14	24.0	4.0	6.52	3.76	2.854	0.018
15	28.0	4.0	6.64	3.83	2.886	0.018
16	32.5	5.0	6.88	3.97	2.949	0.018
17	37.5	5.0	7.25	4.19	3.061	0.020
18	42.5	5.0	7.84	4.40	3.254	0.022
19	47.5	5.0	8.08	4.54	3.340	0.023
20	53.0	6.0	8.19	4.60	3.377	0.024
21	59.0	6.0	8.19	4.60	3.380	0.025
22	65.0	6.0	8.21	4.61	3.384	0.027
23	71.0	6.0	8.27	4.64	3.408	0.028
24	77.0	6.0	8.39	4.71	3.450	0.029
25	85.0	10.0	8.53	4.79	3.500	0.030
26	95.0	10.0	8.63	4.84	3.534	0.030
27	105.0	10.0	8.63	4.84	3.534	0.030
28	115.0	10.0	8.53	4.79	3.499	0.029
29	125.0	10.0	8.34	4.68	3.433	0.029
30	135.0	10.0	8.11	4.55	3.350	0.029
31	145.0	10.0	7.88	4.42	3.269	0.029
32	155.0	10.0	7.68	4.31	3.200	0.030
33	165.0	10.0	7.53	4.23	3.149	0.030
34	175.0	10.0	7.45	4.18	3.123	0.031
35	190.0	20.0	7.44	4.18	3.120	0.030
36	210.0	20.0	7.58	4.25	3.166	0.027
37	230.0	20.0	7.83	4.39	3.252	0.024
38	250.0	20.0	8.16	4.58	3.368	0.024
39	270.0	20.0	8.54	4.79	3.503	0.030
40	290.0	20.0	8.93	5.01	3.637	0.041

* from the surface to the middle of the layers.

Figure 4.67. Deep shear velocity model and resolving kernels estimated from the fundamental and first higher-mode group velocity for path E84, and the fundamental-mode phase velocity for AR, JER-SHI and SHI-HLW paths obtained by Knopoff and Fouda (1975).

- 237 -

Table 4.41. Crustal and upper mantle velocity structure of the Arabian plate obtained from the simultaneous inversion of AR and E84 dispersion curves.

			Velocity Model ARE84			
Layer Number	Layer Depth* (km)	Layer Thickness (km)	Compressional Velocity (km/sec)	Shear Velocity (km/sec)	Density (gm/cc)	Standard Deviation (km/sec)
1	0.2	0.5	3.18	1.84	2.180	0.047
2	0.8	0.5	4.10	2.37	2.334	0.039
3	1.5	1.0	4.67	2.69	2.426	0.028
4	2.5	1.0	5.05	2.91	2.509	0.020
5	3.5	1.0	5.07	2.93	2.514	0.015
6	4.5	1.0	4.93	2.85	2.485	0.015
7	5.5	1.0	4.95	2.86	2.488	0.015
8	7.0	2.0	5.25	3.03	2.550	0.014
9	9.0	2.0	5.78	3.34	2.656	0.014
10	11.0	2.0	5.98	3.45	2.695	0.015
11	13.0	2.0	5.96	3.44	2.692	0.014
12	16.0	4.0	6.03	3.48	2.710	0.014
13	20.0	4.0	6.38	3.68	2.813	0.013
14	24.0	4.0	6.63	3.83	2.885	0.014
15	28.0	4.0	6.78	3.92	2.923	0.014
16	32.5	5.0	6.97	4.03	2.973	0.014
17	37.5	5.0	7.28	4.21	3.071	0.015
18	42.5	5.0	7.86	4.41	3.263	0.017
19	47.5	5.0	8.20	4.60	3.383	0.018
20	53.0	6.0	8.47	4.76	3.480	0.019
21	59.0	6.0	8.64	4.85	3.539	0.020
22	65.0	6.0	8.72	4.89	3.564	0.022
23	71.0	6.0	8.70	4.88	3.559	0.023
24	77.0	6.0	8.62	4.84	3.531	0.023
25	85.0	10.0	8.49	4.77	3.488	0.024
26	95.0	10.0	8.34	4.68	3.431	0.024
27	105.0	10.0	8.18	4.59	3.375	0.024
28	115.0	10.0	8.05	4.52	3.328	0.023
29	125.0	10.0	7.96	4.47	3.295	0.020
30	135.0	10.0	7.89	4.43	3.274	0.018
31	145.0	10.0	7.86	4.41	3.261	0.020
32	155.0	10.0	7.84	4.40	3.255	0.023
33	165.0	10.0	7.83	4.39	3.252	0.024
34	175.0	10.0	7.83	4.39	3.252	0.025
35	190.0	20.0	7.84	4.40	3.256	0.024
36	210.0	20.0	7.90	4.43	3.276	0.022
37	230.0	20.0	8.02	4.50	3.317	0.020
38	250.0	20.0	8.19	4.60	3.380	0.019
39	270.0	20.0	8.41	4.72	3.456	0.021
40	290.0	20.0	8.64	4.85	3.536	0.028

* from the surface to the middle of the layers.

Table 4.42. Crustal and upper mantle velocity structure of the Arabian plate obtained from the simultaneous inversion of JS and E84 dispersion curves.

			Velocity Model JSE84			
Layer Number	Layer Depth* (km)	Layer Thickness (km)	Compressional Velocity (km/sec)	Shear Velocity (km/sec)	Density (gm/cc)	Standard Deviation (km/sec)
1	0.2	0.5	3.23	1.87	2.187	0.072
2	0.8	0.5	4.14	2.39	2.340	0.059
3	1.5	1.0	4.68	2.70	2.429	0.043
4	2.5	1.0	5.03	2.91	2.507	0.031
5	3.5	1.0	5.05	2.92	2.510	0.023
6	4.5	1.0	4.93	2.85	2.484	0.023
7	5.5	1.0	4.95	2.86	2.489	0.024
8	7.0	2.0	5.25	3.03	2.550	0.022
9	9.0	2.0	5.77	3.33	2.655	0.022
10	11.0	2.0	5.97	3.45	2.695	0.023
11	13.0	2.0	5.96	3.44	2.693	0.021
12	16.0	4.0	6.04	3.49	2.711	0.021
13	20.0	4.0	6.38	3.68	2.813	0.021
14	24.0	4.0	6.64	3.83	2.887	0.022
15	28.0	4.0	6.80	3.93	2.928	0.021
16	32.5	5.0	6.99	4.04	2.977	0.022
17	37.5	5.0	7.29	4.21	3.072	0.023
18	42.5	5.0	7.86	4.41	3.262	0.026
19	47.5	5.0	8.21	4.61	3.384	0.027
20	53.0	6.0	8.50	4.77	3.488	0.029
21	59.0	6.0	8.68	4.87	3.552	0.031
22	65.0	6.0	8.76	4.92	3.578	0.034
23	71.0	6.0	8.73	4.90	3.569	0.035
24	77.0	6.0	8.62	4.84	3.532	0.035
25	85.0	10.0	8.47	4.75	3.478	0.037
26	95.0	10.0	8.28	4.65	3.411	0.038
27	105.0	10.0	8.12	4.56	3.351	0.037
28	115.0	10.0	8.00	4.49	3.309	0.033
29	125.0	10.0	7.93	4.45	3.286	0.029
30	135.0	10.0	7.90	4.43	3.275	0.029
31	145.0	10.0	7.89	4.43	3.272	0.032
32	155.0	10.0	7.88	4.42	3.270	0.036
33	165.0	10.0	7.88	4.42	3.268	0.039
34	175.0	10.0	7.87	4.42	3.265	0.038
35	190.0	20.0	7.86	4.41	3.264	0.037
36	210.0	20.0	7.90	4.44	3.277	0.035
37	230.0	20.0	8.01	4.50	3.313	0.032
38	250.0	20.0	8.18	4.59	3.374	0.030
39	270.0	20.0	8.39	4.71	3.451	0.032
40	290.0	20.0	8.63	4.84	3.533	0.043

* from the surface to the middle of the layers.

Table 4.43. Crustal and upper mantle velocity structure of the Arabian plate obtained from the simultaneous inversion of SH and E84 dispersion curves.

Velocity Model SHE84						
Layer Number	Layer Depth* (km)	Layer Thickness (km)	Compressional Velocity (km/sec)	Shear Velocity (km/sec)	Density (gm/cc)	Standard Deviation (km/sec)
1	0.2	0.5	3.22	1.86	2.185	0.049
2	0.8	0.5	4.13	2.38	2.338	0.040
3	1.5	1.0	4.67	2.70	2.428	0.029
4	2.5	1.0	5.04	2.91	2.508	0.021
5	3.5	1.0	5.06	2.92	2.512	0.015
6	4.5	1.0	4.93	2.85	2.485	0.016
7	5.5	1.0	4.95	2.86	2.489	0.016
8	7.0	2.0	5.25	3.03	2.551	0.015
9	9.0	2.0	5.78	3.33	2.655	0.015
10	11.0	2.0	5.97	3.45	2.694	0.016
11	13.0	2.0	5.96	3.44	2.691	0.015
12	16.0	4.0	6.03	3.48	2.710	0.014
13	20.0	4.0	6.37	3.68	2.812	0.014
14	24.0	4.0	6.63	3.83	2.884	0.015
15	28.0	4.0	6.78	3.91	2.923	0.014
16	32.5	5.0	6.97	4.03	2.973	0.015
17	37.5	5.0	7.28	4.21	3.071	0.016
18	42.5	5.0	7.86	4.41	3.262	0.018
19	47.5	5.0	8.19	4.60	3.380	0.019
20	53.0	6.0	8.46	4.75	3.477	0.020
21	59.0	6.0	8.63	4.85	3.535	0.021
22	65.0	6.0	8.71	4.89	3.561	0.022
23	71.0	6.0	8.70	4.88	3.558	0.022
24	77.0	6.0	8.62	4.84	3.531	0.022
25	85.0	10.0	8.49	4.77	3.488	0.023
26	95.0	10.0	8.33	4.67	3.428	0.024
27	105.0	10.0	8.16	4.58	3.368	0.025
28	115.0	10.0	8.03	4.51	3.321	0.025
29	125.0	10.0	7.94	4.46	3.291	0.022
30	135.0	10.0	7.90	4.43	3.276	0.018
31	145.0	10.0	7.88	4.42	3.270	0.016
32	155.0	10.0	7.87	4.42	3.267	0.017
33	165.0	10.0	7.86	4.41	3.263	0.020
34	175.0	10.0	7.83	4.40	3.254	0.021
35	190.0	20.0	7.80	4.38	3.242	0.021
36	210.0	20.0	7.80	4.38	3.242	0.020
37	230.0	20.0	7.90	4.43	3.275	0.020
38	250.0	20.0	8.11	4.55	3.349	0.020
39	270.0	20.0	8.42	4.72	3.460	0.022
40	290.0	20.0	8.79	4.93	3.587	0.027

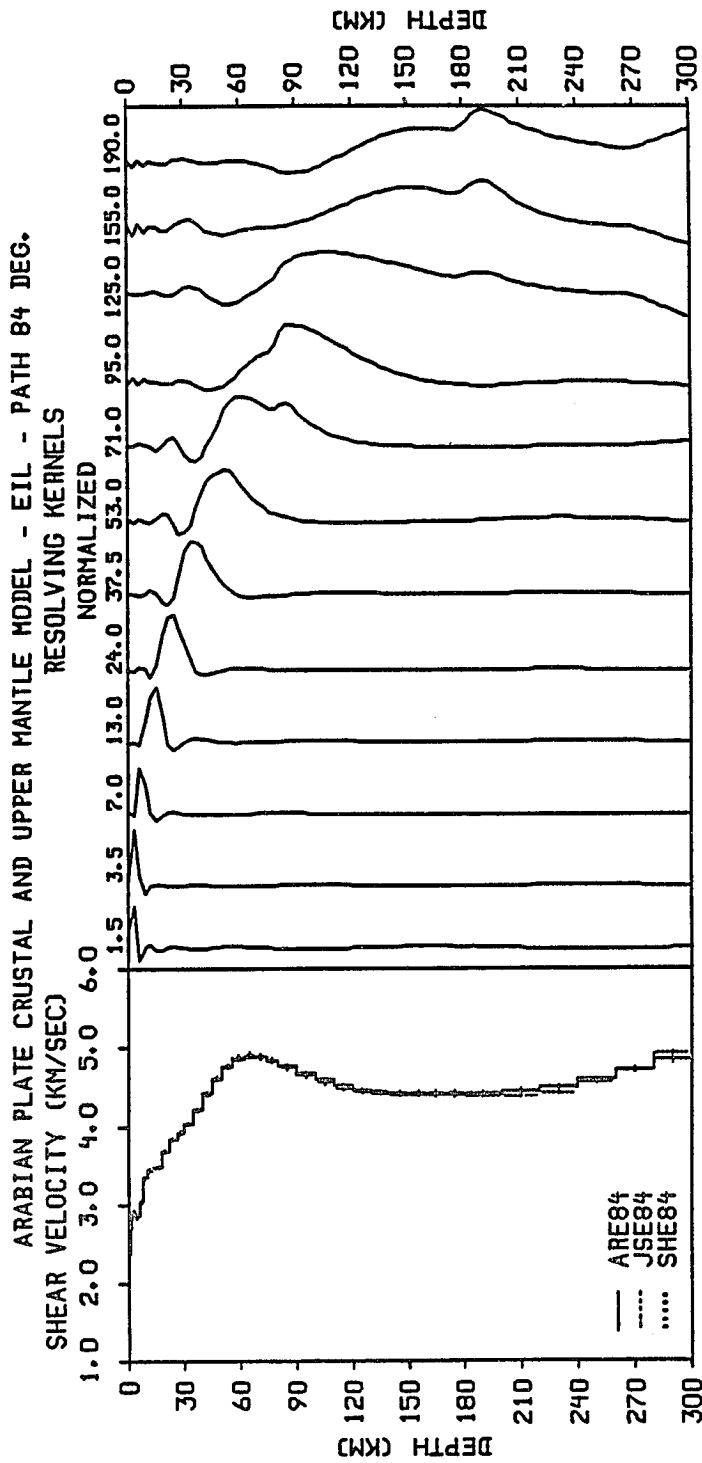* from the surface to the middle of the layers.
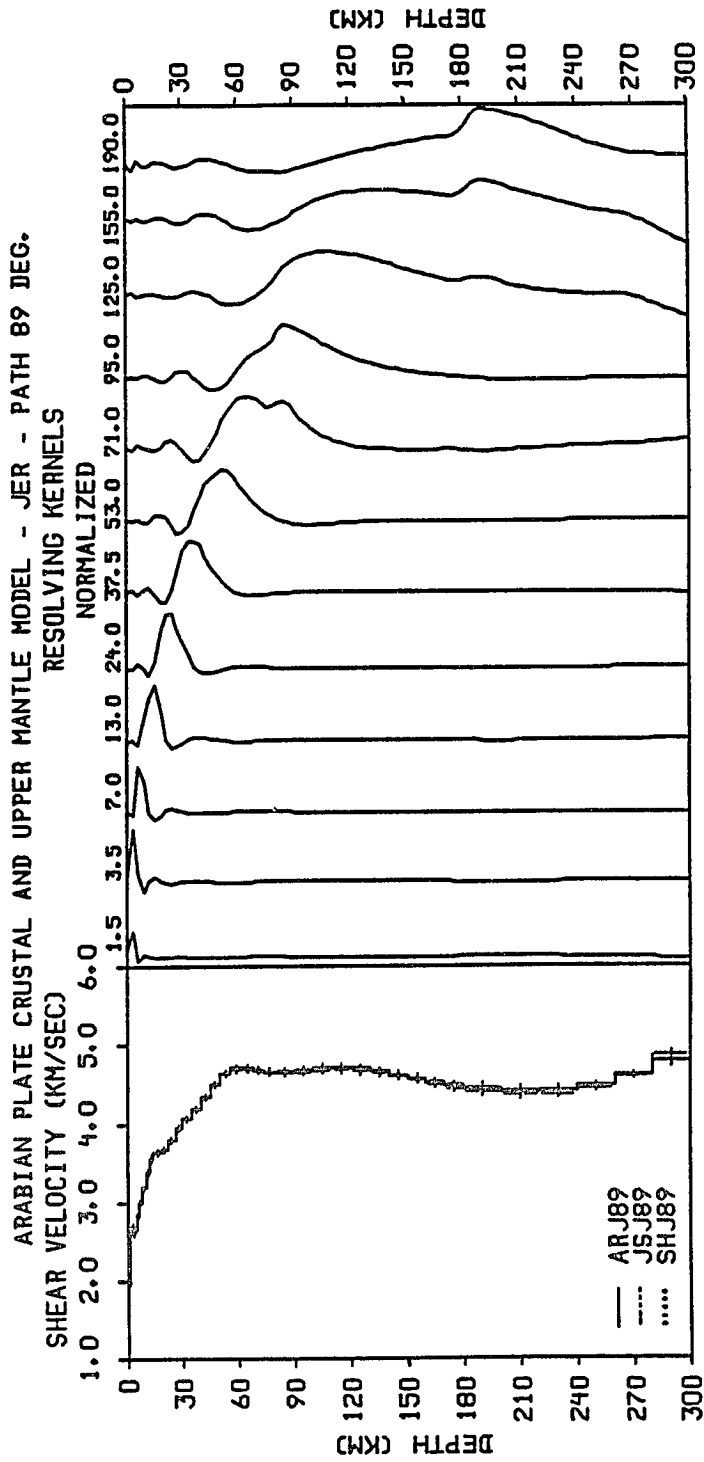
Figure 4.68. Deep shear velocity model and resolving kernels estimated from the fundamental and first higher-mode group velocity for path J89, and the fundamental-mode phase velocity for AR, JER-SHI and SHI-HLW paths obtained by Knopoff and Fouda (1975).

- 241 -

Table 4.44. Crustal and upper mantle velocity structure of the Arabian plate obtained from the simultaneous inversion of AR and J89 dispersion curves.

			Velocity Model ARJ89			
Layer Number	Layer Depth* (km)	Layer Thickness (km)	Compressional Velocity (km/sec)	Shear Velocity (km/sec)	Density (gm/cc)	Standard Deviation (km/sec)
1	0.2	0.5	1.89	1.09	1.806	0.089
2	0.8	0.5	3.37	1.94	2.209	0.074
3	1.5	1.0	4.47	2.58	2.385	0.059
4	2.5	1.0	4.69	2.71	2.433	0.037
5	3.5	1.0	4.53	2.61	2.396	0.031
6	4.5	1.0	4.60	2.65	2.412	0.033
7	5.5	1.0	4.89	2.82	2.475	0.028
8	7.0	2.0	5.20	3.00	2.540	0.029
9	9.0	2.0	5.52	3.19	2.604	0.029
10	11.0	2.0	5.88	3.39	2.676	0.032
11	13.0	2.0	6.17	3.56	2.750	0.031
12	16.0	4.0	6.31	3.64	2.792	0.029
13	20.0	4.0	6.36	3.67	2.809	0.029
14	24.0	4.0	6.57	3.79	2.869	0.030
15	28.0	4.0	6.83	3.94	2.935	0.030
16	32.5	5.0	7.04	4.06	2.992	0.031
17	37.5	5.0	7.25	4.18	3.059	0.033
18	42.5	5.0	7.73	4.34	3.218	0.033
19	47.5	5.0	8.03	4.51	3.321	0.034
20	53.0	6.0	8.27	4.64	3.408	0.036
21	59.0	6.0	8.38	4.71	3.448	0.037
22	65.0	6.0	8.39	4.71	3.450	0.037
23	71.0	6.0	8.34	4.68	3.434	0.038
24	77.0	6.0	8.31	4.66	3.420	0.041
25	85.0	10.0	8.30	4.66	3.418	0.044
26	95.0	10.0	8.34	4.68	3.433	0.045
27	105.0	10.0	8.39	4.71	3.451	0.047
28	115.0	10.0	8.41	4.72	3.458	0.049
29	125.0	10.0	8.39	4.71	3.449	0.051
30	135.0	10.0	8.32	4.67	3.427	0.050
31	145.0	10.0	8.24	4.63	3.397	0.047
32	155.0	10.0	8.15	4.57	3.363	0.044
33	165.0	10.0	8.06	4.52	3.331	0.044
34	175.0	10.0	7.97	4.48	3.301	0.048
35	190.0	20.0	7.90	4.43	3.276	0.053
36	210.0	20.0	7.86	4.41	3.261	0.051
37	230.0	20.0	7.87	4.42	3.265	0.043
38	250.0	20.0	7.98	4.48	3.303	0.038
39	270.0	20.0	8.21	4.61	3.386	0.045
40	290.0	20.0	8.55	4.80	3.507	0.062

* from the surface to the middle of the layers.

- 242 -

Table 4.45. Crustal and upper mantle velocity structure of the Arabian plate obtained from the simultaneous inversion of JS and J89 dispersion curves.

			Velocity Model JSJ89			
Layer Number	Layer Depth* (km)	Layer Thickness (km)	Compressional Velocity (km/sec)	Shear Velocity (km/sec)	Density (gm/cc)	Standard Deviation (km/sec)
1	0.2	0.5	2.03	1.17	1.861	0.106
2	0.8	0.5	3.47	2.00	2.225	0.087
3	1.5	1.0	4.48	2.59	2.388	0.069
4	2.5	1.0	4.66	2.69	2.426	0.042
5	3.5	1.0	4.52	2.61	2.395	0.037
6	4.5	1.0	4.62	2.66	2.415	0.038
7	5.5	1.0	4.90	2.83	2.477	0.033
8	7.0	2.0	5.19	3.00	2.539	0.034
9	9.0	2.0	5.51	3.18	2.601	0.035
10	11.0	2.0	5.87	3.39	2.674	0.038
11	13.0	2.0	6.16	3.56	2.749	0.037
12	16.0	4.0	6.31	3.64	2.793	0.035
13	20.0	4.0	6.37	3.68	2.810	0.034
14	24.0	4.0	6.58	3.80	2.870	0.035
15	28.0	4.0	6.84	3.95	2.938	0.035
16	32.5	5.0	7.05	4.07	2.998	0.037
17	37.5	5.0	7.26	4.19	3.064	0.039
18	42.5	5.0	7.74	4.34	3.221	0.040
19	47.5	5.0	8.03	4.51	3.321	0.041
20	53.0	6.0	8.27	4.64	3.408	0.043
21	59.0	6.0	8.39	4.71	3.450	0.044
22	65.0	6.0	8.40	4.71	3.453	0.044
23	71.0	6.0	8.35	4.69	3.437	0.045
24	77.0	6.0	8.31	4.66	3.420	0.048
25	85.0	10.0	8.28	4.65	3.412	0.052
26	95.0	10.0	8.31	4.66	3.421	0.053
27	105.0	10.0	8.34	4.68	3.434	0.055
28	115.0	10.0	8.36	4.69	3.440	0.058
29	125.0	10.0	8.35	4.69	3.435	0.060
30	135.0	10.0	8.30	4.66	3.418	0.058
31	145.0	10.0	8.23	4.62	3.394	0.054
32	155.0	10.0	8.16	4.58	3.367	0.051
33	165.0	10.0	8.08	4.54	3.339	0.051
34	175.0	10.0	8.00	4.49	3.311	0.056
35	190.0	20.0	7.93	4.45	3.287	0.062
36	210.0	20.0	7.88	4.42	3.270	0.060
37	230.0	20.0	7.89	4.43	3.272	0.051
38	250.0	20.0	7.99	4.48	3.306	0.044
39	270.0	20.0	8.21	4.61	3.385	0.053
40	290.0	20.0	8.53	4.79	3.502	0.073

* from the surface to the middle of the layers.

Table 4.46. Crustal and upper mantle velocity structure of the Arabian plate obtained from the simultaneous inversion of SH and J89 dispersion curves.

Velocity Model SHJ89						
Layer Number	Layer Depth* (km)	Layer Thickness (km)	Compressional Velocity (km/sec)	Shear Velocity (km/sec)	Density (gm/cc)	Standard Deviation (km/sec)
1	0.2	0.5	2.00	1.16	1.851	0.091
2	0.8	0.5	3.45	1.99	2.222	0.075
3	1.5	1.0	4.49	2.59	2.389	0.060
4	2.5	1.0	4.69	2.71	2.431	0.037
5	3.5	1.0	4.53	2.62	2.397	0.032
6	4.5	1.0	4.61	2.66	2.414	0.033
7	5.5	1.0	4.89	2.82	2.476	0.029
8	7.0	2.0	5.20	3.00	2.540	0.029
9	9.0	2.0	5.52	3.18	2.603	0.030
10	11.0	2.0	5.87	3.39	2.675	0.033
11	13.0	2.0	6.16	3.56	2.747	0.032
12	16.0	4.0	6.30	3.64	2.791	0.030
13	20.0	4.0	6.36	3.67	2.808	0.030
14	24.0	4.0	6.57	3.79	2.867	0.030
15	28.0	4.0	6.82	3.94	2.934	0.030
16	32.5	5.0	7.04	4.06	2.992	0.032
17	37.5	5.0	7.25	4.19	3.061	0.033
18	42.5	5.0	7.74	4.34	3.220	0.034
19	47.5	5.0	8.03	4.50	3.319	0.035
20	53.0	6.0	8.25	4.63	3.401	0.037
21	59.0	6.0	8.36	4.69	3.438	0.037
22	65.0	6.0	8.36	4.69	3.441	0.037
23	71.0	6.0	8.33	4.68	3.429	0.039
24	77.0	6.0	8.31	4.66	3.422	0.041
25	85.0	10.0	8.32	4.67	3.425	0.045
26	95.0	10.0	8.37	4.70	3.442	0.046
27	105.0	10.0	8.41	4.72	3.458	0.048
28	115.0	10.0	8.42	4.73	3.461	0.049
29	125.0	10.0	8.38	4.71	3.448	0.050
30	135.0	10.0	8.31	4.66	3.422	0.049
31	145.0	10.0	8.22	4.61	3.388	0.046
32	155.0	10.0	8.12	4.56	3.353	0.044
33	165.0	10.0	8.02	4.50	3.318	0.046
34	175.0	10.0	7.93	4.45	3.286	0.050
35	190.0	20.0	7.84	4.40	3.256	0.054
36	210.0	20.0	7.78	4.36	3.234	0.051
37	230.0	20.0	7.78	4.37	3.235	0.043
38	250.0	20.0	7.92	4.45	3.283	0.038
39	270.0	20.0	8.23	4.62	3.392	0.045
40	290.0	20.0	8.69	4.88	3.554	0.063

* from the surface to the middle of the layers.

CHAPTER 5

ATTENUATION OF CODA WAVES

Development of the theory of coda waves has been the subject of extensive seismological research in recent years. A comprehensive overview of the scattering and attenuation of these high-frequency seismic waves can be found in Herraiz and Espinosa (1986). In this chapter, the generation and excitation of coda is briefly reviewed in the context of scattered surface waves in a laterally heterogeneous medium (Aki, 1969), and attenuation in terms of the instrument and earth Q-filter effects on the dispersion of the coda (Herrmann, 1980). The contribution of this study is concerned with the latter problem. It is considered important because the predominant frequency versus travel time method has provided a relatively simple tool for extracting information on local and regional Q as well. This single-station method, hereafter will be simply referred to as the "coda-Q" method, has been very useful for estimating body-wave magnitudes, $m_b(Lg)$ near 1 Hz frequency, for small earthquakes and yield of underground nuclear explosions using Lg waves (Nuttli, 1973, 1983a, 1983b, 1986). Furthermore, any mapping of seismic hazard in active seismotectonic regions must take into account the spatial variation of attenuation of seismic energy.

In order to exploit the potential of the coda-Q method, a practical analysis procedure for determining the anelastic attenuation quality factor Q and its frequency dependence ζ simultaneously is presented. This approach should simplify the application procedure of the method, improve

-245-

the accuracy of the coda-Q results, provide statistical error estimates, and establish an objective approach for evaluation and comparison purposes.

5.1 Coda Wave Theory

Coda waves are a prominent feature of recorded seismograms of small local earthquakes. They form tails following the arrival of primary waves, such as direct body (P and S) and surface (Lg) waves. These energy trains are viewed as a superposition of many secondary backscattering waves excited by numerous randomly distributed heterogeneities in the Earth's crust and upper mantle (Aki, 1969; Aki and Chouet 1975). This definition of coda waves has been established on the basis of several important observations investigated by, for instance, Aki *et al.* (1958), Aki and Tsujiura (1959), Tsumura (1967), Aki (1969) and Aki and Chouet (1975). The first of these observations relevant to the backscattering model, is that at an epicentral distance shorter than about 100 km, the total duration time of the seismic waves (the length of time from the beginning of P waves to the end of coda) is nearly independent of either distance or azimuth. Second, the similarity in the spectral content of coda waves, among stations, is independent of the travel distance and nature of the wave path. Third, the power spectra of coda waves from different local earthquakes decay as a function of time (measured from the earthquake origin time) in the same manner independent of the epicentral distance, path, or earthquake magnitude (at least for M<6). Fourth, although, the coda excitation depends on the local geology of the station and can be 5-8 times larger for seismographs on sediment than on granite, the amplitude of ambient ground noise tends to be proportional to the site factor of coda excitation. Thus, making

the records total duration for various station sites nearly independent of local geology. Fifth, is that coda waves are not regular plane waves coming from the earthquake epicenter.

Coda waves are high-frequency seismic waves, and very sensitive to details of the earthquake source and travel path. The study of their origin, which includes separating the source and path effects, using deterministic numerical methods is difficult. This is not only due to their sensitivity, but also because they are presumed the result of random processes in which primary waves interact with heterogeneities and produce secondary waves (i.e. scattering). To avoid these difficulties, an entirely statistical treatment has been utilized in analyzing coda waves. This approach allows only a small number of parameters to effectively characterize the Earth's lateral heterogeneity.

In view of the above observations, Aki (1969) suggested that the power spectrum $P(\omega|t)$ of coda waves at a given lapse time t measured from the earthquake origin time can be expressed as

$$P(\omega|t) = S(\omega) \ C(\omega|t) \qquad (5.1)$$

where, $S(\omega)$ expresses only the source parameters as a function of the angular frequency ω, and $C(\omega|t)$, the propagation term, represents the effect of a large geographical area and is independent of distance or details of the path from the source to the station. Relation (5.1) is basically a summary of the coda properties in which the source and path effects are distinctly separated. In order to find mathematical expressions for $S(\omega)$, $C(\omega|t)$ and relating $P(\omega|t)$ to coda amplitudes, Aki (1969) proposed the single-scattering surface-wave model. In this model the following assump-

tions are made. (1) The lateral heterogeneity are approximated by random but uniform two-dimensionally distributed discrete scatterers on the surface. (2) The primary and secondary waves are surface waves of the same kind. (3) The scattering is a weak process, and each backscattering wavelet is due to a single scatterer. (4) The mean free paths of the waves between scatterers are greater than the travel distances from scatterers to receiver. (5) The size of the scatterers is greater than the wavelengths. (6) The seismic station is put at the same place as the earthquake source.

Under these assumptions, $C(\omega|t)$ is considered common to all events of the same area, which implies that different sources share common composition of wave type. Also, $S(\omega)$ is proportional to M_0 the seismic moment, assuming that a point source is valid in the frequency range of the coda. Therefore, expression (5.1) can be written as

$$P(\omega|t) = M_0^2 \, |\phi_0(\omega|r_0)|^2 \, \frac{2N(r_0)}{t} \, e^{-\omega t / Q} \qquad (5.2)$$

where $N(r_0)$ is the number of scatterers within a radius r_0 from the earthquake. $\phi_0(\omega|r_0)$ is a function of frequency only, and expresses the absolute value of the Fourier transform of displacement due to secondary scattered waves. The term $e^{-\omega t/Q}$ includes the dissipation introduced by the medium.

Finally, the relationship between the measured trace amplitude $y(t)$ and the calculated coda spectrum is given by

$$\langle y^2(t)\rangle = \left[\frac{Q}{2\pi \left[- dt / d\omega_p \right]} \right]^{1/2} P(\omega_p|t) \, . \qquad (5.3)$$

This relationship was obtained by approximating the power spectrum by an error function with a peak frequency ω_p measured at time t from the

earthquake origin time. Therefore, by combining equations (5.2) and (5.3), the resulting coda wave model takes the form

$$M_o\sqrt{2N(r_o)} \; |\phi_o(\omega_p|r_o)| = t^{1/2} \; e^{\omega_p t/2Q}\left[-\frac{1}{Q}\frac{dt}{df_p}\right]^{1/4}\sqrt{<y^2(t)>} \quad (5.4)$$

where, Q is the anelastic attenuation quality factor for surface waves comprising the coda, $t^{1/2}$ is the geometric spreading correction, and the peak frequency $f_p = \omega_p/2\pi$. The term $\left|\dfrac{dt}{df_p}\right|^{1/4}$, calculated empirically according to the formula $t/100 = (f/0.82)^{-1.5}$, represents the effect of dispersion applied to the observed amplitude. The left hand side of expression (5.4) describes the effect of the source and scattering mechanism, whereas, the right hand side represent the path effect on coda waves excitation.

5.2 Attenuation Theory

Aki's (1969) coda theory was initially developed to analyze earthquakes in Central California where the value for Q is known. Nevertheless, attenuation is a process closely related to scattering in this theory because it directly influence the general shape, duration, and content of seismograms. Hence, several seismologists have exploited this relationship to express the amplitude and frequency decrease of coda waves as lapse time increases. Aki and Chouet (1975), and Rautian and Khalturin (1978) were first to utilize this theory to estimate Q from studies of coda recorded by a set of narrow-band seismographs. On the other hand, to use coda waves recorded on broad-band instruments, Herrmann (1980) presented equation (5.4), to describe the coda average peak-to-peak amplitude A(t) observed around time t, as follows

$$\frac{A(t)}{\sqrt{8}} = I(f_p)\, Q^{-1/4}\, t^{-1/2} \left[\frac{dt}{df_p}\right]^{-1/4} e^{-\frac{\pi f_p t}{Q}}\, M_o\, B(f_p) \qquad (5.5)$$

where $I(f_p)$ is the instrument magnification at the predominant frequency f_p observed at lapse time t. Suteau and Whitcomb (1979) defined the scattering mechanism $B(f_p)$ as

$$B(f_p) = [2N(r_o)]^{-1/2}\, \phi_o(f_p, r_o)\, .$$

A more generalized form of (5.5), for use in areas other than California, is expressed in terms of the time variable $t^* = t/Q$ rather than simply the lapse time t as follows

$$\frac{A(t^*)}{\sqrt{8}} = Q^{-1/2}\, M_o\, B(f_p)\, C(f_p, t^*) \qquad (5.6)$$

where the coda shape function is

$$C(f_p, t^*) = I(f_p)\, t^{*-1/2} \left[\frac{df_p}{dt^*}\right]^{1/4} e^{\pi f_p t^*}\, . \qquad (5.7)$$

Relation (5.6) is an extension of Aki (1969) coda model (5.4). It takes into account not only the effect of the geographical region, but also the instrument system response and dispersion of coda. Recognizing the dependency of the predominant frequency on Q and I(f), and df_p/dt^* on Q in particular, Herrmann (1980) assumed that the predominant frequency is a function of the earthquake source spectrum, the instrument response, and the Q filter of the Earth. Together these three factors form a peaked and relatively narrow band-pass frequency response. However, the effect of the source spectrum frequency content may be ignored when considering only earthquakes small enough that their corner frequencies are greater than the peak instrument response. In such a filter the Q operator causes the

predominant frequency to decrease as time increases. Under these assumptions the filter response is expressed as

$$I(f) \ e^{-\pi f t^*} .$$

(5.8)

Furthermore, to account for the frequency dependence of Q, the above model can be expressed in terms of $Q = Q_0(f/f_0)^\zeta$. Here, ζ is the frequency dependence factor and f_0 is a reference frequency. Therefore, expression (5.8) becomes

$$I(f) \ e^{-\pi f^{1-\zeta} f_0^\zeta t^*} .$$

(5.9)

It is relatively easy to evaluate either models (5.8) or (5.9). The process involves assuming a particular value of t^* and searching for the frequency f_p of the peak response. Consequently, given the frequency at nearby values of t^*, the term df_p/dt^* can be differentiated numerically, and the coda shape function (5.7) determined. In this manner Herrmann (1980) constructed sets of theoretical master curves representing the continuous decrease in coda wave frequency and amplitude as a function of increasing time for different seismograph systems. Figure 5.1 shows an example of f_p versus t^* master curve (coda-Q method) for a short period WWSSN system having a seismometer natural frequency of 1 Hz, a galvanometer with 1.35 Hz, and a magnification of 1.0 at 1 Hz. Similarly, Figure 5.2 shows an example of $C(f_p,t^*)$ versus t^* master curve (coda shape method) for the same system.

In applying the coda-Q method, coda wave frequency is measured as a function of travel time. Herrmann (1980) proposed that the frequency can be estimated by counting the number of zero crossings of coda trace within
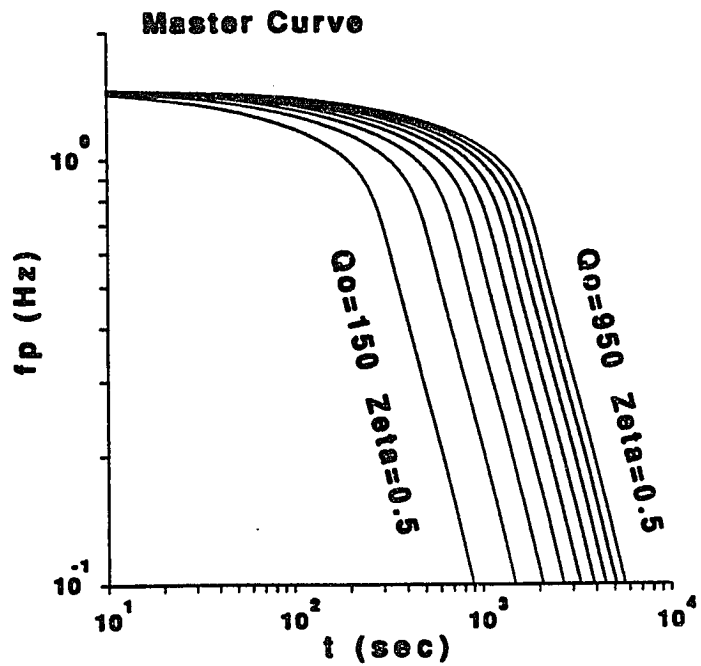
Figure 5.1.   Selected coda-Q master curves for the WWSSN
short-period instrument.
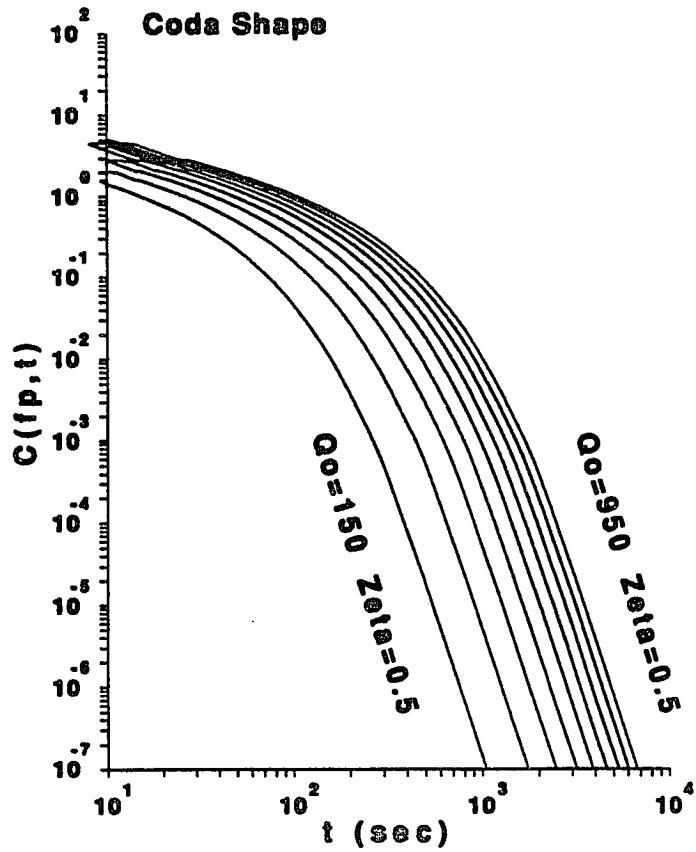
Figure 5.2. Selected coda shape curves for the WWSSN short-period instrument.

a given time interval, and dividing the number of crossings by twice the window length. Although, the drawback to this approach lies in the complexity of seismic traces, Singh and Herrmann (1983) and Raoof and Nuttli (1984) used it to analyze the coda of Lg waves the U.S. and South America, whereas Chen *et al.* (1984) used an alternative relation based on spectral moments to estimate the zero crossing of coda waves in China.

As for the coda shape method, it is the peak-to-peak coda amplitude measured as a function of travel time. In practice, the measured frequencies or amplitudes, obtained from one or more events of the same source region, are plotted versus time on logarithmic axes and superimposed upon the master curves. By performing such curve matching Q_0 and ζ can easily be estimated using either methods. However, in order to get reliable values for these parameters it is essential that observed data properly cover the curvature portion of the master curves. Further discussion on the practical application aspects is presented in Chapter 6.

5.3 Q_0 and ζ Estimation

The objective of the coda-Q method is to accurately estimate the anelastic attenuation quality factor and its dependence on frequency. Although, Nuttli (1986) has addressed some of the causes affecting the determination of Q and ζ, the accuracy of the results obtained by this method also depends, to a large extent, on the master curve matching approach. An inherent error is imposed by the overlaying of observed data with the large number of possible theoretical curves. This subjective, eye fitting, procedure is not only time consuming, but also can lead to biased and inaccurate results.

A straightforward simultaneous and deterministic estimation of Q_0 and ζ is not difficult to achieve in the context of a linear least squares problem (Ghalib *et al.*, 1984). Considering that the predominant frequency at which the system response, including the instrument and Q-filter of the Earth, will be a maximum can be found by differentiating the system response (5.9) and setting the derivative equal to zero. Symbolically,

$$\frac{d}{df} I(f) \; e^{-\pi \, f^{1-\zeta} \, f_0^{\zeta} \, t^*} = 0 \; .$$

Hence, the change of instrument response with respect to frequency becomes,

$$\frac{dI(f)}{df} = (1-\zeta) \; \pi \; f^{-\zeta} \; f_0^{\zeta} \; t^* \; I(f) \; .$$

Rearranging the above equation results in,

$$\frac{t}{G(f)} = \frac{Q_0 \; f^{\zeta} \; f_0^{-\zeta}}{(1-\zeta)} \tag{5.10}$$

where the instrument term is

$$G(f) = \frac{1}{\pi} \frac{\dfrac{dI(f)}{df}}{I(f)} \; .$$

By taking the logarithm of both sides of expression (5.10), the resulting equation is an implicit function of f_p and t. Thus, Q_0 and ζ can be easily estimated with respect to a given reference frequency f_0 and instrument system,

$$\log \frac{t}{G(f)} = \log \frac{Q_0}{1-\zeta} + \zeta \, \log \frac{f}{f_0} \tag{5.11}$$

This extended coda-Q expression (5.11) is simply an extension of Herrmann's (1980) attenuation model (5.9). However, as can be seen from Figure 5.3, equation (5.11) represents a first order linear relationship of the form $Y_i = A(\pm\delta A) + B(\pm\delta B) X_i$, where $A = \log\dfrac{Q_o}{1-\zeta}$ is the intercept and $B = \zeta$ is the slope. To solve (5.11) directly for Q_o and ζ, the unknowns A and B can be determined by using the techniques of linear least-squares theory (Neter *et al.*, 1983; Draper and Smith, 1981). Let N be the total number of observations of a data set, $Y = \log t/G(f)$, and $X = \log f$. Then the estimate for A and B given in matrix form is,

$$\begin{bmatrix} A \\ B \end{bmatrix} = \frac{1}{DET} \begin{bmatrix} \sum X_i^2 & -\sum X_i \\ -\sum X_i & N \end{bmatrix} \begin{bmatrix} \sum Y_i \\ \sum X_i Y_i \end{bmatrix}$$

where the determinant,

$$DET = N \sum X_i^2 - \left[\sum X_i\right]^2$$

and all the summations go from $i = 1$ to $i = N$. The frequency dependence can easily be determined from B the slope of (5.11) as follows,

$$\zeta = \frac{N \sum X_i Y_i - \sum X_i \sum Y_i}{N \sum X_i^2 - (\sum X_i)^2}$$

whereas, calculated from A the intercept of (5.11),

$$Q_o = (1-\zeta)\cdot 10^A$$

where,

$$A = \frac{\sum Y_i - B\sum X_i}{N}$$
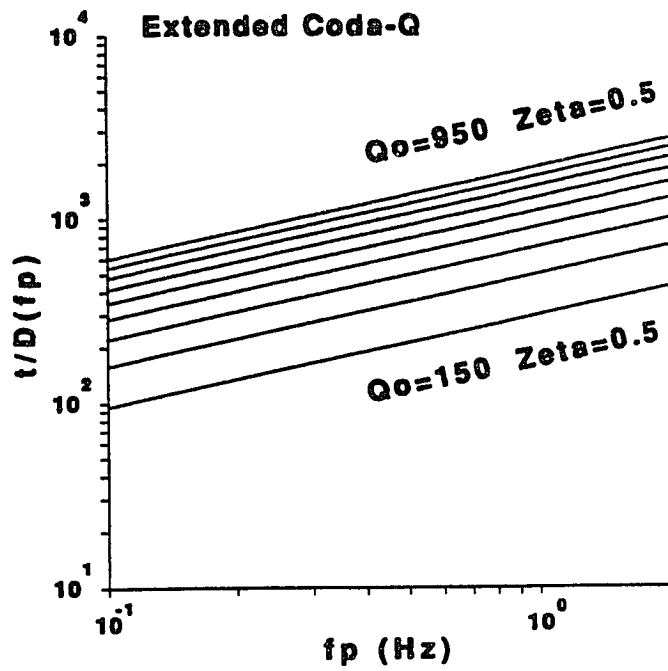
Figure 5.3. Selected extended coda-Q curves for the WWSSN short-period instrument.

At this point, it is important to mention that, given f_o, the coda attenuation model (5.11) also provide a faster and more efficient way to construct the theoretical master curves for both the coda-Q and coda shape methods. Unlike Herrmann's (1980) procedure to evaluate (5.9 or 5.8) and (5.7), it suffices to search for only the highest predominant frequency value at the shortest desirable time. Therefore, by decrementing this starting frequency to calculate t in expression (5.11), the coda-Q master curves can be constructed for any Q_o and ζ pairs. The coda shape master curves are similarly constructed; however, the term df_p/dt still has to be evaluated numerically.

5.4 Error Estimation

It is clear that, rather than experimenting with master curve matching, the advantage of the method described above is providing a deterministic approach for simultaneously finding Q_o and ζ. In addition, as in any least squares application, it provides the necessary statistical means to estimate errors associated with calculated results, and reflect data quality. Traditionally, the standard deviations and correlation coefficients are such statistical parameters.

The standard deviation of the frequency dependence may simply be expressed as,

$$\delta\zeta = \sqrt{\text{var}(\zeta)} \tag{5.12}$$

and the variance of ζ is

$$\text{var}(\zeta) = \frac{N \, S^2}{\text{DET}}$$

where, N is the total number of samples, DET is the determinant defined in

the previous section, and the term

$$S^2 = \frac{\sum Y_i^2 - \frac{(\sum Y_i)^2}{N} - B\left[\sum X_i Y_i - \frac{\sum X_i \sum Y_i}{N}\right]}{N-2}.$$

As for the standard deviation of the quality factor, Jenkins and Watts (1968) define the variance of a non-linear function as follows,

$$\text{var}(Q_0) = \text{var}[F(A,\zeta)]$$

such that, for practical purpose, it takes the form

$$\text{var}(Q_0) = \left[\frac{dF}{dA}\right]^2 \text{var}(A) + \left[\frac{dF}{d\zeta}\right]^2 \text{var}(\zeta) + 2\left[\frac{dF}{dA}\right]\left[\frac{dF}{d\zeta}\right] \text{cov}(A,\zeta)$$

where, A is the intercept of expression (5.11), $\frac{dF}{d\zeta} = -10^A$,

$\frac{dF}{dA} = (1-\zeta)10^A \ln 10$, and the covariance of A and ζ is

$$\text{cov}(A,\zeta) = -\frac{S^2 \overline{X}}{\sum(X_i - \overline{X})^2}$$

where, $\overline{X} = \sum \frac{X_i}{N}$. Therefore, the standard deviation of Q is simply,

$$\delta Q_0 = \sqrt{\text{var}(Q_0)} \tag{5.13}$$

Finally, to statistically describe the quality of data, the correlation coefficient is given as,

$$C = \frac{\sum X_i Y_i - N\overline{XY}}{\sqrt{\sum(X_i - NX)^2 \sum(Y_i - NY)^2}} \tag{5.14}$$

where, $\overline{Y} = \sum \frac{Y_i}{N}$ is the arithmetic mean.

CHAPTER 6

ATTENUATION DATA ANALYSIS

The extended coda-Q method, presented in Chapter 5, provides an efficient deterministic approach for calculating Q_o and ζ simultaneously. It does not only overcome the drawbacks of the master curve matching approach, but also allows for direct estimation of the various statistical parameters. Results of applying the method, to investigate the regional lateral variation of Lg coda wave attenuation across the Arabian plate, are presented in this chapter.

6.1 Coda Wave Data

Stations SHI, EIL and JER provided the microfilms of short-period, vertical component (SPZ) seismograms which are exclusively used in this study. The location coordinates for these stations are given in Chapter 1. Figure 2.1 shows their geographic distribution with respect to the Arabian plate. Though it is far from ideal, the stations provided good coverage of mainly the northern half of the plate. The peak instrument magnification of stations SHI and JER is 50,000, whereas, EIL is set to either 100,000 or 200,000.

Data from stations TAB and MHI ($36.3000°$ N,$59.4945°$ E) were also examined but not included in this study. The purpose was to test the extended coda-Q method and compare the results with Nuttli's (1980) attenuation study of Iran. Unfortunately, TAB and MHI seismograms were found unusable because of their relatively low instrument magnification,

6,250 and 12,500 respectively.

All the selected earthquakes occurred between 1971 and 1974, and located at or near the boundaries of the Arabian and Iranian, Turkish or African plates. Figure 2.1 shows the majority were associated with either the Zagros, Taurus, Red Sea or the Gulf of Aden seismic zones. The locations and origin times of the earthquakes were taken from the Preliminary Determination of Epicenters (PDE) reports and bulletin of the International Seismological Center (ISC). Body wave magnitudes (m_b) ranged from 3.8 to 5.6. The events were of shallow crustal origin. The accuracy of reported earthquakes parameters has been discussed in Chapter 2.

Each seismogram was examined for the arrival of the Lg wave and the quality of high-frequency coda that followed it. Identification of Lg, a superposition of higher-mode Rayleigh and Love waves, was based on previously reported group velocity values. In Iran, they were observed to have periods of 1 to 3 sec, and an onset velocity of 3.45 ± 0.2 km/sec (Nuttli, 1980). An apparent velocity of 3.2-3.4 km/sec and 2-5 sec periods were obtained by Kadinsky-Cade *et al.* (1981), for waves across the Turkish and Iranian plateaus. Hence, by allowing for Lg duration, about 1 minute, the period and amplitude of tailing coda wavelets were carefully measured. The wavelets were picked so that there did not appear to be evidence of interfering wave arrivals that would affect the period or amplitude measurements. In other words, the selected coda wavelets were only those that approximate sine waves and whose entire waveform, not just their peaks and troughs, were clearly visible. Finally, since the 70 mm microfilms were magnified to several times the original seismogram, the periods or frequencies and amplitudes were converted back to the proper record scale. This

procedure was proposed by Nuttli (1983a, 1983b), because experimental evidence indicates that the zero crossing technique does not provide precise enough results.

To further improve the quality of observed data, the following factors, which contribute to the complexity of recorded coda waves and indirectly influence the results, are discussed by Nuttli (1986). First, the interfering arrivals of fundamental-mode Rayleigh waves within the coda time window. They are characterized by lower frequency and often larger amplitudes than the coda waves. Their group velocities vary between 2.6 and 1.4 km/sec. Second, the observed tendency of coda waves to be of constant frequency after a certain lapse time. This time increases as the earthquake or explosion magnitude increases. This may somehow be related to the source. In practice, both of these factors cause the departure of observed data from the coda theoretical model, i.e. the frequency of coda waves decrease as lapse time increases. In this study, these factors are also observed and excluded from the data.

The observed coda frequency varies between 0.144-1.06 Hz, and their travel time ranges from about 184 to 1455 sec. The distance between events and stations varies from about 352.9 to 2463.88 km. According to theory, the backscattering model for coda wave generation does not support using the coda-Q method at large epicentral distances. In spite of this limitation, Nuttli (1983b, 1986) successfully applied the method at such regional distances. Because of the relatively short duration of Lg coda wave at large distances, Nuttli (1983b) suggested that the coda, whose amplitude level soon diminishes by attenuation to that of the background noise, results from scattering near the station. As in this study Nuttli's

work demonstrates that, observed coda frequencies do decrease with increasing lapse time as predicted by Herrmann's (1980) attenuation model. It should be noted that, although other explanations can be afforded, no attempt is made in this study to further investigate these observations and speculations.

A number of examples are given to demonstrate the extended coda-Q method. For the purpose of this study, the reference frequency f_0 in expression (5.11) is set to 1 Hz. Some representative results obtained from single events recorded at SHI, JER and EIL stations, are shown in Figures 6.1 through 6.3. The circles denotes observed data points, and the middle solid line is the theoretical least squares fit which corresponds to the calculated Q_0 and ζ values. The other two solid lines represent the estimated standard deviation of the results. That is, $Q_0+\delta Q_0$ along with $\zeta+\delta\zeta$, and $Q_0-\delta Q_0$ along with $\zeta-\delta\zeta$, respectively. Equations (5.12) and (5.13) are used to calculate the standard deviations, whereas, (5.14) to determine the correlation coefficient factor. In each of these figures, log-log plots of $t/G(f_p)$ versus predominant frequency f_p, and f_p versus t are presented. The first, labelled " LS ", illustrates the extended coda-Q application. The second, labelled " MC ", represent the master curve technique. They are included for comparison purposes, because the master curves are calculated according to Q_0 and ζ values obtained by the extended coda-Q method. In addition, the anelastic attenuation coefficient γ and its standard deviation are included. It is related to Q, frequency f, and group velocity U according to the expression $\gamma = \pi f/QU$ (Nuttli, 1973).

It is sometime necessary to combine data from several events, recorded at the same station, to obtain sufficient range in coda wave
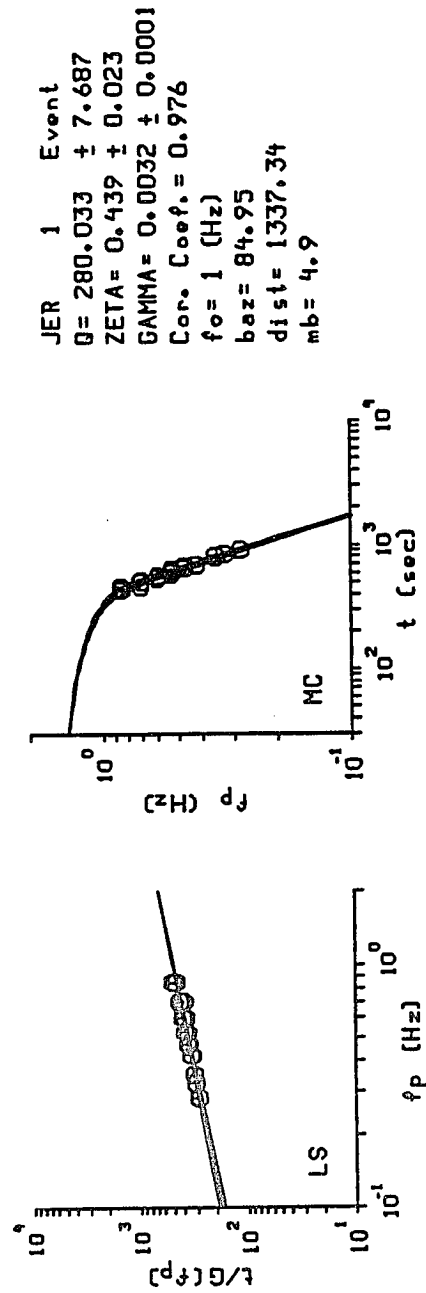
Figure 6.1. Plot of the extended coda-Q method (LS) versus the master curve technique (MC) for single-event data from JER station. The frequency dependence is denoted by ζ, and the anelastic attenuation factor by γ.
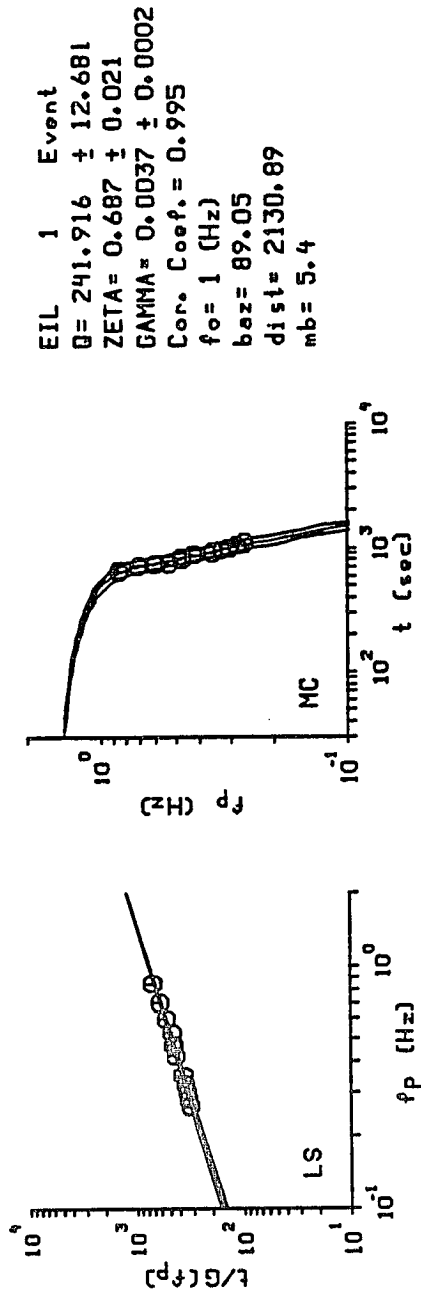
Figure 6.2. Plot of the extended coda-Q method (LS) versus the master curve technique (MC) for single-event data from EIL station. The frequency dependence is denoted by ζ, and the anelastic attenuation factor by γ.
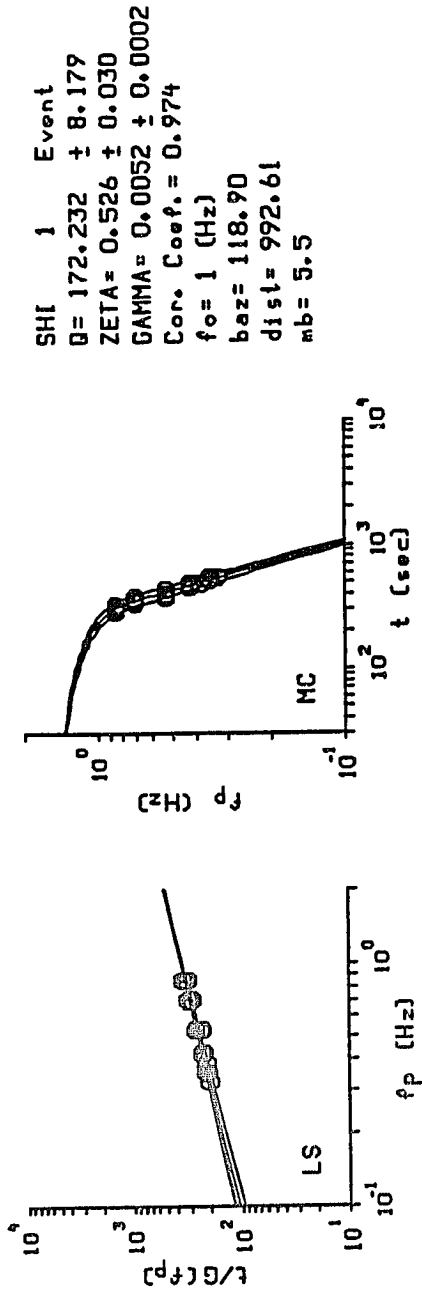
Figure 6.3. Plot of the extended coda-Q method (LS) versus the master curve technique (MC) for single-event data from SHI station. The frequency dependence is denoted by ζ, and the anelastic attenuation factor by γ.

- 266 -

frequency and travel time values, and to therefore improve the accuracy of Q_0 and ζ estimates. For this purpose the events are assumed to be in the same source region. The advantages of the approach are, (1) it maximizes the uniqueness of calculated results, and (2) it minimizes the tradeoff, due to limited frequency range, which causes the estimate of Q_0 to decrease as the value of ζ increases or vice versa. Application of this multiple-event single-station approach is demonstrated in Figures 6.4 and 6.5. The data and results are from events recorded at stations JER and EIL, respectively. The selected events are within approximately the same backazimuth (149.48-150.13, 74.64-75.02 degrees) and epicentral distance (2445.17-2446.94, 1409.05-1482.07 km) from the stations. In each of these examples data from two separate earthquakes are combined. It is clear, from these and the previous examples, that the extended coda-Q provide a simple yet accurate method for estimating Q_0 and ζ from coda waves. Evidence to that is the excellent match between the master curves and observed coda wave frequency data.

In applying the coda shape method, the measured peak-to-peak wavelets amplitude are plotted versus time on logarithmic axes and compared with master curves to estimate Q_0 and ζ. These theoretical curves are usually constructed by first evaluating expression (5.8) or (5.9) for the predominant frequencies f_p at various travel times, second, equation (5.7) for the coda shape function $C(f_p,t)$. However, for comparison purposes Q_0, ζ and the predominant frequencies at various travel times are all determined using the extended coda-Q equation (5.11). Given this information it is relatively easy to evaluate the derivative df_p/dt numerically and construct the coda shape master curve using equation (5.7). Figures 6.6, 6.7 and 6.8
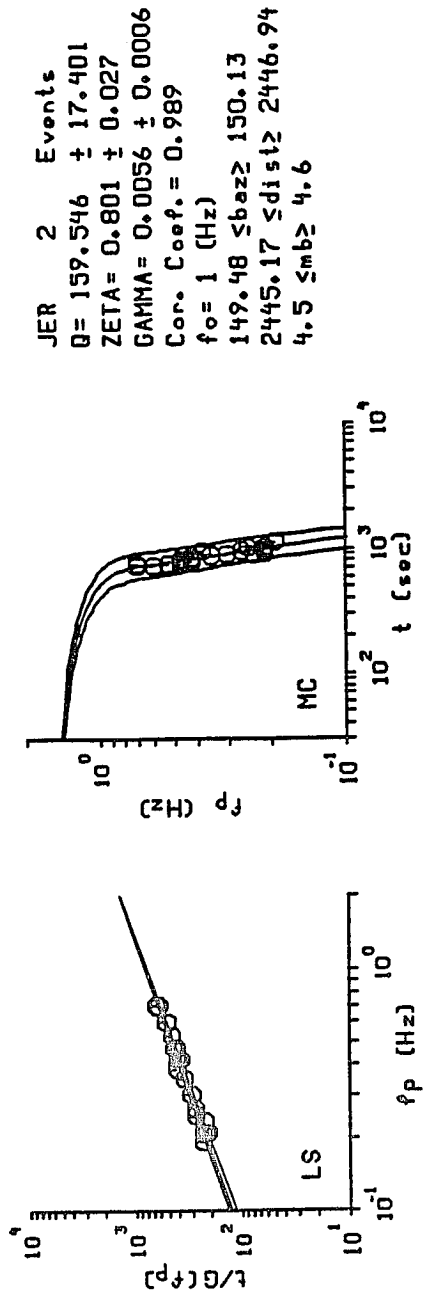
Figure 6.4. Plot of the extended coda-Q method (LS) versus the master curve technique (MC). The frequency dependence is denoted by ζ, and the anelastic attenuation factor by γ. The multiple-event data is from JER station.

JER   2   Events
Q= 159.546 ± 17.401
ZETA= 0.801 ± 0.027
GAMMA= 0.0056 ± 0.0006
Cor. Coef. = 0.989
f_o= 1 (Hz)
149.48 ≤baz≥ 150.13
2445.17 ≤dist≥ 2446.94
4.5 ≤mb≥ 4.6

- 268 -
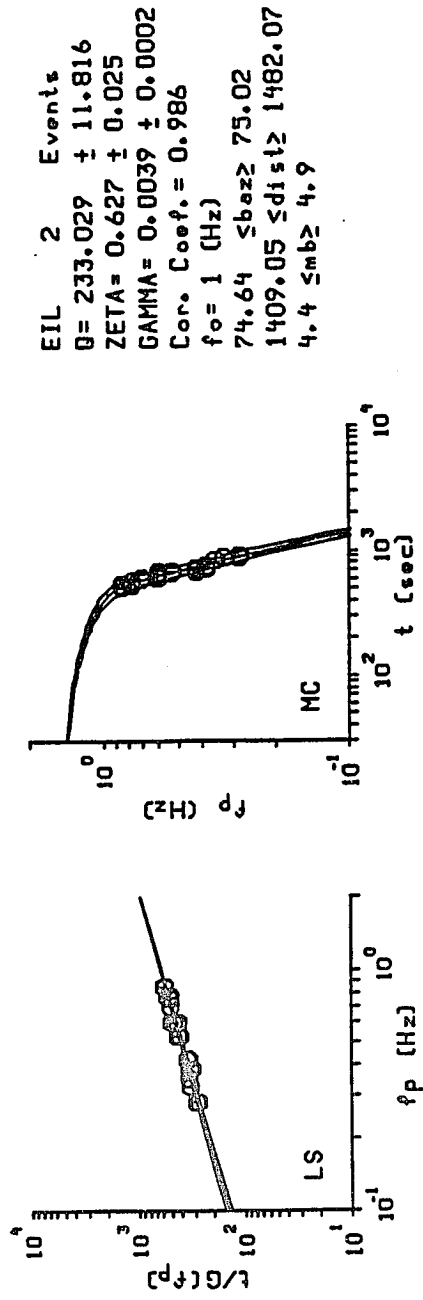
Figure 6.5. Plot of the extended coda-Q method (LS) versus the master curve technique (MC). The frequency dependence is denoted by ζ, and the anelastic attenuation factor by γ. The multiple-event data is from EIL station.

- 269 -

EIL   1   Event
Q= 223.593   ± 17.245
ZETA= 0.650 ± 0.035
GAMMA= 0.0040 ± 0.0003
Cor. Coef. = 0.987
fo= 1 [Hz]
baz= 74.64
dist= 1482.07
mb= 4.4
Lg Wave Coda
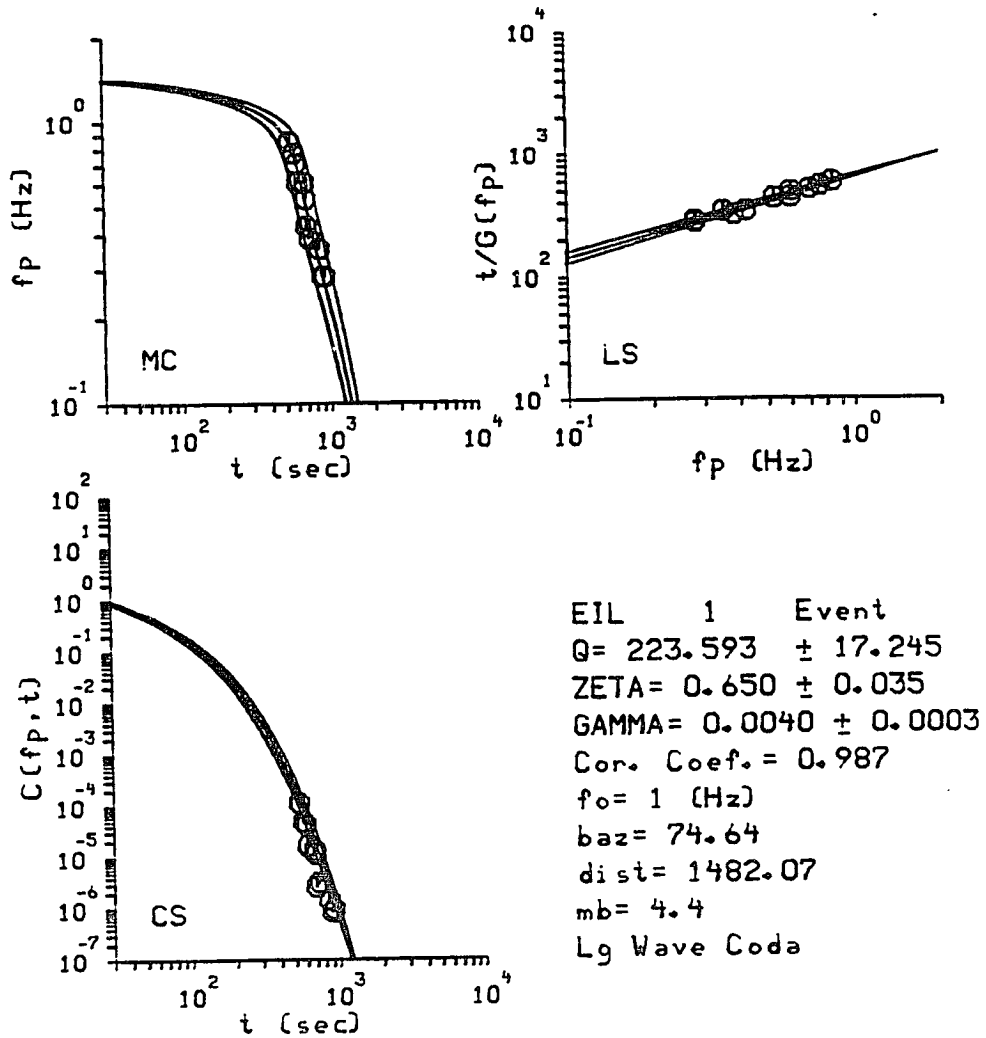
Figure 6.6.   Plot of the extended coda-Q method (LS), master curve technique (MC), and coda shape method (CS). The frequency dependence is denoted by ζ, and the anelastic attenuation factor by γ. The single-event data is from EIL station.

- 270 -
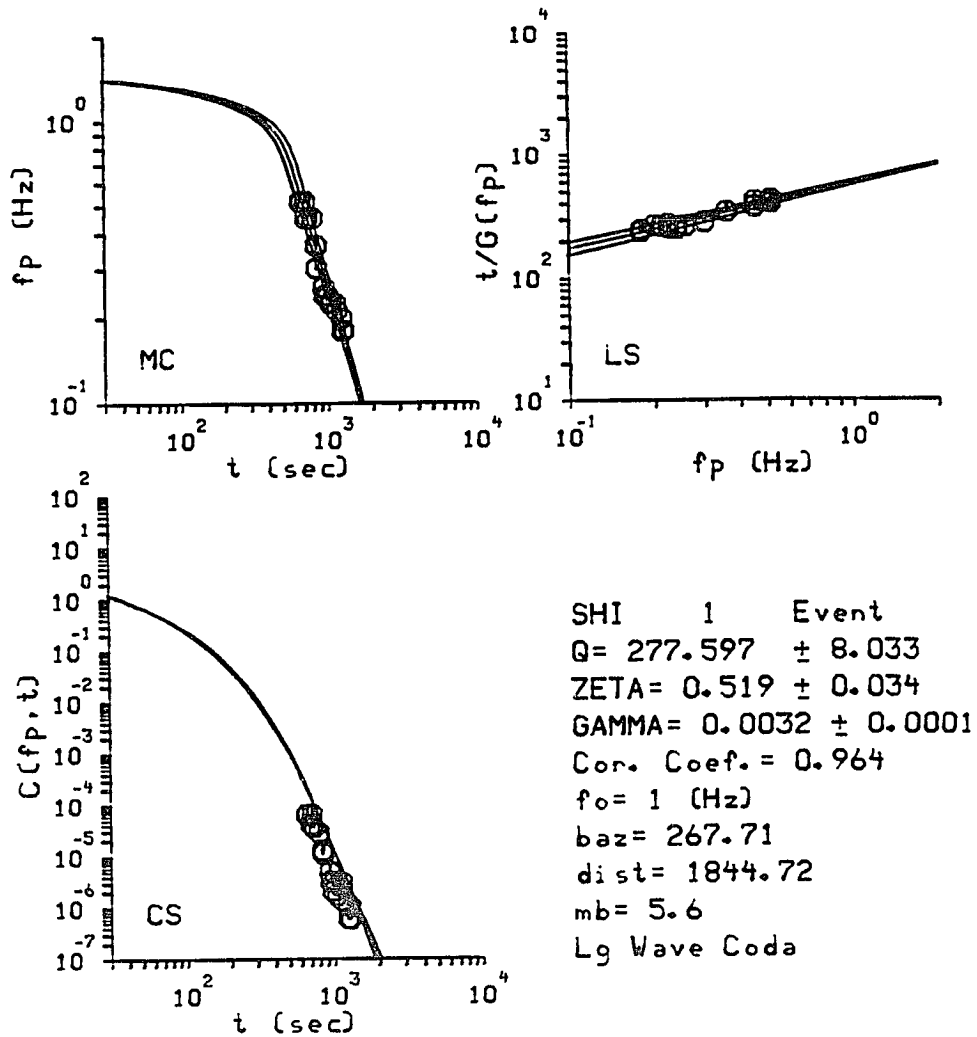
Figure 6.7. Plot of the extended coda-Q method (LS), master curve technique (MC), and coda shape method (CS). The frequency dependence is denoted by ζ, and the anelastic attenuation factor by γ. The single-event data is from SHI station.

- 271 -
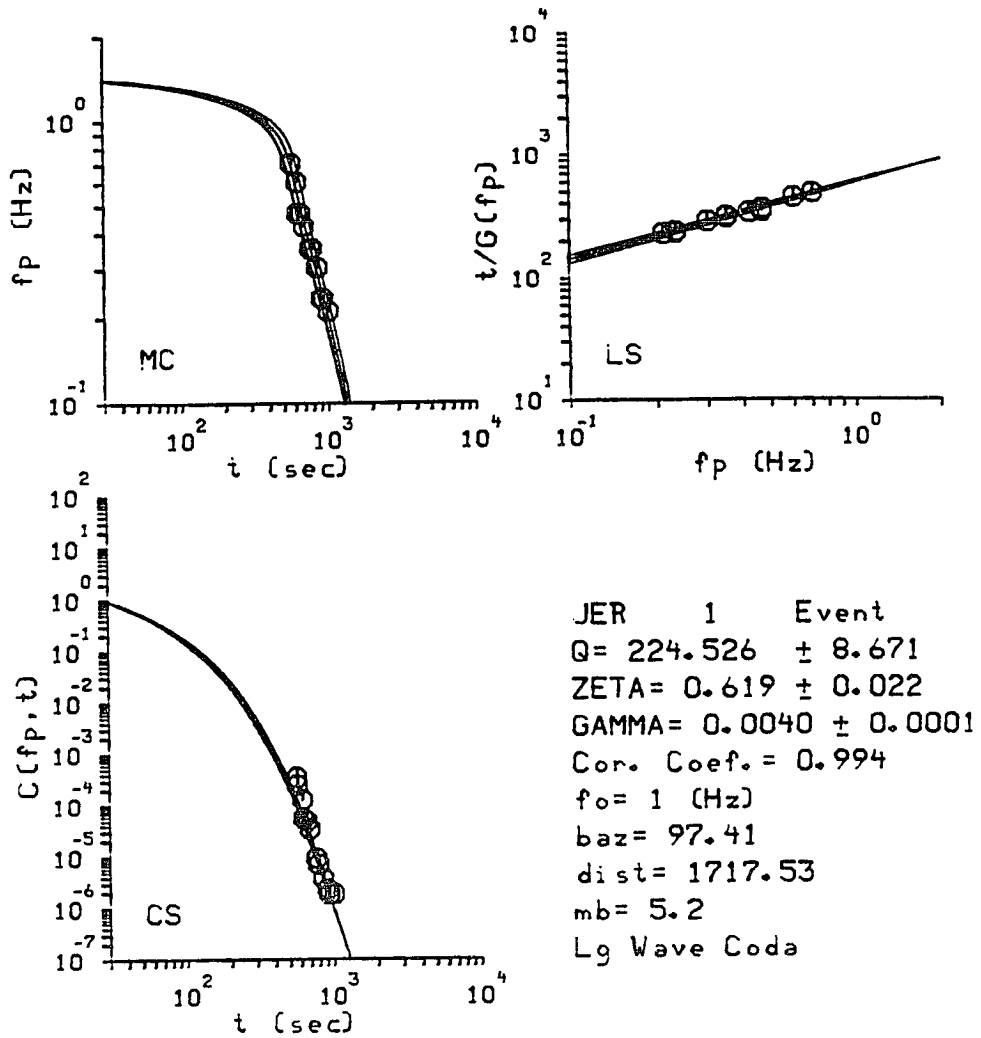
Figure 6.8. Plot of the extended coda-Q method (LS), master curve technique (MC), and coda shape method (CS). The frequency dependence is denoted by ζ, and the anelastic attenuation factor by γ. The single-event data is from JER station.

show single-event examples recorded at EIL, JER and SHI stations. In these figures the coda shape plots are labelled " CS ". The examples show that results of the extended coda-Q method are in good agreement with the coda shape as reflected by the match between the theoretical curves and coda amplitudes.

6.2 Attenuation Variation

Figures 6.9 through 6.17 graphically summarize the variation of Lg coda waves attenuation. Maps showing the quality factor Q_0 are presented in Figures 6.9-6.11, the frequency dependence ζ in Figures 6.12-6.14, whereas, the anelastic attenuation coefficient γ in Figures 6.15-6.17. The results are obtained by analyzing data collected from 104 earthquakes. The parameters for these events are listed in Appendix-B.

An inspection of Q_0 and γ maps, Figures 6.9 and 6.15 in particular, reveal significant spatial variation between the attenuation of Lg coda waves propagating across the Arabian and Iranian plates, and along the Zagros continental collision zone which separates them. In contrast, the pattern of attenuation within the Arabian plate itself shows a relatively gradual lateral variation. The regional pattern is less distinct, because it reflects the influence of stations location and earthquakes distribution with respect to the major tectonic units of the plate. It also reflects the lateral gradual geologic transition between the units themselves. Figures 2.1 and 2.2 show that the units general trend is NW-SE, whereas, the stations are located within the seismic zones and either to the east or west of the plate. Because of such an non-optimal geographic and geologic configuration, almost all of the paths between stations and epicenters traverse more than
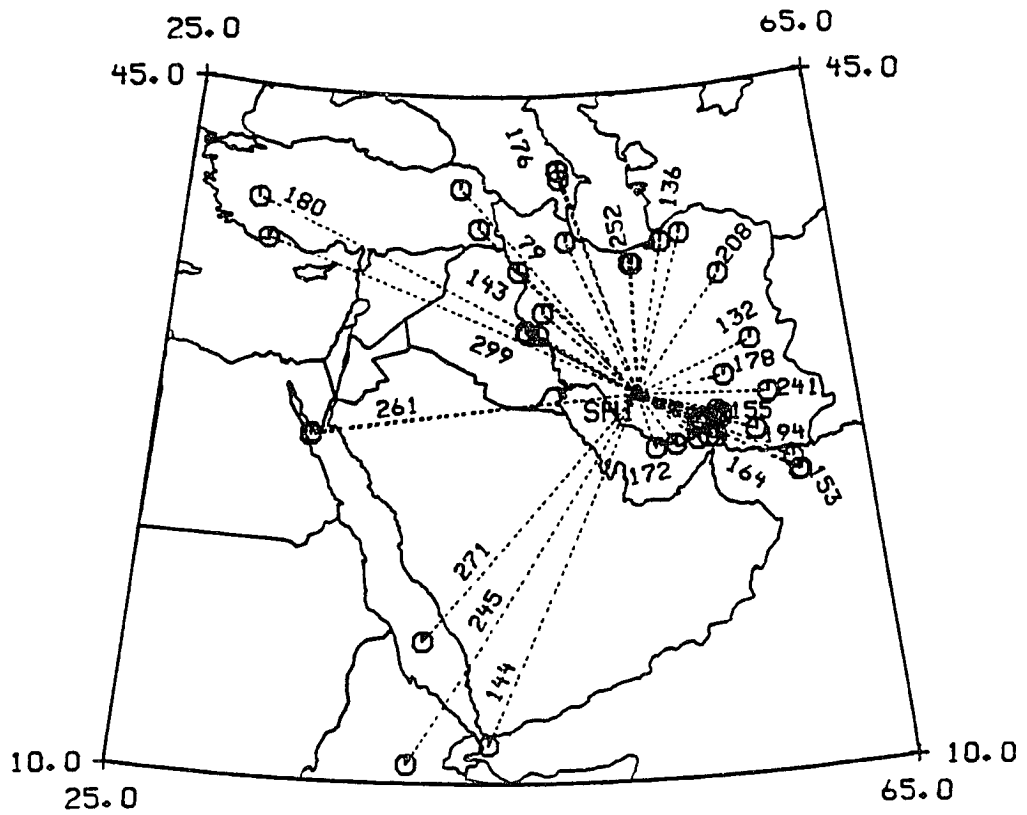
Figure 6.9. The quality factor values of Lg coda waves for individual earthquakes recorded at SHI station. The circles indicate the location of the epicenters.

- 274 -
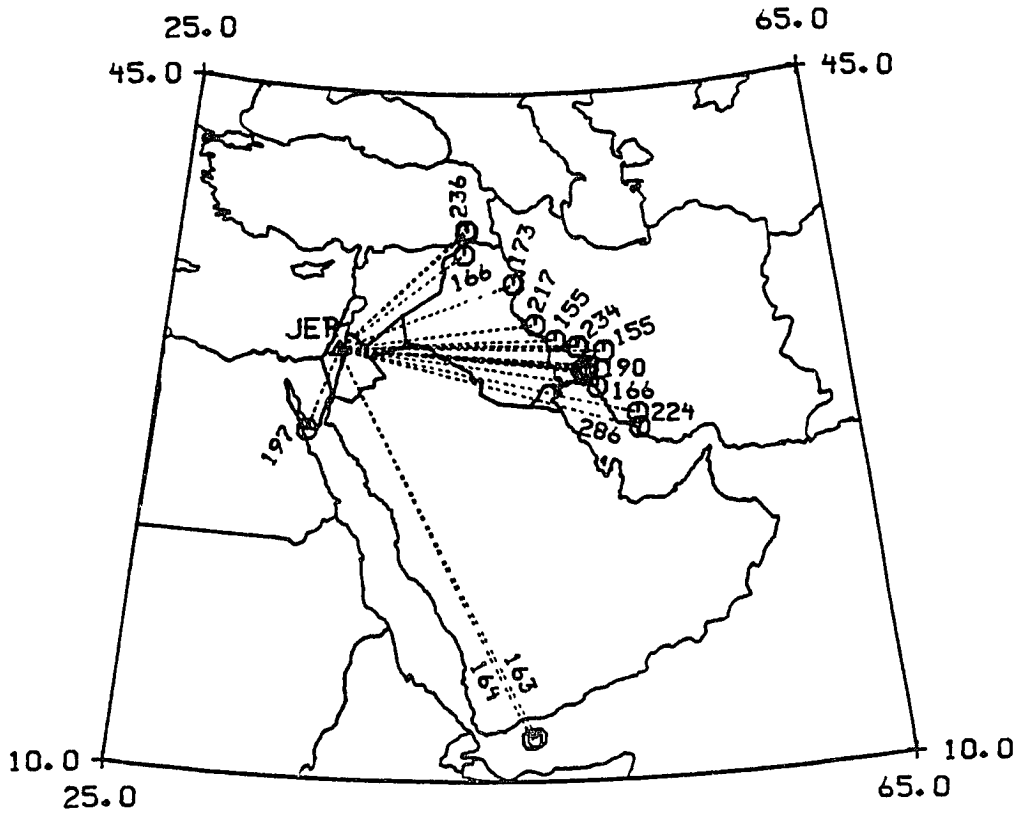
Figure 6.10. The quality factor values of Lg coda waves for individual earthquakes recorded at JER station. The circles indicate the location of the epicenters.
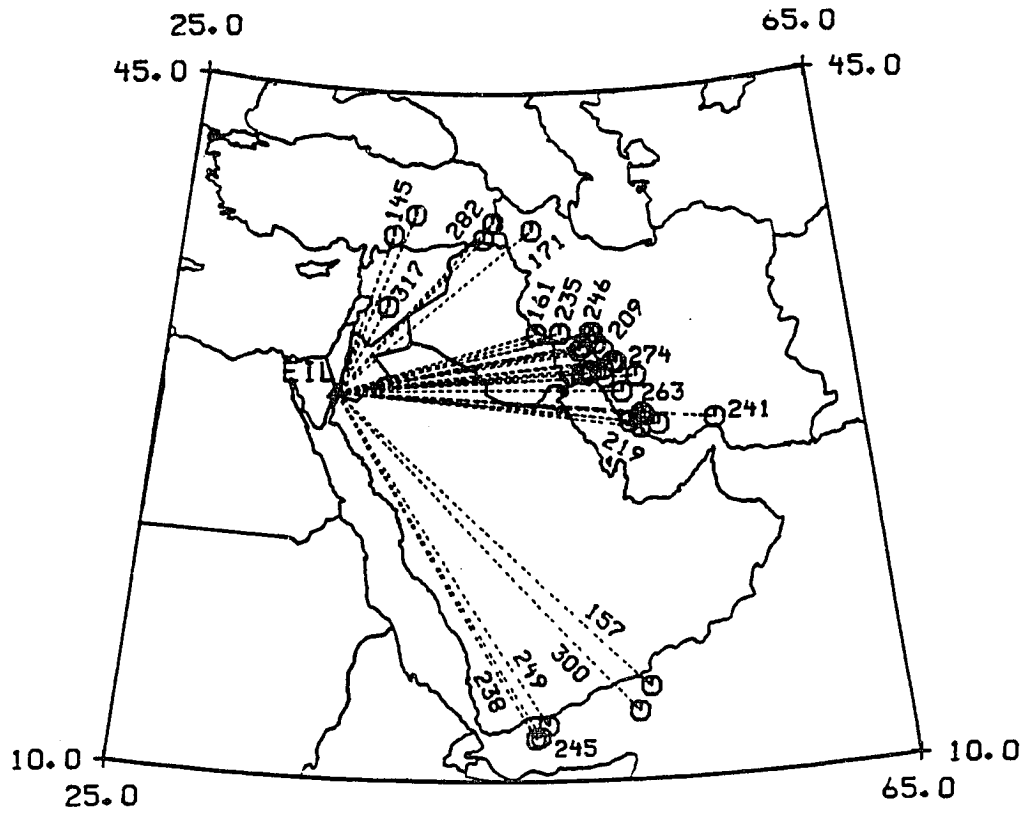
Figure 6.11. The quality factor values of Lg coda waves for individual earthquakes recorded at EIL station. The circles indicate the location of the epicenters.

- 276 -
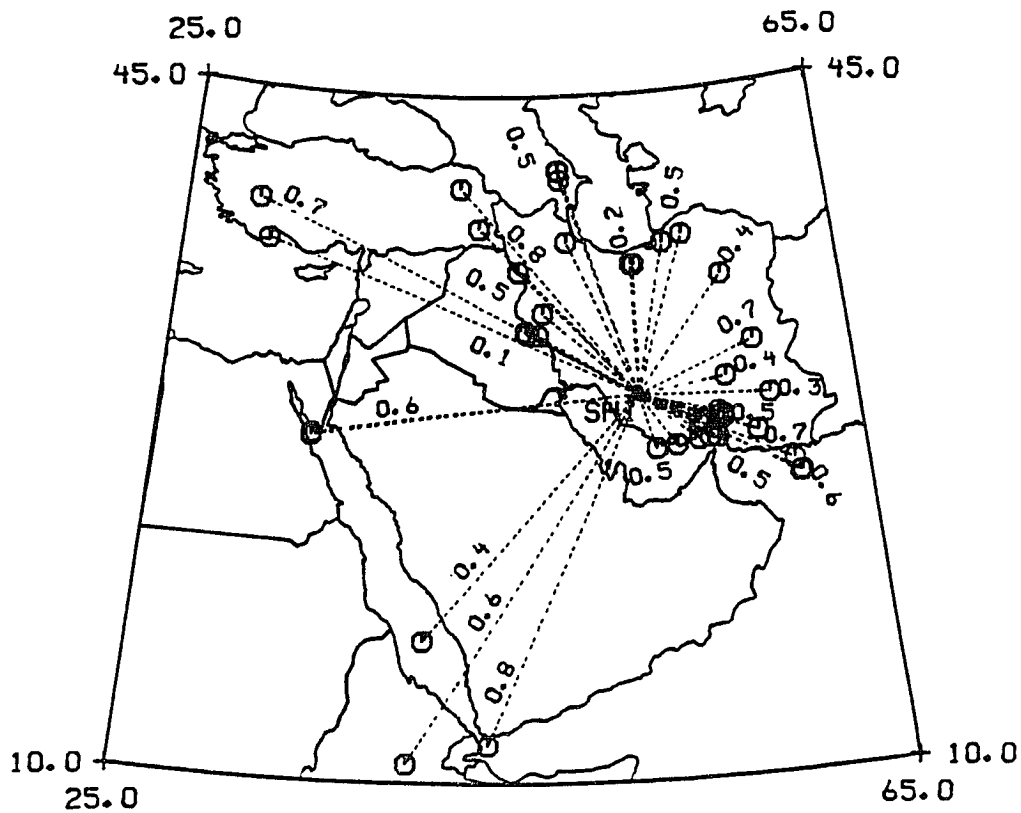
Figure 6.12. The frequency dependence values of Lg coda waves for individual earthquakes recorded at SHI station. The circles indicate the location of the epicenters.
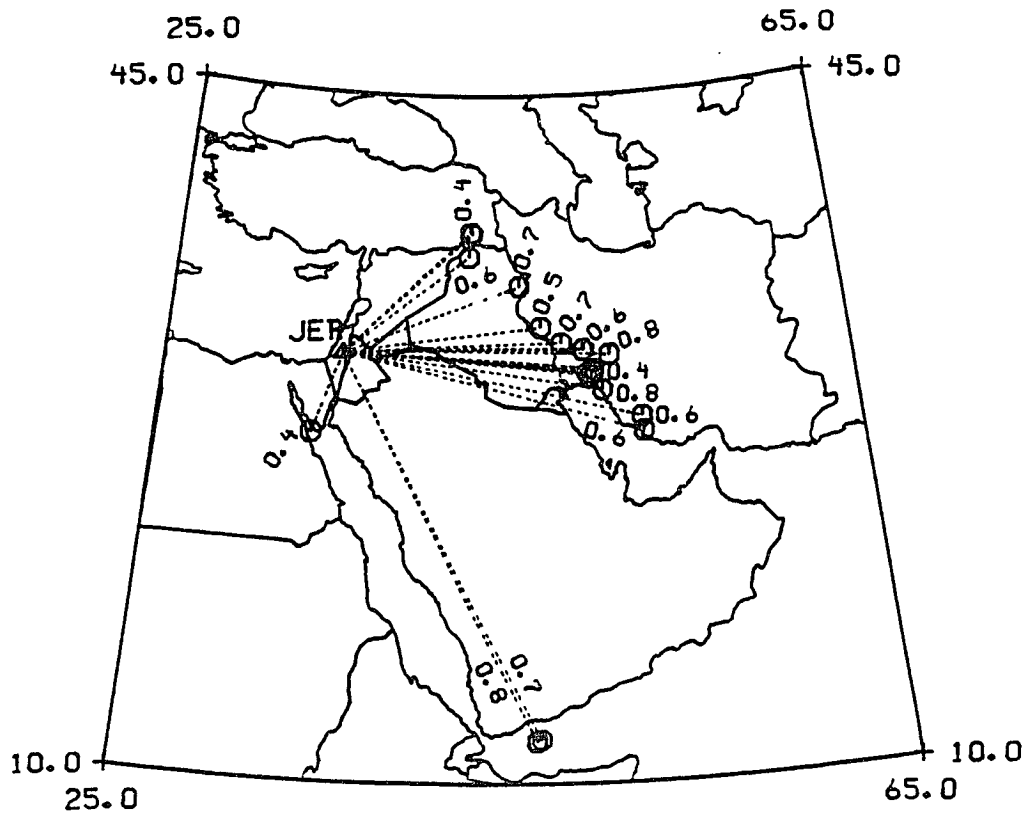
Figure 6.13. The frequency dependence values of Lg coda waves
for individual earthquakes recorded at JER station.
The circles indicate the location of the epicenters.

- 278 -
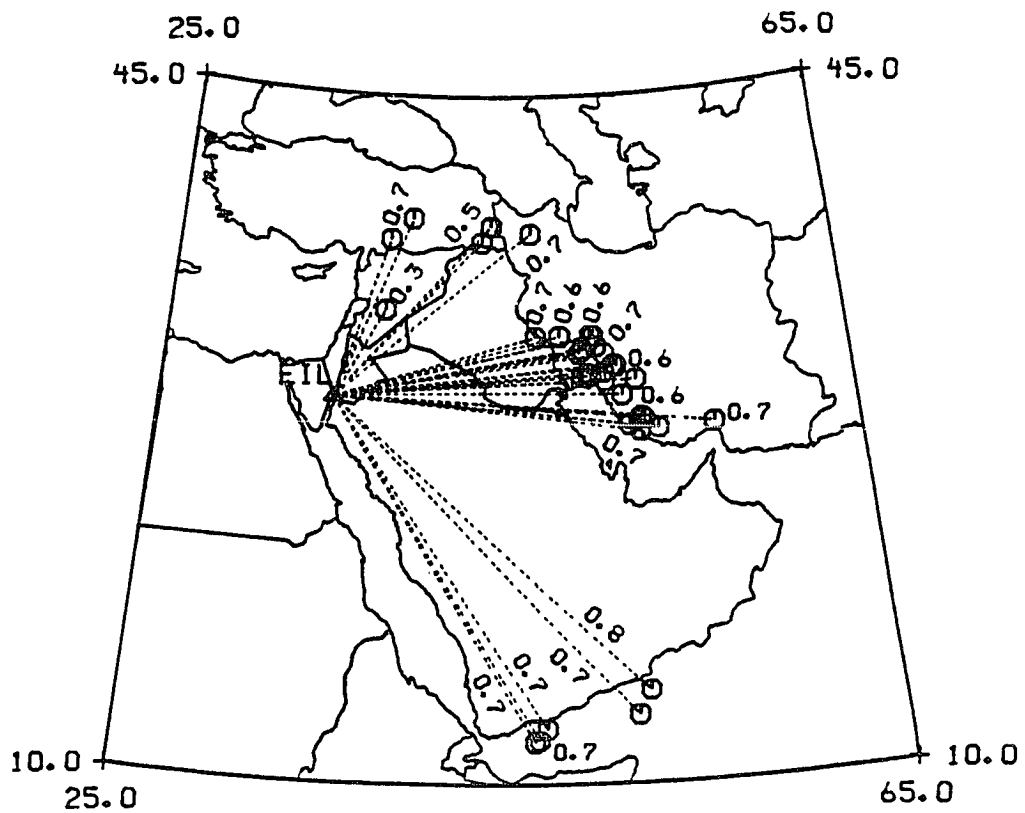
Figure 6.14. The frequency dependence values of Lg coda waves for individual earthquakes recorded at EIL station. The circles indicate the location of the epicenters.

- 279 -
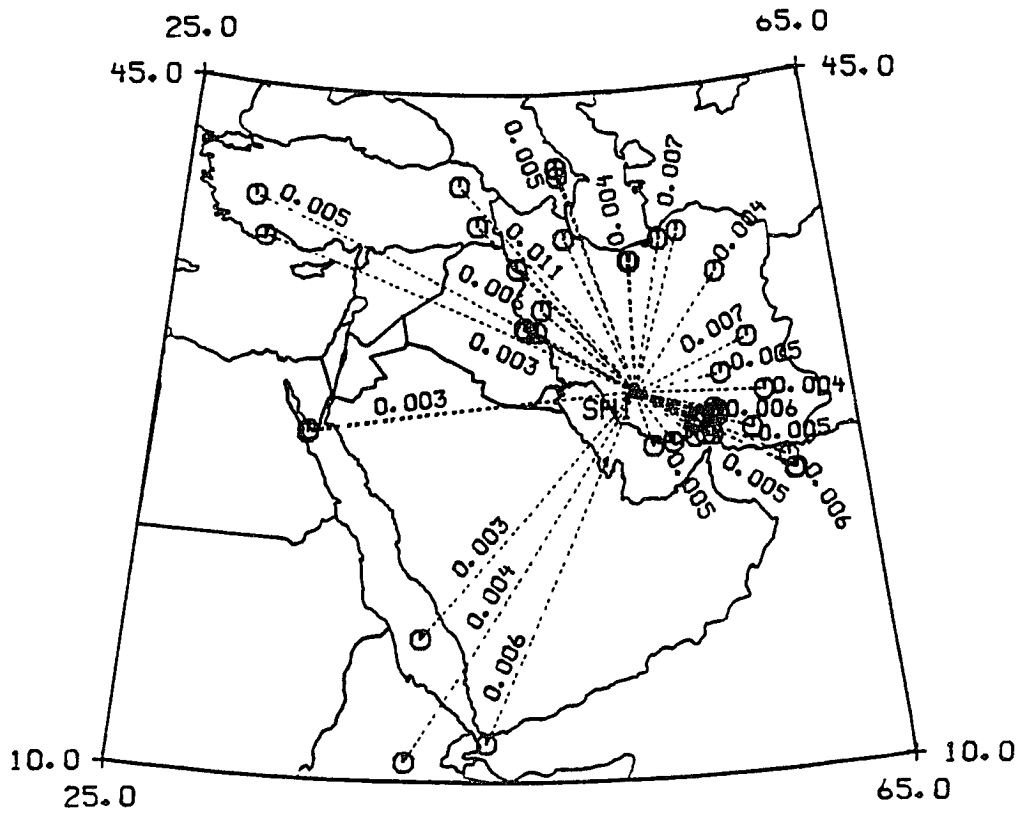
Figure 6.15. The anelastic attenuation values of Lg coda waves for individual earthquakes recorded at SHI station. The circles indicate the location of the epicenters.
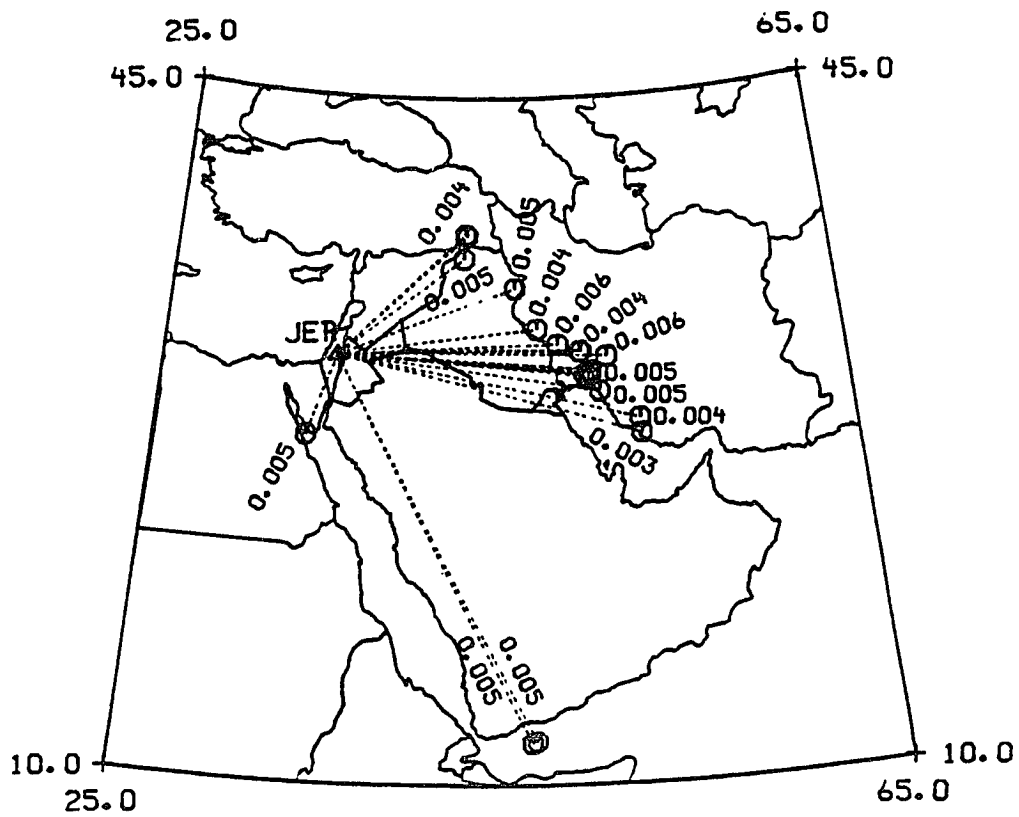
Figure 6.17. The anelastic attenuation values of Lg coda waves for individual earthquakes recorded at EIL station. The circles indicate the location of the epicenters.
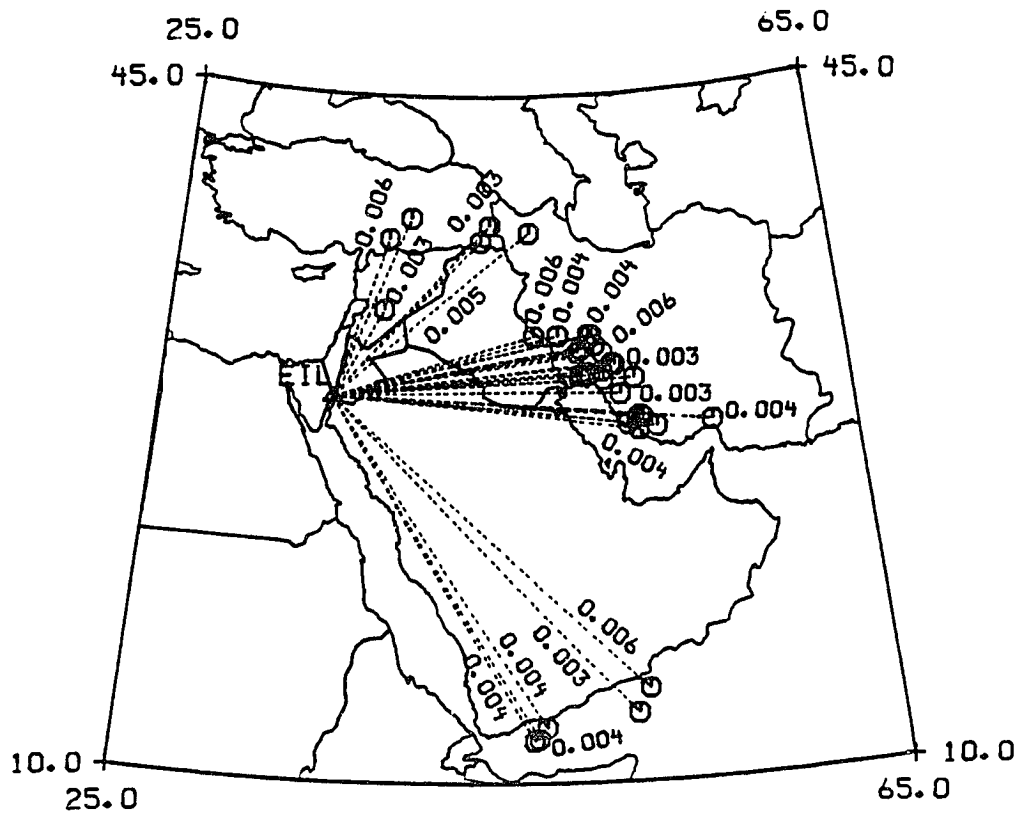
Figure 6.16. The anelastic attenuation values of Lg coda waves for individual earthquakes recorded at JER station. The circles indicate the location of the epicenters.

one physiographic and tectonic feature. Therefore, the calculated results should be considered preliminary and represent an average determination of the crustal attenuation in the region.

Unlike SHI, the EIL and JER stations provide better coverage of the Arabian plate, because more earthquakes have been recorded along the Zagros zone than the Dead Sea fault system. Comparison between Figures 6.9, 6.10 and 6.11, shows that the results obtained from these three stations agree well. Evidence for this, for instance, are the values of the east-west trending paths with Q_0 of 261 for SHI, 263 for EIL, and 224 to 286 for JER. Though differences between the results can be attributed to path azimuthal variation, however, there are additional influencing factors which will be discussed later. Inspection of EIL and JER stations maps indicates that Q_0 gradually increases in the northern and eastern direction, but decreases across the northeastern portion of the plate (Figures 6.10 and 6.11). Variations of Q_0 therefore follow regions of varying levels of deformation and scattering characteristics. From a geological view point, the northeastern section of the Arabian plate represents an area of increasing crustal heterogeneity. Another such area is parallel to the eastern coast of the Mediterranean Sea, along which Q_0 decreases westward (Figure 6.10). A similar pattern of γ variation is observed in Figures 6.16 and 6.17. As for the dependence of Q on frequency, results of this study indicate that ζ values show no significant correlation with the tectonic setting, as suggested by Singh and Herrmann (1983). Inspection of the data and Figures 6.12, 6.13, and 6.14, however, show that Q is highly frequency dependent throughout the region. In general, higher coda Q_0 estimates are accompanied by lower ζ values. It is interesting to note that EIL station paths

across the Arabian shield show clear departures from this observation. Furthermore, the differences sometimes occurring between Q_0 and ζ values for similar paths are probably due to the extended coda-Q intrinsic relationship and trade-off between these parameters.

The results from station JER indicate that the Arabian plate average $Q_0 = 199$, $\zeta = 0.6$, and $\gamma = 0.0047 \text{km}^{-1}$. Results from station SHI, excluding the Zagros region, show an average $Q_0 = 210$, $\zeta = 0.5$, and $\gamma = 0.0046 \text{km}^{-1}$, whereas, EIL station shows $Q_0 = 234$, $\zeta = 0.6$, and $\gamma = 0.0043 \text{km}^{-1}$. Accordingly, $Q_0 = 214$, $\zeta = 0.6$, and $\gamma = 0.0045 \text{km}^{-1}$, represents an average crustal attenuation of the northern Arabian plate. Unfortunately, there are no previously published estimates for the region with which to compare the above results.

It is not surprising to see high attenuation along a seismically active tectonic region like the Zagros zone. Data from five events recorded at SHI station clearly reflect this observation (Figure 6.9). The Lg coda wave propagation paths from these events closely coincide with the general trend of this intensely heterogeneous deformation zone. Three of the events are to the northwest of SHI, while the other two are southeast of this station. Their average backazimuths are 321.59 and 115.39 degrees, and epicentral distances of 1249.56 and 492.62 km, respectively. The average Q_0 for the NW path is 65.09, whereas, the SE path it is 70.05. These low Q_0 are associated with high average ζ values of 0.86 and 0.82. According to these results $\gamma = 0.015 \text{km}^{-1}$ is determined for the NW path, and $\gamma = 0.013 \text{km}^{-1}$ for the SE path. As an example, in Figures 6.9, 6.12, and 6.15 the three northwestern events are shown with $Q_0 = 79$, $\zeta = 0.8$, and $\gamma = 0.011 \text{km}^{-1}$. Although, the events practically share a common path but not a common

source region, this low Q_0 estimate is obtained by combining the f_p versus t data from the three events. It is interesting to observe that Q_0 seems to systematically and symmetrically increase as the event backazimuth shifts away from the central region of high attenuation. Furthermore, it is also important to note that the low Q_0 estimate along the main Zagros thrust zone is also coincident with the low Bouguer gravity field reported by Snyder and Barazangi (1986).

In some respect the most striking results of this study are the relatively high attenuation estimates across the Arabian shield. The results are obtained from earthquakes generated at ridge crests in the Red Sea and Gulf of Aden. The largest Q_0 values determined from the EIL and SHI coda data are 300 and 271, respectively (Figures 6.9 and 6.10). Although they are admittedly low in comparison with other shield regions, the Q_0 maps seems to reveal a notable lateral variation pattern. Figure 6.10 shows that across the Arabian shield Q_0 gradually increases eastward, but decreases abruptly toward the Red Sea. This asymmetrically pattern is similar to that of the simple Bouguer gravity anomaly across the shield reported by Gettings et al. (1983). Unlike the western paths which are mainly within the exposed shield, the eastern paths also traverse parts of the Arabian Platform to the north and south of it. Results for stations EIL and JER indicate lower Q_0 values along the shield's western and eastern edges parallel to the Red Sea (Figure 6.10 and 6.11). On the other hand, SHI results show similar, although less obvious, variation in the north-south direction (Figure 6.9). Recently, Mokhtar et al. (1987) found that Q_β increases gradually from 30 in the upper 50 meters to 150 at about 0.5 km, and 400-700 below that depth. These results are obtained from surface and

body waves data using the Saudi Arabia deep seismic refraction profile which exclusively traverses, for 1000 km, the Arabian shield in a NE-SW direction. It should be noted that their work also shows a similar lateral pattern of attenuation variation across the shield, but with higher Q than estimated in this study. Using two dimensional ray tracing techniques, Mooney *et al.* (1985) interpreted the crustal structure of the Arabian shield as complex and heterogeneous. One may argue that the observed high attenuation is simply a manifestation of the physiographic and tectonic features along the propagation paths within both the shield and the plate. Although this would explain the observed asymmetry, it neither completely justify the low Q_0 values nor the discrepancy between EIL and JER stations results. It would appear more likely that the location of stations with respect to the plate tectonic boundaries is an important contributing factor to the results. JER and EIL are located to the west of the Dead Sea complex transform fault system, whereas, SHI is within the Zagros mountains folded belt. Both of which are major structural and heterogeneous zones. This suggests that propagating waves are not only being attenuated along the paths and at the boundaries, but also multiply reflected within the zones. Since coda Q expresses both absorption and scattering attenuation effects, it seems possible that this multiple bouncing plays a significant role in exaggerating the attenuation estimate, and apparently Q dependence on frequency as well. Although this explanation is speculative and by no means proven, it does provide for the preservation of regional variation pattern. This is because waves along converging propagation paths are almost equally attenuated within the same general area near the station. Finally, the discrepancy between EIL and JER results can be attributed to

the fact that, the latter station is located closer to the section of the Dead Sea transform fault system which is more heterogeneous. Paths from events in the Gulf of Aden to JER sample considerably more of the fault zone than paths to EIL station.

The results obtained from station SHI (Figure 6.15) are especially important, because many of the seismograms used in this study were previously examined by Nuttli (1980) to investigate the attenuation of 1 Hz crustal phases in Iran. For this reason, the earthquakes are selected to cover as complete azimuthal range as possible, and similar to that of Nuttli. The distinction between the two studies is that γ values are estimated by totally different methods, namely the extended coda-Q versus Lg wave sustained maximum amplitude decrease with increasing epicentral distance. Herrmann (1980) demonstrated the correctness of Q inferences from γ, as proposed by Nuttli (1973). Comparison of results within Iran indicates that the pattern of γ variation agree well, and that Nuttli's (1980) values are within the estimated standard deviations obtained in this study. However, the Iranian plate, excluding the Zagros zone, average Q_0 is about 181, $\zeta = 0.4$, and $\gamma = 0.0054 \text{km}^{-1}$. This is obviously greater than Nuttli's value of $\gamma = 0.0045 \text{km}^{-1}$ which corresponds to an apparent Q of 200 for Lg, 150 for Sn, and 125 for Pg. Difference between the results may be due to the following factors. First, coda Q and γ estimates need not be in complete agreement. According to theory, coda γ values should estimate the Q of Lg wave arrival, while the coda Q represents an average Q over a much wider region than that sampled by the direct Lg waves (Herrmann, 1980). Second, measurements of Lg amplitude decay with epicentral distance method, for waves of a given frequency, works well when Q_0 is

approximately constant over the area (Nuttli, 1986). Because of the complex geologic and tectonic settings of Iran, the possibility that this requirement is violated cannot be ruled out. Third, most of the results obtained in this study are from events with large epicentral distances, whereas, Nuttli (1980) included more events closer to the stations. This due to the fact that not all recorded seismograms which are suitable for Lg studies can necessarily be utilized for coda wave analysis. Fourth, the estimation of γ is significantly influenced by the scatter of equalized amplitude data at distances shorter than than 500 km. Inspection of Nuttli's (1980) amplitude-distance plots seems to suggest that Lg amplitudes at distance greater than about 700 km can be fit with a higher γ value, i.e. 0.005km^{-1}.

6.3 Discussion

In a study of the lateral variations of high-frequency seismic wave propagation at regional distance across the Middle East, Kadinsky-Cade *et al.* (1981) attempted to compare heat flow values with the tectonic setting of the region. They concluded that Pollack and Chapman (1977) data, which is based on a spherical harmonic synthesis of heat flow values over $5° \times 5°$ latitude-longitude grid, was not closely enough spaced to provide useful information. Furthermore, Gettings (1982), Gettings and Showail (1982), and Healy *et al.* (1982) report that heat flow measurements at shot points along the Saudi Arabian deep seismic refraction profile did not indicate higher than average values across the Arabian shield.

The high attenuation of Lg coda waves along the Zagros, for instance, suggests that scattering is confined to a very heterogeneous and narrow zone. That is the epicentral distance may not be significantly smaller than

the distance between station and scatterer or epicenter and scatterer as pro-posed Aki (1969). If true, it implies that the coda excitation and attenua-tion, at least in this case, is caused by intrinsic absorption due to rays mul-tipathing within the crust (Herrmann and Kijko, 1983). Further investiga-tion of this observation may have important implications.

If Q_0 is recognized as a measure of the tectonic history of a region, it seems intuitively obvious to expect very low Q_0 values along the Zagros mountains. This is especially so considering that scattering is stronger in the perpendicular than parallel directions to structural boundaries and faults (Aki, 1980). Nevertheless, lateral heterogeneity along the trend of major continental deformation zones is also very intense. In other words, regard-less of the path direction, whether across or along, propagating waves are subject to high attenuation in such regions. In contrast, the Singh and Herrmann (1983) study shows that Q_0 along the Appalachian mountains is 1000, and 400-600 along the northern Rocky mountains in the United States. These results imply the lack or scarcity of scatterers (whether struc-tural, topographic or anomalous elastic properties) throughout the mountain belts. Since both regionalization and coverage effects can be ruled out, these high Q_0 values could be due to, (1) the zero crossing technique for measuring observed coda frequency data, (2) the ambiguity of master curve matching, (3) including non-predominant observed coda frequencies in the data. These frequencies typically arrive at short travel times, and lie above the master curves. They simply exceed the predicted predominant fre-quency of the peak system response, a function of the instrument type, as defined by Herrmann's (1980) model (5.8 or 5.9). Fortunately, using the extended coda-Q technique these frequencies can easily be identified and

discarded.

Finally, owing to the lack of highly sensitive standardized seismological stations and scarcity of recorded earthquakes within the Arabian plate, it is apparent that mapping the attenuation of each of the individual tectonic units is unlikely at this stage. Such a dense network of stations should be capable of detecting and precisely locating earthquakes with magnitudes significantly lower than $m_b = 4.0$. Nevertheless, with the aid of additional data, over a longer period of time than used in this study, it seems possible to better map the tectonic units and their attenuation characteristics, and to develop an adequate 1 s period local $m_b(Lg)$ magnitude scale following Nuttli's (1973) methodology. An appropriate regionalization technique may be incorporated to achieve this objective.

CHAPTER 7

CONCLUSIONS

The Arabian plate is probably one of the least studied seismotectonic regions of the Earth. For pure economic purposes, most of the available publications are only concerned with its surface geology and shallow sedimentary structures. It is well known that better understanding of the evolution and geophysical characteristics of a region has far more implications than pure academic research. It is also well known from the geologic and recent history of the region, that the interior of this plate has had its share of devastating earthquakes. Existing major faults and evidence of past volcanic activities along its western boundary should serve as a reminder of what could happen. If long term and broader economic issues are to be considered, then such topics as seismic hazard mitigation and locating new mineral resources can only be addressed with significantly improved knowledge of the seismotectonic setting and geodynamics of this plate.

The main objective of this study is to advance our understanding of the seismotectonic environment of the Arabian plate by investigating the crustal velocity structure and attenuation of high-frequency seismic waves propagation across the region. In the first part of this work, two complementary approaches are followed to analyze the vertical and lateral velocity variations of the plate seismic structure. The first approach included the calculation of Rayleigh wave long period fundamental and first higher modes group velocity dispersion curves for 104 plate margin events, classifying the mixed-path data into 19 paths, and estimating the shear velocity

-291-

structure by inverting the averaged curves along these paths. The second approach included using the grid-dispersion inversion method to determine pure-path dispersion curves, invert for the shear velocity structure of the individual grid element, and create a three-dimensional velocity model for the Arabian plate. The following conclusions are inferred from this effort:

1. The lateral distribution of calculated Rayleigh wave group velocities correlate well with the surface tectonic provinces of the Arabian plate, and indicate significant spatial variation in its crustal seismic structure. At short periods, this is manifested by observed increase in velocities for paths across the Arabian shield, and velocity decrease for paths traversing the Arabian platform and Mesopotamian foredeep. This is contrary to Knopoff and Fouda (1975) conclusion, who proposed an average phase velocity dispersion curve for the entire plate.

2. Due to the shallow depth of earthquakes associated with the Arabian plate boundaries, the surface waves recorded at stations TAB, SHI, EIL and JER exhibit well developed normally dispersed fundamental and higher modes at short periods. Events whose paths traverse the Mesopotamian foredeep show remarkable sinusoidal fundamental-mode surface waves that are characteristic of sedimentary basins. The mixed-path Rayleigh wave group velocity is found to be as low as 1.92 km/sec at 3.0 sec period, and the highest group velocity is found to be 3.87 km/sec at 68 sec. The first higher-mode velocities are found to vary between 2.74 km/sec and 4.46 km/sec over a period range of 3-21 sec. In general, these velocities are noticeably lower than values obtained for other regions of the earth.

3. The inverted mixed-path dispersion curve models suggest that the velocity structure of the Arabian plate is characterized by a relatively thick, 5-15 km, sedimentary layer. The models also suggest the Conrad and Moho discontinuities vary in depth between 15-20 km and 37-45 km, respectively. The crust is thinner under the shield, and thicker under the Mesopotamian foredeep. Contrary to Knopoff and Fouda (1975), the upper mantle models show a relatively high velocity layer, approximately 100 km thick, followed by a pronounced low velocity layer below 120-140 km depth. The shear velocities within these layers vary over a wide range, depending on the tectonic provinces their paths traverse. Furthermore, the shield crustal structures obtained in this study show remarkable agreement with the Saudi Arabia deep-refraction models inferred by Mooney *et al.* (1985).

4. The estimated three-dimensional model shows significant lateral and vertical velocity variations, and correlates very well with the major tectonic features of the plate. The model clearly delineates the boundaries of the Arabian shield and extension of the Mesopotamian foredeep. Near the surface, i.e., at a 5 km depth, the shear velocity within shield reaches 3.2 km/sec, and drops to approximately 2.6 km/sec within the Mesopotamian foredeep. At a 25 km depth, the difference in velocity between these major tectonic provinces rapidly decreases to 0.3 km/sec, indicating less spatial variation in the lower than upper crust of the Arabian plate. Also, the configuration of velocity and depth contours estimated from the three-dimensional model show remarkable agreement with Brown's (1972) tectonic map for the region.

5. Although, the three-dimensional model shows that the crustal veloci-
ties for the shield region are generally higher than the rest of the plate,
a clear reversal in the lateral velocity distribution is observed below
40.0 km depth. While the shear velocity under the shield decreases
with increasing depth, it gradually increases under the foredeep. This
finding not only agrees with the Woodhouse and Dziewonski (1984)
result, but also compliments it by extending the reversed lateral velo-
city distribution to shallower depths, which is beyond the resolution of
their data.

In the second part of this work, the lateral variation of attenuation of
Lg coda wave across the Arabian plate is investigated. The conclusions
surmised from this effort are:

1. The estimated Q_0 and ζ values reveal significant lateral variation
between the Arabian and Iranian plates, and along the Zagros con-
tinental collision zone, in particular. The regional pattern of attenua-
tion within the Arabian plate itself shows gradual lateral variation. It
is less distinct, because of the influence of station location and earth-
quake distribution with respect to the tectonic features of the plate. It
also reflects the effect of gradual transitions between the various geo-
logical units within the region.

2. At 1 Hz average $Q_0 = 214$, $\zeta = 0.6$, and $\gamma = 0.0045 km^{-1}$ are found for
the Arabian plate. These values are low, and are comparable to
Nuttli's (1980) values for the Iranian plate. The Q_0 values for the
shield are also surprisingly low, because they seem to vary between
157 and 300. This may be attributed to the relatively young age and

intensive metamorphism and deformation of the Arabian shield. The lowest Q_0 values are found along the Zagros region, and they seem to increase gradually away from the axis of this continental collision zone.

3. The "extended coda-Q" method developed in this study, provides an efficient deterministic approach for calculating Q_0 and ζ simultaneously. It also provides a direct mean for estimating the necessary error bounds that can be associated with the quality of data and reliability of calculated results. The primary advantage of this technique is that, it overcomes the limitation and ambiguity of the master curve matching approach. However, due to the intrinsic relationship between Q_0 and ζ, the "extended coda-Q" model does not provide for the independent estimation of either parameter.

Finally, it is important to mention, that the geographic distribution of stations TAB, SHI, EIL and JER provided a reasonable coverage of the Arabian plate. However, the need for a number of additional standardized state-of-the-art seismological stations and networks throughout the region can not be emphasized enough in order to conduct advanced seismological research.

APPENDIX -- A

SURFACE WAVE EVENTS

Table A–1. List of events used in the surface wave analysis.

		Surface Wave Events				
Date	Origin time Hr:Min:Sec	Latitude degrees	Longitude degrees	Depth km	Mag.	Average Path*
1970/04/28	03:20:34.70	27.666	33.631	05.0	4.9	3,7
1970/09/05	11:38:46.10	14.830	53.756	33.0	4.9	5
1971/03/19	13:27:11.70	14.582	56.229	33.0	5.3	4,18
1971/04/15	18:57:24.30	12.856	48.533	33.0	5.0	5,19
1972/01/12	08:15:46.10	27.527	33.748	54.0	5.1	3,7
1972/01/14	22:10:03.70	32.820	46.855	33.0	5.1	8
1972/02/04	16:33:17.70	13.218	49.413	33.0	4.8	1
1972/06/13	00:55:37.30	33.100	46.256	27.0	5.1	8
1972/06/14	04:34:28.10	33.029	46.101	33.0	5.3	8
1972/06/23	08:39:35.80	32.888	46.188	40.0	4.6	8
1972/06/28	09:49:34.90	27.649	33.760	15.0	5.6	3,7
1972/07/02	12:56:06.70	30.096	50.845	31.0	5.4	17
1972/07/03	02:10:00.40	30.105	50.788	38.0	5.0	17
1972/07/03	05:24:15.30	13.897	53.567	33.0	5.0	5
1972/07/16	02:46:50.70	38.261	43.277	40.0	4.9	9,10,17
1972/08/06	15:36:55.40	14.636	55.838	33.0	4.7	4,18
1972/08/06	15:53:55.60	14.707	55.617	33.0	5.2	4,18
1972/08/06	16:06:09.40	14.756	55.590	33.0	5.3	4
1972/08/06	16:44:37.60	14.409	55.607	33.0	5.1	4,18
1972/09/20	20:44:53.20	14.421	56.637	33.0	5.3	1,14,18
1972/09/20	20:52:36.20	14.250	56.516	33.0	4.9	1
1972/11/28	10:19:28.30	14.757	53.773	33.0	4.8	5
1973/02/07	05:27:20.00	32.050	49.428	51.0	5.2	12,17
1973/02/24	00:02:40.10	28.584	52.620	27.0	5.2	13,17
1973/03/13	06:03:49.00	32.052	49.401	33.0	4.9	12,17
1973/03/14	03:45:41.70	32.019	49.358	33.0	4.5	17
1973/03/28	03:36:38.20	28.573	52.671	37.0	5.2	13
1973/03/28	10:45:30.30	11.819	42.698	33.0	4.6	2,6
1973/03/28	14:59:06.70	11.748	42.870	33.0	5.2	2
1973/04/01	06:29:27.70	11.613	42.927	33.0	4.8	2,6
1973/04/04	21:51:58.40	12.160	46.192	33.0	4.5	19
1973/04/05	01:59:12.60	12.253	46.423	33.0	4.6	19
1973/04/07	17:36:42.80	11.690	43.021	33.0	4.7	2
1973/04/13	14:13:56.90	11.943	43.789	33.0	4.8	2
1973/04/22	21:29:57.20	30.742	49.832	57.0	5.0	13,17
1973/05/13	11:19:36.50	14.750	55.668	11.0	5.0	1,4,18
1973/06/25	10:29:02.60	29.995	50.461	48.0	5.0	17
1973/08/05	09:44:52.30	31.056	49.996	33.0	4.6	17
1973/08/23	12:26:24.80	31.773	50.936	41.0	5.0	17
1973/08/24	02:06:01.60	27.832	52.734	33.0	5.1	17
1973/08/25	14:58:10.80	28.079	56.755	56.0	5.4	17
1973/08/30	07:36:23.60	38.031	42.698	33.0	4.8	9,10
1973/09/10	03:02:04.20	38.491	39.621	33.0	4.9	9,10,11
1973/09/27	22:07:16.70	13.221	50.676	33.0	5.0	1,5
1973/09/28	11:32:23.30	13.244	50.722	33.0	5.5	1,5

Table A–1. Continued.

Date	Origin time Hr:Min:Sec	Latitude degrees	Longitude degrees	Depth km	Mag.	Average Path*
			Surface Wave Events			
1973/10/27	15:41:48.80	14.351	53.318	33.0	4.7	1,5
1973/11/02	05:46:37.60	32.664	48.214	55.0	4.9	17
1973/11/05	05:36:06.20	32.924	49.598	51.0	5.2	17
1973/11/05	20:11:57.80	37.943	42.814	47.0	4.7	16
1973/11/13	22:19:24.70	32.627	48.289	48.0	4.8	17
1974/01/07	15:24:38.20	33.303	47.924	32.0	5.0	12
1974/03/07	11:36:02.40	37.599	55.828	21.0	5.1	12
1974/03/11	20:21:34.50	28.459	52.778	44.0	4.7	17
1974/03/12	06:53:52.10	38.405	44.024	50.0	4.5	11,16
1974/04/17	18:27:33.70	17.255	40.365	33.0	5.0	2
1974/05/20	10:42:05.90	13.382	50.233	33.0	5.1	1,5,15
1974/06/15	03:32:48.10	13.715	50.470	33.0	5.2	1,5
1974/08/02	08:23:44.00	30.460	50.589	44.0	4.8	13
1974/08/05	13:19:39.50	27.979	53.548	11.0	5.3	17
1974/10/17	04:10:15.80	30.885	49.580	35.0	4.6	13,17
1974/11/01	12:46:35.70	14.698	52.159	33.0	4.8	15
1974/11/22	09:44:17.00	32.715	49.986	52.0	4.6	17
1974/11/25	16:35:44.50	13.483	51.513	33.0	5.0	1,5,15
1974/11/27	07:39:15.80	33.208	46.903	31.0	4.9	8,17
1974/11/27	16:52:49.90	35.297	45.655	50.0	5.0	16
1975/01/01	00:29:56.80	36.581	36.463	15.0	4.8	9
1975/03/29	09:36:21.00	13.325	50.738	33.0	5.4	15
1975/04/19	13:45:50.10	14.416	56.515	33.0	5.3	4,14
1975/04/19	17:10:54.80	14.514	56.510	33.0	5.0	4
1975/04/19	18:43:59.10	14.462	56.380	33.0	5.1	4
1975/04/19	20:15:43.50	14.424	56.445	33.0	5.4	4,14
1975/04/19	23:29:13.40	14.496	56.411	68.0	5.0	4
1975/04/20	02:06:32.70	14.129	56.353	33.0	5.0	4
1975/04/20	03:41:06.50	14.188	56.513	33.0	5.0	4
1975/04/20	08:56:49.80	14.580	56.493	33.0	5.1	4,18
1975/04/20	09:55:06.30	14.607	56.520	33.0	5.0	18
1975/04/21	02:25:56.70	14.398	56.514	33.0	4.9	18
1975/04/21	03:54:18.20	14.436	56.423	33.0	4.9	18
1975/04/20	21:22:47.10	14.580	56.403	33.0	5.0	4
1975/04/22	03:38:56.70	14.723	54.883	33.0	5.0	5,14,18
1975/04/22	06:35:36.80	14.730	54.858	33.0	5.0	18
1975/04/22	18:25:37.80	14.501	56.514	33.0	5.2	18
1975/04/22	21:35:26.00	14.538	56.594	33.0	5.2	4,14,18
1975/04/22	22:17:49.50	14.398	56.469	33.0	5.0	4
1975/04/22	23:27:13.20	14.375	56.543	33.0	4.8	4,14,18
1975/04/23	15:02:10.50	14.586	56.309	33.0	5.2	4
1975/04/30	23:40:30.70	14.602	56.555	33.0	5.3	4,14,18
1975/05/01	02:37:42.90	14.569	56.437	33.0	5.1	18
1975/12/14	23:16:47.60	14.620	42.240	33.0	5.3	2,6
1975/12/14	23:27:25.90	14.735	42.318	33.0	5.3	2,6

- 298 -

Table A–1. Continued.

		Surface Wave Events				
Date	Origin time Hr:Min:Sec	Latitude degrees	Longitude degrees	Depth km	Mag.	Average Path*
1976/02/05	08:14:05.00	14.142	53.333	33.0	5.0	15
1976/11/16	12:53:33.70	15.905	41.915	33.0	4.9	6
1977/02/28	08:43:55.70	14.878	54.953	33.0	5.1	18
1977/02/28	17:35:06.50	14.811	55.013	33.0	5.1	5,18
1977/12/17	23:57:45.90	13.125	50.943	33.0	5.0	5
1978/02/11	12:54:21.60	13.164	50.948	33.0	5.3	5
1978/03/01	01:58:45.20	13.230	50.209	33.0	5.1	5
1978/09/14	05:01:41.30	12.069	47.211	33.0	4.7	19
1978/09/14	07:14:17.00	12.517	47.832	33.0	4.8	19
1978/09/14	19:03:45.10	12.806	47.778	33.0	4.7	19
1978/11/07	06:44:18.50	11.660	42.596	33.0	4.6	2,6
1978/11/08	07:42:22.20	11.692	42.367	33.0	4.8	2,6
1978/11/08	08:44:45.90	11.352	42.996	33.0	4.6	2,6
1979/09/10	20:57:25.00	12.022	46.032	10.0	4.9	19

*   1 = T164, 2 = T190, 3 = T228, 4 = S166, 5 = S181, 6 = S212, 7 = S267,
    8 = S305, 9 = S310, 10 = S316, 11 = E30, 12 = E67, 13 = E84, 14 =
    E123, 15 = E131, 16 = J54, 17 = J89, 18 = J127, 19 = J147.

APPENDIX – B

CODA WAVE EVENTS

Table B-1. List of station SHI events used in the coda wave analysis.

Date	Origin time (Hr:Min:Sec)	Latitude (degrees)	Longitude (degrees)	Depth (km)	Magnitude
1971/08/09	02:54:36.70	36.25	52.72	27.0	5.2
1971/08/28	16:34:44.40	37.64	55.82	33.0	4.8
1971/09/08	12:53:34.00	29.18	60.01	12.0	5.4
1971/09/09	15:10:03.40	37.30	30.24	23.0	5.3
1971/10/05	18:31:17.70	27.19	55.79	39.0	5.1
1971/10/15	14:19:31.60	37.29	54.60	39.0	4.7
1971/11/03	09:42:50.40	28.26	56.96	33.0	4.7
1971/11/09	00:16:58.20	26.99	54.52	33.0	4.8
1971/11/13	15:47:41.50	10.97	39.68	24.0	5.3
1971/12/09	01:42:30.70	27.24	56.40	15.0	5.3
1971/12/20	01:29:18.50	41.21	48.34	33.0	5.0
1971/12/20	01:41:04.90	41.14	48.39	33.0	5.2
1971/12/20	23:27:38.50	28.35	57.23	33.0	4.9
1972/01/12	08:15:46.10	27.53	33.75	54.0	5.1
1972/01/14	22:10:03.70	32.82	46.85	33.0	5.1
1972/01/18	21:12:01.70	37.54	48.68	33.0	4.9
1972/02/03	02:29:21.90	40.72	48.40	39.0	5.1
1972/02/05	21:52:43.50	33.92	47.13	54.0	4.7
1972/03/08	21:49:10.60	27.61	56.74	45.0	4.9
1972/03/14	14:05:45.80	39.28	29.42	33.0	5.4
1972/03/22	00:51:51.60	40.28	42.13	34.0	4.8
1972/04/03	09:07:16.00	28.12	57.19	52.0	5.0
1972/04/17	15:12:43.50	31.94	59.34	44.0	4.5
1972/05/18	02:42:55.80	27.92	55.84	34.0	4.6
1972/06/06	17:54:43.30	26.86	53.37	54.0	4.9
1972/06/14	04:34:28.10	33.03	46.10	33.0	5.3
1972/06/23	08:39:35.80	32.89	46.19	40.0	4.6
1972/06/28	09:49:34.90	27.65	33.76	15.0	5.6
1972/06/30	17:49:33.40	27.20	56.82	33.0	4.6
1972/07/11	22:49:02.30	36.07	45.71	33.0	4.7
1972/07/16	02:46:50.70	38.26	43.28	40.0	4.9
1972/08/02	21:33:06.30	28.22	56.95	38.0	4.7
1972/08/02	23:03:28.90	28.08	56.85	31.0	5.0
1972/08/03	22:47:45.50	28.20	56.99	62.0	4.8
1972/08/06	01:12:50.40	25.07	61.23	33.0	5.5
1972/08/06	01:32:16.00	25.72	60.90	33.0	5.0
1972/08/08	00:44:55.20	36.30	52.57	47.0	4.7
1972/08/08	19:09:33.50	25.03	61.13	41.0	5.5
1972/10/09	07:18:23.60	28.17	56.03	33.0	5.2
1972/11/04	09:32:22.00	28.54	56.99	33.0	4.9
1972/11/10	04:45:11.70	30.26	57.57	33.0	4.7
1972/11/17	09:09:00.10	27.35	59.09	65.0	5.4
1972/12/01	11:39:03.60	35.42	57.91	33.0	5.4
1973/04/13	14:13:56.90	11.94	43.79	33.0	4.8
1974/04/17	18:27:33.70	17.25	40.37	33.0	5.0

Table B–2. List of station EIL events used in the coda wave analysis.

	Station EIL Events				
Date	Origin time (Hr:Min:Sec)	Latitude (degrees)	Longitude (degrees)	Depth (km)	Magnitude
1973/01/06	15:39:31.00	38.00	46.43	24.0	4.2
1973/01/10	17:02:56.00	31.19	51.28	33.0	4.4
1973/01/18	22:35:18.80	32.75	48.01	57.0	4.4
1973/02/24	00:02:40.10	28.58	52.62	27.0	5.2
1973/03/12	13:21:49.10	32.05	49.35	62.0	4.9
1973/03/12	15:39:58.10	31.88	49.14	33.0	4.5
1973/03/13	06:03:49.00	32.05	49.40	33.0	4.9
1973/03/14	03:45:41.70	32.02	49.36	33.0	4.5
1973/03/28	03:36:38.20	28.57	52.67	37.0	5.2
1973/04/04	21:51:58.40	12.16	46.19	33.0	4.5
1973/04/05	01:59:12.60	12.25	46.42	33.0	4.6
1973/04/05	19:24:01.60	30.92	50.53	33.0	4.0
1973/04/07	10:49:27.20	27.88	52.51	33.0	4.3
1973/04/22	21:29:57.20	30.74	49.83	57.0	5.0
1973/05/03	07:44:24.20	28.20	51.90	41.0	4.6
1973/08/25	14:58:10.80	28.08	56.76	56.0	5.4
1973/09/23	03:43:12.40	30.72	49.25	41.0	4.2
1974/02/18	18:23:36.40	37.57	43.43	18.0	4.0
1974/03/11	20:21:34.50	28.46	52.78	44.0	4.7
1974/03/12	01:45:35.90	32.22	50.15	34.0	4.4
1974/03/12	06:53:52.00	38.40	44.02	50.0	4.5
1974/03/31	20:53:37.60	37.65	37.83	33.0	3.4
1974/04/11	21:02:20.90	29.72	51.56	23.0	3.8
1974/04/29	22:41:11.70	32.73	46.58	33.0	3.8
1974/05/04	22:08:24.50	31.83	50.60	46.0	4.5
1974/05/17	19:46:20.20	31.29	51.11	33.0	4.5
1974/06/05	16:00:13.10	30.50	52.40	60.0	4.1
1974/06/12	10:19:51.10	34.04	37.69	33.0	4.6
1974/06/21	16:03:57.20	12.81	46.84	33.0	4.5
1974/06/13	21:06:10.20	38.73	39.18	33.0	4.5
1974/08/02	08:23:44.00	30.46	50.59	44.0	4.8
1974/08/05	13:19:39.50	27.98	53.55	11.0	5.3
1974/10/17	04:10:15.80	30.89	49.58	35.0	4.6
1974/11/01	12:46:35.70	14.70	52.16	33.0	4.8
1974/11/22	09:04:46.10	32.75	49.82	58.0	4.1
1974/11/22	09:44:17.00	32.72	49.99	52.0	4.6
1974/11/25	16:35:44.50	13.48	51.51	33.0	5.0

- 302 -

Table B–3. List of station JER events used in the coda wave analysis.

Date	Origin time (Hr:Min:Sec)	Latitude (degrees)	Longitude (degrees)	Depth (km)	Magnitude
1973/02/07	05:27:20.00	32.05	49.43	51.0	5.2
1973/03/05	23:59:46.60	27.69	33.64	25.0	4.5
1973/03/12	13:21:49.10	32.05	49.35	62.0	4.9
1973/03/13	06:03:49.00	32.05	49.40	33.0	4.9
1973/03/14	03:45:41.70	32.02	49.36	33.0	4.5
1973/03/28	03:36:38.20	28.57	52.67	37.0	5.2
1973/04/04	21:51:58.40	12.16	46.19	33.0	4.5
1973/04/05	01:59:12.60	12.25	46.42	33.0	4.6
1973/04/22	21:29:57.20	30.74	49.83	57.0	5.0
1973/06/25	10:29:02.60	30.00	50.46	48.0	5.0
1973/08/05	09:44:52.30	31.06	50.00	33.0	4.6
1973/08/06	05:31:45.00	31.08	49.87	48.0	4.5
1973/08/15	04:35:42.90	30.92	49.97	33.0	4.1
1973/08/23	12:26:24.80	31.77	50.94	41.0	5.0
1973/08/24	02:06:01.60	27.83	52.73	33.0	5.1
1973/08/30	07:36:23.60	38.03	42.70	33.0	4.8
1973/11/05	20:11:57.80	37.94	42.81	47.0	4.7
1973/11/08	13:00:52.80	32.41	48.10	46.0	4.2
1974/10/17	04:10:15.80	30.89	49.58	35.0	4.6
1974/11/17	03:25:49.10	36.79	42.59	20.0	3.9
1974/11/27	07:39:15.80	33.21	46.90	31.0	4.9
1974/11/27	16:52:49.90	35.30	45.65	50.0	5.0

- 303 -

BIBLIOGRAPHY

Adams, R. D., and M. Barazangi (1984). Seismotectonics and seismology in the Arab region: A brief summary and future plans, *Bull. Seism. Soc. Am.* **74**, 1011-1030.

Aki, K. (1969). Analysis of the seismic coda of local earthquakes as scattered waves, *J. Geophys. Res.* **74**, 615-631.

Aki, K. (1980). Scattering and attenuation of shear waves in the lithosphere, *J. Geophys. Res.* **85**, 6496-6504.

Aki, k., and B. Chouet (1975). Origin of coda-waves: source, attenuation, and scattering effects, *J. Geophys. Res.* **80**, 3322-3342.

Aki, K., and M. Tsujiura (1959). Correlational study of near earthquake waves, *Bull. Earthq. Res. Inst.* **37**, Tokyo University, 207-232.

Aki, K., M. Tsjiura, M. Hori, and K. Goto (1958). Spectral study of near earthquake waves, *Bull. Earthq. Res. Inst.* **36**, Tokyo University, 71-98.

Ala, M. (1974). Salt diapirism in southern Iran, *Am. Assoc. Pet. Geol.* **58**, 1758-1770.

Al-Shanti, A. M. (1984). Pan-African crustal evolution in the Arabian-Nubian sheild, I.G.C.P. Project 164, *F.E.S. Bull.* **6**, Faculty of Earth Scinces, King Abdulaziz University, Jeddah, Kingdom of Saudi Arabia, p. 632.

Alsinawi, S. A., and I. Benno (1976). The first Microeathquake recording in Iraq, *Tectonophysics* **36**, T1-T6.

Alsinawi, S. A., and H. A. A. Ghalib (1973). On the seismotectonics of the Arab countries, *Proceedings of the 7th Arab Sci. Conference*, Cairo, Egypt.

Alsinawi, S. A., and H. A. A. Ghalib (1975a). Seismicity and seismotectonics of Iraq, *Bull. Coll. Sci.* **16**, College of Science, University of Baghdad, 369-413.

Alsinawi, S. A., and H. A. A. Ghalib (1975b). Historical seismicity of Iraq, *Bull. Seism. Soc. Am.* **65**, 541-547.

Ambraseys, N. N. (1961). The seismicity of southwest Asia: Data from 15-century Arabic manuscript, *Rev. Etude Calamites* **37**, Geneva.

Ambraseys, N. N. (1971). Value of historical records of earthquakes, *Nature* **232**, 375-379.

Ambraseys, N. N. (1978). The relocation of epicenters in Iran, *Geophys. J. R. ast. Soc.* **53**, 117-121.

-304-

Ambraseys, N. N., and M. Barazangi (1989). The 1759 earthquake of the Bekaa valley: Implications for earthquake hazard assessment in the eastern Mediterranean region, *J. Geophys. Res.* 94, 4007-4013.

Arkhangel'skaya, V. M., A. Gergaui, and B. I. Shechkov (1974). On the structure of the earth's crust in the regions of the Arabian peninsula and the Iranian highland according to surface-wave dispersion, *Izv., Earth Physics* 9, 580-584.

Asudeh, I. (1982). Seismic structure of Iran from surface and body wave data, *Geophys. J. R. astr. Soc* 71, 715-730.

Asudeh, I. (1983). I.S.C. mislocation of earthquakes in Iran and geometrical residuals, *Tectonophysics* 95, 61-74.

Backus, G., and F. Gilbert (1967). Numerical applications of a formalism for geophysical inverse problems, *Geophys. J. R. astr. Soc.* 13, 247-276.

Backus, G., and F. Gilbert (1968). The resolving power of gross earth data, *Geophys. J. R. astr. Soc.* 16, 169-205.

Backus, G., and F. Gilbert (1970). Uniqueness in the inversion of gross earth data, *Phil. Trans. R. Soc. Lond.* A 266, 123-192.

Barazangi, M., J. Oliver, and B. Isacks (1977). Relative excitation of the seismic shear waves Sn and Lg as a function of source depth and their propagation from Melanesia and Banda arcs to Australia, *Annali di Geofisica* 30, 385-407.

Baraznagi, M. (1981). Evaluation of seismic risk along the western part of the Arabian plate: Discussion and recommendations, *Bull. Faculty of Earth Sci.* 4, King Abdulaziz University, Jeddah, Saudi Arabia, 77-87.

Ben-Avraham, Z., Z. Garfunkle, G. Almagro, and J. K. Hall (1979). Continental breakup by leaky transform: the Gulf of Elat (Aqaba). *Science* 206, 214-216.

Ben-Menahem, A.(1979). Earthquake catalogue for the Middle East (92 B.C.-1980 A.D.), *Boll. Geofisica Teor. Appl.* 21, 245-310.

Ben-Menahem, A., and E. Aboodi, M. Vered, and R. Kovach (1977). Rate of seismicity of the Dead Sea region over the past 4000 years, *Phys. Earth Planet. Interiors* 14, 17-27.

Ben-Menahem, A., and E. Aboodi (1981). Micro and macroseismicity of the Dead Sea rift and off-coast eastern Mediterranean, *Tectonophysics* 80, 199-233.

Ben-Menahem, A., A. Nur, and M. Vered (1976). Tectonics, Seismicity and structure of the Afro-Eurasian junction - The braking of an incoherent plate, *Phys. Earth Planet. Int.* 12, 1-50.

Berberian, M. (1979). Evaluation of the instrumental and relocated epicenters of Iranian earthquakes, *Geophys. J. R. astr. Soc.* **58**, 625-630.

Berberian, M. (1981). Active faulting and tectonics of Iran, *A.G.U. Geodynamic Series* **3**, 33-69.

Birch, F. (1964). Density and composition of the mantle and core, *J. Geophys. Res.* **69**, 4377-4388.

Bloch, S., A. L. Hales, and M. Landisman (1969). Velocities in the crust and upper mantle of southern Africa from multi-mode surface wave dispersion, *Bull. Seism. Soc. Am.* **59**, 1599-1629.

Brown, G. F. (1972). *Tectonic map of the Arabian peninsula*, Scale 1:4000000, U.S. Geologic Survey.

Bullen, K. E., and B. A. Bolt (1985). *An Introduction to the Theory of Seismology*, Cambridge University Press, Cambridge, p. 499.

Chase, C. G. (1978). Plate kinematics: The Americas, East Africa, and the rest of the world, *Earth Planet. Sci. Lett.* **37**, 355-368.

Chen, P., O. W. Nuttli, W. Ye, and J.Qin (1984). Estimates of short-period Q values and seismic moments from coda waves for earthquakes of the Beijing and Yu-Nan regions of China, *Bull. Seism. Soc. Am.* **74**, 1189-1207.

Clearbout, J. F. (1976). *Fundamentals of Geophysical Data Processing with Applications to Petroleum Prospecting*, McGraw-Hill Book Company, New York.

Cochran, J. R. (1981). The Gulf of Aden: structure and evolution of a young ocean basin and continental margin, *J. Geophys. Res.* **86**, 263-287.

DeMets, C., R. G. Gordon, D. F. Argus, and S. Stein (1990). Current plate motions, *Geophys. J. Int.* **101**, 425-478.

Der, Z. A., R. Massé, and M. Landisman (1970). Effects of observational errors on the resolution of surface waves at intermediate distances, *J. Geophys. Res.* **75**, 3399-3409.

Der, Z. A., and M. Landisman (1972). Theory for errors, resolution, and separation of unknown variables in inverse problems, with application to the mantle and the crust in southern Africa and Scandinavia, *Geophys. J. R. astr. Soc.* **27**, 137-178.

Draper, N. R., and H. Smith (1981). *Applied Regression Analysis*, John Wiley and Sons, Inc., New York, p. 709.

Dziewonski, A., S. Bloch, and M. Landisman (1969). A technique for the analysis of transient seismic signal, *Bull. Seism. Soc. Am.* **59**, 427-444.

El-Isa, Z. H., H. M. Merghelani, and A. Al-Shanti (1984). The Gulf of Aqaba earthquake swarm of 1983 January-April, *Geophys. J. R. astr. Soc.* **78**, 711-722.

El-Isa, Z. H., and A. Al-Shanti (1989). Seismicity and tectonics of the Red Sea and western Arabia, *Geophys. J.* **97**, 449-457.

Fairhead, J. D., and R. W. Girdler (1970). Seismicity of the Red Sea, *Phil. Trans. Roy. Soc. London* A **267**, 49-74.

Falcon, N. L. (1967). The geology of the northeastern margin of the Arabian basement shield, *Adv. Sci.* **24**, 31-42.

Feng, C. C., and T. L. Teng (1983). Three-dimensional crust and upper mantle structure of the Eurasian continent, *J. Geophys. Res.* **88**, 2261-2272.

Forsyth, D. W. (1975). The early structural evolution and anisotropy of the oceanic upper mantle, *Geophys. J. R. astr. Soc.* **43**, 103-162.

Franklin, J. N. (1970). Well-posed stochastic extension of ill-posed linear problems, *J. Math. Anal. Appl.* **31**, 682-716.

Freund, R. (1965). A model of the structural development of Israel and adjacent areas since Upper Cretaceous times, *Geol. Mag.* **102**, 189-205.

Freund, R., Z. Garfunkel, I. Zak, M. Goldberg, T. Weissbrod, and B. Derin (1970). The shear along the Dead Sea rift, *Phil. Trans. Roy. Soc. London* A **267**, 107-130.

Garfunkle, Z., I. Zak, and R. Freund (1981). Active faulting in the Dead Sea rift, *Tectonophysics* **80**, 1-26.

Gettings, M. E. (1982). Heat-flow measurements at shot points along the 1978 Saudi Arabian seismic deep-refraction line. Part 2 Discussion and interpretation, **U.S. Geol. Surv. Open-File Rep. 02-40**, 40 pp.

Gettings, M. E., and A. Showail (1982). Heat-flow measurements at shot points along the 1978 Saudi Arabian seismic deep-refraction line. Part 1 Results of measurements, **U.S. Geol. Surv. Open-File Rep. 02-39**, 98 pp.

Gettings, M. E., H. R. Blank, W. D. Mooney, and J. H. Healy (1983). Crustal structure of southwestern Saudi Arabia, **U.S. Geol. Surv. Open-File Rep. U.S. Geol. Surv. Open-File Rep. 03-59**, 51 pp.

Ghalib, H. A. A., and S. Alsinawi (1974). Seismotectonics of the Arabian Peninsula: A global tectonic approach, *Bull. Coll. Sci.* **15**, College of Science, University of Baghdad, 151-169.

Ghalib, H. A. A., O. W. Nuttli, and R. B. Herrmann (1984). Unique and simultaneous determination of coda Q and its frequency dependence (abstract), *Seism. Soc. Am. Eastern Sec. 56th Annual Meeting*, Saint

Louis University, Saint Louis, MO., Oct. 10-12.

Ghalib, H. A. A., D. R. Russell, and A. Kijiko (1985). Optimal design of a seismological network for the Arab countries, *Pure Appl. Geophys.* **122**, 694-712.

Girdler, R. W., and P. Styles (1974). Two-stage Red Sea floor spreading, *Nature* **247**, 7-11.

Harris, F. J. (1978). On the use of windows for the harmonic analysis with discrete Fourier transform, *Proc. IEEE* **66**, 51-83.

Healy, J. H., W. D. Mooney, H. R. Blank, M. E. Gettings, W. M. Kohler, R. J. Lamson, and L. E. Leone (1983). Saudi Arabian seismic deep-refraction profile, Final Proj. Rep., **U.S. Geol. Surv. Open-File Rep. 2-37**, 429 pp.

Herraiz, M., and A. F. Espinosa (1986). Scattering and attenuation of high-frequency seismic waves: Development of the theory of coda waves, **U.S. Geol. Surv. Open-File Rep. 86-455**, 92 pp.

Herrmann, R. B. (1973). Some aspects of band-pass filtering of surface waves, *Bull. Seism. Soc. Am.* **63**, 703-711.

Herrmann, R. B. (1980). Q estimates using the coda of local earthquakes, *Bull. Seism. Soc. Am.* **70**, 447-468.

Herrmann, R. B. (1985). *Computer Programs in Seismology; Surface Wave Inversion*, Volume **IV**, Department of Earth and Atmospheric Sciences, Saint Louis University, Saint Louis, MO.

Herrmann, R. B., and A. Kijko (1983). Modelling some empirical Lg relations, *Bull. Seism. Soc. Am.* **56**, 157-172.

Jackson, D. D. (1972). Interpretation of inaccurate, insufficient and inconsistent data, *Geophys. J. R. astr. Soc.* **28**, 97-109.

Jackson, D. D. (1979). The use of a priori data to resolve non-uniqueness in linear inversion, *Geophys. J. R. astr. Soc.* **57**, 137-157.

Jackson, J. (1980). Errors in focal depth determination and the depth of seismicity in Iran and Turkey, *Geophys. J. R. astr. Soc.* **61**, 285-301.

Jackson, J., and T. J. Fitch (1979). Seismotectonic implications of relocated aftershock sequences in Iran and Turkey, *Geophys. J. R. astr. Soc.* **57**, 209-229.

Jackson, J., and T. Fitch (1981). Basement faulting and the focal depths of the larger earthquakes in the Zagros mountains (Iran), *Geophys. J. R. astr. Soc.* **64**, 561-586.

Jackson, J., and D. McKenzie (1984). Active tectonics of the Alpine-

Himalayan belt between wetern Turkey and Pakistan, *Geophys. J. R. astr. Soc.* **77**, 185-264.

James, D. E., and A. T. Linde (1971). A source of major error in the digital analysis of World Wide Standard Station seismograms, *Bull. Seism. Soc. Am.* **61**, 723-728.

Jenkins, G. W., and D. G. Watts (1986). *Spectral Analysis and its Application*, Hodlen-Day.

Jupp, D. L. B., and K. Vozoff (1975). Stable iterative methods for the inversion of geophysical data, *Geophys. J. R. astr. Soc.* **42**, 957-976.

Kadinsky-Cade, K., M. Barazangi, J. Oliver, and B. Isacks (1981). Lateral variation of high frequency seismic wave propagation at regional distances across the Turkish and Iranian plateaus, *J. Geophys. Res.* **86**, 9377-9396.

Kadinsky-Cade, K., and M. Barazangi (1982). Seismotectonics of southern Iran: the Oman line, *Tectonics* **1**, 389-412.

Keller, G. R., and D. R. Russell (1980). A crustal structure study of the African continent, *Annals Geo. Survey of Egypt* **10**, 955-960.

Kennett, B. L. N., S. Gregersen, S. Mykkeltveit, and R. Newmark (1985). Mapping of crustal heterogeneity in the North Sea basin via the propagation of Lg-waves, *Geophys. J. R. astr. Soc.* **83**, 299-306.

Knopoff, L. (1972). Observation and inversion of surface-wave dispersion, *Tectonophysics* **13**, 497-519.

Knopoff, L., and A. A. Fouda (1975). Upper-mantle structure under the Arabian peninsula, *Tectonophysics* **26**, 121-134.

Knopoff, L., and F. A. Schwab (1968). Apparent initial phase of a source of Rayleigh waves, *J. Geophys. Res.* **73**, 755-760.

Kovach, R. L. (1978). Seismic surface waves and crustal and upper mantle structure, *Rev. Geophys. Space. Phys.* **16**, 1-13.

Lawson, C. L., and R. J. Hanson (1974). *Solving Least Squares Problems*, Prentice-Hall, Inc., New Jersy.

Le Pichon, X. (1968). Sea-floor spreading and continental drift, *J. Geophys. Res.* **73**, 3661-3705.

Le Pichon, X., and J. Francheteau (1978). A plate-tectonic analysis of the Red Sea-Gulf of Aden area, *Tectonophysics* **46**, 369-406.

Lines, L. R., and S. Treitel (1984). A review of least-squares inversion and its application to geophysical problems, *Geophys. Prosp.* **32**, 159-186.

McKenzie, D. P., D. Davies, and P. Molnar (1970). The plate tectonics of the Red Sea and East Africa, *Nature* **226**, 243-248.

McKenzie, D. (1970). The plate tectonics of the Mediterranean region, *Nature* **226**, 239-243.

Minster, J. B., and T. H. Jordan (1978). Present-day plate motions, *J. Geophys. Res.* **83**, 5331-5354.

Mitchell, B. J., and M. Landisman (1969). Electromagnetic seismograph constants by least-squares inversion, *Bull. Seism. Soc. Am.* **59**, 1335-1348.

Mitchell, B. J., and R. B. Herrmann (1979). Shear velocity structure of the Eastern United States from the inversion of surface wave group and phase velocities, *Bull. Seism. Soc. Am.* **69**, 1133-1148.

Merghelani, H. M., and S. K. Gallanthine (1980). Microearthquakes in the Tihamat-Asir region of Saudi Arabia, *Bull. Seism. Soc. Am.* **70**, 2291-2293.

Mokhtar, T. A., R. B. Herrmann, and D. R. Russell (1988). Seismic velocity and Q model for the shallow structure of the Arabian shield from short-period Rayleigh waves, *Geophysics* **53**, 1379-1387.

Mooney, W. D., M. E. Gettings, H. R. Blank, and J. H. Healy (1985). Saudi Arabian seismic-refraction profile: A traveltime interpretation of crustal and upper mantle structure, *Tectonophysics* **111**, 173-246.

Neter, J., W. Wasserman, and M. Kutner (1983). *Applied Linear Regression Models*, Richard D. Irwin Inc., Homewood, Illinois, p. 547.

Neumann Van Padang, M. (1963). Catalogue of the active volcanoes and solfatarfields of Arabia and the Indian ocean, Part 16, in *Catalogue of the Active Volcanoes of the World*, edited by the International Association of Volocanology.

Niazi, M. (1968). Crustal thickness in the central Saudi Arabian peninsula, *Geophys. J. R. astr. Soc.* **15**, 545-547.

Niazi, M., I. Asudeh, G. Bullard, J. Jackson, G. King, and D. McKenzie (1978). The depth of seismicity in the Kermanshah region of the Zagros mountains (Iran), *Earth Planet. Sci. Lett.* **40**, 270-274.

Nowroozi, A. A. (1971). Seismotectonics of the Persian Plateau, eastern Turkey, Caucasus, and Hindu-Kush regions, *Bull. Seism. Soc. Am.* **61**, 317-341.

Nowroozi, A. A. (1972). Focal mechanism of earthquakes in Persia, Turkey, West Pakistan, and Afghanistan and plate tectonics of the Middle East, *Bull. Seism. Soc. Am.* **62**, 832-850.

Nur, A. and Z. Ben-Avraham (1978). The eastrern Mediterranean and and the

Levant: tectonics of continental collision, *Tectonophysics* 46, 297-311.

Nuttli, O. W. (1973). Seismic wave attenuation and magnitude relations for eastern North America, *J. Geophys. Res.* 78, 876-885.

Nuttli, O. W. (1980). The excitation and attenuation of seismic crustal phases in Iran, *Bull. Seism. Soc. Am.* 70, 469-486.

Nuttli, O. W. (1983a). A methodology for obtaining seismic yield estimates of underground explosions using short-period Lg waves, **Semi-Annual Report no. 1, DARPA Order No. 4397**, 1 October 1982 - 31 March 1983, Saint Louis University, 3-31.

Nuttli, O. W. (1983b). Illustration of use of coda Q method to obtain anelastic attenuation values for paths from Salmon (Mississippi) and NTS events, **Semi-Annual Report, DARPA**, 1 April 1983 - 30 September 1983, Saint Louis University, 1-29.

Nuttli, O. W. (1986). Yeild estimates of Nevada test site explosions obtained from seismic Lg waves, *J. Geophys. Res.* 91, 2137-2151.

Oliver, J., M. Ewing, and F. Press (1955). Crustal structure of the Arctic regions from the Lg phase, *Geol. Soc. Am. Bull.* 66, 1063-1074.

Panza, G. F. (1976). Phase velocity determination of fundamental Love and Rayleigh waves, *Pageoph* 114, 753-763.

Poirier, J. P., B. A. Romanowicz, and M. A. Taher (1980a). Large historical earthquakes and seismic risk in northwest Syria, *Nature* 285, 217-220.

Poirier, J. P., and M. A. Taher (1980b). Historical seismicity in the Near and Middle East, North Africa, and Spain from Arabic documents (VIIth-XVIIIth century), *Bull. Seism. Soc. Am.* 70, 2185-2201.

Pollack, H., and D. S. Chapman (1977). On the regional variation of heat flow, geotherms, and lithospheric thickness, *Tectonophysics* 38, 279-296.

Raoof, M., and O. W. Nuttli (1984). Attenuation of high-frequency earthquake waves in South America, *Pure Appl. Geophys.* 122, 619-644.

Rautian, T. G., and V. I. Khalturin (1978). The use of coda for determination of the earthquake source spectrum, *Bull. Seism. Soc. Am.* 68, 923-948.

Rodi, W. L., P. Glover, T. M. C. Li, and S. S. Alexander (1975). A fast, accurate method for computing group-velocity partial derivatives for Rayleigh and Love modes, *Bull. Seis. Soc. Am.* 65, 1105-1114.

Ross, D., and J. Schlee (1973). Shallow structure and geologic development of the southern Red Sea, *Bull. Geol. Soc.* 84, 3827-3848.

Russell, D. R. (1980). Constrained inversion techniques applied to surface

wave analysis, *M.Sc. Thesis*, University of Texas at El Paso, Texas, El Paso, TX, 76p.

Russell, D. R. (1987). Multichannel processing of dispersed surface waves, *Ph.D. Dissertation*, Saint Louis University, Saint Louis, MO, 150p.

Ruzaikin, A., I. Nersesov, V. Khalturin, and P. Molnar (1977). Propagation of Lg and lateral variations in crustal structure in Asia, *J. Geophys. Res.* **82**, 307-316.

Sborshchikov, I. M., L. A. Savostin, and L. P. Zonenshain (1981). Present plate tectonics between Turkey and Tibet, *Tectonophysics* **79**, 45-73.

Şeber, D., and B. J. Mitchell (1991). Attenuation of surface waves across the Arabian peninsula, *Tectonophysics* (in press).

Sengor, A. M. C. and W. Kidd (1979). Post-collisional tectonics of the Turkish-Iranian plateau and a comparison with Tibet, *Tectonophysics* **55**, 361-376.

Singh, S., and R. B. Herrmann (1983). Regionalization of crustal Q in the continental United States, *J. Geophys. Res.* **88**, 527-538.

Snyder, D. B., and M. Barazangi (1986). Deep crustal structure and flexure of the Arabian plate beneath the Zagros collision mountain belt as inferred from gravity observations, *Tectonics* **5**, 361-373.

Stocklin, J. (1968). Structural history and tectonics of Iran: a review, *Bull. Am. Assoc. Pet. Geol.* **52**, 1229-1258.

Stocklin, J. (1974). Possible ancient continental margins in Iran, in *Geology of Continental Margins*, edited by C. Burk and C. Drake, Springer-Verlag, New York, 873-877.

Sykes, L. R., and M. Landisman (1964). The seismicity of east Africa, the Gulf of Aden and the Arabian and Red Sea, *Bull. Seism. Soc. Am.* **54**, 1972-1940.

Suteau, A. M., and J. H. Whitcomb (1979). A local earthquake coda magnitude and its relation to duration, moment Mo and local magnitude ML, *Bull. Seism. Soc. Am.* **69**, 353-368.

Talwani, M., G. H. Sutton, and J. L. Worzel (1959). Crustal section across the Puerto Rico Trench, *J. Geophys. Res.* **64**, 1545-1555.

Tsumura, K. (1967). Determination of earthquake magnitude from total duration of oscillation, *Bull. Earthq. Res. Inst.* **45**, Tokyo University, 7-18.

Twomey, S. (1977). *Introduction to the Mathematics of Inversion in Remote Sensing and Indirect Measurments*, Elsevier Scientific Publishing Company, Amsterdam.

Wang, C. Y. (1981). Wave theory for seismogram synthesis, *Ph.D. Dissertation*, Saint Louis University, Saint Louis, MO.

Whiteman, A. J. (1970). The existence of of transform faults in the Red Sea depression, *Phil. Trans. Roy. Soc. London* A **267**, 407-408.

Wiggins, R. A. (1972). The general linear inverse problem: Implication of surface waves and free oscillations of the earth structure, *Rev. Geophys. Space Phys.* **10**, 251-285.

Wiggins, R. A. (1976). Interpolation of digitized curves, *Bull. Seism. Soc. Am.* **66**, 2077-2081.

Willis, B. (1928). Earthquakes in the Holly Land, *Bull. Seism. Soc. Am.* **18**, 72-105.

Woodhouse, J. H., and A. M. Dziewonski (1984). Mapping the upper mantle: Three-dimensional Modeling of the earth structure by inversion of seismic waveforms, *J. Geophys. Res.* **89**, 5953-5986.

Zak, I., and R. Freund (1981). Asymmetry and basin migration in the Dead Sea rift, *Tectonophysics* **80**, 27-38.

Zuwaylif, F. H. (1970). *General Applied Statistics*, Addison-Wesley Publishing Company, Reading, Massachusetts, p.311.

VITA AUCTORIS

Hafidh Abbas Ali Ghalib was born on July 23, 1947 in Baghdad, Iraq. Attended the University of Baghdad, Baghdad, Iraq, and received his Bachelor of Science degree in Geology/Geophysics in June 1971, and his Masters of Science in February 1974. He graduated from the International Institute of Seismology and Earthquake Engineering, Tokyo, Japan, and received his Post-Graduate Diploma in Seismology in August 1977. He enrolled in the Saint Louis University graduate program, and expects to receive his Doctor of Philosophy degree in Geophysics in May 1992.